Hydrocarbon migration and leakage dynamics of the Orange Basin, South Africa

vorgelegt von
Diplom-Geowissenschaftler
Alexander Hartwig
geb. in Berlin

von der Fakultät VI – Planen Bauen Umwelt
der Technischen Universität Berlin
zur Erlangung des akademischen Grades

Doktor der Naturwissenschaften
- Dr. rer. nat. -

genehmigte Dissertation

Promotionsausschuss:

Vorsitzender: Prof. Dr. Wilhelm Dominik
Gutachter: Prof. Dr. Brian Horsfield
Gutachter: Prof. Dr. Ralf Littke

Tag der wissenschaftlichen Aussprache: 30. Juni, 2014

Berlin 2014

DEDICATED

To My Family

For their endless support and patience. Danke!

EIDESSTATTLICHE ERKLÄRUNG

Hiermit versichere ich, Alexander Hartwig, dass die vorliegende Dissertation ohne unzulässige Hilfe Dritter und ohne Benutzung anderer als der angegebenen Literatur angefertigt wurde. Die Stellen der Arbeit, die anderen Werken wörtlich oder inhaltlich entnommen sind, wurden durch entsprechende Angaben der Quellen kenntlich gemacht. Diese Arbeit oder darin enthaltene Teile sind in gleicher oder ähnlicher Form weder an der Fakultät VI – Bauen Planen Umwelt der Technischen Universität Berlin noch einer anderen wissenschaftlichen Einrichtung zum Zwecke der Promotion eingereicht worden.

STATEMENT OF ORIGINAL AUTHORSHIP

I, Alexander Hartwig, hereby state, that to the best of my knowledge and belief, this thesis does not contain any previously published material or any material that has been written by another person, except where due reference is made. This thesis or any parts thereof have not previously been submitted to the Fakultät VI – Bauen Planen Umwelt at the Technical University of Berlin or any other institution for the purpose of attaining a doctoral degree.

Alexander Hartwig
Berlin, Juli 2014

ACKNOWLEDGEMENTS:

First of all, I would like to thank Prof. Dr. Rolando di Primio and Dr. Zahie Anka for their guidance, support, and the time they dedicated to the research project and me. Their enthusiasm and the numerous fruitful discussions on the subject matter helped to make this thesis possible. I would like to thank Prof. Dr. Brian Horsfield for supervising the thesis research and for introducing me to the study of organic geochemistry long before this thesis project even started. With the invaluable feedback and the shared knowledge of you three I was able to improve my skills as a scientist.

A special thanks goes to Ferdinand Perssen for the help and technical expertise provided in the pyrolysis GC-lab.

I would like to express my gratitude to Tony L. Albrecht and John P. Klein who initiated the research project between Forest Exploration International (South Africa) (PTY) (Ltd) and the Section 4.3 for Organic Geochemistry at GFZ, as well as for their extensive support and constructive feedback during the course of the work. I further want to thank the Forest Exploration International staff in Cape Town for organizing our visits and handling the data requests and exchanges.

I would like to thank Dave van der Spuy for his feedback and sharing his knowledge on South African geology. I am grateful to Forest Exploration International (South Africa) (PTY) (Ltd), the Petroleum Oil and Gas Corporation of South Africa (Pty) (Ltd), Anschutz Overseas South Africa (Pty) (Ltd), and the Petroleum Agency SA for providing the data and for permission to publish our results. The IODP project and the IODP Bremen core repository are acknowledged for providing core sample material for this study.

I was fortunate to share the most delighting multi-cultural office with Ilya Ostanin, Enmanuel Rodrigues, and Jingqiang Tang, and many thanks to Julia Nickel and Philipp Kuhn for the fun times and keeping things “running”.

A big thank you goes to Luiyin Berbesi, Nikolaus Baristeas, Gabriela Marcano, Mareike Noah, Nicolaj Mahlstedt, Markus Loegering, Alex Vetter, Steffi Pötz, Jacqueline Calzada-Mendoza, Soumaya Abbassi, Victoria Sachse, Hans-Martin Schulz, and all the great colleagues in Section 4.3 Organic Geochemistry, who made the time at GFZ a fun and unforgettable experience.

My full-hearted gratitude goes to my parents, Elke and Wilfried, for their endless support and patience throughout all of this work. Finally, I cannot be thankful enough for Sarah’s moral support, her patience, and motivating spirit, especially on weekends during the last two years, which prevented this thesis from turning into a never ending story.

ABSTRACT

The aim of this study is to delineate the active hydrocarbon (HC) kitchen and to characterize the hydrocarbon migration dynamics in the Orange Basin through time, and to investigate its potential impact on global climate on a geologic time scale by integrating seismic interpretation, organic geochemical analysis, and 3D petroleum system modeling techniques. The Orange Basin is located on the western passive margin offshore South Africa and contains more than 8 km of synrift and drift sediments related to the opening of the South Atlantic. The Kudu and Ibhubesi gas/condensate fields prove an early Cretaceous sourced petroleum system. The present-day fluid flow indicators and frequent gas shows during drilling suggest a recently active oil kitchen, the location of which was largely unconstrained, partially due to the limited knowledge on the Cenozoic margin evolution.

The seismic interpretation revealed NW-SE trending basement structures interpreted as continuations of the Paleozoic Pan African Fold Belt, similar to those found offshore Namibia and on the conjugate South American margin. The interpretations further contributed to studies on the margin segmentation and SDR emplacement, lending support to the theory, that early rifting resulted in reactivation and dextral movement along Paleozoic zones of structural weakness. An early Eocene aged paleo-pockmark field covering 2800 km^2 was identified along the northern Orange Basin slope and dated using a revised Cenozoic chronostratigraphic framework. Using 3D seismic attribute analysis it was possible to highlight the role of faults in the occurrence of these features.

A source rock characterization study demonstrated how richness and quality of Cretaceous black shales and mudstones, improve northward along the southwest African margin. Previous research emphasized the richness of the oil-prone sources. In fact, this study suggests, that Aptian and Albian source rocks in the Cape Basin are rich in degraded and terrestrial organic matter, thus being more gas- and condensate-prone. Compositional kinetic models were determined for this study, providing the first such description for Cretaceous source rocks of the southwest African margin. Application of the kinetic models and the revised chronostratigraphy show that the present-day kitchen is located in the Cenozoic depocenters along the slope.

Paleo- and present-day HC leakage was investigated using five migration models with varying flow algorithms and fault properties. They predict a main phase of primary generation during the mid to late Cretaceous-Paleocene, accompanied by widespread surface leakage before the consolidation of Upper Cretaceous regional seals. A major phase of HC leakage might have occurred during the Paleocene and Eocene when the active kitchen was located along the shelf. This suggests a thermogenic origin for petroleum fluids that created the early Eocene paleo-pockmark field. The modeled HC leakage rates of 10^{-2} to 10^{-3} teragram/year are marginal when compared to other present-day methane contributors to the atmosphere, such as wetlands and anthropogenic sources. Nevertheless, the identified early Eocene fluid flow and thermogenic gas escape event is an example of the carbon-release processes that occurred during the Paleocene-Eocene Thermal Maximum in petroliferous sedimentary basins. In conclusion, this study demonstrates that paleo and present-day HC leakage can be adequately reproduced with a 3D basin model.

ZUSAMMENFASSUNG

Für diese Studie werden die Methodiken der Seismikinterpretation, der organisch-geochemischen Analyse und 3D Beckenmodellierung integriert, um die Lage der aktiven Erdölküche des Orange Beckens zu bestimmen, die Kohlenwasserstoff-(KW)-Migrationsdynamik und -Leckage über geologische Zeiträume zu charakterisieren und deren möglichen Einfluss auf das globale Klima zu untersuchen. Das Orange Becken befindet sich am passiven westlichen Kontinentalrand Südafrikas und enthält mehr als 8 km mächtige Sedimentschichten die während der Atlantiköffnung und dem Zerfall Gondwanas abgelagert wurden.

Die Kudu und Ibhubesi Gas-Kondensatfelder, die häufig während der Erdölexploration durchteuften gashaltigen Sedimente weisen auf ein aktives Erdölsystem hin. Die Lage der rezenten Erdölküche ist aufgrund der geringen Kenntnisse über die känozoische Ablagerungsgeschichte im Orange Becken weitgehend unbekannt.

Durch die Interpretation seismischer Daten wurden NW-SE streichende Strukturelemente im Basement entdeckt, welche als Fortsetzungen paläozoischer Strukturen des Pan-Afrikanischen Faltengürtels interpretiert werden, ähnlich denen offshore Namibias und am gegenüberliegende Südamerikanischen Kontinentalrand. Des Weiteren trugen die Interpretationen zu neuen Erkenntnissen über seewärts einfallenden Reflektoren und der Segmentierung des südatlantischen Kontinentalrandes bei. Die Ergebnisse unterstützen die Theorie, dass die Reaktivierung von paläozoischen Störungszonen während der frühen Riftphase zu dextralen Bewegungen entlang diese Schwächezonen führte. Außerdem wurde ein 2800 km^2 großes Paläo-Pockmarkfeld entdeckt, welches anhand einer überarbeiteten känozoischen Chronostratigraphie auf ein früheozänes Alter datiert wird. Bezüglich der Lage der Paläo-Pockmarks konnte mit Hilfe von 3D-seismischen Attributanalysen ein Zusammenhang mit den im Untergrund vorkommenden Störungen hergestellt werden.

Die Erdölmuttergesteinseigenschaften wurden anhand von Kernproben kreidezeitlicher Tonsteine aus DSDP Bohrungen untersucht. Aus den Analysen geht hervor, dass sich das KW-Potenzial nordwärts entlang des südostatlantischen Kontinentalrandes verbessert. Frühere Studien betonten stets das KW-Potenzial der ölbildenden Muttergesteine. Im Gegensatz dazu konnte gezeigt werden, dass der Großteil der Abt- und Albmuttergesteine im Kapbecken vorwiegend terrestrisches organisches Material beinhalten und somit eher gas- und kondensatbildend sind. An den Proben wurden auch bulk- und kompositionskinetische Messungen durchgeführt und somit liefert diese Studie die erste kompositionskinetische Beschreibung der KW-Bildung für kreidezeitliche Erdölmuttergesteine am südostatlantischen Kontinentalrand. Durch Anwendung der überarbeiteten Chronostratigraphie und den kinetischen Modellen bei der Beckenmodellierung, konnte gezeigt werden, dass sich die rezente Erdölküche im Bereich der känozoischen Ablagerungsräume entlang des Schelfrandes befindet.

Die KW-Migrationsdynamik wurde anhand von fünf verschiedenen Migrationsmodelle mit unterschiedlichen Störungseigenschaften simuliert. Daraus geht hervor, dass sich die Hauptphase der primären KW-Genese von der mittleren bis späten Kreidezeit und bis ins

frühe Paläozän ereignete, welche anfangs mit weitläufiger KW-Leckage einherging, bis die spätkreidezeitichen „seals“ konsolidiert waren. Vermutlich ereignete sich eine weitere Phase der KW-Leckage im Paläozän und Eozän, als sich die damalig Erdölküche entlang des Schelfrandes befand. Dies unterstützt die Annahme, dass die Migration thermogener KW eine bedeutende Rolle bei der Entstehung des früheozänen Paläo-Pockmarkfeldes spielte. Die KW-Leckagerate liegt in der Größenordnung von 10^{-2} bis 10^{-3} Teragramm pro Jahr, welche weit unter derer von Sumpfgebieten und anthropogenen Methanquellen liegt. Trotzdem liefert das früheozäne Fluid- und thermogene KW-Leckageereignis ein Beispiel dafür, wie während des Paläozän/Eozän-Temperaturmaximums Kohlenstoffmoleküle aus einem Sedimentbecken in die Atmo-und Hydrosphäre abgegeben wurden. Die Studie zeigt, dass sich rezente und paläo Leckageereignisse anhand von 3D Beckenmodelle angemessen reproduzieren lassen.

TABLE OF CONTENTS:

ACKNOWLEDGEMENTS: V

ABSTRACT VII

ZUSAMMENFASSUNG IX

TABLE OF CONTENTS XI

LIST OF FIGURES: XV

LIST OF TABLES: XX

LIST OF PUBLICATIONS XXIII

1. INTRODUCTION 1
1.1. Study area and scientific problematics 2
1.2. Goals of the study 5
1.3. Background and summary of the three main publications 7
1.4. Geologic and geochemical background 9
1.4.1. The Organic Carbon Cycle 9
1.4.2. The Formation of Petroleum 10
1.4.3. Hydrocarbon seeps and the petroleum plumbing system 12
1.4.4. Climate change and carbon isotopic excursions in the geologic past 13
1.4.5. South Atlantic margin evolution 16
1.5. Methodology 19
1.5.1. Organic geochemical analysis 19
1.5.2. Seismic interpretation 20
1.5.3. 3D petroleum system modeling 23
1.5.3.1. Burial history - deposition, compaction, and pressure modeling 23
1.5.3.2. Thermal model - heat flow analysis 24
1.5.3.3. Petroleum generation and fluid properties 25
1.5.3.4. Migration modeling 25

2. SOURCE ROCK CHARACTERISTICS AND COMPOSITIONAL KINETIC MODELS OF CRETACEOUS ORGANIC-RICH BLACK SHALES OFFSHORE SOUTHWESTERN AFRICA 28
2.1. Introduction 28
2.2. Study area and sample locations 29
2.2.1. Southeast Atlantic margin evolution 29
2.2.2. Sample locations 31
2.2.2.1. DSDP site 361 32
2.2.2.2. DSDP site 530A 33
2.2.2.3. DSDP site 364 34
2.3. Material and Methods 34
2.3.1. Sample material 34
2.3.2. Methods 34
2.3.2.1. Rock-Eval and TOC 34
2.3.2.2. Pyrolysis - gas chromatography and Thermovaporization - gas chromatography 35
2.3.2.3. Bulk kinetics 35

2.3.2.4. Micro-scaled sealed vessel pyrolysis - gas chromatography and development of compositional kinetics 38
2.4. Results and Interpretation 39
2.4.1. Bulk characterization 39
2.4.1.1. Rock-Eval and TOC measurements 39
2.4.1.2. Bulk pyrolysis 41
2.4.2. Bulk kinetic parameters 47
2.4.3. Compositional kinetic model and calculated fluid physical properties 52
2.5. Discussion 55
2.5.1. Organofacies variation along the southwest African margin 55
2.5.2. Source rock properties 56
2.6. Conclusions 61

3. EVIDENCE OF A WIDESPREAD PALEO-POCKMARKED FIELD IN THE ORANGE BASIN: AN INDICATION OF AN EARLY EOCENE MASSIVE FLUID ESCAPE EVENT OFFSHORE SOUTH AFRICA. 62
3.1. Introduction 63
3.2. Geological setting 64
3.2.1. Late Jurassic and Cretaceous 66
3.2.2. Cenozoic 68
3.3. Data and Methods 69
3.4. Results 70
3.4.1. Slope seismostratigraphy 70
3.4.1.1. Upper Cretaceous 70
3.4.1.2. Late Maastrichtian - Paleocene 71
3.4.1.3. Eocene - Mid-Miocene 71
3.4.1.4. Mid-Miocene - Quaternary 73
3.4.2. Present-day seafloor fluid escape features 73
3.4.3. Circular depressions on horizon E-1 74
3.4.4. Late Cretaceous faults 75
3.5. Discussion 76
3.5.1. Origin of paleo-pockmarks 76
3.5.1.1. Shallow fluid sources 76
3.5.1.2. Deep fluid sources 77
3.5.2. Controls on pockmark location and lineation trends 78
3.5.3. Geologic process related to the early Eocene fluid flow event 81
3.6. Conclusions 83

4. CONSTRAINING PETROLEUM GENERATION AND MIGRATION IN THE ORANGE BASIN, SOUTH AFRICA: A 3D BASIN MODELING STUDY 84
4.1. Introduction 85
4.2. Geologic setting and petroleum system elements 88
4.2.1. Source rocks 91
4.2.2. Reservoir and seal rocks 91
4.3. 3D Model input and calibration 92
4.3.1. Depth maps 92
4.3.2. Faults 94

4.3.3. Lithofacies definition 94
4.3.4. Source rock definition and petroleum generation kinetics 96
4.3.4.1. Upper Hauterivian lacustrine synrift source rock (Synrift II) 96
4.3.4.2. Barremian - lower Aptian marine/deltaic source rock 97
4.3.4.3. Upper Aptian - lower Albian marine/deltaic source rock 97
4.3.4.4. Cenomanian/Turonian (C/T) marine condensed section 98
4.3.5. Boundary conditions 100
4.3.5.1. Sediment-water interface temperature (SWIT) and paleobathymetry 101
4.3.5.2. Heat flow 101
4.3.6. Erosion 102
4.3.7. Thermal calibration 104
4.3.8. Migration modeling 105
4.4. Results & Discussion 106
4.4.1. Timing of generation and present-day maturity 106
4.4.1.1. Synrift source rock 106
4.4.1.2. Barremian to early Albian aged source rocks 110
4.4.1.3. Cenomanian/Turonian (C/T) source rock 110
4.4.2. Migration and Accumulation 111
4.4.3. Petroleum system evolution 116
4.4.4. Ibhubesi filling history 119
4.4.4.1. The role of faults during migration 121
4.5. Conclusions 122

5. COMPLEMENTARY RESULTS AND INTERPRETATIONS ON THE HYDROCARBON MIGRATION DYNAMICS AND THE EARLY SOUTH ATLANTIC MARGIN EVOLUTION 126
5.1. Interpretation of light hydrocarbons and d13C stable isotope data from extracted rock samples and reservoir fluids from the Orange Basin 126
5.2. Additional seismic interpretation results on synrift structures in the Orange Basin and new insights into the South Atlantic margin evolution and segmentation 132
5.2.1. New findings on the South Atlantic margin segmentation in the Orange Basin 133
5.2.2. Synrift basement structures in the Orange Basin 136
5.3. A new approach to the evaluation of paleo- and present-day hydrocarbon leakage dynamics using 3D basin models 138
5.3.1. Hydrocarbon loss calculations 138
5.3.2. Paleo and present-day hydrocarbon leakage as calibration tools for 3D basin models 140
5.3.3. The Paleocene-early Eocene paleo-leakage event in the Orange Basin from a global paleo-climate perspective 143

6. INTEGRATION & SUMMARY 146
6.1. Interpretation of the relative timing of paleo-fluid flow events using a refined Cenozoic chronostratigraphy 146
6.2. Basement structures along the South African continental margin 147
6.3. Source rock characteristics of Cretaceous organic-rich black shales and mudstones from the South Atlantic margin 147
6.4. Modeling hydrocarbon migration dynamics in the Orange Basin 148
6.5. Hydrocarbon leakage on a geologic time scale 149

7. OUTLOOK 151
ABBREVIATIONS 153
REFERENCES 155
APPENDIX A 175

LIST OF FIGURES:

Figure 1-1: Study area in the Orange Basin showing the seismic coverage made available for this study and the locations of known present-day and paleo-fluid flow and hydrocarbon leakage sites. Transects 1, 2, and 3 refer to cross-sections extracted from the 3D basin model of Chapter 4. 3
Figure 1-2: Extent of the study areas from previous seismic interpretation and basin modeling studies in the Orange Basin..... 4
Figure 1-3: Integrated basin analysis approach. 8
Figure 1-4: Organic-geochemical analysis workflow following the PhaseKinetics(R) approach of di Primio and Horsfield (2006) with the respective source rock parameter that is investigated during each step (white boxes). 19
Figure 1-5: Seismic interpretation workflow to generate 3D basin modeling inputs..... 21
Figure 1-6: Examples (a-h) of seismic anomalies at the sediment surface and in the sediment column as interpreted on seismic from the Orange Basin. A Miocene (Mio.) and a Top-Cretaceous (K/T) unconformity are included for reference. 22
Figure 2-1: Equatorial and southwest African margin basin overview with DSDP site locations; BeB = Benguela Basin, BrB = Bredasdorp Basin, KB = Kwanza Basin, LB = Lüderitz Basin, LCB = Lower Congo Basin, NB = Namibe Basin, OB = Orange Basin, WB = Walvis Basin; base map: Amante and Eakins (2009)..... 31
Figure 2-2: Main lithologic units of the investigated DSDP sites according to Bolli et al. (1978a,b), Hay and Sibuet (1984) and Forster et al. (2008)..... 32
Figure 2-3: HI vs. OI plot of studied samples (kerogen type maturation pathways after Espitalié et al., 1978). 40
Figure 2-4: Tmax vs. HI plot of studied samples, for legend see figure 2 (kerogen type maturation pathways after Cornford, 1998)..... 41
Figure 2-5: Representative Py-GC chromatograms of selected source rocks samples; a) sample no. 1, a wax-rich Type II kerogen SR; b) sample no. 15, a Type II kerogen SR; c) sample no. 19, a Type III kerogen SR; d) sample no. 23, a heterogeneous Type II kerogen SR; e) sample no. 27, a Type IIS kerogen SR..... 42
Figure 2-6: Kerogen type classification of Py-GC results according to Eglinton et al. (1990).. 44
Figure 2-7: a) Petroleum type prediction according to Horsfield (1989); b) detail of (a) Petroleum type prediction in relation to HI. 46
Figure 2-8: Petroleum type of P-N-A oils according to di Primio and Horsfield (1996). 47
Figure 2-9: Kerogen type and activation energy distribution from DSDP sites offshore southwestern Africa (well lithologies and TOC adapted from Bray et al. (1998)). 49
Figure 2-10: Transformation rate curves for a geologic heating rate of 3°K/Ma calculated from bulk kinetic models. 51
Figure 2-11: Compositional kinetic models for the six investigated samples. 53
Figure 2-12: Psat vs. Bo plot from compositional kinetic model, light grey area corresponds to naturally occurring petroleum fluids (di Primio and Horsfield, 2006). 53
Figure 2-13: GOR vs. Temperature plot from compositional kinetic model. 54
Figure 3-1: Location of the paleo-pockmark field and seismic coverage of the study area in the Orange Basin on the southwest African margin. Yellow outline shows the extent of the paleo-pockmark field; red star = location of Figure 3-6 and Figure 3-7; 64
Figure 3-2: Generalized chronostratigraphic chart of the Orange Basin showing the sequence stratigraphic horizons used in this study, global and local sea level variations, and margin evolution (modified from Broad et al., 2006; Cenozoic ages: Weigelt &

Uenzelmann-Neben, 2004; sea level curves: Haq et al., 1987; Hardenbol et al., 1998; Dingle et al. 1983; McMillan, 2003; Wigley & Compton, 2006;). 65
Figure 3-3: Seismic transect through the northern Orange Basin showing the margin structure (a) uninterpreted, (b) interpreted; for location shown in Figure 3-1, thick black lines= major regional unconformity, white lines= faults, also shown is the location of Figure 3-4. Note the truncated Upper Cretaceous sequences in the east and progradation of late Upper Cretaceous and thin Cenozoic sequences. 67
Figure 3-4: Detail of the gravity-faulted slope of Figure 3-3, showing late Maastrichtian and Cenozoic progradation and the location of the wavy reflector horizon E-1, (a) uninterpreted, (b) interpreted, thick black lines= major regional unconformity, white lines= faults. Some faults reach down into the Aptian/Albian source rock intervals. 69
Figure 3-5: a) Location map of seafloor pockmarks, mud volcanoes, and early Eocene paleo-pockmarked surface. (b) Northward view of the seafloor in TWT contour at the shelf break showing present-day seafloor pockmarks. (c) Variance extracted along paleo-pockmark horizon E-1 showing circular and elongated depressions. Note the NE-SW alignment of the depressions and the NNW-SSE trend of reactivated Cretaceous faults (visualized in black to red colors). Location of cross-sections BB' in Figure 3-7 and of maps in Figure 3-6 and Figure 3-8 are plotted. 72
Figure 3-6: Paleo-pockmarks and NNE-SSW lineation trend on horizon E-1 as seen on (a) TWT contour and (b) variance map extracted along the horizon. Locations maps plotted in Figure 3-5, green arrow points north. 73
Figure 3-7: (a) Uninterpreted and (b) interpreted seismic crossline showing the structure of the shelf and Late Cretaceous to Cenozoic sediments. The pockmarks on horizon E-1 are located above faults. Pockmark density increases where the Late Campanian/Maastrichtian wedge (green area) pinches out. Locations of profile BB' is plotted in Figure 3-5. 74
Figure 3-8: (a) Variance time-slice through the seismic reflections below the horizon E-1 showing large faults with higher offsets (red) and small discontinuities (black and dark grey) interpreted as fractures and (b) their relation to the paleo-pockmarks. Some NE-SW oriented fractures (light blue) seem to coincide with the pockmark lineation, the majority of the faults and fractures trend NW-SE (yellow). Locations maps plotted in Figure 3-5. 76
Figure 3-9: 3D view of the paleo-pockmarked horizon in relation to fault and fracture patterns of underlying sediments (for location see fig. 5c). The horizontal seismic variance time-slice depicts discontinuities caused by large listric faults and fractures within the sediments of the Late Maastrichtian (green overlay) and listric faults in the non-fractured Paleocene sediment wedges (orange overlay). The TWT horizon slice of paleo-pockmark horizon E-1 is outlined in red. Note the higher relief and density of paleo-pockmarks on horizon E-1 above the chaotic structure of the Late Campanian/Maastrichtian prograding wedge. The L-Maastrichtian/ Paleocene wedge pinch-out (orange transparency) coincides with the downslope occurrence of pockmarks on horizon E-1. 80
Figure 3-10: Conceptual model of the events leading to early Eocene fluid escape. (a) Progradation of Late Cretaceous sediments, (b) Late Cretaceous uplift, slope destabilization and gravity faulting of the shelf edge, (c) erosion on the shelf, rapid deposition and burial of Prograding slope wedge, (d) Paleocene wedge deposition, disequilibrium compaction of fine-grained sediments, and maturation of source rock generate overpressure, (e) overpressure leads to upward migration of pore fluids and

gas below the Paleocene wedge and through the faulted shelf creating pockmarks along the shelf. 82
Figure 4-1: Location of the Orange Basin offshore South Africa with a general overview of the study area, the seismic reflection dataset analyzed, and the 3D basin model coverage, superimposed on bathymetry. Locations of fluid and hydrocarbon leakage indicators are shown according to Boyd et al. (2011), Petroleum Agency SA (2012), and Hartwig et al. (2012a). 87
Figure 4-2: General chronostratigraphy of the Orange Basin (left, modified from Hartwig et al., 2012a) and horizons defined in the 3D model input (right). Note that horizons, affected by erosion have modified top horizon ages due to the modeling setup of the modeling software. See text for details. 89
Figure 4-3: E-W transects and projected wells extracted from the 3D basin model depicting the present-day margin geometry and a simplified view of the layers assigned lithologies (for location see Fig. 1). Note that the thickness of the Cretaceous sequences increases from south to north, while the Cenozoic sequences' thickness decreases in the same direction. 93
Figure 4-4: Facies maps for the (a,b) mid. and upper Albian, (c,d) Cenomanian, and (e) Turonian layers including conceptual channels were constructed in order to test their potential as carrier beds and stratigraphic traps. The maps of the Albian/ lower Cenomanian are based on the location of large incised valleys from the seismic interpretation, also reported by Brown et al. (1995). 95
Figure 4-5: Facies maps of the source rock intervals: a) Synrift II layer; b) Barremian Aptian layer; c) Aptian/Albian Type III source rock layer; d) Aptian/Albian and Albian Type II source rock layer; e) Turonian/Cenomanian source rock layer. 99
Figure 4-6: Heat flow trend (black line) used in this study based on Hirsch et al. (2010) with a variable early Cenozoic heat flow "spike" (orange dashed line) for the southern study area due to volcanic activity 100
Figure 4-7: Cumulative erosion of a) Late Cretaceous, b) Paleocene, and c) Mio-Pliocene layers. Note the Pliocene-aged slumping event in 4c. The total study area is outlined in grey dashed lines. 101
Figure 4-8: Basal heatflow maps for the (a) post-rift Cretaceous uplift, (b) Cenozoic volcanism, (c) Cenozoic uplift events, and (d) present-day. 102
Figure 4-9: Calibration of thermal model against vitrinite reflectance and temperature data at different well locations in the northern and southern sectors of the basin. 105
Figure 4-10: Modeled present-day thermal maturity shown as vitrinite reflectance and (f–j) present-day transformation ratio (TR) maps of the defined source rocks. Synrift source rock characteristics (a, f) are shown only for potential synrift structures. The Aptian-Albian Type III kerogen source rock (c, h) has significantly lower TR than the lower Cretaceous Type II kerogens and thus a remaining primary hydrocarbon generation potential in the Cretaceous depocenter 108
Figure 4-11: 1D time extractions showing the evolution of vitrinite reflectance, transformation ratio for all potential source rocks at different locations and layer temperature and heat flow for selected source rock intervals. Present-day kitchen areas in the western deepwater part are controlled by Cenozoic burial and characterized by an ongoing l increasing TRs (a, f). In contrast, the recent kitchen areas along the eastern coastal margin with potential synrift source rocks (b, d) are predominately controlled by paleo-heat flow. Primary generation in the Cretaceous depocenter ended during the

latest Cretaceous/ early Paleocene, which is represented by TRs of 100% at those times (c, e). 109
Figure 4-12: Modeled petroleum saturation, hydrocarbon accumulations, and migration vectors extracted from the 3D Hybrid migration basin model along a W-E transects (for location see Figure 4-1). Lateral migration occurs within Lower Cretaceous sand-rich sequences and channels, which are the main carrier systems. Note that the early Cretaceous source rocks act as seals for downward-expelled hydrocarbons, creating accumulations in the transitional sequence such as the Kudu field offshore Namibia. The Ibhubesi-type accumulations in Albian channel sandstones (Transect 1) were recreated by incorporating a shale-rich layer at mid-Albian level. Recent- and present-day generated hydrocarbons in the western deepwater areas migrate up-dip into roll-over structures and subtle anticlines. Vertical hydrocarbon migration occurs above structural closures and anticlines and at seafloor outcrops of lower Cretaceous sequences along the eastern margin, where “sniffer” anomalies have also been reported (see Figure 4-1). 112
Figure 4-13: 3D view of modeled petroleum saturation within the conceptual Albian channels and deepwater sediments as calculated by the Hybrid method (blue tones denote high values). The vitrinite reflectance of the Aptian source rock layers is shown below the Albian channel layers. The recent and present-day deepwater kitchen areas charge the deepwater sediments as propose in Figure 4-12..... 115
Figure 4-14: Hydrocarbon accumulations as predicted for the main carriers by a) the IP method and b) the Hybrid method (see text for details). Hybrid model accumulations generally have higher vapor contents than IP- model accumulations. The IP method generates liquid HC accumulations in sand-rich basinfloor fans in the western deepwater OB. These areas correlte to areas with higher petroleum saturations calculated by the Hybrid method (Figure 4-13) 116
Figure 4-15: Petroleum system elements chart for the Cretaceous depocenter and the deepwater Cenozoic wedge in the Orange Basin. 118
Figure 4-16: Predicted hydrocarbon accumulations in the Ibhubesi area from the (a) “open model” with open faults and (b) the “ initial model” with variable fault properties. The blue outline marks drainage areas used for calculating hydrocarbon losses through time (Figure 4-17.) See text for details. 120
Figure 4-17: Liquid and vapor hydrocarbon losses for the Ibhubesi area as calculated from the open fault scenario (“open model”) (a, b) and the initial scenario with open faults during tectonically active periods and closed faults for tectonically quiet periods (“initial model”) (c, d). In both models, the highest losses occur during phases of margin uplift. The Ibhubesi reservoirs are filled to spill since the early Cenozoic. If faults are closed (c, d), leakage occurs mainly through the seal. 121
Figure 5-1: Iso-sterane diagram for K-B1 and K-E1 well samples. 127
Figure 5-2: Maturity from $d^{13}C$ isotope measurements of Kudu, Ibhubesi reservoir fluids, and A-F1 well extract; a) $d^{13}C$ methane vs. $d^{13}C$ ethane; b) $d^{13}C$ ethane vs. $d^{13}C$ propane. 128
Figure 5-3: Gas-type from $d^{13}C$ methane and gas wetness according to Laughrey and Baldassre (1998). 130
Figure 5-4: Gas type derived from iso-butane/butane ratio vs. gas wetness according to Laughrey and Baldassre (1998). 130
Figure 5-5: Thompson diagram to help determine source and relative maturity of light hydrocarbons..... 131

Figure 5-6: Oblique view of the Orange Basin margin showing the SDR interpretation with its distinct concave-down morphology. The different wedges are signified by different colors and can be correlated along the margin. The offshore end marks the limit of seismic coverage. The SDR order is best visualized by the northernmost seismic interpretation along the South African-Namibian border. Note the undulating morphology of individual SDR boundaries, which is a result of differential subsidence and variations in magma volumes. 135
Figure 5-7: TWT on acoustic basement. The interpretation shows the location of coast parallel synrift graben in the metamorphic basement and a NW trending basement high in central study area, interpreted as a remnant of the early rift phase. Similar trending basement structures also occur along the conjugate margin. (a) Basement features that were identified across several 2D seismic lines. (b) Interpolated top of economic basement map. This map was gridded using all basement reflections, even if they were not identified on the next 2D seismic line. 137
Figure 5-8: Estimated Hydrocarbon top-outflow and accumulation rates for each time step of the Hybrid (Hy) and Invasion Percolation (IP) models using various fault property scenarios..... 140
Figure 5-9: Oil (green) vs. gas (red) top-outflow rates from the initial variable-fault property Hybrid model. Oil outflow rates are highest before the regional seal is consolidated, whilst the highest gas outflow rates are reached during the early Eocene after the onset of secondary cracking (compare with Figure 4-15)..... 142

LIST OF TABLES:

Table 1-1: Kerogen types and precursor material, compiled from Tissot and Welte (1984) and Hunt (1996). 12
Table 2-1: Sample information and Rock Eval results 36
Table 2-2: Bulk kinetic parameters 50
Table 2-3: Calculated fluid properties 54
Table 2-4: Bulk kinetic comparison 60
Table 4-1: Source rock description 96

LIST OF PUBLICATIONS

In the scope of this thesis the following peer-reviewed articles and conference contributions were produced.

PRINTED ARTICLES

Hartwig, A., Anka, Z., di Primio, R., 2012. Evidence of a widespread paleo-pockmarked field in the Orange Basin: An indication of an early Eocene massive fluid escape event offshore South Africa. Marine Geology 332-334, 222–234.

Hartwig, A., di Primio, R., Anka, Z., Horsfield, B., 2012. Source rock characteristics and compositional kinetic models of Cretaceous organic rich black shales offshore southwestern Africa. Organic Geochemistry 51, 17–34.

SUSBMITTED ARTICLE

Hartwig, A., Anka, Z., di Primio, R., Constraining Petroleum Generation and Migration in the Orange Basin, South Africa: A 3D Basin Modeling Study, AAPG Bulletin, submitted.

CO-AUTHORED PRINTED ARTICLES:

Koopmann, H., Franke, D., Schreckenberger, B., Schulz, H., Hartwig, A., Stollhofen, H., di Primio, R., 2014. Segmentation and volcano-tectonic characteristics along the SW African continental margin, South Atlantic, as derived from multichannel seismic and potential field data. Marine and Petroleum Geology 50, 22–39.

Maystrenko, Y.P., Scheck-Wenderoth, M., Hartwig, A., Anka, Z., Watts, A.B., Hirsch, K.K., Fishwick, S., 2013. Structural features of the Southwest African continental margin according to results of lithosphere-scale 3D gravity and thermal modelling. Tectonophysics 604, 104–121.

ORAL AND POSTER PRESENTATIONS AT CONFERENCE:

Hartwig, A., di Primio, R., Anka, Z., 2012. 3D Petroleum System Modeling of the Orange Basin, offshore South Africa. SAMPLE SPP Colloquium 2012, 12.-15. June 2012, Tutzingen, Germany. (Abstract, Poster)

Koopmann, H., Hartwig, A., Schulz, H., Schreckenberger, B., Franke, D., 2012. New findings on the aspect of margin segmentation along the South African margin, in: EGU General Assembly 2012. Vienna, Austria. (Abstract, Poster)

Hartwig, A., Anka, Z., di Primio, R., Albrecht, T., 2012. 3D Petroleum System Modeling of the Orange Basin, Offshore South Africa, AAPG 2012, 22.-25. April 2012, Long Beach, CA, USA. (Abstract, Talk)

Hartwig, A., di Primio, R., 2011. Source rock characteristics of organic-rich black shales offshore southwestern Africa, IMOG 2011, 18.-23. Sept. 2011, Interlaken, Switzerland. (Abstract, Poster)

Hartwig, A., Anka, Z., di Primio, R., Albrecht, T. 2011. Wide-spread pockmarked surface: evidence for a Paleogene massive fluid escape event in the Orange Basin, South Africa. SAMPLE SPP Colloquium 2012, 7.-10. June 2011, Potsdam, Germany. (Abstract, Poster)

Hartwig, A., Anka, Z., di Primio, R., Albrecht, T. 2011. Wide-spread pockmarked surface: evidence for a Paleogene massive fluid escape event in the Orange Basin, South Africa. EGU 2011, 03.-08. April 2011, Vienna, Austria. (Abstract, Talk)

Maystrenko, Y. P., Scheck-Wenderoth, M., Hartwig, A., Anka, Z., Watts, A. B., Hirsch, K., 2011. 3D structural model of the West African continental margin. EGU 2011, 03.-08. April 2001, Vienna Austria. (Abstract, Poster)

Hartwig, A., Boyd, D., Kuhlmann, G., Adams, S., Campher, C., Anka, Z., di Primio, R., Albrecht, T., 2010: Characterization of Hydrocarbon Generation and Migration Dynamics Based on Seismic Interpretation and Basin Modeling: an Integrated Study of the Orange Basin, South Africa. AAPG ICE Calgary, 12.-15. Sept. 2010, Calgary, Canada. (Abstract, Poster)

Hartwig, A., Boyd, D., Kuhlmann, G., Adams, S., Campher, C., Anka, Z., di Primio, R., Albrecht, T., Singh, V., 2010. Modeling hydrocarbon generation and migration dynamics of the Orange Basin, South Africa. SAMPLE SPP Colloquium 2010, 14.-17. June 2010, Kiel, Germany. (Abstract, Poster)

CONTRIBUTIONS BY THE PROJECT PARTNERS

The research for this thesis was conducted within the framework of the “Methane on the Move” (MOM) Project at the Section of Organic Geochemistry of the Helmholtz-Centre Potsdam – GFZ German Research Centre for Geosciences. Forest Exploration International (South Africa) (PTY) (Ltd) provided the funding for the PhD research project “Characterization of hydrocarbon migration dynamics in the Orange Basin, South Africa”. The 2D and 3D exploration seismic data sets, exploration well data, and exploration reports were provided by Forest Exploration International (South Africa) (PTY) (Ltd), PetroSA (Pty) (Ltd), Anschutz Overseas South Africa (Pty) (Ltd), and the Petroleum Agency South Africa (PASA). Tony Albrecht (until April 2012) and Anschen Friedrichs (since May 2012) of Forest Exploration International (South Africa) (PTY) (Ltd) handled the exchange of data.

The sampling of International Ocean Drilling Program (IODP) cores was conducted by Prof. Dr. Rolando di Primio and Alexander Hartwig at the IODP core repository in Bremen, Germany.
Rock-Eval and TOC measurements were carried out at Applied Petroleum Technology (APT) in Kjeller, Norway.

Open- and closed-system pyrolysis GC and bulk kinetic measurements were performed at the Section of Organic Geochemistry of GFZ, Potsdam, Germany, with the help of Ferdinand Perssen.

Author contributions to the listed publications other than the strategic planning and topic discussion are given below:

Chapter 2 published as: Hartwig, A., di Primio, R., Anka, Z., Horsfield, B., 2012. Source rock characteristics and compositional kinetic models of Cretaceous organic rich black shales offshore southwestern Africa. Organic Geochemistry 51, 17–34.

> The compositional kinetics and PVT predictions were compiled with the help of Prof. Dr. Rolando di Primio.

The results of the basin-wide seaward dipping reflector (SDR) interpretation presented in Chapter 5.2.1. are published as:
Koopmann, H., Franke, D., Schreckenberger, B., Schulz, H., Hartwig, A., Stollhofen, H., di Primio, R., 2014. Segmentation and volcano-tectonic characteristics along the SW African continental margin, South Atlantic, as derived from multichannel seismic and potential field data. Marine and Petroleum Geology 50, 22–39.
Koopmann, H., Hartwig, A., Schulz, H., Schreckenberger, B., Franke, D., 2012. New findings on the aspect of margin segmentation along the South African margin, in: EGU General Assembly 2012. Vienna, Austria. (Abstract, Poster)

> The publications are part of the PhD research of Hannes Koopmann at the Federal Institute for Geosciences and Natural Resources (BGR) who studies the continental margin evolution offshore South Africa. These publications resulted from a collaboration project planned within the framework of the South Atlantic Margin Processes and Links with onshore Evolution (SAMPLE) Priority Program 1375 funded by the German Research Foundation (DFG). H. Koopmann, D. Franke, and B. Schreckenberger carried out the overall strategic planning and discussion on the topic. The regional seismic interpretation of SDRs and compilation of results in the Orange Basin, other than on BGR seismic surveys, were conducted by A. Hartwig and H. Koopmann. The regional seismic interpretation of SDRs offshore Namibia and compilation of results were conducted by H. Schulz and H. Koopmann. The publications

are included in Chapter 5 of this thesis because they are a direct result of the regional seismic interpretation conducted in the course of this project. The ensuing discussions to the above publications provided the background to and further encouraged the inclusion of Chapter 5.2.2.

The basin-wide seismic interpretation conducted for this thesis served as input to the 3D crustal modeling study mentioned in Chapter 5.2.1 and published as: Maystrenko, Y.P., Scheck-Wenderoth, M., Hartwig, A., Anka, Z., Watts, A.B., Hirsch, K.K., Fishwick, S., 2013. Structural features of the Southwest African continental margin according to results of lithosphere-scale 3D gravity and thermal modelling. Tectonophysics 604, 104–121.
Maystrenko, Y. P., Scheck-Wenderoth, M., Hartwig, A., Anka, Z., Watts, A. B., Hirsch, K., 2011. 3D structural model of the West African continental margin. EGU 2011, 03.-08. April 2001, Vienna Austria. (Abstract, Poster)

These publications resulted from a collaboration project planned within the framework of the South Atlantic Margin Processes and Links with onshore Evolution (SAMPLE) Priority Program 1375 funded by the German Research Foundation (DFG). Y.P. Maystrenko, M. Scheck-Wenderoth, A.B. Watts, K.K. Hirsch, and S. Fishwick conducted the 3D crustal modeling and overall topic discussion. A. Hartwig carried out the regional seismic and geologic interpretation with the help of Z. Anka for the Orange Basin that was used as modeling input. The publications are included in Chapter 5 of this thesis because they are a direct result of the regional seismic interpretation conducted in the course of this project. The ensuing discussions to the above publications provided the background to and further encouraged the inclusion of Chapter 5.2.2.

1. Introduction

The research for this study was conducted within the framework of the "Methane on the Move" (MOM) program that aims at modeling methane migration and emission from the subsurface and evaluating its possible impact and feedback mechanisms on global climate at geologic time scales. The focus lies on improving our understanding of the processes that affect sedimentary organic carbon during burial and remobilization. This is achieved by integrating sedimentary basin and lithospheric modeling with ocean and atmosphere modeling through several sub-projects that assess methane exchange within respective parts of the carbon cycle.

Greenhouse gas emissions from underlying thermal sources and the deep biosphere can make an extremely significant contribution to the carbon cycle. CO_2 dominates the carbon molecule exchange between the bio-, hydro-, and atmospheric reservoirs of the surface carbon cycle (Kroeger et al., 2011; Ridgwell and Edwards, 2007). In the subsurface carbon cycle, on the other hand, methane derived through thermal or microbial cracking of sedimentary organic matter in wetlands and sedimentary basins is the dominant contributor to organic carbon exchange from the geosphere to the surface reservoirs (Kroeger et al., 2011; O'Connor et al., 2010; Tissot and Welte, 1984). As a greenhouse gas, methane is more than 20 times more effective than CO_2, but upon release to the hydro- and atmosphere it quickly disseminates in oceanic and terrestrial reservoirs or transforms into CO_2 (Etiope, 2009; Kroeger et al., 2011; O'Connor et al., 2010). Nevertheless, few climate modeling studies have taken thermogenic methane sources from deep sedimentary systems into account.

Sedimentary basins constitute a quantitatively significant source and sink of greenhouse gases in both marine and terrestrial systems. The physical and chemical alterations that affect organic matter during basin subsidence and uplift control the distribution of fossil energy resources worldwide. The total mass of organic carbon in sedimentary basins is estimated to be ten million gigatonnes (Gt) (Hunt, 1996; Kroeger et al., 2011; Ridgwell and Edwards, 2007). Thus, it is several orders of magnitude larger than that contained in all fossil-fuel resources and living biomass together. Fossil energy resources continue to be the major foundation of the industrialized nations, and improved techniques for detecting and modeling the occurrence of subsurface accumulations are sought. In order to better constrain the carbon flux from sedimentary basins to surface and intermediate subsurface reservoirs, the thermal and burial history of the basins have to be modeled, and sediment surface seeps need to be studied. Such hydrocarbon seepage has been documented offshore by the study of seafloor pockmarks, mud volcanoes, and seismic chimneys, and onshore with flux measurements at mud volcanoes and oil and gas seeps (e.g. Andresen, 2012; Etiope et al., 2009; Judd and Hovland, 2007; Løseth et al., 2009; Westbrook et al., 2009). Recent studies in these topics have started to emphasize the potential for hydrocarbon leakage to influence global climate. Even though the methane leakage rates related to source rock maturation alone are most likely too low to cause rapid climate changes (Berbesi et al.,

2013), they are a main contributor to meta-stable reservoirs, such as methane hydrates (Judd and Hovland, 2007; Etiope, 2009; Kroeger et al., 2011). Several authors (Dickens et al., 1997, 1995) have put methane hydrate dissociation forward as the driving mechanism that initiated global climate aberrations in the geologic past, such as the Paleocene-Eocene Thermal Maximum (PETM) (Dickens et al., 1995; Zachos et al., 2001, 2008). However, more recent publications (Bowen and Zachos, 2010; Bowen, 2013; Carozza et al., 2011; Dunkley Jones et al., 2010; Higgins and Schrag, 2006; Kroeger et al., 2011; Zeebe et al., 2009) emphasize that methane hydrate dissociation on its own cannot explain all the observations made for the PETM, but acknowledge it as an important factor in feedback mechanisms during climate change. Thus, if focused through the clathrate cycle, transient methane leakage may have significant effects on global climate.

3-Dimensional (3D) basin modeling studies, which are widely used for petroleum exploration, allow us to simulate and constrain the timing of petroleum generation, migration, and sequestration in sedimentary basins on a geologic time scale. When constrained by observations on present and past gas leakage events, they can provide a method to link thermogenic methane emissions from the subsurface through sediment surface seeps to the hydro- and atmosphere, and thus the sedimentary subsurface carbon reservoirs to the hydro- and atmospheric reservoirs.

1.1. Study area and scientific problematics

The Orange Basin (OB) is located offshore southwestern Africa (Figure 1-1). The sedimentary succession of the basin consists of 8 km thick synrift and drift sequences related to the continental break-up of Gondwana and the opening of the South Atlantic taking place during the late Jurassic (Gerrard and Smith 1982). On the shelf, the basin contains a thick Cretaceous rift-drift sequence and a thin Cenozoic cover, which develops into a series of prograding wedges at the shelf break (Weigelt and Uenzelmann-Neben, 2004; Paton et al., 2008). Up to date, 38 exploration wells were drilled and led to the discovery of the Kudu and Ibhubesi gas fields proving the existence of a Deep Gas and an Albian Gas play, respectively (Petroleum Agency SA, 2012). The Deep Gas Play consists of gas generated from Barremian-to-Aptian-aged source rocks that is stratigraphically trapped in Barremian-aged aeolian sandstones, with proven reserves of 1.38 trillion cubic feet (tcf) in the Kudu field (~ 39.1 billion m3; Tullow Oil, 2007). The Albian Gas Play has Aptian-to-Albian-sourced gas and condensate which is trapped in Albian and Cenomanian-aged fluvial channel sandstones. Well tests in the Ibhubesi field showed that individual compartments contain between 28 - 520 billion cubic feet (bcf) of gas and condensate (~0.79 - 14.73 billion m3) with total gas reserves of 1.15 tcf (32.56 billion m3, Berge et al., 2002). Further potential for hydrocarbon accumulations exists in syn-rift grabens and Cretaceous turbidites in the deep water Orange Basin (Petroleum Agency SA, 2012). The study area covers a surface area of 95.600 km2 in water depths between 100-2850 m within offshore economic zone of the Republic of South Africa (Figure 1-1).

Several authors have conducted seismic interpretation and petroleum system modeling studies to understand the hydrocarbon migration dynamics of this basin (e.g. Schmidt, 2004; Paton et al., 2007; Kuhlmann et al., 2010; Boyd et al., 2011). Evidence of recent and present-day fluid and gas leakage processes, such as "sniffer" anomalies near the seafloor (Jungslager, 1999), seabed pockmarks and seismic chimneys (Ben-Avraham et al., 2002; Boyd et al., 2012; Kuhlmann et al., 2010; Paton et al., 2007) as well as mud diapirs (Ben-Avraham et al., 2002; Viola et al., 2005) have been identified on 2D seismic surveys and mapped within the Orange Basin, offshore South Africa (Figure 1-1). They are postulated to be dominantly associated with active hydrocarbon leakage. In some cases gas-hydrate dissociation was put forward as a possible source (Ben-Avraham et al., 2002). The present-day fluid flow indicators as well as the frequent gas shows encountered during drilling in lower Cretaceous sediments suggest an active or recently active phase of petroleum generation. Although it is difficult to distinguish gas-hydrate derived gas from thermogenic gas from deeper sources and reservoirs, seismic evidence for the presence or absence of a bottom-simulating reflector (BSR) can be used to narrow-down the source of the leaking hydrocarbon.

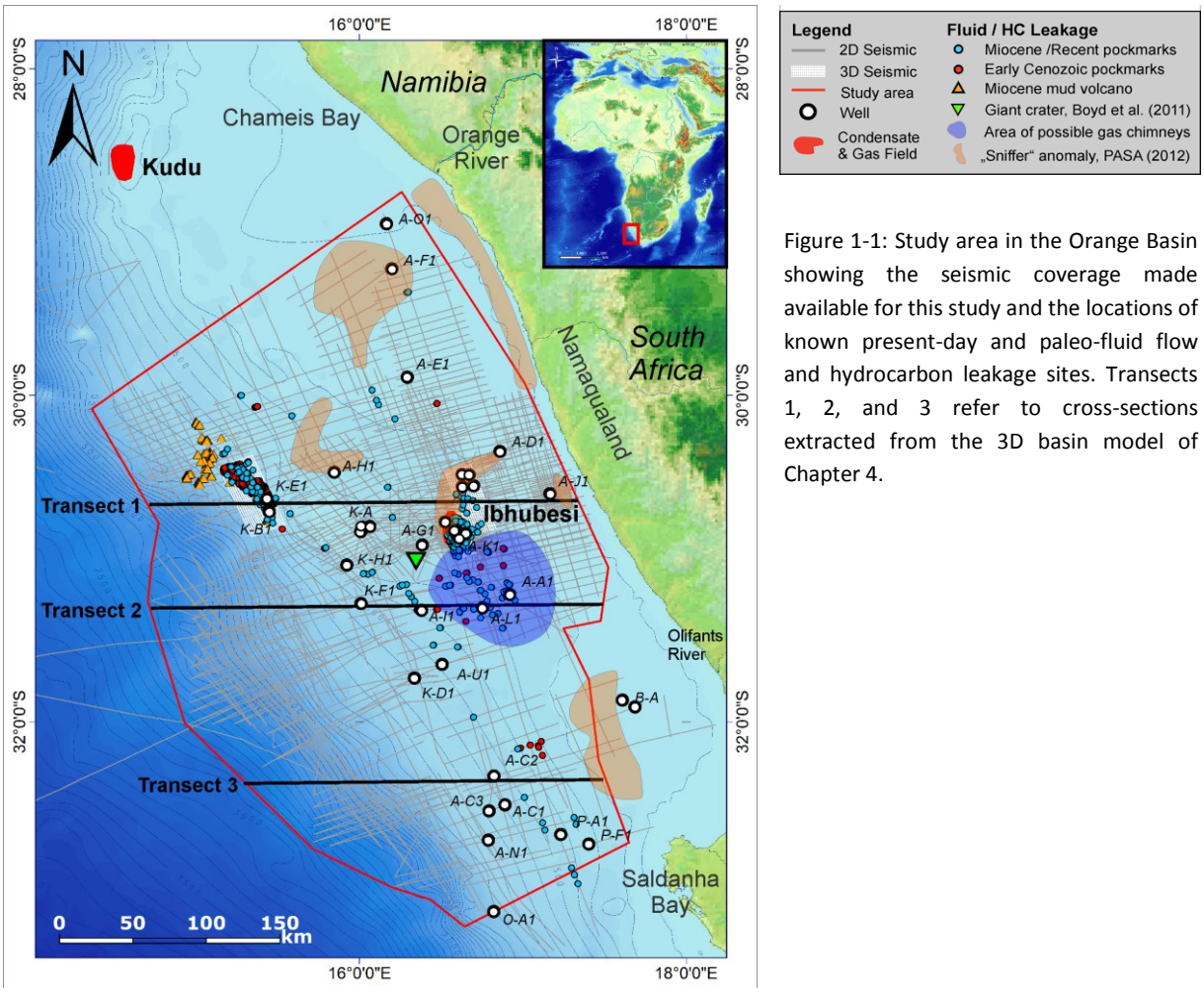

Figure 1-1: Study area in the Orange Basin showing the seismic coverage made available for this study and the locations of known present-day and paleo-fluid flow and hydrocarbon leakage sites. Transects 1, 2, and 3 refer to cross-sections extracted from the 3D basin model of Chapter 4.

Previous modeling studies by Davies & Van der Spuy (1992, 1D model) of the Kudu wells offshore Namibia, and of the southern Orange Basin by Paton et al. (2007, 2D model), Boyd et al. (2011, 2D model), and Kuhlmann et al. (2011, 3D model) address the timing of petroleum maturation and generation. All these studies indicate that the main phase of hydrocarbon generation and migration occurred during the late Cretaceous, which may have continued into the early Cenozoic in the Kudu area (Davies and Van der Spuy, 1992). Paton et al. (2007) and Kuhlmann et al. (2011) further proposed active present-day petroleum generation in the Cenozoic depocenter of the deepwater southern Orange Basin. Kuhlmann et al. (2011) suggest long-distance eastwards migration from that deepwater present-day kitchen to explain hydrocarbon leakage sites in the near-shore basin.

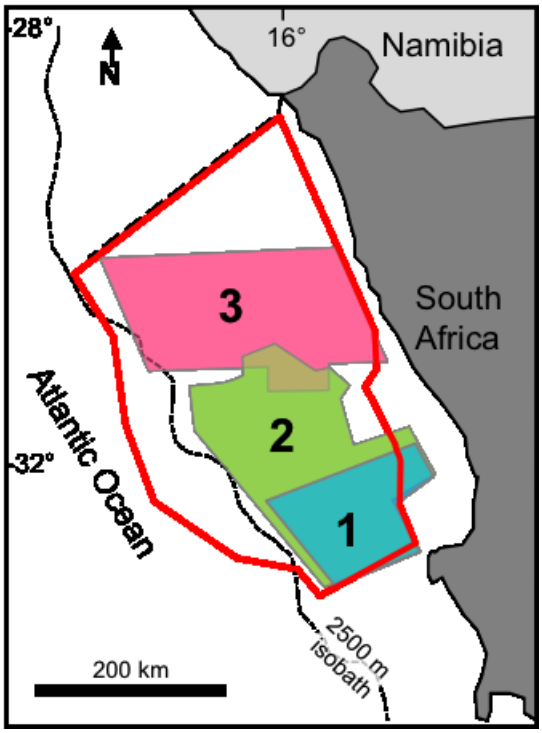

Figure 1-2: Extent of the study areas from previous seismic interpretation and basin modeling studies in the Orange Basin. 1 - Paton et al. (2007); 2 - Kuhlmann et al. (2010); 3 - Boyd et al. (2012); red outline – this study.

Nonetheless, the location of the recent and/or active oil and gas kitchen, as well as the hydrocarbon migration pathways, within the Orange Basin as a whole remains largely unconstrained. There are several reasons for this:

(1) The limited amount of data and knowledge that is available about the Cenozoic stratigraphy of the basin in comparison to the Cretaceous stratigraphy. This has made it difficult to reconstruct phases of burial and uplift, erosion, or non-deposition over the last 65 million years (My). In all previous models, the Cenozoic sedimentation pattern is usually summarized in a Paleogene and a Neogene event with intermittent erosion. The Cretaceous basin evolution, on the other hand, is modeled in great detail.

(2) The previous studies by Ben-Avraham et al. (2002), Paton et al. (2007), Kuhlmann et al. (2010), and Boyd et al. (2011) could not incorporate the full seismic coverage of the basin to

consistently map the distribution of fluid flow features or build their models across the entire basin. They were limited to the 2D exploration seismic specific their project study areas (Figure 1-2), which excluded the deepwater Cenozoic sediment wedge and coast-parallel synrift grabens.

One problem with many surface hydrocarbon seep studies is that the thermogenic hydrocarbon source is either unknown, or unaccounted for. This is the case for present-day hydrocarbon surface seeps and even more for paleo-hydrocarbon leakage. 3D petroleum system modeling can be used to investigate whether surface seeps and active source rocks are in causal relationship to one another.
The use of paleo-fluid flow features for basin model calibration is largely constrained by the scale and data quality, which document the event. Several authors (Andresen and Huuse, 2011; Andresen, 2012; Anka et al., 2013; Gay et al., 2006a; Imbert and Ho, 2012) have demonstrated that it is possible to constrain such paleo-leakage to a mechanism and time period. Using a 2D seismic interpretation and basin modeling approach Naeth et al. (2005) have demonstrated that it is possible to correlate the location of carbonate mounds to hydrocarbon migration pathways in the Porcupine Basin, Ireland. In a recent study Anka et al. (2013) reported a similar correlation of present-day and paleo-fluid flow features with structural elements and hydrocarbon migration pathways in the Lower Congo Basin as interpreted from 2D seismic and 2D basin modeling. In the present study, an attempt is made to use both present-day and paleo-leakage sites to test the validity of a thermogenic hydrocarbon source for past and present-day fluid flow presented in Hartwig et al. (2012a, Chapter 3) using a 3D basin model. The 3D modeling approach provides a 3-dimensional full-physics solution for hydrocarbon migration that is superior to 2D cross-section models. The 3D model allows the modeler to constrain the source, timing, direction, and magnitude of hydrocarbon migration in the context of basin evolution. To the author's knowledge the modeling of and calibration to interpreted paleo-leakage events using 3D basin modeling techniques has not been attempted to date.

1.2. Goals of the study

In the light of the above-mentioned problematics, the goals of this study can be outlined as follows:

1. To unify the previous interpretations of fluid flow and natural gas seepage in the Orange Basin. In an attempt to provide a basin-wide and consistent interpretation of their distribution through time, their association to heat flow anomalies or structural/ stratigraphic elements and their relationship to the hydrocarbon system;

2. To further constrain the Cenozoic basin evolution -
- By conducting an extensive literature review on the Cenozoic basin evolution;

- By incorporating the areas of Cenozoic depocenters, namely the deep-water Orange Basin, into the study area;
- By linking the offshore Cenozoic deposits with the onshore sediments and the sediment supply history of the Orange and Oliphants rivers;

3. To further characterize the Cretaceous source rocks of the Orange Basin -
- By organic-geochemical laboratory analysis, such as open- and closed-system pyrolysis-gas chromatography;
- By generating bulk- and compositional kinetic models for the primary generation of petroleum;

4. To generate a 3D petroleum system model of the entire South African Orange Basin -
- For the characterization and timing estimation of gas generation, migration, and leakage dynamics through geologic time;
- To expand the model area to include the deepwater Cenozoic sediment wedge and the near-shore synrift structures;
- To delineate synrift structures and an economic basement for the study area;
- To test whether present-day and paleo-fluid flow features can be used to constraint petroleum system models;

1.3. Background and summary of the three main publications

The article entitled “Evidence of a widespread paleo-pockmarked field in the Orange Basin: An indication of an early Eocene massive fluid escape event offshore South Africa” by Hartwig et al. (2012a) (chapter 3) attempts to unify and correlate the data and literature on the sedimentology and stratigraphy of Cenozoic onshore (e.g. Dingle and Hendey, 1984; Dingle et al., 1983) and shallow shelf deposits (e.g. Corbett, 1996; Dingle, 1973; Wigley and Compton, 2006) of the Orange basin with the seismic stratigraphy of the distal deepwater Orange basin (e.g. Weigelt and Uenzelmann-Neben, 2004). It is an effort to provide a consistent early Cenozoic seismic interpretation that is applicable to the entire Orange Basin. In addition, it investigates a prominent anomalous seismic reflector identified in a 3D seismic survey of the present-day shelf break. It is interpreted and dated as a paleo-fluid flow event by means of 3D seismic interpretation methods and by applying the refined Cenozoic chronostratigraphy. This expands the basin’s catalogue of existing fluid flow features, documenting several episodes of fluid flow and hydrocarbon migration in the basin. The new insights on the Cenozoic chronostratigraphy, in turn, are tied to the Cenozoic tectonic and magmatic events reported for the western African margin (e.g. Moore et al., 2008; Pether et al., 2000) to refine the basin’s petroleum system model, which is discussed in the article entitled “Constraining petroleum generation and migration in the Orange Basin, South Africa: A 3D basin modeling study” by Hartwig et al. (submitted to AAPG) (chapter 4).

Previous modeling studies used analogue kinetic models to simulate source rock maturation. Paton et al. (2007) and Boyd et al. (2011) used the organofacies-based kinetic models of Pepper and Corvi (1995) for kerogen Types I, II, and III (organofacies B, C, and DE), while Kuhlmann et al. (2011) used a Type II Woodford shale kinetic model to describe the Cretaceous source rocks. Even though a close relationship between kerogen type and source rock bulk kinetics exists, organic matter heterogeneity, common in deltaic sequences with high terrestrial input, can lead to considerable variations in hydrocarbon generation rates (di Primio and Horsfield, 2006; Schenk et al., 1997b; Tegelaar and Noble, 1994). Schmidt et al. (2004) conducted bulk kinetic experiments on early Cretaceous source rock samples from DSDP site 361 offshore South Africa. They identified two types of source rocks, a marine source rock with type II kerogen that starts to generate petroleum at lower temperatures than the analogue type II kerogen models they used, and a type III kerogen-rich set of samples that was not further investigated. A significant variability in kerogen stability has also been reported for lower Cretaceous source rocks of the Angolan margin (Burwood, 1999). Additionally, Mello et al. (1988) reported sulfur-rich kerogens for the Brazilian margin. Despite the significant oil discoveries and ongoing exploration efforts in the South Atlantic, kinetic models of South Atlantic Cretaceous source rocks as well as the petroleum-type and composition they generate are scarce or non-existent.

These observations in source rock and kerogen variability, as well as the lack of compositional kinetic models for Cretaceous source rocks of the southwest African margin are the motivations for the research article entitled “Source rock characteristics and compositional kinetic models of Cretaceous organic-rich black shales offshore southwestern

Africa" by (Hartwig et al., 2012b) (Chapter 2). The study investigates Aptian, Albian, and Turonian to Coniacian aged thermally-immature, organic-rich black shale and mudstone intervals from DSDP sites located in the southeast Atlantic. The goal was to determine trends and differences in organofacies, petroleum type, and composition and to tie them back to the general evolution and geology of the rift-to-drift transition in the South Atlantic. The compositional kinetic data from the artificial maturation experiments of Hartwig et al. (2012b) can be used to elucidate changes in the physical properties of petroleum fluids under varying pressure and temperature conditions (PVT behavior, di Primio and Horsfield, 2006; di Primio et al., 1998; di Primio and Skeie, 2004) and may explain the vast differences in petroleum types, presently found along the margin.

The research article entitled "Constraining petroleum generation and migration in the Orange Basin, South Africa: A 3D basin modeling study" by Hartwig et al. (submitted to AAPG) uses the resulting compositional kinetic models to investigate the differences in timing of petroleum generation and migration under consideration of such kerogen type variability. The modeling results are further compared to the locations and of relative timing of known present-day and paleo-fluid flow features in the basin.
The qualitative assessment of hydrocarbon leakage and its potential to impact climate is addressed in Chapter 5.3. The discussion on the timing, driving factors and relative amounts of leaked hydrocarbons relies heavily on the results of the three research articles by Hartwig et al. (2012a,b and 2013 submitted) mentioned above.

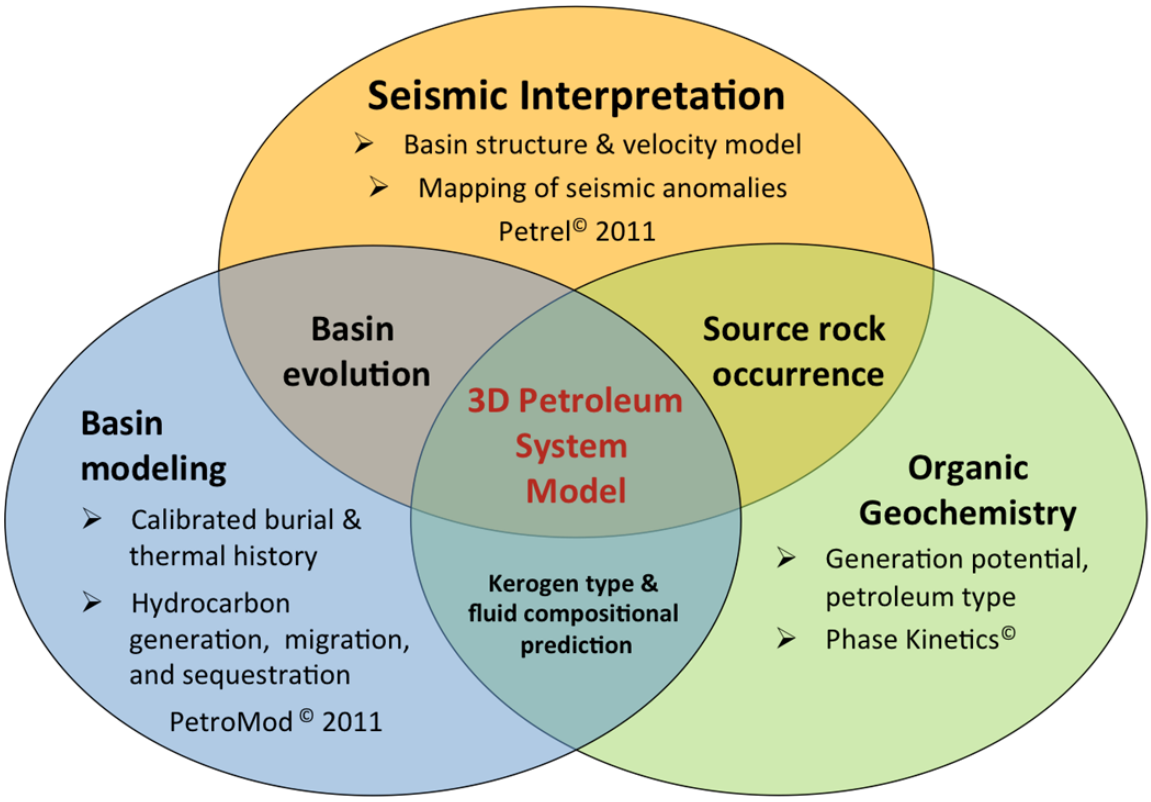

Figure 1-3: Integrated basin analysis approach.

This multi-facetted basin-wide approach consisting of seismic interpretation, basin analysis, and petroleum system modeling tied to a source rock compositional kinetics study, as well as integrating previous works, sheds new light on the south-eastern South Atlantic margin evolution. The reinterpretation of the extensive seismic dataset provides a new coherent framework that was used for two collaboration projects that study the South African volcanic margin evolution from the southern tip of South Africa to the Walvis Ridge in the north, thus providing a supra regional view. These results are referred to in Chapter 5.2. For additional details on the work and interpretation the reader is referred to the original publications:

(1) Maystrenko et al. (2013, published in the peer reviewed journal "Tectonophyscis") entitled "Structural features of the Southwest African continental margin according to results of lithosphere-scale 3D gravity and thermal modelling" who investigate the deep lithospheric structure, and

(2) Koopmann et al. (2013, published in the peer reviewed journal "Marine and Petroleum Geology", as part of the Doctoral thesis of Hannes Koopmann) entitled "Segmentation and volcano-tectonic characteristics along the SW African continental margin, South Atlantic, as derived from multichannel seismic and potential field data" giving new insights into the volcanic margin evolution and the accompanying presentation of Koopmann et al. (2012) entitled "New findings on the aspect of margin segmentation along the South African margin" presented at the European Geoscience Union General Assembly 2012 in Vienna, Austria.

1.4. Geologic and geochemical background

1.4.1. The Organic Carbon Cycle

On Earth, carbon is the basic element of life and occurs in the atmo-, bio-, and geosphere in various forms (Hunt, 1996). In the atmosphere it is predominately contained in carbon dioxide (CO_2) and methane (CH_4), both of which are considered greenhouse gases (Falkowski et al., 2000; Kroeger et al., 2011). These are also the two most common carbon compounds in the geosphere (Hunt, 1996). In sedimentary rocks, the greater part of carbon occurs in its oxidized form as carbonate and to a smaller part in its reduced form as organic matter (OM) from biological processes (Hunt, 1996; Tissot and Welte, 1984). Carbon molecules are readily exchanged between the atmosphere, the bio- and hydrosphere, and the geosphere.

The recycling of carbon to the atmospheric and hydrospheric CO_2 reservoirs and its implications for global climate have gained more and more attention from the scientific community over the last two decades (Falkowski et al., 2000; Kroeger et al., 2011).

The following discussion presents the basics of organic matter deposition and preservation as well as of petroleum generation and migration. Details can be found in textbooks such as Tissot and Welte (1984), Hunt (1996) as well as Killops and Killops (2005).

Carbon is unique on earth, with is ability to form stable carbon-carbon chains of variable length, rings, and other complex molecules through covalent bonds (Hunt, 1996), thus providing the organic framework for life. Photosynthesis is the process by which

inorganically bound carbon, in the form of CO_2 enters the biosphere. It is incorporated into the cells of primary producers, autotrophs such as phytoplankton and plants, to produce organically bound carbon. Heterotrophic organisms consume these organic carbon compounds and oxidize them during respiration releasing CO_2 to the atmo- and hydrosphere or incorporate them into their carbonate shells. Dead organisms and their carbonate shells may either be oxidized by abiotic chemical processes (fire, weathering), thus releasing the carbon back to the atmo- and hydrosphere as CO_2, or through microbial activity in the form of CO_2 or biogenic methane. This cycle forms the surface part of the global organic carbon cycle (Cycle I, Tissot and Welte, 1984) with durations of days to tens of years. Since organic matter is generally unstable under geologic conditions, only a very small percentage of the organic matter within soil and sediments, approx. 0.1%, leaves the surface cycle and enters the subsurface part of the global carbon cycle, which lasts millions of years (Cycle II, Tissot and Welte, 1984). The organic matter that enters the geosphere may be altered to form kerogen and later petroleum. Geologic and tectonic processes, such as burial, uplift, erosion, and volcanism (Barker and Pawlewicz, 1987; Davies, 1997; Hunt, 1996; Kroeger et al., 2011) control whether the organic matter is oxidized or preserved and how fast the transformation to kerogen, bitumen, and petroleum takes place. A sufficient amount of organic matter has to be preserved in the sediments, approx. 0.5% of the total weight, in order to be considered a potential source for petroleum. Organic matter preservation is best when deposited under reducing conditions and low sedimentation rates. These are predominately found in anaerobic marine environments, such as in oxygen minimum zones below upwelling areas along continental shelves with high primary productivity, in stagnant lakes or silled basins with a stratified water column, and to a lesser extent in wetlands and hypersaline environments (Hunt, 1996; O'Connor et al., 2010; Tissot and Welte, 1984; Welte et al., 1997).

CO_2 dominates the carbon molecule exchange between the bio-, hydro-, and atmospheric reservoirs of the surface cycle (Kroeger et al., 2011; Ridgwell and Edwards, 2007). In the subsurface cycle, on the other hand, methane formed in wetlands and in sedimentary basins is the dominant contributor to organic carbon exchange from the geosphere to the surface reservoirs (O'Connor et al., 2010). CO_2 contributions from the oxidization of sedimentary organic matter and volcanic exhalations play a secondary role (Etiope et al., 2009; Kroeger et al., 2011; Zachos et al., 2008).

1.4.2. The Formation of Petroleum

The transformation of organic matter into petroleum during burial is divided into three stages: diagenesis, catagenesis, and metagenesis.

Diagenesis occurs within a few hundred meters of the surface under mild temperature conditions. If the depositional environment allows the accumulation of large quantities of plant derived material, peat and brown coal can form during this stage. Microbial activity in marine and terrestrial environments leads to the decomposition of OM into kerogen precursors, first producing CO_2 and water in aerobic conditions close to the surface. This is

accompanied by sediment compaction and a rapid reduction of oxygen availability leading to anaerobic conditions. Once nitrate and sulfate nutrient sources are depleted, microbial fermentation and CO_2 reduction dominate which produce predominately methane (Hunt, 1996; Judd and Hovland, 2007; Milkov, 2011; O'Connor et al., 2010; Ridgwell and Edwards, 2007; Tissot and Welte, 1984). Simultaneously, a series of low temperature reactions occur that transform most of the remaining biomass into kerogen (Hunt, 1996). Kerogen is organic matter that is insoluble in organic solvents and acids (Tissot and Welte, 1984). It is classified into four different types depending on the source and precursor material (Table 1-1), which determines their hydrogen, carbon, and oxygen contents. Terrestrial plant material is more resistant to microbial degradation, than marine OM, due to a higher abundance of aromatic structures (Tissot and Welte, 1984; Welte et al., 1997). Therefore plant material retains some of its cellular structure forming particles, called macerals, which are classified into liptinite, vitrinite, and inertinite, according to their reflectance and also microscopically visible structure (Bustin et al., 1985; Tissot and Welte, 1984). The end of diagenesis roughly corresponds to a vitrinite reflectance of 0.5%, equivalent to temperatures of approximately 60 to 80 degree Celsius (°C). At this phase, high molecular weight compounds constitute the first liquid petroleum that is being generated (Tissot and Welte, 1984).

As the sediments are buried deeper, temperature and pressure increase, while porosity, permeability, and water content decrease. The exposure to these higher temperatures leads to thermal degradation of residual OM and kerogen (catagenesis) into bitumen and petroleum. Bitumen is an intermediate for oil generation from type I and II kerogens (Hunt, 1996). These processes typically occur in the temperature range of 80 to 150°C and at depths between 2 to 4 kilometers (km) depending on the geothermal gradient. This is the principal stage of oil formation in which hydrocarbons of medium to low molecular weight compounds are formed. Upon further increase in burial depth, additional light hydrocarbon compounds and wet gas are formed from the remaining kerogen and heavier hydrocarbons (Tissot and Welte, 1984). Methane is the dominant hydrocarbon being formed at the end of catagenesis, which corresponds to a vitrinite reflectance of about 2.0%.

The expulsion of petroleum from the fine-grained, low permeability organic-rich source rocks by discrete flow, diffusion, and solution processes is referred to as primary migration. Secondary migration of petroleum is buoyancy and capillary pressure driven as it moves through porous carrier and reservoir rocks, and along faults and fractures. If the petroleum reaches a low-permeability sediment layer or fault that prevent further migration, an oil and/or gas accumulation is formed. If no such seal is encountered, the hydrocarbons will eventually escape to the sediment surface (Hantschel and Kauerauf, 2009; Hunt, 1996).

If burial depth increases further, the last stage of OM evolution at very high temperature and pressure conditions at depths beyond 4 km and up to 10 km is referred to as metagenesis (Hunt, 1996). At this stage most of the kerogen has lost its labile components and does not produce any significant amounts of petroleum. Primary cracking of condensed kerogen structures and secondary cracking of reservoired hydrocarbons now dominate and lead to large amounts of methane being liberated. Coal is transformed into anthracite and then metaanthracite, while residual kerogen is condensed into graphitic carbon (Tissot and

Welte, 1984; Bustin et al., 1985). Traditionally this is considered as the end of petroleum generation. However, Mahlstedt and Horsfield (2012) demonstrated that most kerogen types, especially those with high terrestrial OM content, can generate significant quantities of methane well into this high level of thermal maturity.

Table 1-1: Kerogen types and precursor material, compiled from Tissot and Welte (1984) and Hunt (1996).

Kerogen Type	Source and depositional environment	Common coal macerals
I	Lacustrine, sapropelic, spores, algae bacteria	Liptinite, sporinite, cutinite, resinite
II and IIS	Marine and marine carbonate/evaporite, sapropelic, algae, plankton, bacteria, minor terrestrial	Liptinite, alginite
III	Terrestrial, deltaic, humic, plant material	Vitrinite, telinite, telocollinite
IV	Oxidized humic, inert carbon, reworked	Inertinite, fusinite

1.4.3. Hydrocarbon seeps and the petroleum plumbing system

Only a fraction of all generated petroleum accumulates in economic reservoirs, generally less than 15% (Hunt, 1996). The rest of the petroleum is dispersed throughout the sedimentary column or seeps to the surface (Hunt, 1996; Judd and Hovland, 2007; Kroeger et al., 2011). Hydrocarbon surface seeps have been found in nearly all petroliferous sedimentary basins around the globe (Davy et al., 2010; Etiope and Ciccioli, 2009; Hunt, 1996; Judd and Hovland, 2007; Marcano et al., 2013). They have been studied for different reasons. Knowledge on the controlling factors of seep locations not only reduces exploration risk, but also gives insights into the basin "plumbing", especially with respect to hydrocarbon migration and leakage dynamics (Andresen, 2012; Andresen et al., 2011; Anka et al., 2013; Heggland, 1998; Ostanin et al., 2012). They have also been studied for their impact on the bio-, hydro-, and atmosphere (Berbesi et al., 2014; Gay et al., 2006c; Hovland et al., 2005) and for their potential as geohazards (Buffett and Archer, 2004; Cathles et al., 2010; Judd and Hovland, 2007; Ligtenberg and Connolly, 2003).

Surface seeps occur in active petroleum systems that have generated sufficient amounts of hydrocarbons for secondary migration (Hunt, 1996). Seeps are usually located at outcrops of mature source rocks and carrier and reservoir formations, along outcropping unconformities, and above structures that penetrate the sediments, such as mud volcanoes, salt domes, and igneous intrusions (Cartwright et al., 2007; Hunt, 1996; Judd and Hovland, 2007). Their expression as gas chimneys, pockmarks, (Gay et al., 2006a, 2006b; Loncke et al., 2004; Løseth et al., 2009), pipe structures, and authigenic carbonate mounds in marine

environments can be identified on seismic reflection data (Andresen, 2012; Anka et al., 2013; Løseth et al., 2011; Moss and Cartwright, 2010a; Naeth et al., 2005; Ostanin et al., 2012), as well as on bathymetry and side scan sonar (Loncke et al. 2004; Judd and Hovland, 2007).

Folds and faults seem to focus and control the location of gas and fluid leakage in active and passive margins (Anka et al., 2013; Buffett and Archer, 2004; Cartwright et al., 2007; Loncke et al., 2004; Løseth et al., 2009; Ostanin et al., 2012; Pilcher and Argent, 2007; Yassir, 2003). Additionally, there is ample evidence for a close association of seafloor fluid flow features with gas-hydrate subcrops in passive margin settings and deep lake systems (Baristeas et al., 2012; Ben-Avraham et al., 2002; Cartwright et al., 2007; Imbert and Ho, 2012; Judd and Hovland, 2007; Westbrook et al., 2009). Methane of biogenic and thermogenic origin and pore water are the main components of the involved gas and liquid phases, respectively (Hovland and Judd, 2007; Westbrook et al., 2009; Kroeger et al., 2011).

In marine environments, gas and fluid flow to the sediment surface may be initiated by pressure changes, for example a drop in hydraulic pressure of the water column due to tidal or eustatic sea-level changes (Judd and Hovland, 2007; Kiel, 2009; Liebetrau et al., 2010; Linke et al., 2010), or by temperature changes that can lead to the dissociation and dissolution of gas hydrates (Bowen, 2013; Haacke et al., 2007; Imbert and Ho, 2012; Majorowicz et al., 2012; Westbrook et al., 2009). Tectonic triggering and submarine landslides have also been proposed as driving mechanisms (Hasiotis et al., 1996; Judd and Hovland, 2007; Maslin et al., 2004). This is evident from the numerous petroleum seeps found in tectonically active areas along plate boundaries and fold belts (Hunt, 1996).

Evidence for paleo-leakage events and sustained paleo-leakage has been identified on seismic data by mapping buried and stacked pockmarks (Andresen and Huuse, 2011; Andresen, 2012; Anka et al., 2013; D. Cole et al., 2000; Gay et al., 2006a, 2006b; Hartwig et al., 2012a; Imbert and Ho, 2012). Once paleo-fluid flow features are identified, the onset and duration of the paleo-leakage event that created them can be inferred (Andresen and Huuse, 2011; Gay et al., 2006a; Ostanin et al., 2012). The identification of such fossil leakage episodes, both at a local as well as regional scale, could provide evidence for an association between methane release from the geosphere and observed carbon isotopic excursions in the paleo-climatic record (Bowen, 2013; Dickens et al., 1997, 1995; Dunkley Jones et al., 2010; Imbert and Ho, 2012; O'Connor et al., 2010; Zachos et al., 2001, 2008), linking thus earth system processes to paleo-climate evolution.

1.4.4. Climate change and carbon isotopic excursions in the geologic past

Hydrocarbon seepage or leakage sites lead to a renewed exchange of carbon, in the form of CO_2 and methane, from the subsurface to the surface carbon cycle. Biogenic and thermogenic gases are directly exchanged with the hydro- and atmosphere. Petroleum liquids may either be microbially biodegraded in the sediment column and/or near the oil-water contact in low-temperature reservoirs that are cooler than 80°C (Head et al., 2003;

Kassold et al., 2008; Wilhelms et al., 2001), or oxidized by various processes (Tissot and Welte, 1984; Hunt, 1996).

A differentiation between biogenic and thermogenic gas sources is achieved by measuring the $d^{13}C$ stable carbon isotope ratio, with the commonly used PDB standard (Peedee belemnite; Tissot and Welte, 1984; Hunt, 1996; Milkov, 2011). The ratio of ^{13}C to ^{12}C in Earth's crust is consistent through geologic time and can thus be used to differentiate between the sources of reservoired carbon gases (Hunt, 1996; Milkov, 2011; Schoell, 1983). Biogenic methane is depleted in ^{13}C isotopes and has a lower $d^{13}C$ value than the OM preserved in sediments, while the biogenic CO_2 is enriched in ^{13}C isotopes relative to the OM (Head et al., 2003; Hunt, 1996; Milkov, 2011; Schoell, 1983; Tissot and Welte, 1984). This technique has found wide application in studying the source, quantity, and timing of greenhouse gases released from the geosphere to the hydro- and atmosphere to understand their effect on present and past global climate (Dunkley Jones et al., 2010; Etiope and Ciccioli, 2009; Kroeger et al., 2011; Zachos et al., 2001, 2008).

On a geologic timescale, global climate has been very variable, going from extremely cold conditions with large polar ice caps and low latitude glaciation, for example during the Carboniferous, to extremely warm conditions when the earth's poles where mostly ice-free, such as during the Cretaceous. These changes are largely driven by oscillations in earth's eccentricity, precession, and obliquity in its orbit around the sun (Zachos et al., 2001). The long-term climatic changes are further enhanced or countered by tectonic plate movements, which control the location of orogenic belts, subduction zones, and oceanic spreading centers, which in turn influence changes in eustatic sea-level and large-scale weather systems.

From a source rock perspective, climate and sea-level are primary factors that lead to transgressions, periods of rising sea level, during which the world's economically most important Jurassic and Cretaceous source rocks were deposited (Hunt, 1996; Klemme and Ulmishek, 1991; Kroeger et al., 2011). Extreme climatic conditions may also be linked to mass extinctions, as proposed for the end-Triassic (Ruhl et al., 2011), to the rapid evolution of mammals during the late Paleocene (Zachos et al., 2001; Zeebe and Zachos, 2013 and references therein) or to the clastic supply and deposition of major deltas and deep-sea fan systems along passive continental margins (Anka and Séranne, 2004; Anka et al., 2009; Séranne and Nzé Abeigne, 1999).

The study of $d^{13}C$ changes in the benthic deep-sea foraminifera fossil record from cores of the Ocean Drilling Program (ODP) and Deep Sea Drilling Program (DSDP) has given insights into the evolution of global climate over the past 65 million years (My) (Bowen, 2013; Dickens et al., 1995; Zachos et al., 2001, 2008). This is specially true for the occurrence of climatic aberrations, climate anomalies that stand out from the orbitally-forced climate cycle, that are accompanied by perturbations of the global carbon cycle as seen in the stable isotope record (Zachos et al., 2001). The Paleocene Eocene Thermal Maximum (PETM) is probably the most widely studied carbon isotope excursion of the Cenozoic, when average global surface temperatures rose by 5-9°C and culminated in the Early Eocene Climatic

Optimum (Bowen, 2013; Dickens et al., 1995; Dunkley Jones et al., 2010; Higgins and Schrag, 2006; Zachos et al., 2001, 2008; Zeebe and Zachos, 2013; Zeebe et al., 2009).

Several hypotheses have been put forward to explain the rapid decrease of the $d^{13}C$ values within a few thousand years during the PETM (Bowen, 2013; Zachos et al., 2008), such as rapid dissociation of methane hydrates (Dickens et al., 1995; Dickens et al., 1997) accompanied by long-term perturbations of the carbon respiration cycle (Bowen, 2013), or volcanic exhalation of carbon gases (Higgins and Schrag, 2006; Lourens et al., 2005; Svensen et al., 2004), widespread oxidation of OM and changes in ocean circulation (Higgins and Schrag, 2006). The exact carbon source has not been identified yet, but an overall consensus exists on OM-derived carbon greenhouse gases having been rapidly released from the geosphere into the hydro- and atmosphere during this event (Bowen, 2013; Dickens et al., 1995; Dunkley Jones et al., 2010; Higgins and Schrag, 2006; Kroeger and Funnell, 2012; Kroeger et al., 2011; Svensen et al., 2010, 2004; Zachos et al., 2001, 2008; Zeebe and Zachos, 2013; Zeebe et al., 2009) at a similar or higher rate and magnitude as that of anthropogenic greenhouse gases released since the industrial revolution (Dickens et al., 1995; Kroeger et al., 2011; Zeebe and Zachos, 2013).

As a greenhouse gas, methane is more than 20 times more effective than CO_2, but upon release to the hydro- and atmosphere it quickly disseminates in oceanic and terrestrial reservoirs or transforms into CO_2 (Etiope, 2009; Kroeger et al., 2011; O'Connor et al., 2010). Although methane is the most abundant subsurface carbon gas, the most obvious sources for thermogenic methane on a geologic timescale, namely buried OM in petroliferous basins, is generally not well constrained in paleo-climate studies (Kroeger et al., 2011). Kroeger and Funnell (2012) demonstrate how a feedback mechanism of warm climate to sedimentary basins can lead to an earlier onset of petroleum generation than expected and propose the possibility of a synchronization of maximum and enhanced petroleum generation across basins. However, in a more recent work Berbesi et al. (2014) invoke the need of a focusing mechanism for petroleum leakage to have the potential of impacting past and present climate. Clearly, such processes need to be included in future climate models. Even though the methane release rates related to source rock maturation are most likely too low to cause catastrophic climate changes (Berbesi et al., 2014), they are a main contributor to meta-stable reservoirs, such as methane hydrates (Buffett and Archer, 2004; Etiope, 2009; Judd and Hovland, 2007; Majorowicz et al., 2012). Although methane hydrate dissociation is an unlikely mechanism to initiate global climate aberrations, it may be an important aspect of feedback mechanisms during climate change. In order to better model the carbon flux from sedimentary basins to surface and intermediate subsurface reservoirs, the thermal history of the basins has to be constrained. 3D petroleum system modeling studies, which are widely used for petroleum exploration, allow us to simulate the timing of petroleum generation, migration, and sequestration on a geologic time scale. Thus, they provide a potential link to connect thermogenic methane emissions from the subsurface through surface seeps to the hydro- and atmospheric reservoirs.

1.4.5. South Atlantic margin evolution

The geologic evolution of the continental margin basins along the South Atlantic can be subdivided into synrift, rift-to-drift transition, and drift phases that were related to the progressive opening of the South Atlantic (e.g. Beglinger et al., 2012; Davison, 1999; Koopmann et al., 2013; Marcano et al., 2013; Torsvik et al., 2009).

The break-up of Gondwana was accompanied by Triassic to Jurassic intra-continental rifting, forming north-south trending grabens and half-grabens along the present-day southwest African margin (Coward et al., 1999; Gerrard and Smith, 1982; Karner and Driscoll, 1999). On the other hand, the Argentine margin, which is the conjugate to the South African Atlantic margin, hosts east-west and northwest-southeast trending rift structures (Autin et al., 2013; Loegering et al., 2013; Marcano et al., 2013). This hints at a complex South Atlantic pre-rift evolution that involved NW-SE extension (Franke et al., 2006; Koopmann et al., 2014; Loegering et al., 2013) and the reactivation of Paleozoic basement structures on both sides of the incipient South Atlantic rift (Autin et al., 2013; Kounov et al., 2013). The emplacement of true oceanic crust began during the early Cretaceous (134 Ma ago) and propagated from south to north (e.g. Blaich et al., 2009; Kounov et al., 2013; Nürnberg and Müller, 1991 and references therein). The rift structures of the South Atlantic margin basins contain continental and fluvio-deltaic deposits and host lacustrine organic-rich black shales of late Jurassic to early Cretaceous age (Davison, 1999; Karner and Driscoll, 1999; Loegering et al., 2013; Macdonald et al., 2003; Marcano et al., 2013). These synrift source rocks were deposited in deep anoxic or saline lakes and are known to have sourced oil accumulations on the southwest African and Brazilian margin (e.g. Muntingh, 1993; Schiefelbein et al., 2000). A review of their source rock characteristics is given by Mello et al. (1988a, 1988b), Burwood (1999), Coward et al. (1999), and Schiefelbein et al. (2000).

The South Atlantic can be divided into southern and central segments that are separated by the Rio Grande Rise – Walvis Ridge (e.g. Torsvik et al. 2009; Blaich et al., 2009; Marcano et al., 2013). The existence of an evaporite rift-to-drift transitional sequence characterizes the central segment (Anka et al., 2009; Beglinger et al., 2012; Hudec and Jackson, 2004; Séranne and Anka, 2005; Torsvik et al., 2009), and is absent in the southern segment. The southern segment, which contains the Orange Basin, is characterized by the existence of a prominent seaward dipping reflector (SDR) wedge (Bauer et al., 2000; Franke et al., 2006; Gladczenko et al., 1997; Jackson et al., 2000; Koopmann et al., 2014) that can be subdivided into several sequences (Koopmann et al., 2014, 2012) providing evidence for extensive volcanism along the margin during the final rift phase (Gladczenko et al., 1997). Onshore evidence include the large igneous province (LIP) of the Paraná-Etendeka flood basalts that erupted within a short time period 133-130 Ma and the accompanying NW-SE and margin parallel trending dike swarms (Jackson et al., 2000; Torsvik et al., 2009). They can be linked to the Gough and Tristan da Cunha hotspots via their plume trails that formed the Rio Grande Rise – Walvis Ridge, respectively (Gladczenko et al., 1997; Jackson et al. 2000; Blaich et al., 2009; Torsvik et al., 2009). The presence of SDRs in the central segment has been inferred for the Brazilian margin, but they appear to be absent on the conjugate Angolan margin (Torsvik et al., 2009).

In the southern segment the beginning of the rift-to-drift transition is marked by the first marine incursions during the Barremian to Aptian, when continental red beds grade into marine sandstones overlain by organic-rich black shales (Broad et al., 2006). These black shales were deposited throughout the early Aptian to mid Albian in an anoxic marine environment that resulted from restricted ocean circulation over the Falkland Plateau into the Cape Basin (Bolli et al., 1978b; Herbin et al., 1987). During the mid/late Albian the westward spreading Falkland Plateau cleared southern Africa providing a deepwater passage through the Agulhas Gap that led to increasing bottom water ventilation in the South Atlantic (Macdonald et al., 2003; Torsvik et al., 2009; Zimmerman et al., 1987).

In the central segment the transitional sequence consists of early Aptian transgressive siliciclastic sediments that grade into fluvial to lagoon deposits which are overlain by a thick evaporite sequence (Anka and Séranne, 2004; Beglinger et al., 2012; Davison, 1999; Hudec and Jackson, 2004; Séranne and Anka, 2005). The late Aptian salt sequence was deposited in a restricted shallow-water environment stretching along the margin basins of equatorial West Africa and Brazil up to the Cameroon Volcanic Ridge, collectively known as the Aptian Salt Basins (Anka and Séranne, 2004; Coward et al., 1999; Hudec and Jackson, 2004; Torsvik et al., 2009).

Along the equatorial South Atlantic margin the drift succession begins in the late Aptian with continuous deepening of the South Atlantic leading to the first marine incursions and deposition of marine carbonates (Anka and Séranne, 2004; Torsvik et al., 2009)These carbonates contain organic-rich and sapropelic limestones and were deposited in a restricted marine environment that lasted throughout the Albian (Schiefelbein et al, 2000; Hudec and Jackson, 2004). They are known to have sourced oil accumulations offshore Brazil (Mello et al., 1988a, 1988b) and in the onshore Kwanza Basin (Burwood, 1999) and possibly in the offshore Lower Congo and Angola Basins.

The drift succession of the southwest African margin is dominated by Albian siliciclastic and Upper Cretaceous progradational/aggradational fluvio-deltaic sequences (Broad et al., 2006). Continental and shallow marine siliciclastic sediments dominate the conjugate margin of southeast Argentina (Loegering et al., 2013). Early Albian oxygen deficiency in the Cape Basin was favorable for sapropelic black shale deposition (Zimmermann et al., 1987). These organic-rich intervals are the main source rocks of gas accumulations in the Orange Basin (e.g. Jungslager, 1999; Kuhlmann et al., 2011; van der Spuy, 2003).

The Upper Cretaceous sediments of the central segment are characterized by increasing clastic content and halokinesis (Hudec and Jackson, 2004; Séranne and Anka, 2005). Both, the Argentine and southwest African margin contain Upper Cretaceous prograding sequences (Gerrard and Smith 1982; Paton et al., 2007; Loegering et al., 2013). While the southern African margin underwent extensive shelf erosion and severe gravity faulting of the shelf edge due to margin uplifting (Brown Jr. et al., 1995; de Vera et al., 2010), the Argentine shelf remained more stable.

A major episode of black shale deposition occurred during the Cenomanian-Turonian oceanic anoxic event (OAE 2), a period of oxygen deficiency observed throughout the South Atlantic (Forster et al., 2008; Herbin et al., 1987; Zimmerman et al., 1987). These black shales

have been recognized as potentially oil-prone source rocks along the southwest African margin (Aldrich et al., 2003; Bray et al., 1998; Burwood, 1999) and also the Brazilian margin (Mello et al., 1989) and possibly in the ultra-deep offshore of the Angola Basin (Anka et al., 2010).

Along the central South Atlantic margins terrigenous clastic sedimentation continues up to the present-day with a major Oligocene erosion event and subsequent incision of submarine canyons and the progradation of deep-sea fans, such as the Congo fan (Anka and Séranne, 2004; Anka et al., 2009). In the southern segment, Cenozoic sedimentation rates decreased (Dingle et al., 1983; Séranne and Anka, 2005). Sediments consist of pelagic clays and nannofossil ooze (e.g. Weigelt and Uenzelmann-Neben, 2004). The Argentine margin, on the other hand, saw an increase of sedimentation rates, especially during the Oligocene-Miocene (Loegering et al., 2013) that might be correlated to recent Andean uplift (Marcano et al., 2013).

More details on the Cenozoic and Cretaceous evolution of the Orange Basin are given in the geologic backgrounds sections of Chapters 3 and 4.

1.5. Methodology

1.5.1. Organic geochemical analysis

All samples were obtained from the Integrated Ocean Drilling Program (IODP) Bremen Core Repository at the University of Bremen, Germany. The sample intervals were selected based on the Initial Reports of the Deep Sea Drilling Project Vol. 40 and 75 (e.g.: Bolli et al., 1978a,b; Deroo et al., 1984). Overall, 29 samples were studied (Table 2-1), of which 21 were taken from Aptian and Albian aged carbonaceous limestones, black shales, and silty black shales, and 8 from Turonian to Coniacian aged shales and mudstones. Aliquots of each sample were cut with a water-cooled saw and dried, before being pulverized with a rotating disc mill.

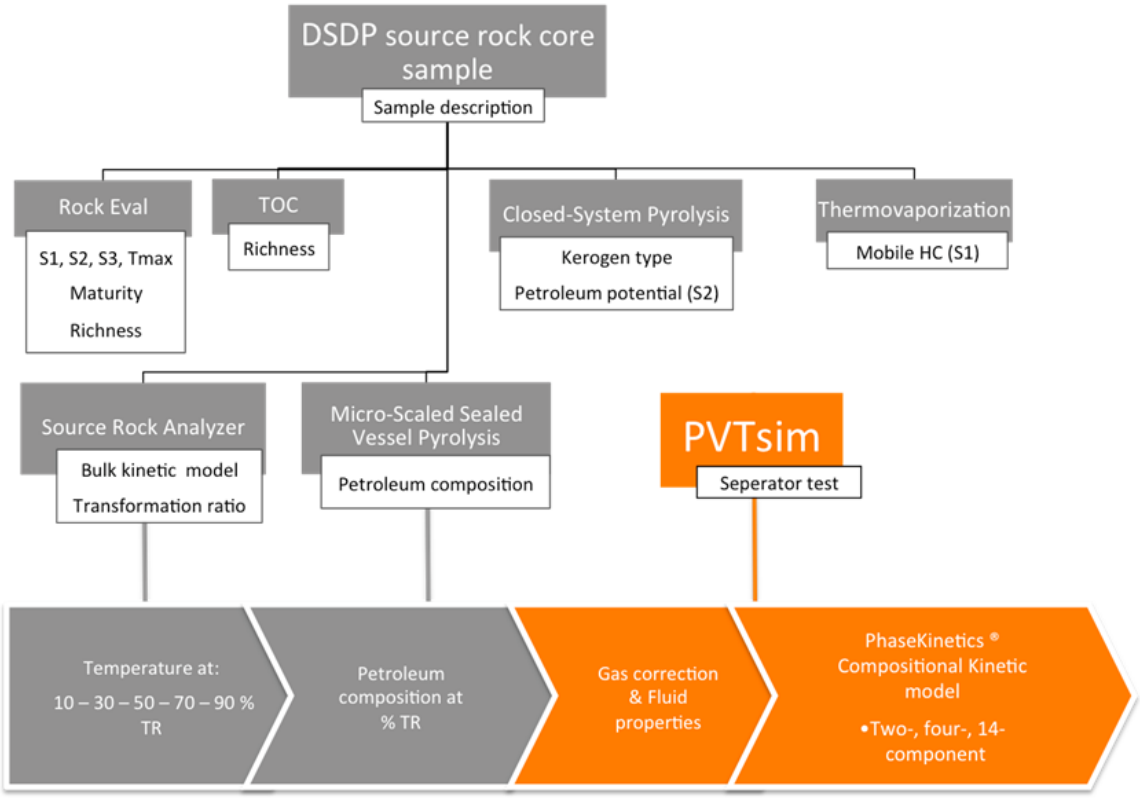

Figure 1-4: Organic-geochemical analysis workflow following the PhaseKinetics(R) approach of di Primio and Horsfield (2006) with the respective source rock parameter that is investigated during each step (white boxes).

The organic geochemical analysis methods are outlined in Figure 1-4 and more details are presented in Chapter 2. The procedure follows the PhaseKinetics approach of di Primio and Horsfield (2006), which combines open- and closed-system pyrolysis and gas-chromatography techniques with artificial maturation series experiments to derive a compositional kinetic model, in this case for potential Cretaceous-aged source rocks from the southeast Atlantic.

1.5.2. Seismic interpretation

The seismic dataset (Figure 1-1) consists of (i) 600 2D exploration-seismic reflection lines, acquired from 1976 to 2002, covering an area of about 95,000 km2 and with maximum recording depth of 7000 milliseconds (ms) two-way-travel time (TWT), and (ii) two exploration 3D seismic reflection cubes: one covering an area of 1095 km2 along the present-day shelf break and upper slope, between 265 and 610 m water depth, and a second survey covering 1074 km2 on the shelf in less than 250m water depth above the Ibhubesi gas/condensate field. The seismic cubes are pre-stack time migrated and have a line spacing of 25m. The chronostratigraphy is based on initial reports from Leg 40 DSDP sites 360 and 361 (Bolli et al., 1978c) and well reports of 32 exploration wells, tied to the seismic lines. 2D and 3D data were loaded in the commercial seismic interpretation software Petrel 2011.1.2 from Schlumberger.

The 3D seismic cubes were further investigated using time-slices and seismic attribute maps extracted along the horizons. The term seismic attribute loosely refers to all types of measurements along a seismic trace taken within a limited time window around a reflector (Bacon et al., 2009). The two most common attributes used for this study are dip-azimuth and variance. The latter is a coherence-type attribute used to image vertical discontinuities, most commonly faults, in the amplitude distribution (van Bemmel and Pepper, 2000).

The seismic interpretation was conducted in several steps following the workflow outlined in Figure 1-5. First, the well tops of 22 seismic reflectors were interpreted and correlated across the various seismic surveys to generate a 3-dimensional structure grid in TWT. The interpreted ages of the well tops were taken from the well reports and cross-referenced with the literature (e.g. Dingle et al. 1983, McMillan, 2004; Weigelt and Uenzelmann-Neben, 2004). They provide the basis for relative ages of all interpreted non-processing-related seismic anomalies (pockmarks, mounds, etc.) and the age assignment of the petroleum system model. The sequences lithology descriptions are based on well reports and the literature (Gerrard and Smith, 1982; Dingle et al., 1983; McMillan, 2003; Weigelt and Uenzelmann-Neben, 2004; Wigley and Compton, 2006).

Second, the economic basement for the petroleum system model was determined, by interpreting the seismic reflections and structures below the seismic reflector of the break-up unconformity. Thus identifying synrift structures such as grabens and half-grabens, and SDRs, that were in part reported by Gerrard and Smith (1982) Dingle et al. (1983) Bauer et al. (2000) as well as structural trends in the Paleozoic basement that have remained very elusive.

The third step consisted on finalizing the interpretation of faults, which were identified and mapped throughout the first two steps. The fault interpretation was limited to large regional features that can be followed across several 10s of kilometers. A detailed study was conducted in the 3D seismic cube located above the densely faulted shelf break of the northern Orange Basin (Chapter 3).

The seismic domain conversion from TWT to true vertical depth (TVD) makes up the fourth step. The velocity model is derived from interval velocities that were calculated between the interpreted TWT horizons using check-shot data from the exploration wells. The convergent

interpolation algorithm of the Petrel 2011.1.2 software generated negative values for areas with very low well density and interval thickness, such as in the deep water below the present-day shelf break. On the other hand, very high values were calculated across intervals with large thickness variations and only few well penetrations such as the Aptian and Albian in the northwestern depocenter. In order to constrain the algorithm, minimum and maximum interval velocity values were assigned for each individual interval based on Bauer et al. (2000), who conducted a refraction seismic study from onshore South Africa across the offshore Orange Basin. Of the 32 exploration wells, only four penetrated the top of the basement, generally along the eastern coastal margin of the basin. Therefore, the interval velocities for the basement and synrift intervals (pre-6At) were taken from Bauer et al. (2000). The resulting velocity model was used to calculate TVD structure grids, which in turn were cross-checked with the existing well tops.

In a fifth step seismic anomalies (Figure 1-6) were mapped, analyzed, and categorized into the following three classes: (1) processing-related, (2) present-day and paleo-sediment surface anomalies and (3) present-day and paleo-anomalies within the sedimentary column. Analogues were taken from the studies of Cartwright et al. (2007), Judd and Hovland (2007), and Løseth et al. (2009) and previous studies of the fluid flow features in the Orange Basin conducted by Ben-Avraham et al. (2002), Kuhlmann et al. (2010), and Boyd et al. (2012).

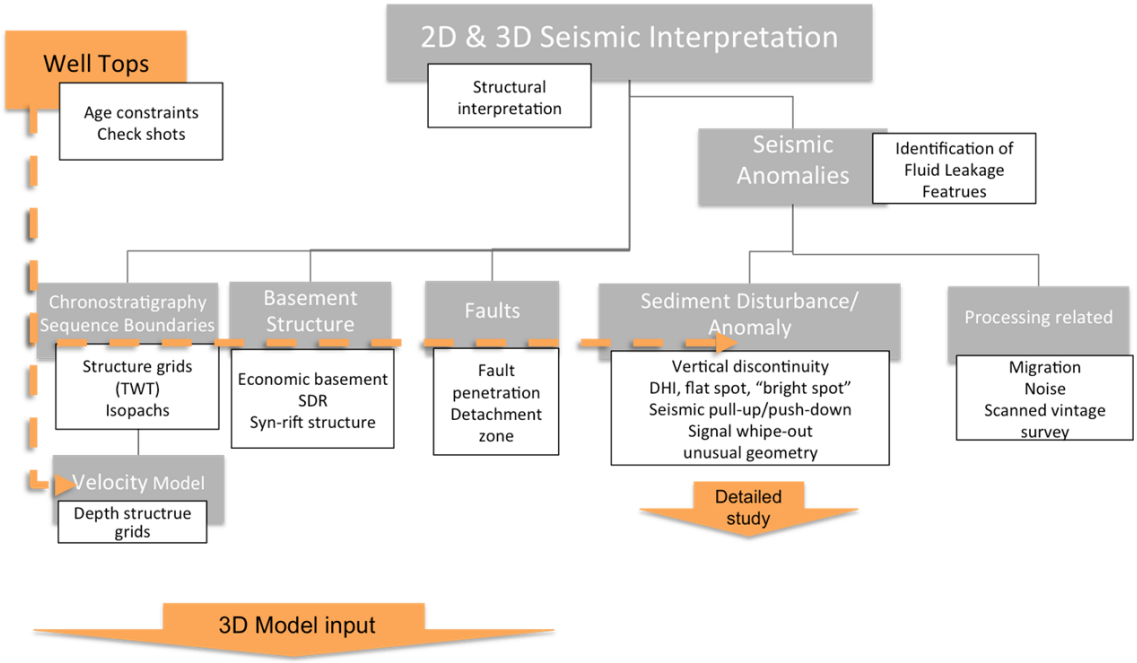

Figure 1-5: Seismic interpretation workflow to generate 3D basin modeling inputs.

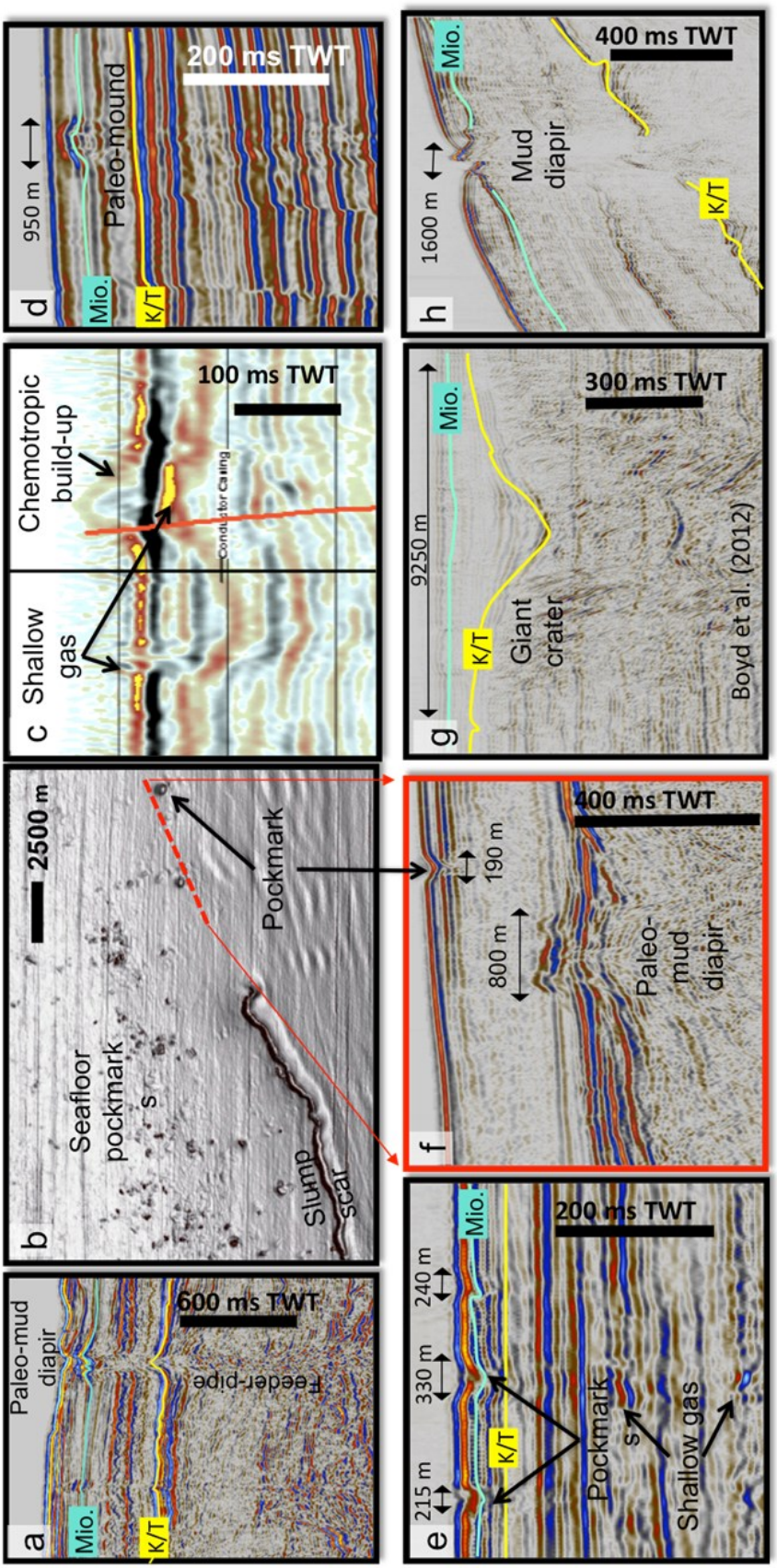

Figure 1-6: Examples (a-h) of seismic anomalies at the sediment surface and in the sediment column as interpreted on seismic from the Orange Basin. A Miocene (Mio.) and a Top-Cretaceous (K/T) unconformity are included for reference.

1.5.3. 3D petroleum system modeling

The geologic elements and processes that lead to the formation of a petroleum accumulation make up a petroleum system (Magoon and Dow, 1994). The basic elements of a conventional petroleum system are an organic-rich source rock, a porous reservoir, and low-permeability seal rocks, and a trap, as well as the basic geologic processes that lead to petroleum generation, migration, accumulation, and entrapment (Hunt, 1996; Magoon and Dow, 1994). 3D petroleum system modeling studies combine all these elements and processes in a numerically-based basin model. It is used to simulate the physical and chemical processes during burial and diagenesis and allows to make predictions regarding petroleum occurrences (Al-Hajeri et al., 2009; Hantschel and Kauerauf, 2009; Peters et al., 2007). Nowadays, petroleum system modeling is widely used for petroleum exploration and usually integrated with geophysical exploration methods (Al-Hajeri et al., 2009). Basin models are constructed and calibrated using various types of geophysical, geochemical, and petrophysical data from remote sensing programs, wells, and outcrops. Based on the input parameters, sediment compaction and the evolution of porosity, pressure, temperature, and permeability are calculated through time, thus providing the means to investigate the timing of hydrocarbon generation and expulsion from a source rock versus the timing of reservoir and trap formation. Further, hydrocarbon composition and phase predictions coupled with migration simulations are used to predict the location and size of accumulations and to conduct a qualitative and quantitative hydrocarbon mass balance evaluation. By running multiple iterations with varying input parameters, basin modeling allows constraining the geologic uncertainties, thus lowering the exploration risk. Although this modeling technique is primarily used to predict petroleum accumulations, it can also be used to study migration losses, and thus hydrocarbon leakage at the sediment surface.
Hantschel and Kauerauf (2009) give a detailed description of petroleum system modeling workflows with the underlying mathematical theories that are used for the commercial 3D basin modeling software PetroMod. The following methodology outline is based on Hantschel and Kauerauf (2009) and gives an overview of critical modeling steps used for this study. A detailed discussion of these input parameters is given in Chapter 4.

1.5.3.1. Burial history - deposition, compaction, and pressure modeling

A 3D basin model is based on depth structure maps of regionally important chrono- and/or lithostratigraphic rock formations. The structure maps are derived from a combination of 2D and/or 3D seismic interpretations, well formation picks, and outcrop measurements. The structure maps define the top or base of a layer, which in turn represents a distinct stratigraphic event with a beginning and ending time. One basic assumption of modeling is that a model layer's thickness and timing of deposition and non-deposition or erosion are known. Deposition, non-deposition, and erosion may occur simultaneously in different parts of the modeled area during one event. Layer lithologies are based on well data. If that is unavailable, depositional analogues have to be sought. The lithology assignment and

calibration is important for determining rock properties within the model, such as the porosity and thermal conductivity. During model simulation, the layers are first decompacted using compaction algorithms for the assigned lithologies. During the next step porosity reduction is forward modeled and can be calibrated against present-day porosities (Al-Hajeri et al., 2009; Hantschel and Kauerauf, 2009). Compaction results in the reduction of porosity, thus changing the pore pressure distribution (Allen and Allen, 2013). Pressure and compaction affect basin geometry and rock parameters, which ultimately control the permeability and the temperature distribution in the model (Al-Hajeri et al., 2009; Allen and Allen, 2013; Hantschel and Kauerauf, 2009).

1.5.3.2. Thermal model - heat flow analysis

The lithology calibration is usually followed by the heat flow analysis. This calibration process attempts to replicate present-day subsurface temperature gradients and the basin's thermal history. The main input parameters for this step are the basal heatflow, the sediment surface temperature, subsidence rates, and amounts of erosion.

The thermal properties of the rocks (thermal conductivity, heat capacity, radiogenic heat production), basal heat flow, and sediment surface temperature are the primary controls on the temperature gradient in the model (Al-Hajeri et al., 2009; Hantschel and Kauerauf, 2009). It is typically calibrated against well data (corrected bottom hole and drill stem test temperatures) and also surface measurements.

The reconstruction of the thermal history is more complex. It can be calibrated against thermal maturity indicators. The most common are vitrinite reflectance and Rock-Eval T_{max}, less common are thermal alteration index and biomarkers. All of them have to be evaluated for possible effects of reworking or other chemical alteration and abnormal maturity that may be caused by erosion, migrating petroleum, hydrothermal alteration, or proximity to igneous intrusions. The two main model parameters that control the thermal history are basal heat flow, subsidence and erosion rates. In order to constrain these, the tectonic setting and geologic evolution of a basin need to be understood (Allen and Allen, 2013). A first estimate for a paleo heat flow may be derived from the tectonic setting by looking at analogues, such as a rift or passive margin, an intracratonic basin or subduction zone (Allen and Allen, 2013), and can be further refined by crustal modeling (Hirsch et al., 2010; Kusznir et al., 1995; Maystrenko et al., 2013; Van Wees et al., 2009). The timing and magnitudes of erosion and changes in paleo heat flow can also be refined using apatite fission track analysis or fluid inclusion studies. Due to the limited temporal resolution of most basin models and the often limited availability of geologic calibration data, the paleo heat flow solutions may represent a sum of thermal events that affected a certain basin. Overall, the paleo heat flow solutions and erosion estimates have to be geo*logic*, i.e. have to fit the basin evolution and structure.

The reconstructed thermal model allows calculating the rates of chemical reactions using kinetic models. These models are based on Arrhenius type reactions and are temperature sensitive (Boreham et al., 1999; di Primio and Horsfield, 2006; Schenk et al., 1997b; Tegelaar

and Noble, 1994). This allows constraining and even calibrating the thermal model with measured maturity data.

1.5.3.3. Petroleum generation and fluid properties

Following thermal calibration, the timing of petroleum generation and expulsion from the source rock are simulated according to kinetic models and hydrocarbon expulsion models. The kinetic models are based on first order, parallel pseudo-reactions that describe the decomposition (primary cracking) of kerogen and bitumen to petroleum (Boreham et al., 1999; Schenk et al., 1997a, 1997b; Stainforth, 2009; Tegelaar and Noble, 1994) and also secondary cracking of oil to gas (Dieckmann, 1998; Dieckmann et al., 1998; Schenk et al., 1997a, 1997b). The temperature dependence of these chemical reaction rates can be described with the Arrhenius equation (Boreham et al., 1999; Schenk et al., 1997b; Tegelaar and Noble, 1994). The complexity of kinetic models varies from bulk kinetic models to multi-component models with 14 or more hydrocarbon components that group hydrocarbons according to their carbon chain lengths and boiling point ranges to accurately reflect petroleum properties. Bulk kinetic models can be used to calculate the timing of generation and quantities of hydrocarbons generated by a source rock. In addition to this, multi-component kinetic models allow to simulate hydrocarbon phase behavior and to predict basic petroleum fluid properties (di Primio and Horsfield, 2006). Correct calculation of the pressure-volume-temperature (PVT) relationships of the fluids is a prerequisite for simulating basin-wide migration and to make predictions for fluid density and API gravity, viscosity, bubble point pressure, gas-oil-ratio (GOR), and oil formation volume factor (Bo)(di Primio and Horsfield, 2006; Hantschel and Kauerauf, 2009).

In order to study the timing of hydrocarbon generation and to make a first approximation of generated volumes, the basic source rock characteristics, such as initial total organic carbon content (TOC), initial Hydrogen Index (HI), and kerogen type have to be known. These data are typically derived from organic-geochemical analysis of source rock samples and ideally coupled with an immature source rock maturation series study. This allows deriving the organofacies type, which is strongly linked to the depositional environment, and the above-mentioned bulk and multi-component kinetic models, respectively. A description of one such methodology is given in Chapter 2. If such information is unavailable, as it is the case for many frontier exploration areas, analogue models for the depositional environment of the source rock may be used. The analogues help determining the organofacies type, and thus basic source rock parameters and a bulk kinetic model.

1.5.3.4. Migration modeling

In PetroMod 2011.1.1 hydrocarbon migration is modeled using a Hybrid Method, which is a combination of Darcy flow and Flowpath calculations. Based on a pre-defined permeability threshold, usually 10^{-2} millidarcy (mD) at 30% porosity, the model's cells are treated as either a carrier (and reservoir, such as sandstone) or a low permeability facies (such as silt and shale) (Hantschel and Kauerauf, 2009). Darcy flow is calculated in low permeability layers

where three-phase flow (water, oil, gas) is modeled at very small time intervals taking capillary pressure, buoyancy, friction, and fluid viscosity into account to provide an accurate migration model. The Flowpath method (ray tracing) is used for flow in carrier rocks and assumes instant petroleum migration, which is mainly buoyancy controlled, and therefore simplifies the algorithm reducing calculation times (Hantschel and Kauerauf, 2009). The flowpaths are constructed based on the carrier layer's geometry, thus defining drainage areas that contribute to a hydrocarbon accumulation. Drainage areas are used to analyze migration paths and shadows, spill points within the carrier system and along faults, as well as losses through the seal within a basin model.

An alternative to the Darcy-based Hybrid method is the Invasion-Percolation (IP) method. The IP modeling approach is buoyancy driven and assumes instant flow during each model time step until a capillary balance is reached (Hantschel and Kauerauf, 2009). This method is based on percolation experiments, which demonstrate and allow predictions on how oil moves through a water-wet carrier system (Carruthers and Ringrose, 1998; Vasseur et al., 2013). After expulsion from the source rock, a critical saturation is needed to initiate the buoyancy-driven flow of oil in water. The capillary entry pressure of the pore throats restricts the flow of oil (Carruthers and Ringrose, 1998). In high permeability carriers, such as sandstones, oil moves vertically until reaching a low permeability flow barrier, such as mudstones, below which micro accumulations may form. Pressure build-up in these accumulations leads to vertical breakthrough into the low-permeability layer or to horizontal flow along the barrier. The migrating oil flows in the form of discrete stringers, the shape and size of which are flow rate dependent. Subsequent pulses of migrating oil will predominately follow the paths of previous stringers (Carruthers and Ringrose, 1998; Hantschel and Kauerauf, 2009; Vasseur et al., 2013).

In IP simulations, the generation and expulsion of petroleum from the source rock control the timing of migration. The stringer pathways are calculated through a connectivity analysis of each cell in the model, based on absolute permeability and capillary entry pressure (Kroeger et al., 2009). The main advantages of IP over the Hybrid method, however, are (1) the use of one migration calculation method for the entire model, especially across cells with large permeability differences, which may be found at the reservoir-seal boundaries of incised valleys in low-permeability rocks; (2) less processing power is needed than for Darcy-based methods, resulting in faster simulation times per iteration; (3) thus allowing higher resolution migration modeling over large areas. On the other hand, the biggest drawbacks of IP in comparison to the Hybrid method are (1) the rough estimate for the timing of migration, which mainly depends on the temporal resolution and on the timing of generation; (2) that modeled migration pathways are not reproducible in detail, because the IP method assigns a random value for capillary pressure based on statistical variations for the lithology type to represent rock heterogeneities; and (3) multi-phase flow and compositional changes are not handled as well as in Darcy and Flowpath calculations (Hantschel and Kauerauf, 2009).

In order to unravel the migration dynamics in a basin multiple migration scenarios should be run, including a test of the different migration algorithms. As mentioned, each algorithm has

its strengths and weaknesses. The final interpretation is strongly dependent on the available data and also the interpreter's experience. Migration models allow constraining the uncertainties regarding timing of migration and trap formation. They further help to identify the mechanisms that lead to the remobilization of petroleum, such as spilling, or breakthrough at seals and faults. Petroleum system models are a powerful tool for establishing a relationship between the geologic processes that lead to changes in pressure, temperature, or basin geometry, and their effect on hydrocarbon migration. The best calibration method for migration models is a comparison with fluid data from known production. Ideally, the model should reproduce the known oil or gas fields, shows, even seeps, and predict the fluid properties.

2. Source rock characteristics and compositional kinetic models of Cretaceous organic-rich black shales offshore southwestern Africa

The contents of this chapter have been accepted for publication and printed in the international peer-reviewed journal “Organic Geochemistry” as follows:

Hartwig, A., di Primio, R., Anka, Z., Horsfield, B., 2012. Source rock characteristics and compositional kinetic models of Cretaceous organic rich black shales offshore southwestern Africa. Organic Geochemistry 51, 17–34.

Abstract

The source rock potential of Cretaceous organic-rich whole rock samples from deep sea drilling project (DSDP) wells offshore south-western Africa was investigated using bulk and quantitative pyrolysis techniques. The sample material was taken from organic-rich intervals of Aptian-, Albian-, and Turonian-aged core samples from DSDP site 364 offshore Angola, DSDP well 530A north of the Walvis Ridge offshore Namibia, and DSDP well 361 offshore South Africa. The analytical program included TOC, Rock Eval, pyrolysis GC, bulk kinetics and micro-scale sealed vessel pyrolysis (MSSV) experiments. The results were used to determine differences in the source rock petroleum type organofacies, petroleum composition, gas-oil-ratio (GOR), and pressure-volume-temperature (PVT) behavior of hydrocarbons generated from these black shales for petroleum system modeling purposes.

The investigated Aptian and Albian organic-rich shales proved to contain excellent quality marine kerogens. The highest source rock potential was identified in sapropelitic shales in DSDP well 364, containing very homogeneous Type II and organic sulfur-rich Type IIS kerogen. They generate P-N-A low wax oils and low GOR sulfur rich oils, whereas Type III kerogen-rich silty sandstones of DSDP well 361 show a potential for gas/condensate generation. Bulk kinetic experiments on these samples indicate that the organic sulfur contents influence kerogen transformation rates, Type IIS kerogen being the least stable. South of the Walvis Ridge, the Turonian contains predominantly a Type III kerogen. North of the Walvis Ridge, the Turonian black shales contain Type II kerogen and have the potential to generate P-N-A low and high wax oils, the latter with a high GOR at high maturity.

Our results provide the first compositional kinetic description of Cretaceous organic-rich black shales, and demonstrate the excellent source rock potential, especially of the Aptian-aged source rock, that has been recognized in a number of the South Atlantic offshore basins.

2.1. Introduction

The South Atlantic margin hosts several petroliferous sedimentary basins, especially offshore Brazil (Mello et al., 1988b; Davison, 1999) and in the Lower Congo and Angola Basins offshore southwestern Africa (Beglinger et al., 2012; Coward et al., 1999). Further to the

south, significant petroleum discoveries have been made in the Orange and Bredasdorp Basins offshore southern Africa (Jungslager, 1999; van der Spuy, 2003).
The main sources for these hydrocarbon accumulations are lower Cretaceous lacustrine and lower to upper Cretaceous marine black shales. The kerogen types, richness, and biomarker signatures of these source rocks and their derived oils have been reported in previous studies by Mello et al. (1988a, 1998b), Davison (1999), and Mello and Katz (2000) for the Brazilian margin, and by Bolli et al. (1978a, 1987b), Burwood (1999), Mello and Katz (2000), van der Spuy (2003), and Adekola et al. (2012) for the southwestern African margin.
In order to adequately describe the petroleum potential of a given source rock, bulk and screening data (TOC and Rock Eval) are not sufficient, as they do not take the thermal stability of the organic matter into account (Schenk et al., 1997). Even though a close relationship between kerogen type and source rock bulk kinetics exists, organic matter heterogeneity, common in deltaic sequences with high terrestrial input, as well as high sulfur contents, frequently found in marine carbonate source rocks, can lead to considerable variations in hydrocarbon generation rates (di Primio and Horsfield, 2006; Schenk et al., 1997a, 1997b; Tegelaar and Noble, 1994). Considering that significant variability in kerogen stability has been reported for lower Cretaceous organic-rich shales from the Angolan margin (Burwood, 1999) and that oils from Aptian source rocks of the Brazilian margin are known to be sulfur-rich (Mello et al., 1988b), this aspect is very important for maturity studies of South Atlantic margin basins. A further refinement of prospectivity studies can be achieved by using compositional kinetic data from artificial maturation experiments to elucidate changes in the physical properties of petroleum fluids under varying pressure and temperature conditions (PVT behavior, di Primio et al., 1998; di Primio and Horsfield, 2006). These datasets can be used to predict the phase behavior and migration dynamics, especially secondary migration, in basin modeling studies (e.g. Primio and Skeie, 2004).
Up to date, data on the kinetics of South Atlantic Cretaceous source rocks as well as the petroleum-type and composition they generate are scarce or non-existent. In this study we investigated Aptian, Albian, and Turonian to Coniacian aged thermally immature, organic-rich black shale and mudstone intervals from DSDP sites located in the southeast Atlantic to determine trends and differences in organofacies, petroleum type, composition, and to model the physical properties of the generated hydrocarbons. This data can be used as input for petroleum system modeling studies of South Atlantic margin basins.

2.2. Study area and sample locations

2.2.1. Southeast Atlantic margin evolution

The geologic evolution of the continental margin basins along southwestern Africa can be subdivided into synrift, rift-to-drift transition, and drift phases that were related to the progressive opening of the South Atlantic (Beglinger et al, 2012; Torsvik et al., 2009).
The break-up of Gondwana was accompanied by Triassic to Jurassic intracontinental rifting, forming north-south trending grabens and half-grabens along the present-day southwest African margin (Gerrard and Smith, 1982; Coward et al., 1999; Karner et al., 1999). The rift

structures contain continental and fluvio-deltaic deposits and host lacustrine organic-rich black shales of late Jurassic to early Cretaceous age (Karner et al., 1999; Macdonald et al., 2003). These synrift source rocks were deposited in deep anoxic or saline lakes and are known to have sourced oil accumulations on the southwest African and Brazilian margin (e.g. Schiefelbein et al., 2000; Muntingh, 1993). A review of their source rock characteristics is given in Burwood (1999), Coward et al. (1999), and Schiefelbein et al. (2000).

The initial opening of the South Atlantic and emplacement of oceanic crust began during the early Cretaceous (137 - 126 Ma ago) and propagated from south to north (e.g. Nürnberg and Müller, 1991; Blaich et al., 2009).

South of the Walvis Ridge the first marine incursions mark the beginning of the rift-to-drift transition during the Barremian to Aptian. It is marked by the sedimentation of continental red beds which grade into marine sandstones overlain by organic-rich black shales (Broad et al., 2006). These black shales were deposited throughout the early Aptian to mid Albian in an anoxic marine environment that resulted from restricted ocean circulation over the Falkland Plateau into the Cape Basin (Bolli et al., 1978a; Herbin et al., 1987). During the mid/late Albian the westward spreading Falkland Plateau cleared southern Africa providing a deepwater passage through the Agulhas Gap that led to increasing bottom water ventilation in the South Atlantic (Zimmermann et al., 1987; Macdonald et al., 2003).

North of the Walvis Ridge and along equatorial West Africa, the transitional sequence consists of early Aptian transgressive clastics that grade into fluvial to lagoonal deposits which are overlain by a thick evaporitic sequence (Hudec and Jackson, 2004; Séranne and Anka, 2005). The late Aptian salt sequence was deposited in a restricted shallow-water environment stretching along the margin basins of equatorial West Africa and Brazil up to the Cameroon Volcanic Ridge, collectively known as the Aptian Salt Basins (Coward et al., 1999; Torsvik et al., 2009).

Along the equatorial South Atlantic margin the drift succession begins in the late Aptian with continuous deepening of the South Atlantic leading to the first marine incursions and the deposition of marine carbonates (Séranne and Anka, 2005; Torsvik et al., 2009). These carbonates contain organic-rich and sapropelic limestones and were deposited in a restricted marine environment that lasted throughout the Albian (Schiefelbein et al, 2000; Hudec and Jackson, 2004). They are known to have sourced oil accumulations in the onshore Kwanza Basin (Burwood, 1999) and maybe in the offshore Lower Congo and Angola Basins.

The drift succession of the southwest African margin is dominated by Albian siliciclastic and Upper Cretaceous progradational/aggradational fluvio-deltaic sequences (Broad et al., 2006). Early Albian oxygen deficiency in the Cape Basin was favorable for sapropelic black shale deposition (Zimmermann et al., 1987). These organic-rich intervals are the main source rocks of gas accumulations in the Orange Basin (e.g. Jungslager, 1999; van der Spuy, 2003; Kuhlmann et al., 2011).

North of the Walvis Ridge, Upper Cretaceous sedimentation is characterized by an increasing clastic content and halokinesis (Hudec and Jackson, 2004; Séranne and Anka, 2005). Whereas the southern African margin underwent extensive shelf erosion and severe gravity faulting of the shelf edge due to margin uplifting (Brown et al., 1995; de Vera et al., 2010).

A major episode of black shale deposition occurred during the Cenomanian-Turonian oceanic anoxic event (OAE 2), a period of oxygen deficiency observed throughout the South Atlantic (Herbin et al., 1987; Zimmermann et al., 1987; Forster et al., 2008). These black shales have been recognized as potentially oil-prone source rocks along the southwest African margin (Aldrich et al., 2003; Bray et al., 1998; Burwood, 1999)and also the Brazilian margin (Mello et al., 1989) and possibly in the ultra deep offshore of the Angola Basin (Anka et al., 2010).

Along the equatorial West African margin terrigenous clastic sedimentation continues up to the present-day with a major Oligocene erosion event and subsequent incision of submarine canyons and the progradation of deep-sea fans, such as the Congo fan (Anka and Séranne, 2004; Anka et al., 2009). Cenozoic sediments of the southwest African margin consist of pelagic clays and nannofossil ooze (e.g. Weigelt and Uenzelmann-Neben, 2004).

2.2.2. Sample locations

The samples were taken from Aptian to Albian and Turonian to Coniacian aged, thermally immature, organic-rich intervals of cores recovered from DSDP sites 361 and 364 of LEG 40, and DSDP site 530A of LEG 75 (Figure 2-1).

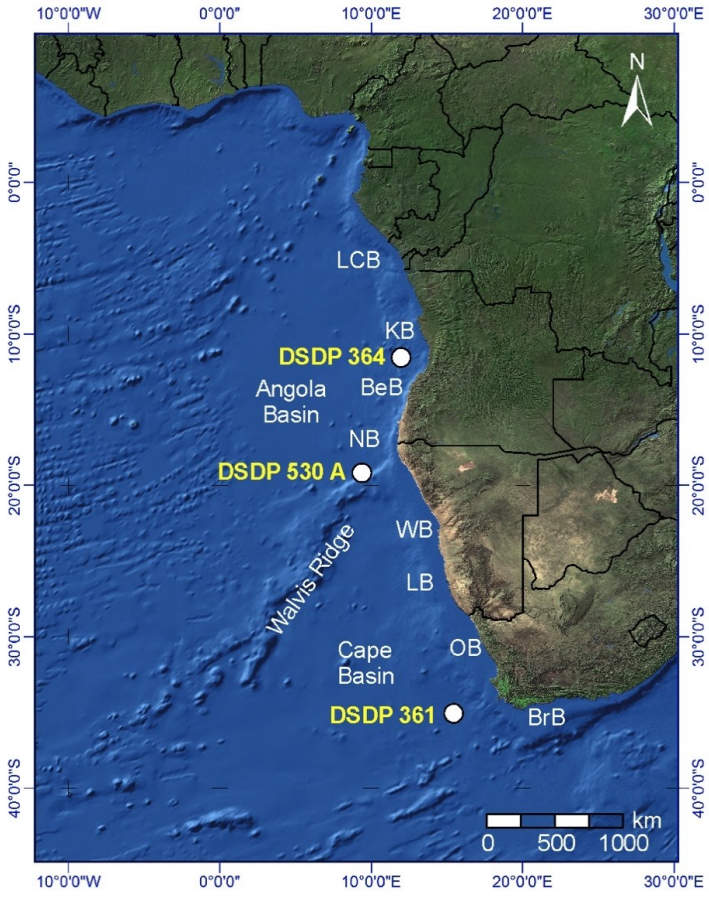

Figure 2-1: Equatorial and southwest African margin basin overview with DSDP site locations; BeB = Benguela Basin, BrB = Bredasdorp Basin, KB = Kwanza Basin, LB = Lüderitz Basin, LCB = Lower Congo Basin, NB = Namibe Basin, OB = Orange Basin, WB = Walvis Basin; base map: Amante and Eakins (2009).

2.2.2.1. DSDP site 361

DSDP site 361 was drilled in 4549 m water depth on the lower continental rise of the Cape Basin, 300 km southwest of Cape Town. The well penetrated 1314 m of upper Eocene to lower Aptian aged sediments (Bolli et al., 1978a). The sedimentary succession of the Cape Basin was subdivided into seven lithologic units, four of them were described at DSDP site 361 (Figure 2-2). A detailed description is given in the Initial Reports of the Deep Sea Drilling Project Vol. 40 (Bolli et al., 1978a). Briefly, the Aptian sediments consist of sapropelic shale, greenish-grey sandy mudstone, and sandstone deposited as coarse turbidites with intercalated carbonaceous shales (unit 7). The upper Aptian to Maastrichtian (unit 6) consists of non-carbonate, terrigenous grey to greenish black shales with intercalated, finely cross-bedded siltstones and sandy mudstones deposited in a distal fan turbidite facies. The late Maastrichtian and Paleocene interval is made up of brown to greenish grey pelagic clay (unit 5) with a sharp transition to carbonate-rich light brown to greenish grey mud and nannofossil ooze (unit 4) of late Paleocene to Eocene age.

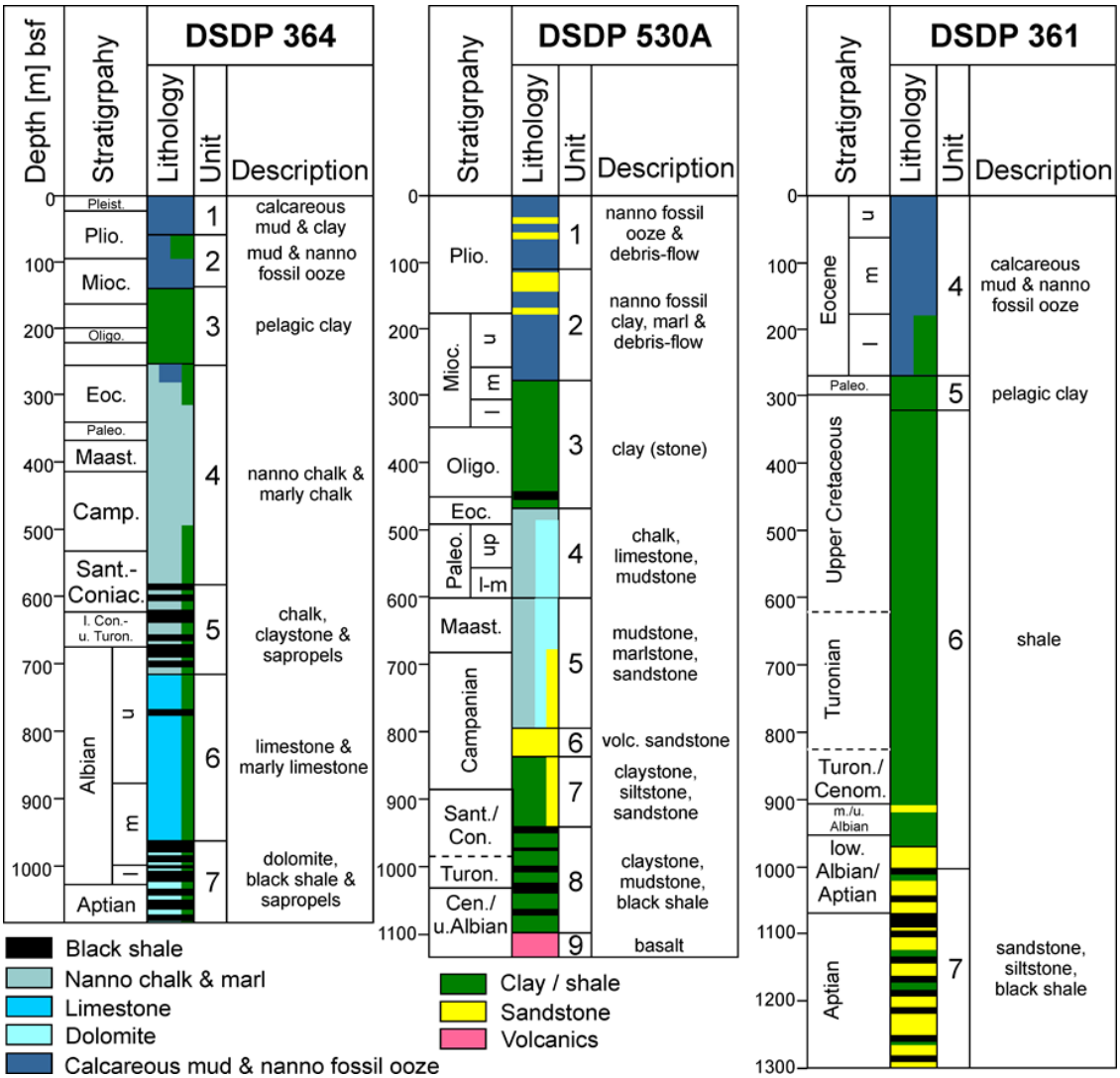

Figure 2-2: Main lithologic units of the investigated DSDP sites according to Bolli et al. (1978a,b), Hay and Sibuet (1984) and Forster et al. (2008).

The highly carbonaceous Aptian sediments contain wood fragments and reworked coaly substance derived from a near shore flora and rapidly buried by turbidity currents (Bolli et al., 1978a). The intercalated sapropelic black shales are reported to have total organic carbon (TOC) contents of up to 15% and contain predominately amorphous marine organic matter and bituminous material (Herbin et al. 1987; van der Spuy, 2003). The decrease in organic matter content and increasing cross-bedding observed in Aptian to Albian sediments reflects the changes of the depositional environment from an early Aptian anoxic ocean basin to an increasingly ventilated deep sea environment with stronger bottom currents (Bolli et al., 1978a; Zimmermann et al., 1987). An interval of detrital organic matter enrichment with TOC contents up to 4.0% reflects renewed oxygen deficiency in the Cape Basin during the Cenomanian-Turonian OAE (Herbin et al., 1987). According to Raynaud and Robert (1978) vitrinite reflectance (VR_o) values for the Aptian black shales range between 0.5 and 1.0%, although Schmidt (2004) reports mean values of 0.27 to 0.35% VR_o for the same interval.

2.2.2.2. DSDP site 530A

DSDP site 530A was drilled in 4629 m water depth and penetrated the abyssal basin floor with a typical seismic stratigraphy representative for the southeastern corner of the Angola Basin, 20 km north of the Walvis escarpment. The well was drilled to a sub-bottom depth of 1121 m where it encountered basalt, the age of the penetrated sediments ranges from late Albian to Holocene (Hay and Sibuet, 1984). The sedimentary succession was subdivided into nine lithologic units (Figure 2-2). A detailed description is given in the Initial Report of the Deep Sea Drilling Project Vol. 75, and is summarized below.

The deepest lithologic unit consists of basalt (unit 9) and is overlain by late Albian to early Santonian green clay- and marlstones with intercalated black shales (unit 8). The following lithologic units contain numerous turbidite sequences and are of early Santonian - early Campanian, Maastrichtian, and Maastrichtian - Eocene age. They consist of multi-colored claystones, siltstones, and sandstone (unit 7), mudstone and chalk (unit 5), and mudstone, chalk, and clastic limestone with shallow water carbonate debris (unit 4), respectively. A Campanian volcanogenic turbiditic sandstone sequence makes up unit 6. Oligocene - Miocene aged green and red mudstone (unit 3) with intercalated clay-rich debris flows are overlain by Pleistocene calcareous biogenic sediments with intercalated clays from debris flows and fine-grained turbidites (unit 2), and Pleistocene-Holocene nannofossil ooze (unit 1).

The Albian and Turonian green and black shales contain a mixture of terrigenous and, especially in the latter, marine organic matter with TOC contents up to 16.5% (Meyers, 1984). They were transported and rapidly buried by turbidites and are thermally immature (VR_o= 0.48%, Meyers, 1984; Herbin et al., 1987). The black shales reflect an anoxic depositional environment, whereas the green shales indicate periodic bottom water re-oxidation by weak currents (Forster et al., 2008).

2.2.2.3. DSDP site 364

DSDP site 364 was drilled in 2448 m water depth on the seaward edge of the salt plateau at the transition from the outer Kwanza Basin to the Benguela Basin, 335 km SSW of Luanda. The well penetrated to a sub-bottom depth of 1086 m being several tens of meters short of penetrating the salt sequence, recovering Pleistocene to upper Aptian aged sediments that were subdivided into seven lithologic units (Bolli et al., 1978b; Figure 2-2). The oldest lithologic unit (unit 7) consists of late Aptian to middle Albian dolomitic limestone with sapropelic black shales deposited in a highly saline environment, overlain by middle Albian limestone and marly limestone (unit 6) with a gradual transition to late Albian to Coniacian aged (unit 5) marly chalks and finely laminated sapropelic black shales. Late Coniacian to Eocene aged nannofossil chalk (unit 4) deposition ends with a late Eocene - Oligocene hiatus, above which terrigenous input increases, as indicated by mid Oligocene to lower Miocene pelagic clay and radiolarian mud (unit 3). Neogene sedimentation begins with nannofossil ooze (unit 2) and lasts until the early Pliocene. It is overlain by calcareous mud and black clay with plant debris (unit 1).

The two phases of sapropelic limestone deposition encountered in the sediment record at DSDP site 364 are evidence for repeated stagnant bottom water conditions, though conditions seem to have been less anoxic throughout the Cenomanian to Coniacian as evidenced by bioturbated limestones (Bolli et al., 1978a). The organic matter is predominately amorphous marine matter with TOC contents of up to 24.0% and is thermally immature (VR_o= 0.45 %, (Foresman, 1978; Herbin et al., 1987).

2.3. Material and Methods

2.3.1. Sample material

All samples were obtained from the Integrated Ocean Drilling Program (IODP) Bremen Core Repository at the University of Bremen, Germany. The sample intervals were selected based on the Initial Reports of the Deep Sea Drilling Project Vol. 40 and 75 (Bolli et al., 1978a, 1978b; Deroo et al., 1984). Overall, 29 samples were studied (Table 2-1), of which 21 were taken from Aptian and Albian aged carbonaceous limestones, black shales, and silty black shales, and 8 from Turonian to Coniacian aged shales and mudstones. Aliquots of each sample were cut with a water-cooled saw and dried, before being pulverized with a rotating disc mill.

2.3.2. Methods

2.3.2.1. Rock-Eval and TOC

Rock-Eval analysis was performed using a Rock-Eval 6 instrument providing T_{max}, and bulk parameters S_1, S_2, and S_3 (Espitalié, 1987). Total organic carbon (TOC) content was measured using a Leco SC-632 instrument. The following temperature programs were run: Pyrolysis: 300°C for 3 minutes then pyrolized at 25 °C/min to 650 °C; Oxidation: 400 °C (for 3 min)

heated at 25 °C/min to 850 °C (held for 5 min). The measurements were conducted at Applied Petroleum Technology AS, Norway.

2.3.2.2. Pyrolysis - gas chromatography and Thermovaporization - gas chromatography

Pyrolysis - gas chromatography (Py-GC) was conducted to infer the bulk petroleum quality of the whole rock samples using a Quantum MSSV-2 Thermal Analysis System©. Between 3 - 20 mg of powdered whole rock sample was weighed into a glass tube and held in place by glass wool. The sample was heated in a flow of helium, and products released over the temperature range 300-600°C (40° K/min) were focused in a nitrogen-cooled cryogenic trap, and then heated to 300°C and released onto a capillary column for gas chromatography.

Thermovaporization - gas chromatography (Thermovap-GC) was used to analyze free hydrocarbons in the samples and performed using a Quantum MSSV-2 Thermal Analysis System©. Milligram quantities of each sample were sealed in a glass capillary and heated to 300°C in the injector unit for 5 minutes. The tube was then cracked open using a piston device coupled with the injector, and the released volatile hydrocarbons analyzed by gas chromatography.

For both Py-GC and Thermovap-GC, online gas chromatography was conducted using a 50m x 0.32mm BP-1 capillary column equipped with a flame ionization detector. Boiling ranges (C1, C2-C5, C6-C14, C15+) and individual compounds (n-alkenes, n-alkanes, alkylaromatic hydrocarbons and alkylthiophenes) were quantified by external standardization using n-butane. Response factors for all compounds were assumed the same, except for methane whose response factor was 1.1.

2.3.2.3. Bulk kinetics

For bulk kinetics modeling the whole rock samples were analyzed by non-isothermal open system pyrolysis at four different laboratory heating rates (0.7, 2.0, 5.0 and 15 °K/min) using a Source Rock Analyzer©. The generated bulk petroleum formation curves serve as input for the bulk kinetic model consisting of an activation energy distribution and a single frequency factor A.

Table 2-1: Sample information and Rock Eval results

Sample ID	sample no.	location	DSDP Site	Leg	H	Cor	Sc	Top (cm)	Bot (cm)	Depth [mbsf]	S1 (mg/g)	S2 (mg/g)	S3 (mg/g)	Tmax (°C)	PP (mg/g)	PI (wt. ratio)	HI (mg HC/g TOC)	OI (mg CO2/g TOC)	TOC (%)*	Chrono-stratigraphic Age	Lithology (from DSDP reports)
G007868	1	Walvis Ridge	530	75	A	95	CC	41.0	42.0	1014.41	1,87	96,67	11,53	407	98,54	0,02	721	86	13,4	lower Turonian	green claystone, black shale
G007869	2	Walvis Ridge	530	75	A	97	4	27.0	28.0	1030.77	0,67	53,63	6,1	410	54,3	0,01	506	58	10,6	lower Turonian	claystone, black shale
G007870	3	Walvis Ridge	530	75	A	97	4	79.0	80.0	1031.29	0,21	13,51	2,12	415	13,72	0,02	225	35	6,01	lower Turonian	claystone, black shale
G007871	4	Walvis Ridge	530	75	A	98	3	55.0	56.0	1038.55	0,25	12,79	2,98	411	13,04	0,02	196	46	6,51	lower Turonian	claystone, mudstone, black shale
G007873	5	Walvis Ridge	530	75	A	104	3	9.0	10.0	1088.09	0,09	4,49	1,45	428	4,58	0,02	175	57	2,56	Albian	grey siltstone, black shale, green limestone
G007874	6	Walvis Ridge	530	75	A	104	3	99.0	100.0	1088.99	0,15	7,44	1,69	413	7,59	0,02	144	33	5,15	Albian	grey siltstone, black shale, green limestone
G007875	7	Walvis Ridge	530	75	A	105	3	85.0	86.0	1097.85	0,49	27,52	2,11	405	28,01	0,02	385	30	7,14	Albian	siltstone, limestone, black shale
G007876	8	Walvis Ridge	530	75	A	105	3	126.0	127.0	1098.26	0,14	7,81	1,34	409	7,95	0,02	180	31	4,33	Albian	siltstone, limestone, black shale
G007877	9	Cape Basin	361	40	*	24	2	98.0	99.0	812.98	0,08	0,37	1,03	417	0,45	0,18	23	65	1,58	Turonian	shale
G007878	10	Cape Basin	361	40	*	28	5	75.0	76.0	1007.25	1,22	39,91	2,29	406	41,13	0,03	510	29	7,82	lower Albian	shale, carbonaceous
G007879	11	Cape Basin	361	40	*	28	5	137.0	138.0	1007.87	0,67	18,68	1,49	405	19,35	0,03	365	29	5,12	lower Albian	shale, carbonaceous
G007880	12	Cape Basin	361	40	*	29	2	50.0	51.0	1031.00	0,17	2,56	1,79	414	2,73	0,06	63	44	4,09	lower Albian	shale, carbonaceous
G007881	13	Cape Basin	361	40	*	29	2	112.0	113.0	1031.62	0,16	3,19	1,37	416	3,35	0,05	83	36	3,84	lower Albian	shale, carbonaceous
G007882	14	Cape Basin	361	40	*	32	6	36.0	37.0	1066.86	0,16	3,45	1,39	416	3,61	0,04	67	27	5,14	upper Aptian	mudstone
G007883	15	Cape Basin	361	40	*	33	3	50.0	51.0	1070.5	0,88	45,06	3,57	419	45,94	0,02	554	44	8,13	Aptian	shale
G007884	16	Cape Basin	361	40	*	36	2	67.0	68.0	1097.67	0,19	1,76	1,59	414	1,95	0,1	37	33	4,8	Aptian	shale, carbonaceous
G007885	17	Cape Basin	361	40	*	37	1	75.0	76.0	1105.75	1,11	21,83	4,68	412	22,94	0,05	315	68	6,92	Aptian	shale
G007886	18	Cape Basin	361	40	*	37	1	140.0	141.0	1106.4	0,29	2,33	2,31	409	2,62	0,11	37	36	6,35	Aptian	shale
G007887	19	Cape Basin	361	40	*	40	4	126.0	127.0	1148.76	0,83	5,06	2,24	401	5,89	0,14	97	43	5,22	Aptian	shale
G007888	20	Cape Basin	361	40	*	47	1	136.0	137.0	1267.86	0,19	1,09	1,19	411	1,28	0,15	28	30	3,93	Aptian	shale, carbonaceous, sandy
G007889	21	Angola Basin	364	40	*	21	4	133.0	134.0	602.48	0,89	48,95	6,99	409	49,84	0,02	485	69	10,1	upper Coniacian	marly chalk and mudstone

Table 2-1: Sample information and Rock Eval results - continued

Sample ID	sample no.	location	DSDP Site	Leg	H	Cor	Sc	Top (cm)	Bot (cm)	Depth [mbsf]	S1 (mg/g)	S2 (mg/g)	S3 (mg/g)	Tmax (°C)	PP (mg/g)	PI (wt. ratio)	HI (mg HC/g TOC)	OI (mg CO2/g TOC)	TOC (%)*	Chrono-stratigraphic Age	Lithology (from DSDP reports)
G007890	22	Angola Basin	364	40	*	23	1	137.0	138.0	645.37	3,45	112,38	8,98	407	115,83	0,03	764	61	14,7	low. Con. - up. Turon.	marly chalk
G007891	23	Angola Basin	364	40	*	23	3	128.0	129.0	648.28	1,32	92,24	7,62	413	93,56	0,01	769	64	12	low. Con. - up. Turon.	marly chalk
G007892	24	Angola Basin	364	40	*	24	1	52.0	53.0	673.02	1,75	58,36	6,61	401	60,11	0,03	526	60	11,1	upper Albian	calcareous mudstone and black sapropelic shale
G007893	25	Angola Basin	364	40	*	39	2	97.0	98.0	969.47	0,81	37,67	2,93	407	38,48	0,02	442	34	8,52	middle Albian	marly limestone and black shale, minor sapropelic
G007894	26	Angola Basin	364	40	*	42	2	11.0	12.0	1025.61	3,6	147,24	6,88	415	150,84	0,02	398	19	37	lower Albian	marly dolomitic limestone, alternating black shale
G007895	27	Angola Basin	364	40	*	44	2	113.0	114.0	1045.63	2,13	117,13	3,74	409	119,26	0,02	377	12	31,1	Albian / Aptian	dolomitic limestone, alternating black shale
G007896	28	Angola Basin	364	40	*	44	2	142.0	143.0	1045.92	1	45,97	2,72	401	46,97	0,02	476	28	9,66	Albian / Aptian	dolomitic limestone, alternating black shale
G007897	29	Angola Basin	364	40	*	45	1	87.0	88.0	1062.87	1,57	66,99	2,36	408	68,56	0,02	663	23	10,1	Albian / Aptian	dolomitic limestone, alternating black shale

2.3.2.4. Micro-scaled sealed vessel pyrolysis - gas chromatography and development of compositional kinetics

Closed system pyrolysis - gas chromatography with micro-scaled sealed vessel (MSSV) (Horsfield et al., 1989) was employed for the artificial maturation experiments. Milligram quantities of each sample were sealed in glass capillaries and artificially matured at 0.7 °K/min using a special MSSV prep-oven. Temperatures required to bring about 10, 30, 50, 70, and 90% conversion were derived from the Source Rock Analyzer data used primarily for kinetics determinations. The tubes were placed in the Quantum MSSV-2 Thermal Analysis System© and then cracked open using a piston device coupled with the injector. Volatile products were analyzed as described above for Py-GC and Thermovap-GC.

The PhaseKinetics (di Primio and Horsfield, 2006) approach allows linking the source rock organic facies to the petroleum type it generates. Using data from a combination of open and closed system pyrolysis techniques bulk kinetic and compositional information can be obtained, corrected and integrated into a compositional kinetic model which allows the prediction of the hydrocarbons physical properties (gas-oil-ratio "GOR", saturation pressure "P_{sat}", and formation volume factor "B_O").

For the purpose of PVT modeling the fluid description consists of fourteen compounds. Seven in the gas fraction (C_1, C_2, C_3, i-C_4, n-C_4, i-C_5, n-C_5) determined from the MSSV analysis. The gas composition is corrected based on a GOR - gas-wetness correlation from natural black oils (di Primio et al., 2005). The other seven compounds describe the liquid phase consisting of a pseudo-C_6 (all compounds detected eluting in the n-C_5 to n-C_6, excluding n-C_5) and compound groups of $C_{7\text{-}15}$, $C_{16\text{-}25}$, $C_{26\text{-}35}$, $C_{36\text{-}45}$, $C_{46\text{-}55}$, $C_{56\text{-}80}$. Their physical properties were calculated using the above description of the corrected gas phase composition and the estimation procedure of di Primio et al. (1998) to determine the amount and molecular weight of the C_7+ fraction. Afterwards, the compositional data was assigned to the bulk kinetic model according to the degree of transformation represented by the potentials. For example, a sample's compositional description representing 10 and 30% transformation from the MSSV experiments were used to populate the sample's bulk kinetic-derived potentials from 0 - 20% and 20 - 40% transformation.

2.4. Results and Interpretation

2.4.1. Bulk characterization

2.4.1.1. Rock-Eval and TOC measurements

At DSDP site 361 TOC contents of Aptian and Albian aged samples vary from 3.85 - 8.13 % (Table 2-1). Rock Eval Hydrogen Indices (HI´s) of 315 - 554 mg HC/g TOC, indicative of a mixed Type II/III kerogen (Figure 2-3), were measured in samples with higher TOC (> 5.0%), whereas low HI ranges of 28 - 97 mg HC/g TOC correspond to lower TOC contents (< 5.0%) and Type III kerogen. One Turonian aged black shale was sampled at site 361 displaying a low HI of 23 mg HC/g TOC indicative of Type III kerogen and TOC content of 1.58%.

At DSDP site 530A the HI of Albian aged sediments ranges from 59 - 385 mg HC/g TOC with TOC contents varying from 0.45 - 7.4% displaying a loose correlation of increasing HI with increasing TOC content in a mixed Type II/III kerogen. The Turonian interval is represented by organic-rich Type II (10.6 - 13.4% TOC) and Type III (0.9 - 6.5%TOC) kerogen samples with HI's of 506 - 721 mg HC/g TOC and 64 - 225 mg HC/g TOC, respectively.

The TOC contents of Aptian and Albian aged samples from DSDP site 364 vary between 9.66 and 37.0% (Table 2-1**Error! Reference source not found.**). The HI's range from 377 to 663 mg HC/g TOC (Figure 2-4) that is characteristic for Type II kerogen. Turonian to Coniacian aged samples from DSDP site 364 show uniform high TOC contents of 10.1 to 14.7%. The highest HI value (769 mg HC/g TOC) was measured in an upper Turonian/lower Coniacian sapropelic black shale.

All investigated samples are immature with Tmax temperatures in the range of 401 - 419 °C (Figure 2-4), one higher Tmax value of 428°C was measured, but is still indicative of immature organic matter and may be attributed to the organic matter composition.

The results of the source rock screening are in agreement with the previous studies of Herbin et al. (1987) and Schmidt (2004). The average and maximum HI's (214 and 472 mg HC/g TOC, respectively) reported for DSDP site 530A by Forster et al. (2008) are generally lower than observed in this study. This may be related to the heterogeneous suite of samples that they studied, whereas this study focuses only on the black-shale intervals.

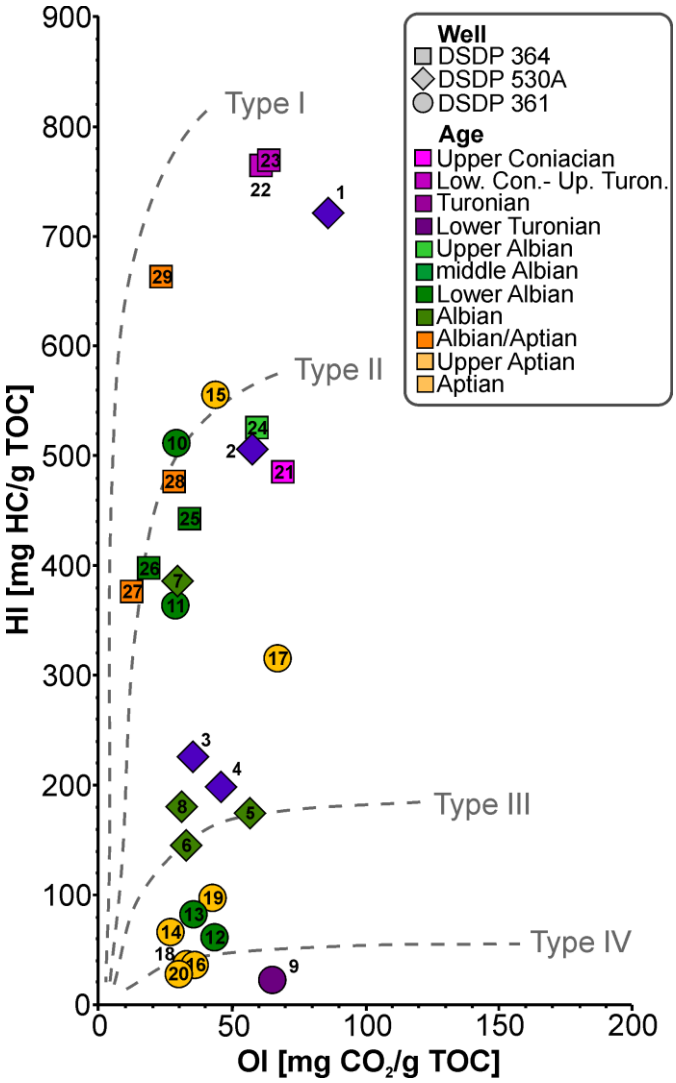

Figure 2-3: HI vs. OI plot of studied samples (kerogen type maturation pathways after Espitalié et al., 1978).

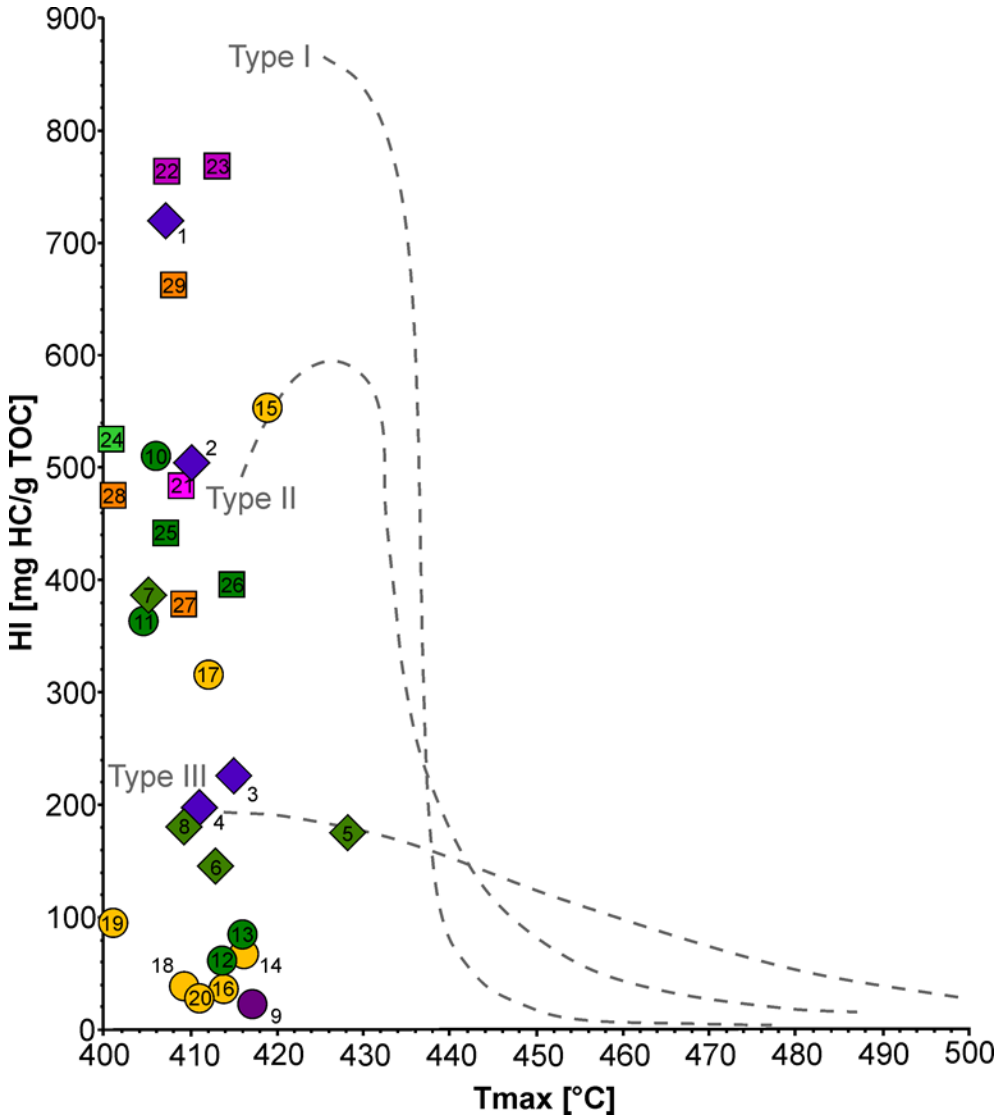

Figure 2-4: Tmax vs. HI plot of studied samples, for legend see figure 2 (kerogen type maturation pathways after Cornford, 1998).

2.4.1.2. Bulk pyrolysis

Open-system pyrolysis - gas chromatography was conducted to further characterize the organic matter composition and the petroleum-type generated by the samples with TOC contents exceeding 1.0%.

The individual resolved compounds were determined up to n-C_{30}, beyond this chain-length the GC-signals were within the error of measurement. Apart from the n-alk-1-ene/n-alkane doublets, the most abundant compounds were light aromatics such as benzene, toluene, ethylbenzene, xylenes, alicyclic compounds such as naphthalenes, and sulfur compounds, mainly thiophenes. Typical sample gas chromatograms are shown in Figure 2-5.

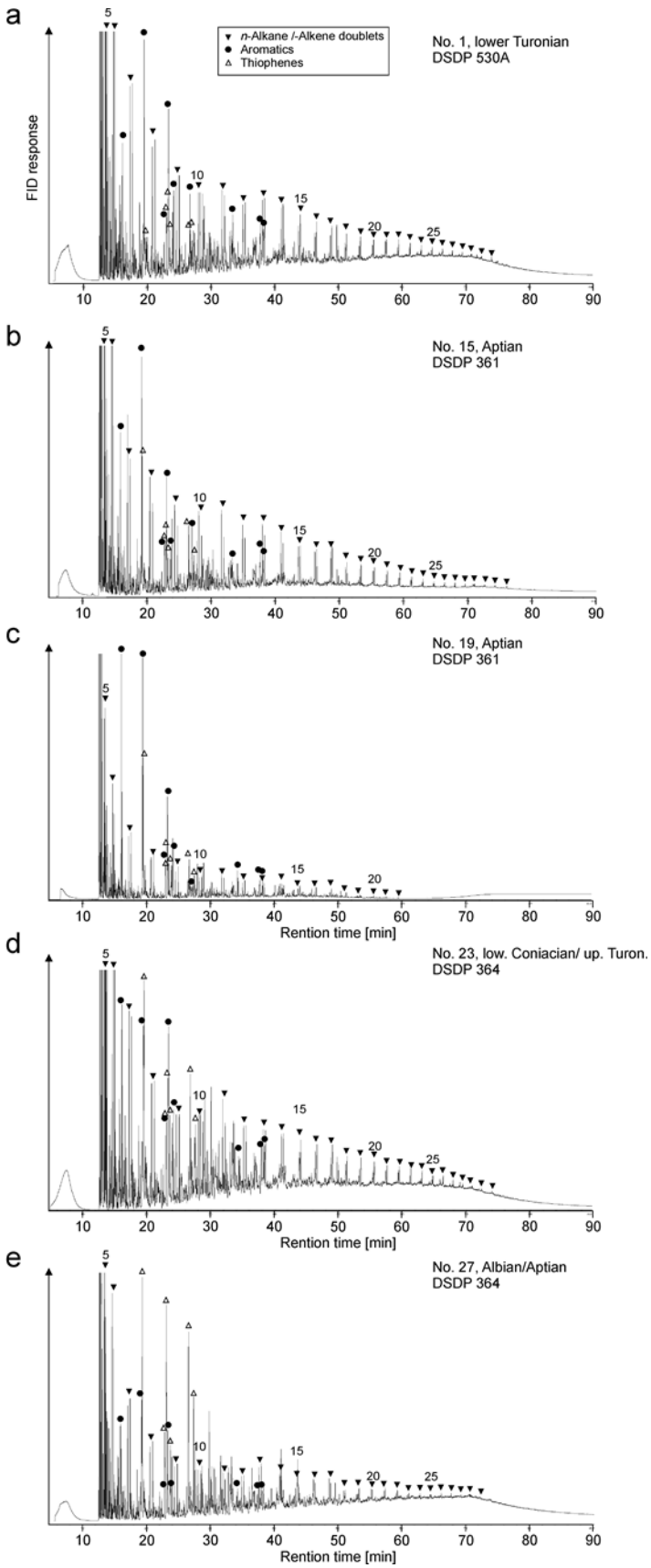

Figure 2-5: Representative Py-GC chromatograms of selected source rocks samples; a) sample no. 1, a wax-rich Type II kerogen SR; b) sample no. 15, a Type II kerogen SR; c) sample no. 19, a Type III kerogen SR; d) sample no. 23, a heterogeneous Type II kerogen SR; e) sample no. 27, a Type IIS kerogen SR.

The n-alkene/n-alkane doublet distribution in the Py-GC chromatograms is typical for organic matter of predominantly marine origin (Bordenave, 1993; Horsfield, 1997; van de Meent et al., 1980). The n-alkyls are probably derived from lipids and aliphatic biopolymers incorporated into the marine organic matter (Tissot and Welte, 1984; Horsfield, 1997). Together with other light aromatic compounds, xylenes and phenol (the latter is derived from lignocellulosic precursors) are frequently linked to a terrestrial input of organic matter (van de Meent et al., 1980; Tissot and Welte, 1984).

The most common sulfur compounds were 2-methyl-thiophene, 2,5-dimethyl-thiophene, 2-ethyl-5-methyl-thiophene and 2,3,5-trimethyl-thiophene. They occurred partially in greater abundance than n-alkyls of the same carbon number, whereas 2,4- and 2,3-dimethyl-thiophene were present in similar amounts as n-alkyls of the same carbon number. Sulfur-rich source rocks are generally deposited in evaporitic and/or anoxic carbonate platform environments (di Primio and Horsfield, 1996; Schaeffer et al., 1995). These organic sulfur-rich marine kerogens are termed Type IIS kerogen (Eglinton et al., 1990; Orr, 1986).

Eglinton et al. (1990) showed, that the amount of thiophenes generated during pyrolysis of organic matter can be used to evaluate its organic sulfur content and to differentiate between the predominant kerogen types by using a ratio of 2,3- dimethylthiopene, ortho-xylene, and nC9:1 to represents the organic sulfur, aromatic, and aliphatic compounds of the organic matter (Fig.: 6). The investigated samples show a wide range of kerogen types including Types II, IIS, and III, but with a systematic distribution. The Aptian and some lower Albian aged samples from DSDP site 361 and 364 contain sulfur-rich Type IIS kerogen. Generally, the Albian aged black shales from all three sites contain Type II kerogen and also Type III kerogen at DSDP sites 361 and 530A. In these cases an input of terrestrial organic matter is further supported by a lower HI (< 225 mg HC/g TOC), an increase in the relative abundance of xylenes, and the presence of phenol. Type II kerogen dominates the organic matter in the Turonian to Coniacian aged samples, except for a low TOC, low HI sample indicating Type III kerogen at DSDP site 361 Figure 2-6.

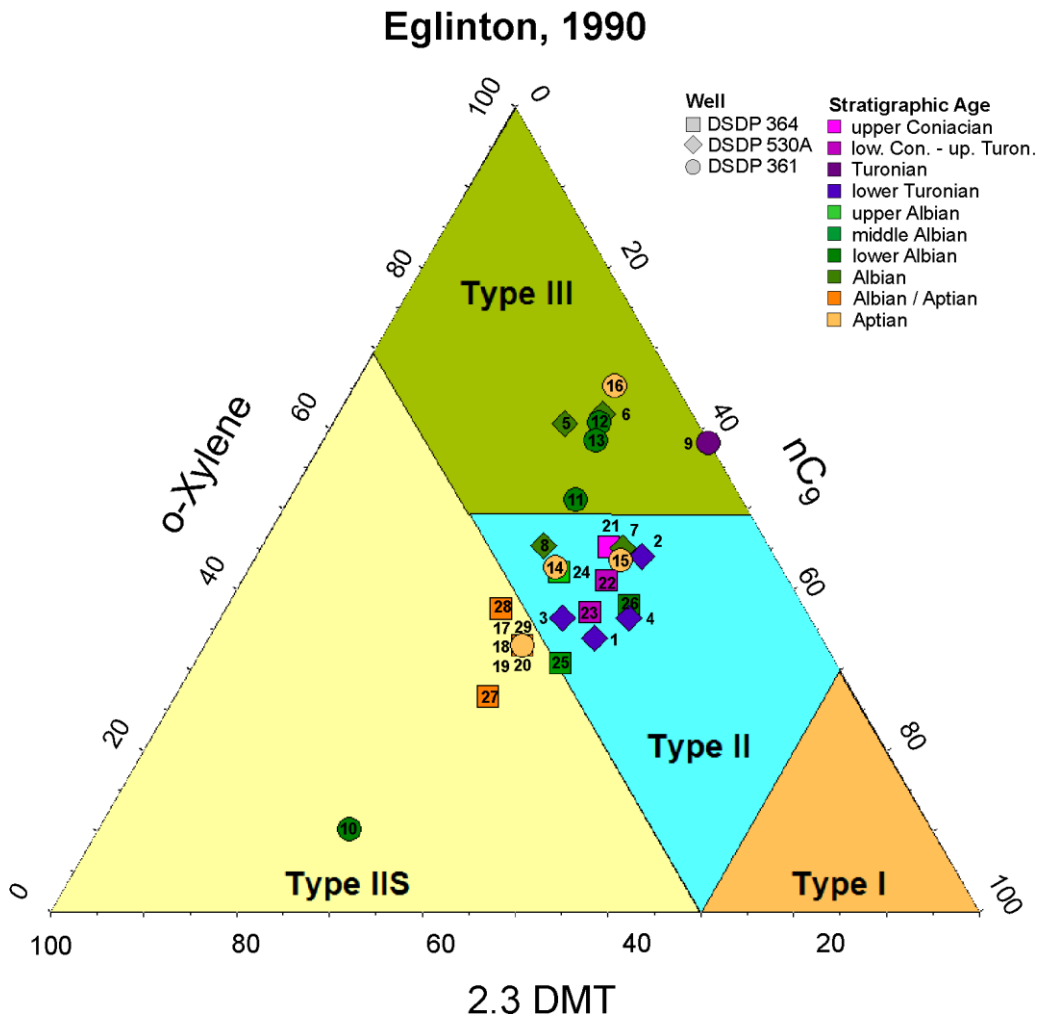

Figure 2-6: Kerogen type classification of Py-GC results according to Eglinton et al. (1990).

Horsfield (1997, 1989) related the petroleum fluid type generated under natural conditions to the alkyl chainlength distribution (CLD) generated from source rocks by open system pyrolysis. This approach allows defining the petroleum type organofacies, which permits to recognize the gas-condensate, paraffinic-naphthenic-aromatic (PNA) petroleum (high- and low-wax varieties), and paraffinic petroleum-generating (high- and low-wax varieties) potentials of individual source rock samples (Figure 2-7a and b). The majority of the investigated samples plot in the low wax paraffinic-naphthenic-aromatic (P-N-A) oil area with a gradual transition into the gas and condensate field. Source rocks of the low wax P-N-A oil generating facies are generally deposited in a restricted marine environment found on stagnant shelves and silled basins (Horsfield, 1997). The majority of the organic matter is derived from marine organisms, such as algae and bacteria, and to a minor degree from terrigenous organic matter. The gas and condensate generating facies is generally deposited in continental- deltaic settings with low petroleum generating potential (Horsfield, 1997). The low HI (23 - 97 mg HC/g TOC) Aptian and Turonian samples of DSDP site 361 fall into this category, as well as two high HI Aptian samples from DSDP sites 361 and 364 (HI = 315 and 663 mg HC/g TOC, respectively; Figure 2-7b). HI values of up to 300 mg HC/g TOC have been reported for coals and rock samples with Type III kerogen (Bordenave, 1993), but in the case

of DSDP site 361 it may be more indicative of a mixing of Type II and III kerogens. The interpretation of the gas and condensate generating facies of the Type II kerogen Aptian sample from DSDP site 364 is more complicated. However, it has been noted that alginite-rich marine shales with Type II kerogen of the Bakken and Alum shale also plot into the gas and condensate facies (Horsfield, 1997; Muscio and Horsfield, 1996). Thus, in these cases aromatization and condensation reactions enhance inert carbon formation, and lead to a predominance of low molecular weight hydrocarbons in the generated petroleum from artificially matured source rocks (Muscio and Horsfield, 1996). One Turonian sample from DSDP site 530A plots in the high wax P-N-A oil generating facies, which is typical for lower delta plain and inner shelf environments.

In nature sulfur-rich marine source rocks have been found to generate sulfur-rich heavy oils at low maturities (di Primio and Horsfield, 1996; Lehne and Dieckmann, 2007; Orr, 1986). In the CLD diagram it is not possible to distinguish P-N-A oils typically derived from marine organic matter, from sulfur-rich heavy oils generated by Type IIS kerogen (di Primio and Horsfield, 1996). Therefore, the classification of di Primio and Horsfield (1996), who use a ratio of 2,5-dimethylthiophene, toluene, and nC_9:1 + nC_{25}:1, was applied to further distinguish the P-N-A oils (Figure 2-8). The majority of the source rock samples plot in the intermediate and aromatic field, as would be expected from a restricted marine depositional environment with terrestrial influence as inferred from the previous results. Concerning the classification of Aptian and lower Albian aged samples from DSDP sites 361 and 364 as Type IIS kerogen, only the source rocks of the latter well are likely to produce sulfur-rich heavy oils.

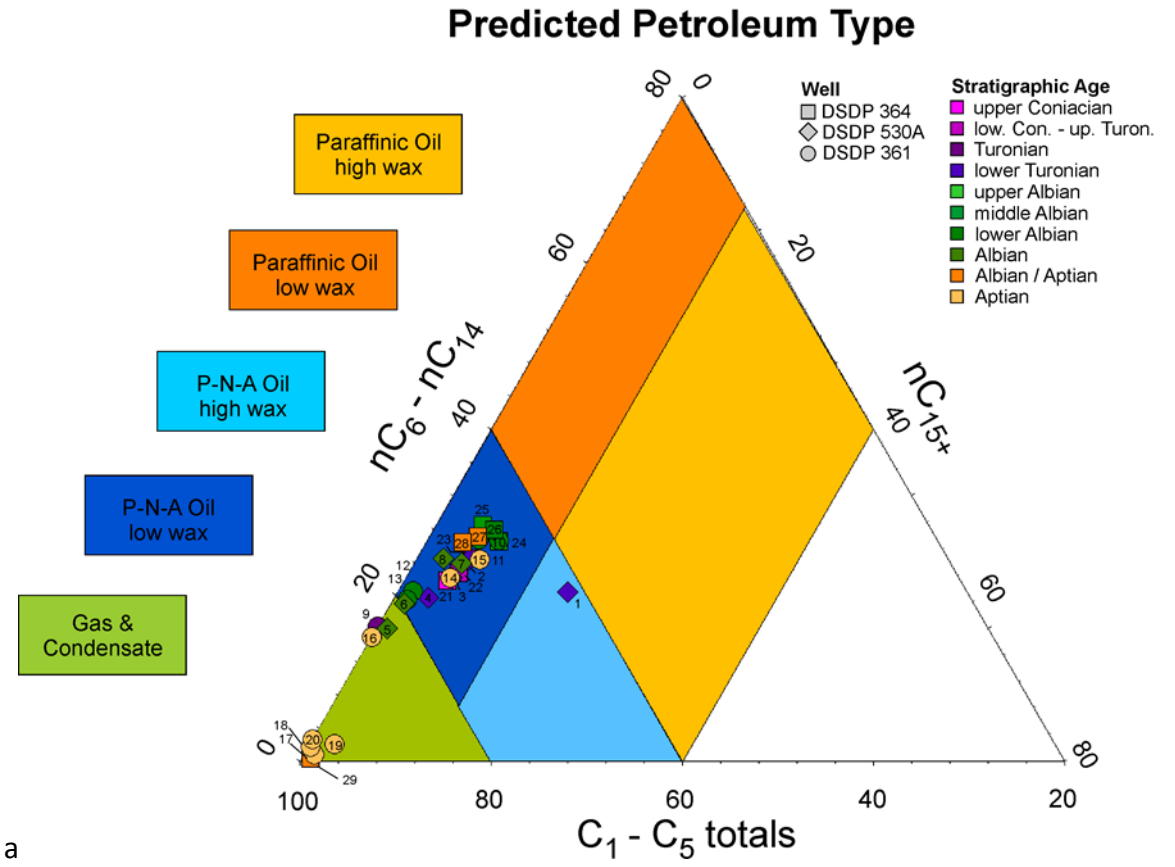

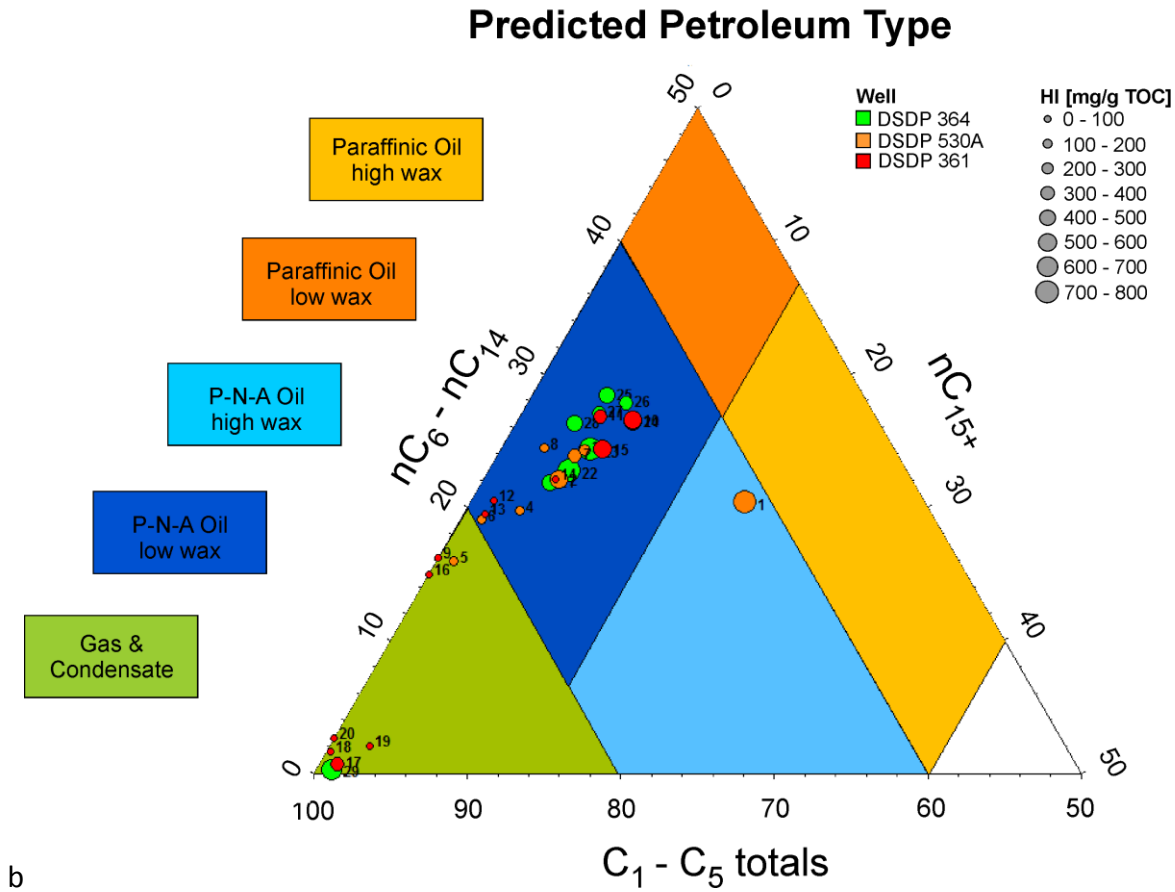

Figure 2-7: a) Petroleum type prediction according to Horsfield (1989); b) detail of (a) Petroleum type prediction in relation to HI.

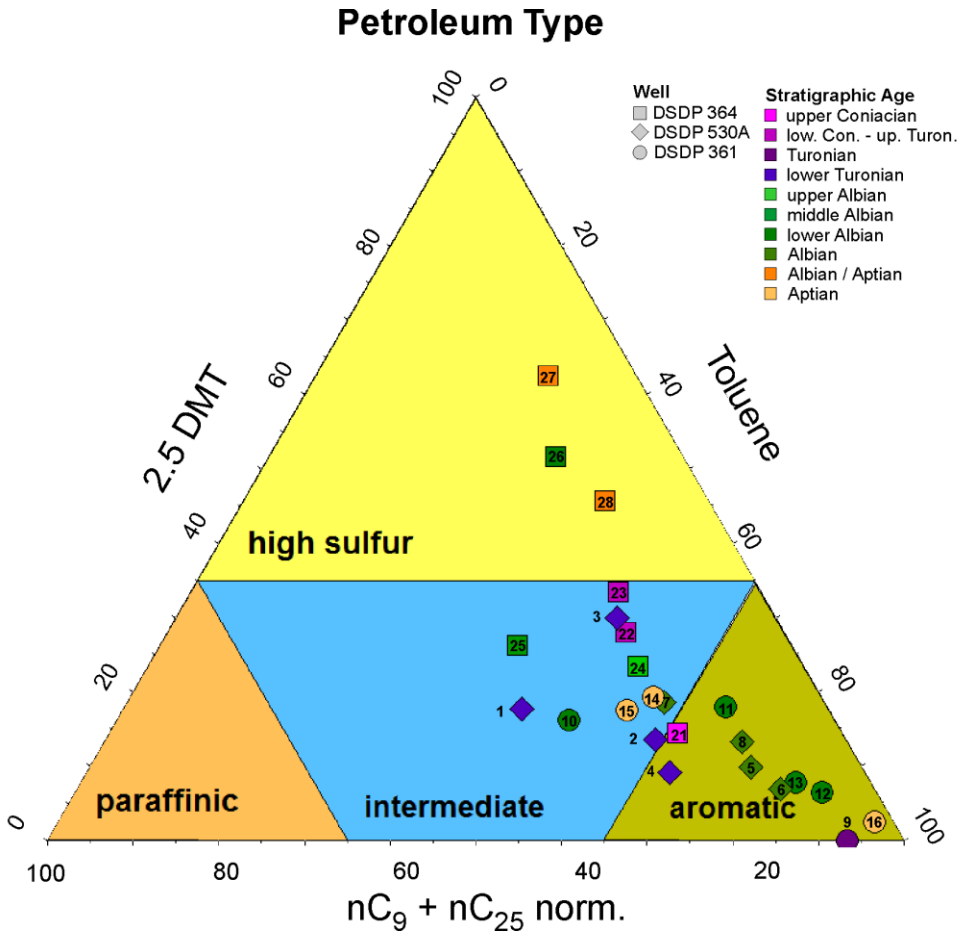

Figure 2-8: Petroleum type of P-N-A oils according to di Primio and Horsfield (1996).

2.4.2. Bulk kinetic parameters

The samples for bulk kinetic analysis were chosen to represent the different kerogen types based on the results of the preceding bulk source rock characterization and are listed in Table 2-2.

The calculated activation energy distributions and frequency factors of the investigated samples are shown in Figure 2-9. In general, the activation energies are in the range of 40 - 64 kcal/mol. This distribution is characteristic for heterogeneous marine organic matter (Reynolds and Burnham, 1995; Schenk et al., 1997b; Tegelaar and Noble, 1994). One Aptian sample has a wide activation energy distribution in the range of 47 - 71 kcal/mol, characteristic for terrestrial kerogen. Within each well, a trend of increasing organic matter heterogeneity with decreasing depth, and consequently also successively younger age, can be observed from the distribution of activation energies (Figure 2-9). Peak activation energies occur between 52 - 54 kcal/mol, 51 - 59 kcal/mol, and 53 - 54 kcal/mol at DSDP sites 530A, 361, and 364, respectively. The frequency factors vary from 5.38 $x10^{13}$ - 3.0.4 $x10^{16}$/sec.

A closer look at the bulk kinetic parameters reveals significant differences in petroleum generation properties of the investigated samples. At DSDP 361 the onset and peak petroleum generation temperatures of the lower Albian (samples 10 and 11) and Aptian source rock samples (samples 15, 17, 19) are very variable. Assuming a geologic heating rate of 3°K/My, the onset of petroleum generation occurs at 98°C from the lower Albian organic matter versus 110°C from the Aptian Type II kerogens and 120°C for Aptian Type III kerogen (sample 19, Figure 2-5c). A similar significant variability of 21°K can be observed from the peak generation temperatures of 128°C, 138°C, and 149°C respectively. This may be related to the higher abundance of alginite in the lower Albian black shales, compared to ligneous precursors of the thermally more stable aromatic compounds in the organic matter of Aptian age (Raynaud and Robert, 1978).

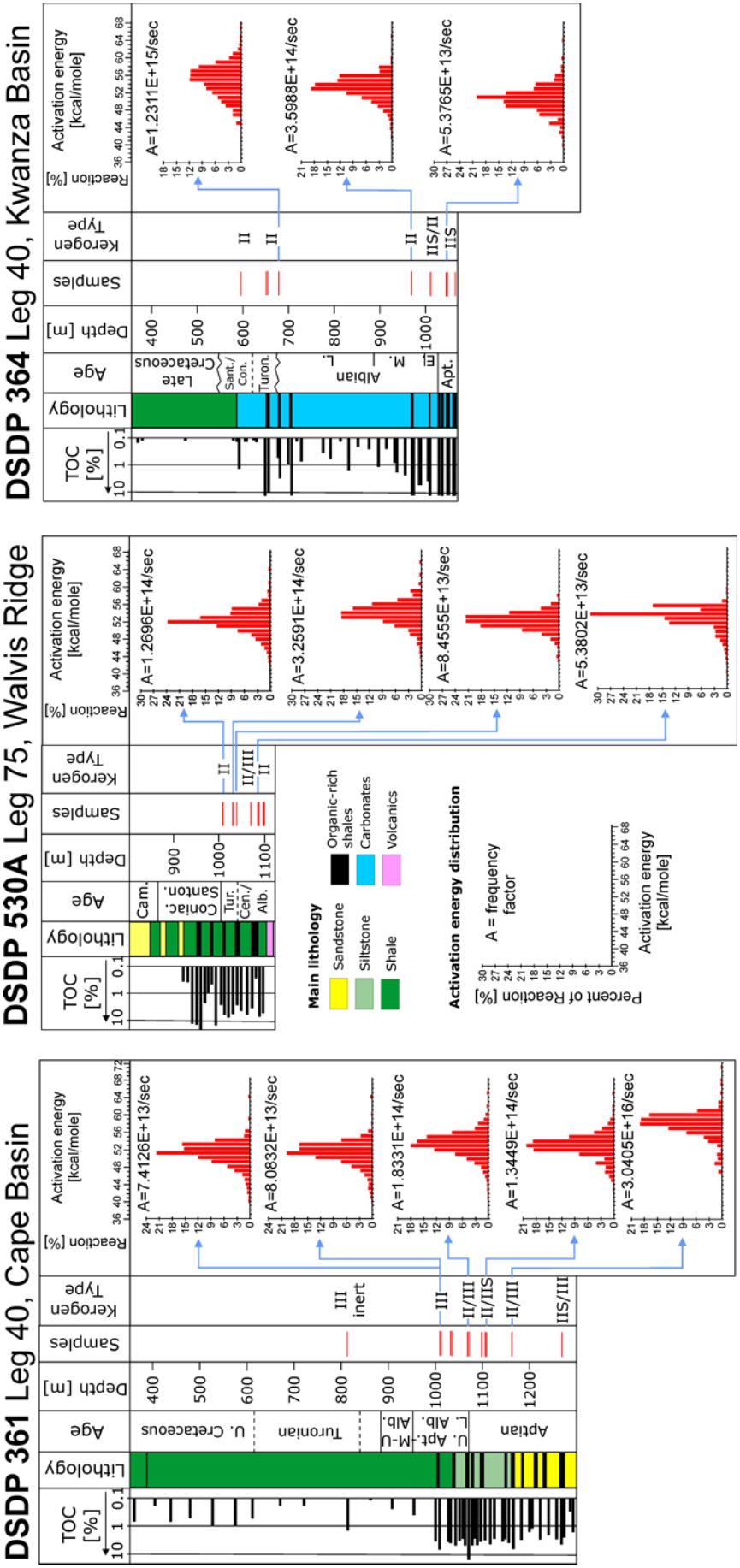

Figure 2-9: Kerogen type and activation energy distribution from DSDP sites offshore southwestern Africa (well lithologies and TOC adapted from Bray et al. (1998)).

Table 2-2: Bulk kinetic parameters

Sample no.	1	2	4	5	10	11	15	17	19	23	25	27
DSDP site	530A	530A	530A	530A	361	361	361	361	361	364	364	364
Age	lower Turonian	lower Turonian	lower Turonian	Albian	lower Albian	lower Albian	Aptian	Aptian	Aptian	Con.-Turon.	middle Albian	Albian/ Aptian
A [1/S]	1.27 E + 14	3.26E + 14	8.46E + 13	5.38E + 13	7.41E + 13	8.08E + 13	1.83E + 14	1.34E + 14	3.04E + 16	1.23E + 15	3.60E + 14	5.38E + 13
Ea [kcal]												
40	0,0		0,2	0,2	0,3	0,2						0,3
41	0,2		0,1	0,1	0,3	0,4	0,1	0,2				0,2
42	0,2	0,2	0,3	0,3	0,6	0,6	0,2	0,1			0,3	0,4
43	0,4	0,1	0,4	0,4	0,8	0,9	0,2	0,3			0,1	1,0
44	0,6	0,3	0,7	0,5	1,0	0,8	0,3	0,2			0,5	0,8
45	0,9	0,4	0,5	0,9	1,3	1,2	0,5	0,6		1,1	0,4	3,3
46	1,5	0,5	0,6	1,2	1,9	1,9	0,8	1,0		0,0	0,8	1,2
47	2,3	1,0	1,2	1,7	3,6	2,9	1,2	1,9	0,8	2,0	1,2	5,6
48	3,5	1,0	2,1	2,8	5,3	4,9	1,7	2,0	0,1	2,0	2,1	6,1
49	4,4	2,7	4,2	2,9	8,9	7,3	3,3	4,3	1,5	3,6	3,3	13,5
50	7,7	3,0	8,8	3,1	12,1	13,2	5,1	2,3	1,2	4,7	4,9	13,9
51	12,5	6,2	18,3	13,6	21,6	19,9	7,7	8,1	1,5	5,4	7,1	20,3
52	23,9	8,9	21,6	14,7	15,4	17,0	12,7	18,6	0,4	6,7	10,7	13,5
53	16,2	18,5	21,8	31,9	15,8	17,0	18,2	20,2	1,0	8,1	18,9	7,0
54	9,4	18,5	11,7	6,3	8,2	7,3	16,8	18,8	2,7	8,6	17,9	6,6
55	9,1	15,8	4,4	17,4	1,4	2,6	14,6	10,4	4,2	11,9	12,6	2,2
56	2,7	11,4	2,1	1,3	1,2	1,1	8,7	4,7	7,1	11,8	12,2	2,0
57	2,1	5,6	0,1	0,0	0,0	0,0	3,2	2,6	11,9	11,6	3,0	0,6
58	0,7	2,0	0,6	0,2	0,1	0,2	2,4	1,5	17,6	9,8	3,1	0,6
59	0,7	2,5	0,0	0,3	0,1	0,0	1,1	0,9	20,0	5,9	0,3	0,0
60	0,1	0,0	0,2	0,0	0,1	0,2	0,7	0,5	18,0	2,8	0,3	0,4
61	0,5	0,6	0,1	0,0	0,0	0,0	0,1	0,4	8,7	2,0	0,0	0,0
62	0,0	0,0	0,0	0,0	0,0	0,0	0,4	0,4	0,9	0,7	0,2	0,0
63	0,0	0,3	0,0	0,2	0,0	0,0	0,0	0,0	1,4	0,5	0,0	0,0
64	0,4	0,0	0,2		0,3	0,4	0,0	0,0	0,0	0,3	0,0	0,4
65		0,0					0,4	0,4	0,5	0,3	0,0	
66		0,3							0,0	0,0	0,2	
67									0,2	0,3		
68									0,1	0,1		
69									0,0			
70									0,0			
71									0,3			

On the other hand, samples 10 and 17, interpreted to be organic-sulfur enriched (Figure 2-6), reach 50% conversion at slightly lower temperatures (2°K difference) than their sulfur-poor age equivalents (samples 11 and 15, respectively, Figure 2-10). In this case sulfur-richness seems to have only a minor control on the timing of petroleum generation.

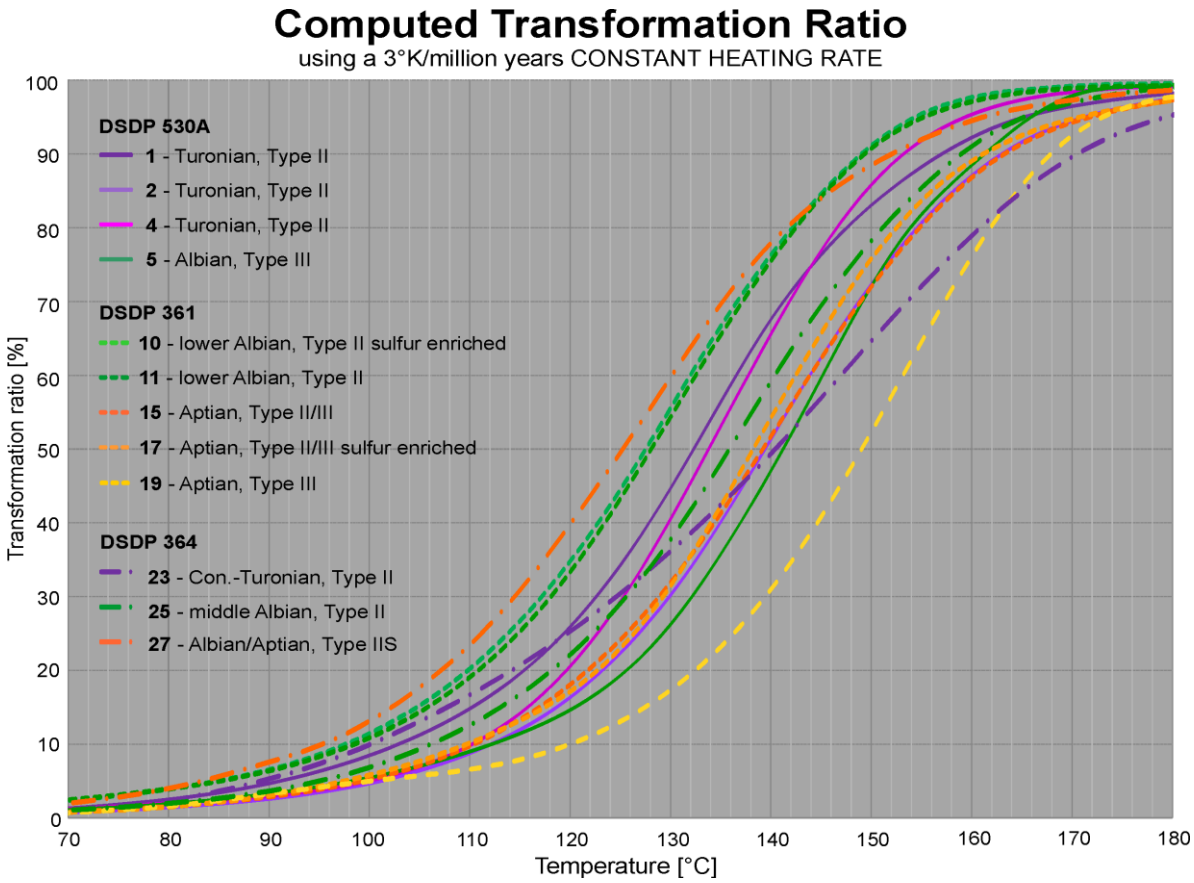

Figure 2-10: Transformation rate curves for a geologic heating rate of 3°K/Ma calculated from bulk kinetic models.

At DSDP site 530A, the Albian aged sample 5 shows a narrow distribution of peak activation energies, though it was interpreted to contain predominantly Type III kerogen with a HI of 175 mg HC/g TOC. Type III kerogen is normally associated with a broad distribution of activation energies (Tissot et al., 1987). In this case, the abundance of aromatic compounds and the predicted aromatic character of the generated petroleum indicate a relatively homogenous Type III kerogen.

The Turonian aged samples have a narrow activation energy distribution typical for Type II kerogen (Reynolds and Burnham, 1995; Tissot et al., 1987). The shallowest sample from this site, predicted to generate P-N-A high wax oil, displays a dominant activation energy peak at 52 kcal/mol. Considering the high HI of 721 mg HC/g TOC, this is interpreted as reflecting a very homogenous organic matter type.

In case of the Aptian Type IIS source rock sample 27 from DSDP site 364, peak generation occurs 10°C earlier as compared to Type II kerogen sample 25 (Figure 2-10). It is therefore

the only example, which documents the early generation of sulfur-rich petroleum in this suite of source rocks. The broad distribution of activation energies with a low mean value (Figure 2-9) and the high relative amounts of thiophenes (Figure 2-5e) are typical for Type IIS kerogens (Tegelaar and Noble, 1994; di Primio and Horsfield, 1996; Schenk et al., 1997b). The overall trend in source rock properties is also documented in the ternary plot of di Primio and Horsfield (1996). There the prediction of high-sulfur heavy oil, associated with the early generation of petroleum is predicted for sample 27, but not for the sulfur-rich samples 10 and 17, contrary to the Type IIS characterization using the method of Eglinton et al. (1990).

The Turonian aged sample 23 from DSDP site 364 displays a very wide distribution of activation energies, which is not very common in such a high HI/TOC source rock (HI 769 mg HC/g TOC, 12% TOC). The Py-GC chromatogram of this sample (Fig. 5d) shows a relative abundance of both, thiophenes (labile) and aromatic (stable) compounds, when compared to the other samples, suggesting a very heterogeneous kerogen composition. This variability is also reflected in its potential for intermediate to high sulfur P-N-A low wax oil and in the broad TR curve (Figure 2-10). The onset of petroleum generation is within the same temperature range as all other samples, but at 50% conversion it is one of the highest stability samples. At high maturity, 90% transformation, it is the most stable, generating petroleum up to 170°C.

2.4.3. Compositional kinetic model and calculated fluid physical properties

Compositional kinetic models were generated for six samples, which represent the variability observed from the bulk kinetic measurements (Figure 2-11). The compositional evolution and physical properties of the fluids generated by these source rocks were determined based on the MSSV analysis of source rock aliquots at increasing degrees of transformation as shown in Table 2-3. Natural hydrocarbon fluids that were generated from the same source rock as a function of increasing maturity display a linear correlation of P_{sat} and GOR and of P_{sat} and B_O (di Primio et al. 1998). This has also been shown to exist in source rock maturation series investigated by MSSV pyrolysis (di Primio and Horsfield, 2006). The petroleum fluids from all investigated samples show an increase of P_{sat} and B_O with increasing TR and in a cross plot of these two properties plot the samples analyzed in the area of natural petroleum fluids (Figure 2-12). In general, the lowest GOR fluids were generated from samples rich in more labile kerogen and sulfur (samples 15 and 27, respectively; Figure 2-13). The P-N-A high wax oil source rock from DSDP 530A generated a fluid with a high GOR at high maturity. The Aptian condensate-prone sample showed the highest GORs and GOR range of the dataset. These results confirm the observations of di Primio and Horsfield (2006) on the timing of generation and GOR evolution for petroleum fluids from different organofacies types.

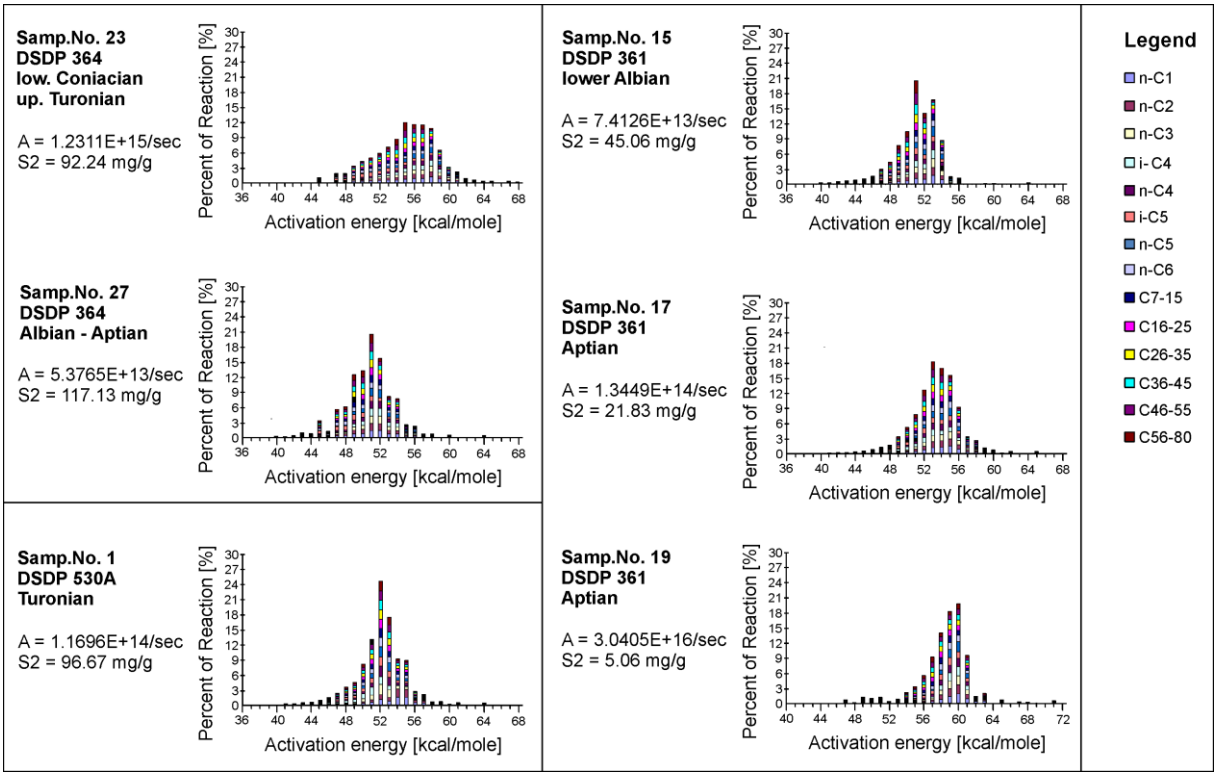

Figure 2-11: Compositional kinetic models for the six investigated samples.

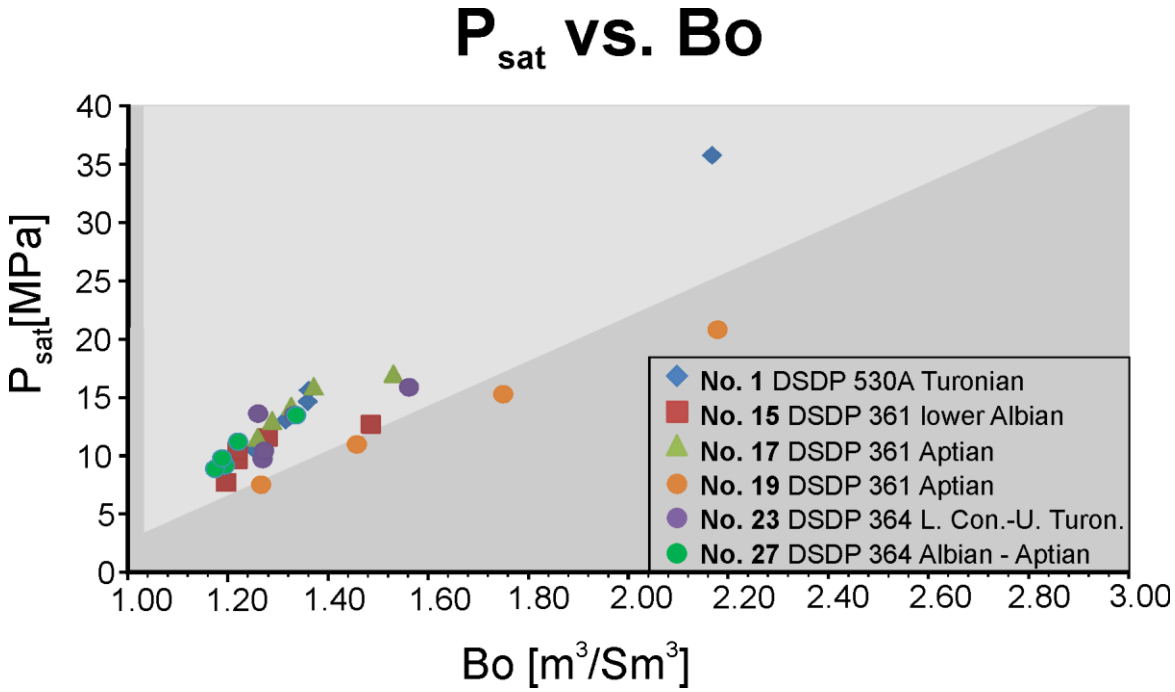

Figure 2-12: Psat vs. Bo plot from compositional kinetic model, light grey area corresponds to naturally occurring petroleum fluids (di Primio and Horsfield, 2006).

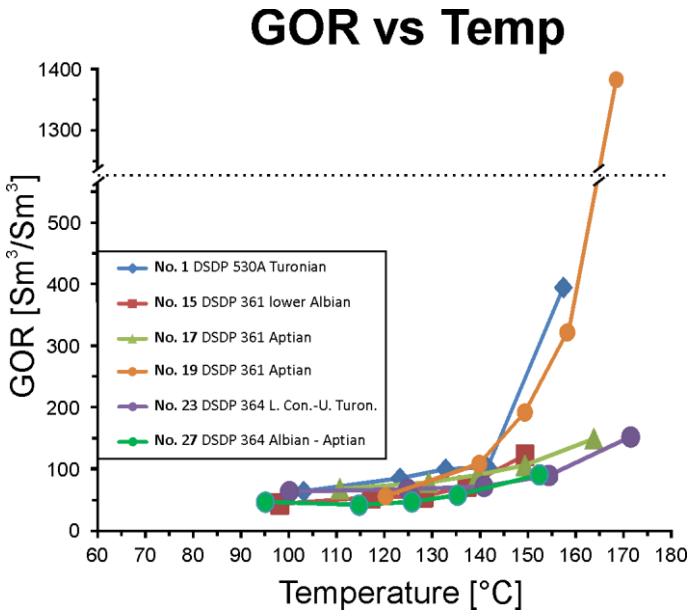

Figure 2-13: GOR vs. Temperature plot from compositional kinetic model.

Table 2-3: Calculated fluid properties

sample no.	TR [%]	10	30	50	70	90
1 DSDP 530A lower Turonian	Temp [°C] at 3°/Ma	103,00	123,00	132,50	141,25	157,00
	GOR [Sm3/Sm3]	65,10	86,30	101,00	103,80	394,70
	Bo [m3/Sm3]	1,254	1,316	1,36	1,362	2,167
	Psat [MPa]	10,62	13,12	14,70	15,66	35,65
10 DSDP 361 lower Albian	Temp [°C] at 3°/Ma	98	117	128	137	149
	GOR [Sm3/Sm3]	44,6	55,4	56,8	73,9	123,7
	Bo [m3/Sm3]	1,197	1,22	1,22	1,28	1,486
	Psat [MPa]	7,806	9,761	10,514	11,653	12,762
15 DSDP 361 Aptian	Temp [°C] at 3°/Ma	110,50	129,00	139,25	149,00	163,33
	GOR [Sm3/Sm3]	69,30	79,50	91,80	107,30	150,20
	Bo [m3/Sm3]	1,26	1,29	1,33	1,37	1,53
	Psat [MPa]	11,665	13,092	14,32	16,004	17,075
19 DSDP 361 Aptian	Temp [°C] at 3°/Ma	120,00	139,50	149,00	158,50	168,00
	GOR [Sm3/Sm3]	57,30	109,60	192,90	322,10	1395,80
	Bo [m3/Sm3]	1,27	1,46	1,75	2,18	NA
	Psat [MPa]	76,24	110,51	153,24	208,12	576,73
23 DSDP 364 low. Coniacian - up. Turonian	Temp [°C] at 3°/Ma	100,00	124,60	140,50	154,00	171,00
	GOR [Sm3/Sm3]	65,00	68,50	73,30	90,90	153,20
	Bo [m3/Sm3]	1,27	1,27	1,26	1,33	1,56
	Psat [MPa]	9,806	10,502	13,67	13,546	15,916
27 DSDP 364 Albian/Aptian	Temp [°C] at 3°/Ma	95	114,5	125,50	135	152
	GOR [Sm3/Sm3]	48,00	43,20	48,40	59,10	92,10
	Bo [m3/Sm3]	1,20	1,18	1,19	1,22	1,34
	Psat [MPa]	9,258	8,967	9,86	11,287	13,532

2.5. Discussion

2.5.1. Organofacies variation along the southwest African margin

The observed organofacies variability of the investigated samples correlates very well with the evolution of the South Atlantic Ocean basins. Zimmermann et al. (1987) proposed that the early and mid Cretaceous sapropels and black shales of the South Atlantic were deposited in silled basins with restricted bottom water ventilation. The Type IIS kerogens of the Aptian aged samples from the Cape and Angola Basin are evidence for the initial highly reducing conditions along the entire South Atlantic margin during that time (Figure 2-9). At the end of evaporite deposition at DSDP site 364, a highly saline shallow marine carbonate environment developed (Bolli et al., 1978b; Séranne & Anka, 2005; Torsvik et al., 2009). Still high evaporation rates led to saline bottom water formation and a highly stratified dysoxic water column. Zimmermann et al. (1987) inferred that anoxic conditions existed throughout the South Atlantic below a paleowaterdepth of 400 m. Thus favoring the formation of sulfur-rich sapropelic black shales during the late Aptian and well into the early Albian Angola Basin. The sulfur content of the Type II kerogen in the Angola Basin decreases during the middle and late Albian. This underlines the transition from an evaporitic restricted to a restricted marine environment north of the Walvis Ridge in response to the gradual widening of the South Atlantic and decreasing influence of the Walvis Ridge as a flow barrier (Zimmermann et al., 1987).

In the Cape Basin, progradation of the Orange Basin shelf starting during the early Aptian led to an increased input of clastic sediments and terrestrial organic matter through turbidity currents. During the Albian a deepwater passage to the southern ocean, the Agulhas Gap, was created between the westward moving Falkland Plateau and southern Africa. This led to increasing bottom water ventilation in the Cape Basin (Zimmermann et al., 1987). The mixed Type II/ III kerogens at DSDP sites 361 and 530A can be related to these restricted marine depositional environments with a strong terrestrial influence. The terrestrial influence of organic matter transported with turbidites at DSDP site 530A is evident from the numerous aromatic compounds identified on the Py-GC traces of the older Albian samples (Figure 2-8). Further to the south and north of the Walvis Ridge turbidite derived sediments have also been reported for this time (Forster et al., 2008; Light et al., 1993). Frequent hemipelagic black shale intervals containing Type II marine kerogen are evidence of recurring oxygen depletion (e.g. Bolli et al., 1978a, 1978b; Forster et al., 2008; van der Spuy, 2003).

We observed that some of the Aptian and Albian aged intervals present at DSDP site 361 contain sulfur-enriched Type II and Type III kerogens. While there are numerous examples of Type IIS kerogens (e.g. Orr, 1986; Eglinton et al., 1990; di Primio and Horsfield, 2006), Type III kerogens normally contain low amounts of organic sulfur, if enriched, they are associated to marine-influenced coals (Eglinton et al., 1989). The terrigenous organic matter, rich in pollen and spores, was transported to this site by turbidity currents with sediments derived from the outlets of the paleo Orange and Olifants Rivers (Gilbert, 1978). Thus, based on the HI/OI

ratio and CLD characterization according to Horsfield (1997), samples 18, 19, and 20 are interpreted to contain Type III kerogen, although according to the classification of Eglinton et al. (1990; Figure 2-6) they are sulfur-rich. The maceral analysis of the same interval showed that the organic matter consists primarily of 40-60% ligneous black debris and 30-60% of amorphous sapropelic matter (Raynaud and Robert, 1978), therefore the samples can be described to contain organic sulfur-enriched type II/III kerogen. Bolli et al. (1978a) observed the formation of gypsum on the laminae of black shale cores after drying. They attributed this to the presence of unoxidized organic-bound sulfur in the sapropelic matter, which supports our interpretation.

After a Cenomanian-Turonian hiatus that has been observed throughout the South Atlantic, reducing conditions returned during the Turonian OAE and lasted into the Coniacian in northern South Atlantic (Zimmermann et al., 1987; Herbin et al., 1987). The Turonian samples north of the Walvis Ridge display a relatively higher abundance of n-alkyls, indicative of higher contents of marine organic matter. A higher relative abundance of organic-sulfur compounds in the Turonian aged samples versus older black shales has also been observed by Forster et al. (2008), emphasizing the reducing conditions of the depositional environment. Additionally, the fact that phenol is relatively scarce or even absent on Py-GC signals emphasizes the low contribution of ligneous precursors, associated with terrestrial organic matter (van de Meent et al., 1980; Bordenave, 1993; Horsfield, 1997). This is especially the case for the Turonian-Coniacian aged samples of the Angola Basin, which show the highest HI values in this study, up to 769 mg HC/g TOC, and are very characteristic for a restricted marine environment. Organic-rich black shales of the Turonian OAE are also present in the southern South Atlantic (e.g. Herbin et al., 1987; Mello et al., 1989; Bray et al., 1998). Contrary to the restricted circulation north of the Walvis Ridge, the widened Agulhas Gap provided better ventilation of the ocean basin (Zimmermann et al., 1987). At DSDP site 361 the black shales contain Type III kerogen and predominately detrital organic matter.

2.5.2. Source rock properties

The overall source rock quality of the Cretaceous black shales improves northward along the southwest African margin. The average TOC contents as well as the marine organic matter content are higher north of the Walvis Ridge than in the Cape Basin.

The mixed Type II/III source rocks at DSDP site 361 consist of thin very good oil-prone Type II kerogen source rock intervals and thicker fair to good wet-gas and gas prone Type II/III and III kerogen source rock intervals with a cumulative (recovered) thickness of 16 and 40 m, respectively (at 27% overall core recovery, Bolli et al., 1978a; van der Spuy, 2003). As a result of the strong terrigenous influence the Aptian and early Albian source rocks have a potential to generate gas and condensate to paraffinic-aromatic-naphthenic low wax oil. The bulk and

compositional kinetic results suggest that, depending on the predominant kerogen constituents, the kinetic variability encompasses a 21°K temperature range. Assuming an average geothermal gradient of 3°C/100 m, this would translate into a difference of up to 700 m of burial for the onset of petroleum generation and should be considered as the error margin for kinetic predictions in future petroleum system modeling studies. The labile organic matter of the Albian source rocks seems to be related to higher contents of algal matter reported for this interval by Raynaud and Robert (1978). Additionally, petroleum generation from the more labile kerogen occurs within a relatively short temperature range. These Aptian and Albian aged black shales are assumed to be the main source rocks of the Orange Basin (Adekola et al., 2012; Bray et al., 1998; Petroleum Agency SA, 2003). The overall higher thickness of the condensate-prone black shales would explain the numerous gas shows and known commercial gas and condensate fields Kudu and Ibhubesi. Equivalent oil- and wet gas prone Aptian source rocks with a cumulative thickness of more than 200 m are also the main source of oil and gas fields in the Bredasdorp Basin, southeast of the Orange Basin (van der Spuy, 2003 and references therein). The Turonian sample from the Cape Basin is a black shale with poor source rock potential with Type III/IV kerogen. However, Aldrich et al. (2003) and van der Spuy (2005) argue that the Turonian black shales contain Type II kerogen along the slope, in the distal Orange Basin. Additionally, Bray et al. (1998) reports a Cenomanian/Turonian oil-prone source rock in the Walvis Basin south of the Walvis Ridge, offshore northern Namibia, and Adekola et al. (2012) for the northern Orange Basin.

The Albian, and especially the Turonian, aged black shales at DSDP site 530A have good to very good oil-prone source rock potential, respectively, and are immature in terms of petroleum generation. The black shale intervals make up 8.6% (cum. thickness 11 m) of the recovered Albian - Santonian core sections (68.6% Cretaceous core recovery, Hay and Sibuet, 1984). The mixed Type II/III kerogen of the Albian black shales has the potential to generate aromatic to intermediate low wax oil, while the Turonian black shales rich in algal-derived Type II kerogen generate intermediate low wax and high wax oils, the latter with a potentially high GOR at high maturity.

The sapropelic black shales at DSDP site 364 are immature with respect to petroleum generation and have very good to excellent source rock potential. They make up 10.4% (~23 m) of the recovered Cretaceous core sections (66% Cretaceous core recovery). The Aptian and lower Albian sapropelic black shales consist of thermally labile Type IIS kerogen with the potential to generate low GOR high-sulfur oils. The late Albian and Coniacian-Turonian aged black shales have the potential to generate P-N-A low wax intermediate oils. The kinetic variability of the Aptian and Albian kerogen types at DSDP site 364 covers a 10°K temperature range, similar to DSDP site 361. The Turonian black shales contain Type II kerogen with a wide activation energy distribution, resulting in a slower transformation rate than in any of the other investigated samples.

Parallels can be drawn to the Aptian/Albian M. Binga Fm. and the early Albian Micrites from the onshore and offshore Kwanza Basin, respectively. The M. Binga Fm. is a thin, 5-10 m, organic-rich micrite containing labile Type II kerogen known to be the source of petroleum in the onshore Tobias and Galinda oil fields, as well as contributing to several onshore oil reservoirs near Luanda. The source rock and its generated oils have characteristically high gammacerane content. The early Albian Micrites are an up to 100 m thick unit of Type II kerogen-rich carbonates found in the offshore Kwanza Basin, thought to be the source of several oil shows in offshore exploration wells (Burwood, 1999). A time equivalent of the Turonian black shales from DSDP sites 530A and 364 is the basal section of the upper Cretaceous Iabe Formation. It consists of marine-derived organic matter-rich black shales with syn- and post-depositionally altered thickness (up to 400 m thick; Burwood, 1999; Cole et al. 2000). Burwood (1999) notes, that the Cretaceous Iabe kerogens can have a wide distribution of activation energies, which is also the case for the Coniacian-Turonian sample 23 from the Angola Basin. They are the main source of oils produced from deep water turbidite reservoirs within the Lower Congo Coastal and North Angola Offshore Basins (Cole et al., 2000; Costa et al., 2001).

The calculation of petroleum phase behavior under subsurface conditions in combination with modern basin modeling software allows simulating and reconstructing hydrocarbon migration and entrapment. Migration pathways can be recognized, daughter compositions predicted, and gas- and oil-leg volumes quantified. Accordingly, the development of compositional kinetic models of petroleum generation was performed for five source rock samples representative of the total kinetic variability observed. The fluids generated are mainly black oils, ranging into heavy sulfur-rich oils in the case of the sulfur-rich Aptian samples or wax-rich in the case of Turonian samples. Gas and condensate generation is predicted for terrestrially influenced Aptian and Albian samples at elevated maturities.

Theoretically, the compositional kinetic models for the source rocks from DSDP site 364 and 530A can be extended to age equivalent black shales from the conjugate margin offshore Brazil, analogous to previous work by Schiefelbein et al. (2000) who conducted a detailed geochemical comparison of crude oils from both South Atlantic margins. However, bulk kinetic parameters for a given source rock cannot be directly compared with literature data and other studies, unless they were measured on the same sample (Tegelaar and Noble, 1994). This is related to the heterogeneous composition of the organic matter within a formation, which can result in different bulk kinetic models for samples from a single well (Dieckmann and Keym, 2006; Peters et al., 2006). Keym et al. (2006) report variations of up to 21°C for peak petroleum generation within one core of the Upper Jurassic Draupne Formation, Norwegian North Sea.
A simple comparison of the kinetic modeling results for DSDP sites 361 and 364 from this study to data published by Schmidt (2004) and Burwood (1999) can, however, be attempted (Table 2-4). For this comparison it should be kept in mind that the kinetic models were not

derived from identical samples and that they were calculated using different experimental setups and temperature programs.

Schmidt (2004) distinguishes two types of Aptian source rocks from DSDP site 361 according to their kinetic parameters. Two oil shale samples containing Type II kerogen, and T_{max} of 125.2 - 128.2 °C, and two low HI, Type III kerogen samples with T_{max} 167.8 - 170 °C (Schmidt, 2004). T_{max} of the Aptian Type II kerogen samples from Schmidt (2004) are up to 16°C lower than in this study. Though the kinetic parameters differ, it should be noted, that the shapes of the activation energy distributions and stability trends are similar. This supports our assumption, that organic matter type in black shales at DSDP site 361 exerts a strong control on kerogen bulk kinetics.

Burwood (1999) provides a summary of source rock properties of the Angolan margin including an overview of the typical bulk kinetic parameters for Cretaceous source rocks of the Kwanza Basin. The Aptian/Albian aged Middle Binga Formation is a proven source rock of the onshore Kwanza Basin. It contains micrites rich in Type II organic matter with average HI values of 614 mg HC/g TOC and average TOC contents of 6.3%. The Kwanza Offshore Basins hosts another slightly younger sedimentary unit that contains organic-rich intervals known as the Albian Micrites. They contain Type II kerogen with an average HI of 684 mg HC/g TOC and average TOC contents of 1.8% (Burwood, 1999). The bulk kinetic data of Burwood (1999) can be used to calculate and compare T_{max} and TR curves of these two units to the DSDP samples of this study. The bulk source rock parameters, activation energy distribution, and calculated TR curves of the Middle Binga Formation and the Albian Micrites are similar to the time-equivalent samples from DSDP site 364 of this study (Table 2-4). It is noteworthy that T_{max} for the Aptian aged Middle Binga Formation is about 10°C lower than for the Albian Micrites, similar to the T_{max} difference between the Albian/Aptian sample 27 and middle Albian sample 25 of this study. This comparison supports our observation that Aptian source rock intervals in the Angola Basin contain thermally more labile organic matter than the Albian source units, and in a general sense indicates that the kinetic predictions are robust. The results provided in this communication thus can be integrated into source rock maturation and petroleum generation, migration and accumulation modeling of major basins in the South Atlantic margins.

Table 2-4: Bulk kinetic comparison

sample no.	location	stratigraphic age	depth [m]	TOC [%]	HI [mg HC/g TOC]	kinetic modeling software	Ea range	Ea at maximum potential	Arrhenius factor [s-1]	Tmax assuming geologic heating rate of 3°K/Ma	Tmax 1°K/Ma
this study											
10	DSDP 361	lower Albian	1007.25	7,82	510	Kmod	40 - 56	51	7,4126E+13	128,3	
11	DSDP 361	lower Albian	1007.87	5,12	365	Kmod	40 - 56	51	8,0832E+13	130,6	
15	DSDP 361	Aptian	1070.5	8,13	554	Kmod	41 - 60	53	1,8331E+14	140	
17	DSDP 361	Aptian	1105.75	6,92	315	Kmod	41 - 62	53	1,3449E+14	138	
19	DSDP 361	Aptian	1148.76	5,22	97	Kmod	47 - 71	59	304E+14	149	
Schmidt (2004)											
11277	DSDP 361	Aptian	1068,72	11,00	407	Optkin	40 - 52	50	4,1E+13	125,2	
11280	DSDP 361	Aptian	1099,75	11,50	36	Optkin	44 - 53	63	1,8E+17	170	
11281	DSDP 361	Aptian	1106,54	13,20	28	Optkin	45 - 56	63	2,6E+17	167,8	
11287	DSDP 361	Aptian	1182,71	11,00	556	Optkin	43 - 57	50	2,5E+13	128,2	
this study											
1	DSDP 530A	Turonian	1014,41	13,40	721	Kmod	41 - 59	52	1,2696E+14	132,8	127,2
2	DSDP 530A	Turonian	1030,77	10,60	506	Kmod	42 - 59	53/54	3,2591E+14	139,4	132,7
4	DSDP 530A	Turonian	1038,55	6,51	196	Kmod	40 - 58	52/53	8,4555E+13	134,2	127,5
5	DSDP 530A	Albian	1088,09	2,56	175	Kmod	40 - 56	53	5,3802E+13	141,5	138,2
25	DSDP 364	middle Albian	969,47	8,52	442	Kmod	42 - 58	53	3,5988E+14	135,7	131,1
27	DSDP 364	Albian/Aptian	1045,63	31,10	377	Kmod	40 - 58	53	5,3765E+13	125,4	122,3
Burwood (1999)											
Teba-Itombe	Kwanza Basin / Kongo Basin	Late Cret., Ceno.-Maast.	N.A.	4,80	358	Optkin	46 - 60	54	2,202E+14	145,7	133
Albian Micrites	Kwanza area	early Albian	N.A.	1,80	684	Optkin	44 - 58	54	1,765E+14	147,1	135
Middle Binga Fm.	Kwanza Basin	Apt./Albian	N.A.	6,30	614	Optkin	44 - 63	52	5,967E+13	138,5	129

2.6. Conclusions

The overall bulk source rock properties of organic-rich Cretaceous black shales, such as richness and quality, show an improving trend from south to north along the margin. The late Aptian and Albian black shales at DSDP site 361 and 530A and organic-rich dolomitic mudstone at DSDP site 364 show very good to excellent source rock potential.

The kerogen type improves from a (sometimes sulfur-enriched) terrestrially influenced Type II and Type III in the Cape Basin to a predominately Type II to Type IIS north of the Walvis Ridge and in the Angola Basin. The investigated Turonian aged black shale from the Cape Basin is a poor Type III/IV black shale. At DSDP sites 364 and 530A the Turonian to Coniacian black shales have a very good oil-prone marine source rock potential with high HI and TOC contents. The Organofacies trends correlate well with the evolution of the South Atlantic.

The major differences in activation energy distribution are caused by variations in the organic matter type, while the sulfur content has a minor effect in reducing kerogen stability, except in Type IIS kerogen.

The Cretaceous source rocks of the southwest African margin generate mainly low GOR black oils of paraffinic-naphthenic-aromatic petroleum types with some potential for high sulfur heavy oils in the Angola Basin and wax-rich fluids with high GOR at high maturity in the offshore Kwanza Basin. A potential for gas and condensate generation at high maturities exists in terrestrially influenced Aptian and Albian black shale intervals.

To the best of our knowledge, this study provides the first compositional kinetic description for Cretaceous source rocks from the southwest African margin that is available for academic research.

Acknowledgements

This research is part of the PhD project of A. Hartwig conducted at the Helmholtz Center Potsdam German Research Center for Geoscience (GFZ). We are grateful to the IODP project for supplying sample material and to Forest Exploration International (South Africa) for providing funding. Special thanks goes to Ferdinand Perssen (GFZ Potsdam) for his excellent technical assistance. We are thankful for the comments and suggestions from the reviewers Dr. Idiz and Dr. Zhang who helped to improve the manuscript.

3. Evidence of a widespread paleo-pockmarked field in the Orange Basin: An indication of an early Eocene massive fluid escape event offshore South Africa

The contents of this chapter have been accepted for publication and printed in the international peer-reviewed journal “Marine Geology” as follows:

Hartwig, A., Anka, Z., di Primio, R., 2012. Evidence of a widespread paleo-pockmarked field in the Orange Basin: An indication of an early Eocene massive fluid escape event offshore South Africa. Marine Geolology 332-334, 222–234.

Abstract

The detailed interpretation and seismic attribute analysis of 2D and 3D seismic reflection data set revealed the presence of a distinct seismic horizon displaying circular and elongated depressions in early Eocene sediments along the northwestern slope of the Orange Basin on the southwest African margin. Their occurrence within a single seismic horizon indicates a contemporaneous formation process. We interpret the depressions as paleo-pockmarks, which occur as single pockmarks, predominantly NNE-SSW aligned pockmark trains, and coalescing elongated pockmarks. The paleo-pockmarked surface covers an area of 2800 km^2 and has been mapped by integrating the 3D dataset with industrial 2D seismic grids.

The spatial and temporal occurrence of the paleo-pockmarks is associated to two episodes of rapid sedimentation during the late Maastrichtian to Paleocene, comprising fine-grained shelf-eroded material. We propose that they were formed during the early Eocene by the seepage of both (1) overpressured pore fluids from disequilibrium compaction of upper Maastrichtian sediments and (2) thermogenic gas from underlying Cretaceous mature source rocks. We show that the location of the pockmarks is controlled by the underlying faults system of the paleo-slope.

The Paleocene-Eocene transition is known for its series of hyperthermal events characterized by negative excursions of the carbon isotope curve. The early Eocene widespread event of fluid and thermogenic gas escape identified in this work can be an example of the type of carbon-release processes occurring in hydrocarbon-prone sedimentary basins during this time.

Keywords: pockmarks, hydrocarbon leakage, mud volcano, southwest Africa, Orange Basin, PETM

3.1. Introduction

Surface and submarine pockmarks, mud volcanoes and diapirs, seafloor mounds, and cold seeps are widely accepted as evidence for fluid and gas migration and leakage processes from underlying intervals in sedimentary basins (Cartwright et al., 2007; Gay et al., 2007; Judd and Hovland, 2007). Fluid and gas escape features and associated seismic anomalies, such as bottom simulating reflectors (BSR), chimney and pipe structures have been identified and characterized in various marine environments around the world (Berndt et al., 2004); Haacke et al. 2007; Judd and Hovland, 2007, and references within; Cartwright et al., 2007; Løseth et al., 2009; Westbrook et al., 2009; Løseth et al., 2011) and specifically in the South Atlantic margin (Andresen and Huuse, 2011; Cartwright et al., 2007; Gay et al., 2007; Moss and Cartwright, 2009; Pilcher and Argent, 2007; Swart, 2009) Evidence of fluid and gas leakage processes, such as "sniffer" anomalies near the seafloor (Jungslager, 1999), also mud diapirs (Ben-Avraham et al., 2002; Viola, et al. 2005), pockmarks and seismic chimneys (Ben-Avraham et al., 2002; Paton et al, 2007; Boyd et al., 2011; Kuhlmann et al., 2010), have previously been identified on 2D seismic surveys in the Orange Basin, offshore South Africa. They have been related, by means of numerical modeling, to the underlying petroleum system (Paton et al. 2007; Kuhlmann et al., 2011).

Pockmarks form through episodic focused fluid and gas flow (Cole et al., 2000; Cartwright et al., 2007; Judd and Hovland, 2007; Pilcher and Argent, 2007; Cathles et al., 2010;). They appear as sub-circular depressions at the seafloor in various sub-aqueous environments (Judd and Hovland, 2007; King and Maclean, 1970). On average, their diameters vary from 10 - 200 m in diameter (Judd and Hovland, 2007 and references therein; Pilcher and Argent, 2007;), but also mega pockmarks with diameters of 800 - 1000 m (Cole et al., 2000; Gay et al. 2006c; Pilcher and Argent, 2007), and even giant pockmarks with diameters exceeding 10 km have been reported in some areas (Davy et al. 2010). Focused fluid flow at the sediment-water interface has been studied extensively giving insights into the basin "plumbing" system, especially in regard to hydrocarbon migration dynamics (Heggland, 1998; Andresen et al., 2011), and also on its impact on the bio-, hydro-, and atmosphere (Hovland et al., 2005; Judd and Hovland, 2007), and as a potential geohazard (e.g. Ligtenberg and Connolly, 2003; Judd and Hovland, 2007; Cathles et al., 2010).

Buried and stacked pockmarks, identified on seismic, provide evidence for paleo-leakage (Cole et al., 2000; Gay et al., 2006a,b; Andresen and Huuse, 2011). Once paleo-fluid flow features have been identified, the onset and duration of the paleo-leakage event that created them can be discussed (Gay et al., 2006a, Andresen and Huuse, 2011). The identification of such fossil leakage episodes, both at a local and regional scale, could be part of the evidence for an association between methane release from the geosphere and some of the observed carbon isotopic excursions in the paleo-climatic record, especially for the Paleocene-Eocene Thermal Maximum (e.g. Dickens et al. 1995 and 1997; Zachos et al., 2008; Kroeger et al., 2011).

In this contribution we present evidence of early Eocene sediment structures related to hydrocarbon leakage and paleo-fluid flow events derived from 3D seismic interpretation and attribute analysis of a 3D seismic dataset in the Orange Basin. Further, we discuss the

possible triggering factors and fluid sources by comparison to present-day known seepage mechanisms.

3.2. Geological setting

The study area is located in the Orange Basin and has a surface of 95.600 km^2 located in water depths between 100-2850 m (Figure 3-1). The sedimentary succession of the basin consists of 8 km thick synrift and drift sequences related to the continental break-up of Gondwana and the opening of the South Atlantic, taking place during the late Jurassic (Gerrard and Smith 1982). The margin evolution and basin structure have been documented based on exploration seismic datasets and well reports (de Vera et al., 2010; Dingle et al., 1983; Gerrard and Smith, 1982; Kuhlmann et al., 2010; Paton et al., 2008). Brown et al., (1995) and Muntingh and Brown (1993) provided the sequence stratigraphic framework of the late Jurassic and Cretaceous used in this study (Figure 3-2). In contrast to the Cretaceous, Cenozoic sequences characterization is very limited, and only, based on DSDP and ODP sites (Bolli et al., 1978; Weigelt and Uenzelmann-Neben, 2004, Séranne and Anka, 2005), vibro-core data (Wigley and Compton, 2006) and time-equivalent onshore sediments (Partridge and Maud, 2000 and references within).

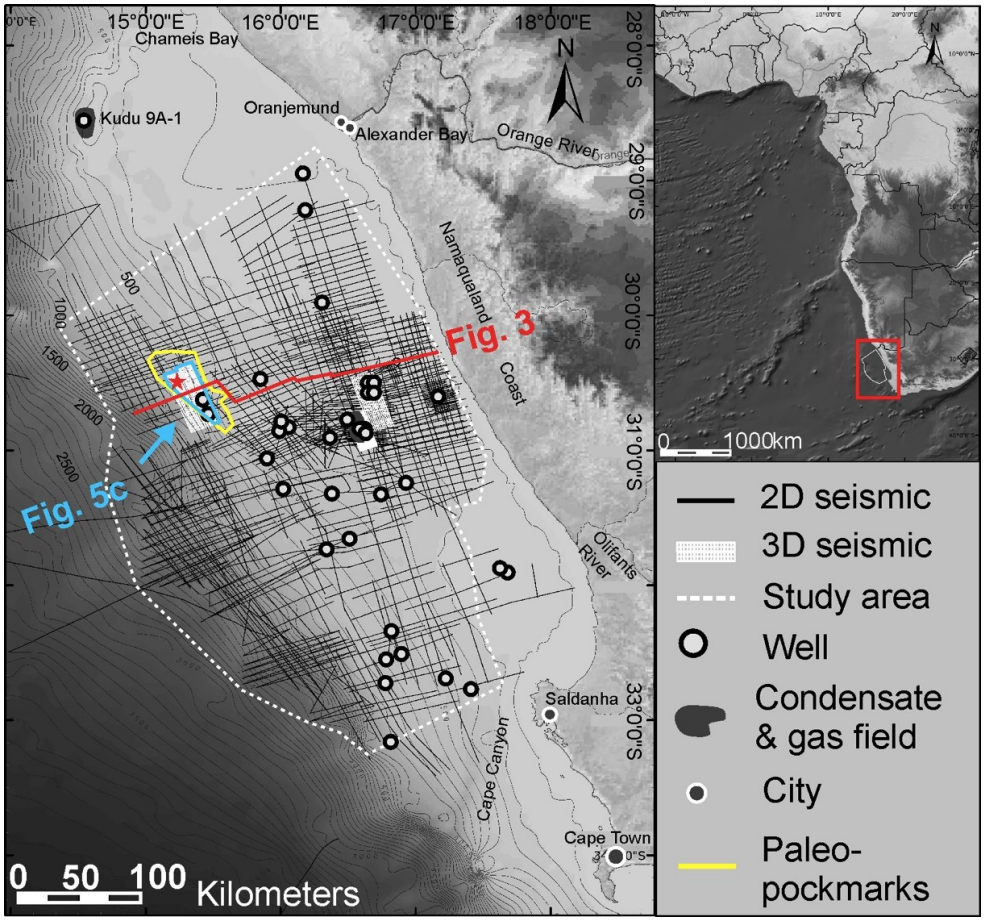

Figure 3-1: Location of the paleo-pockmark field and seismic coverage of the study area in the Orange Basin on the southwest African margin. Yellow outline shows the extent of the paleo-pockmark field; red star = location of Figure 3-6 and Figure 3-7;

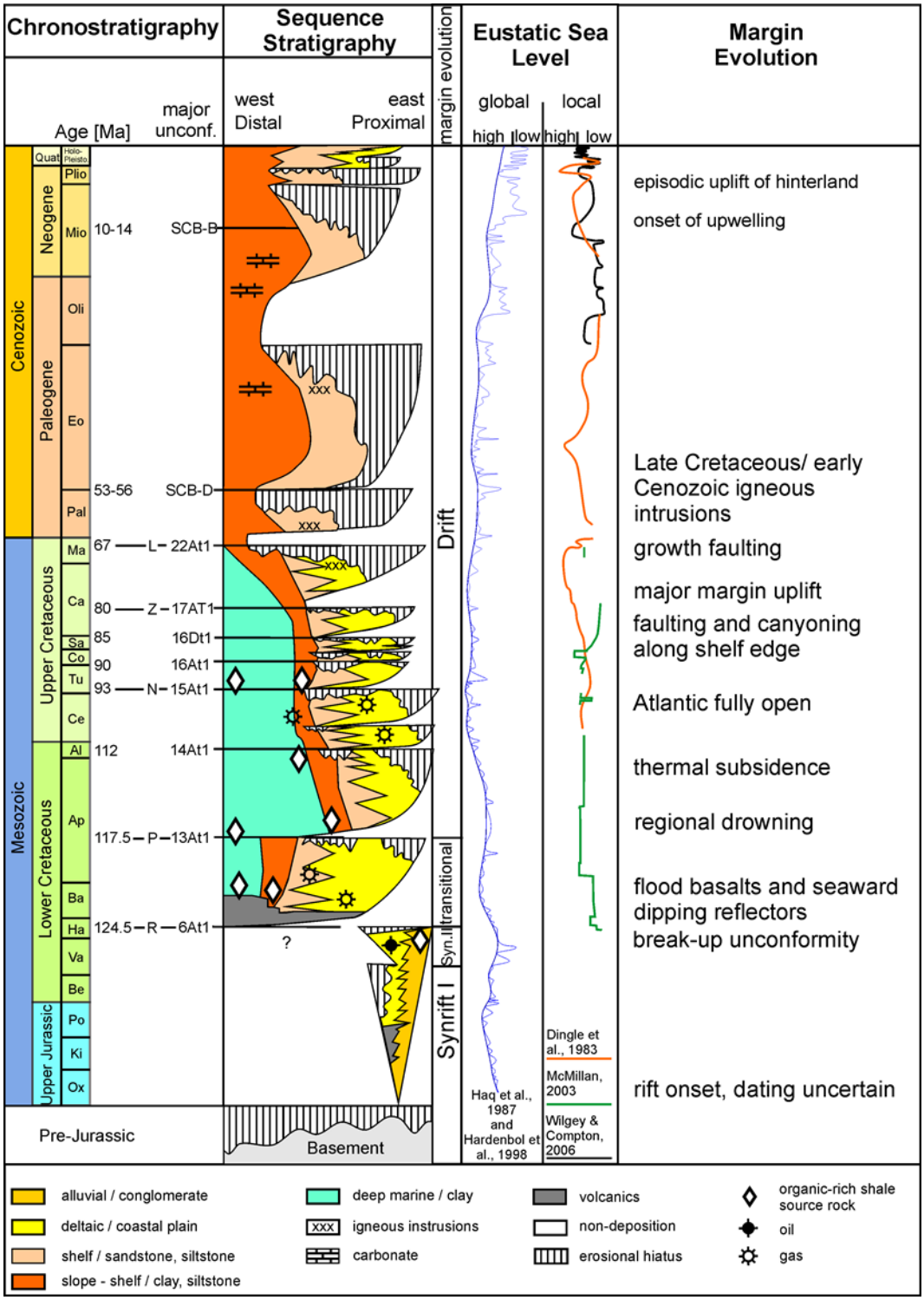

Figure 3-2: Generalized chronostratigraphic chart of the Orange Basin showing the sequence stratigraphic horizons used in this study, global and local sea level variations, and margin evolution (modified from Broad et al., 2006; Cenozoic ages: Weigelt & Uenzelmann-Neben, 2004; sea level curves: Haq et al., 1987; Hardenbol et al., 1998; Dingle et al. 1983; McMillan, 2003; Wigley & Compton, 2006;).

3.2.1. Late Jurassic and Cretaceous

Rifting was initiated during the middle to late Jurassic, at about 130 Ma (Macdonald et al. 2003) and resulted in the formation of north-northwest trending rift and half-grabens subparallel to the present day southwest African margin (Gerrard and Smith 1982, Muntingh 1993; Broad et al., 2006). The rift sequence overlain by an up to 2000 m thick Barremian-Aptian aged rift-to-drift transitional sequence, which was deposited on a ramp-like margin (6At1-13At1). The mid-Albian to Cenomanian consists of deltaic and fluvio-marine deposits with a cumulative thickness exceeding 3500 m (Gerrard and Smith, 1982; McMillan, 2003), topped by organic-rich shales of a Cenomanian/Turonian marine condensed section (15At1, Figure 3-3; McMillan, 2003). It is overlain by an aggradational sequence of Coniacian to late Santonian/early Campanian age (Muntingh, 1993; McMillan, 2003; Paton et al., 2008). Late Cretaceous margin uplift, tilting (Gallagher and Brown, 1999; Kounov et al., 2009), and subsequent erosion of the inner shelf resulted in the deposition of a Campanian-Maastrichtian progradational sequences (16Dt1/17At1 – 22At1,) onto an already unstable shelf (Broad et al., 2006). Intense faulting of the northern margin and the formation of growth- and roll-over structures caused significant thickness variations in the Cenomanian-Campanian succession (Brown et al., 1995, de Vera et al., 2010).

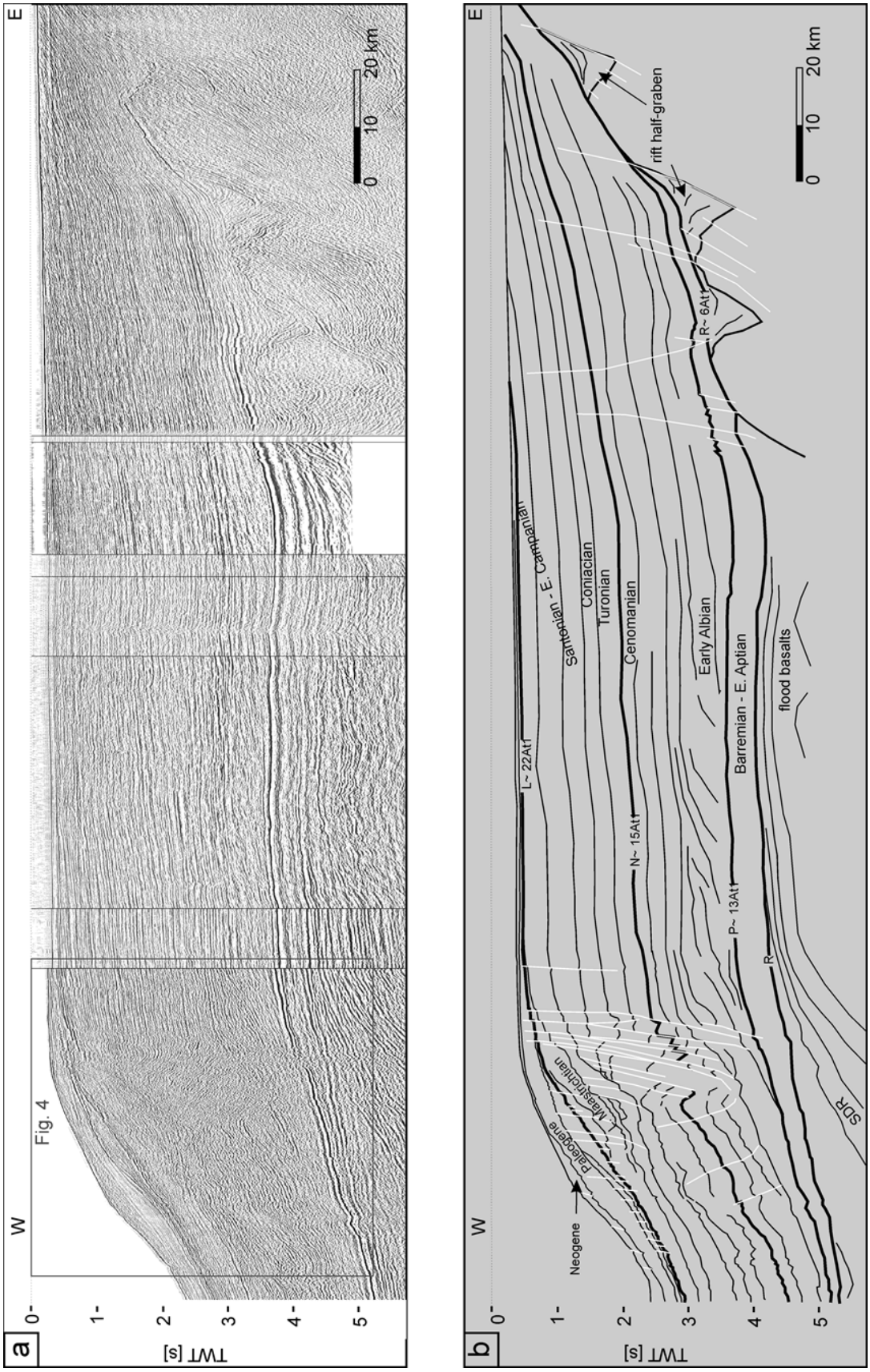

Figure 3-3: Seismic transect through the northern Orange Basin showing the margin structure (a) uninterpreted, (b) interpreted; for location shown in Figure 3-1, thick black lines= major regional unconformity, white lines= faults, also shown is the location of Figure 3-4. Note the truncated Upper Cretaceous sequences in the east and progradation of late Upper Cretaceous and thin Cenozoic sequences.

3.2.2. Cenozoic

In general, Cenozoic depocenters have an elongated shape parallel to the steep slope and form a thin (50 - 250 m thick) cover on the continental shelf (Dingle et al., 1983; Light et al., 1992; McMillan, 2003) The Cenozoic-Cretaceous transition is marked by an easily recognizable late Maastrichtian - early Paleocene seismic reflector named reflector D (=Davie) by Emery et al. (1975), horizon L by Gerrard and Smith (1982), and reflector SCB-D (Weigelt and Uenzelmann-Neben 2004; Figure 3-4). It separates lower Eocene sediments from sediments of Maastrichtian to Paleocene age in the outer and Albian to Cenomanian aged sediments on the inner shelf. Evidence for late Cretaceous/ early Cenozoic igneous activity can be found onshore and offshore the southwestern African margin. The age of intrusions range from 77 to 59 My along the Namaqualand coast and 50 - 30 My for the Chameis Bay in the northern Orange Basin (Moore et al., 2008; Phillips et al., 2000; Verwoerd and de Beer, 2006)

In the southern Orange Basin Paleogene sediments exceed 1500 m thickness and are affected by growth-faults and toe-thrusts (McMillan, 2003; Paton et al., 2008; de Vera et al., 2010). The Paleogene – Neogene transition is marked by a regional erosional event recognized throughout South Africa (Siesser and Dingle, 1981; Dingle et al., 1983; Weigelt and Uenzelmann-Neben, 2004; Wigley and Compton, 2006). This was possibly related to a phase of tectonic uplift (Partridge and Maud, 2000; Hirsch et al., 2010)

The oldest sediments above the slump-scarred unconformity are around 14 My old (Weigelt and Uenzelmann-Neben, 2004). They were generally deposited in a shallow marine environment (Partridge and Maud, 2000) forming a thin cover on the shelf and prograding wedge along the slope.

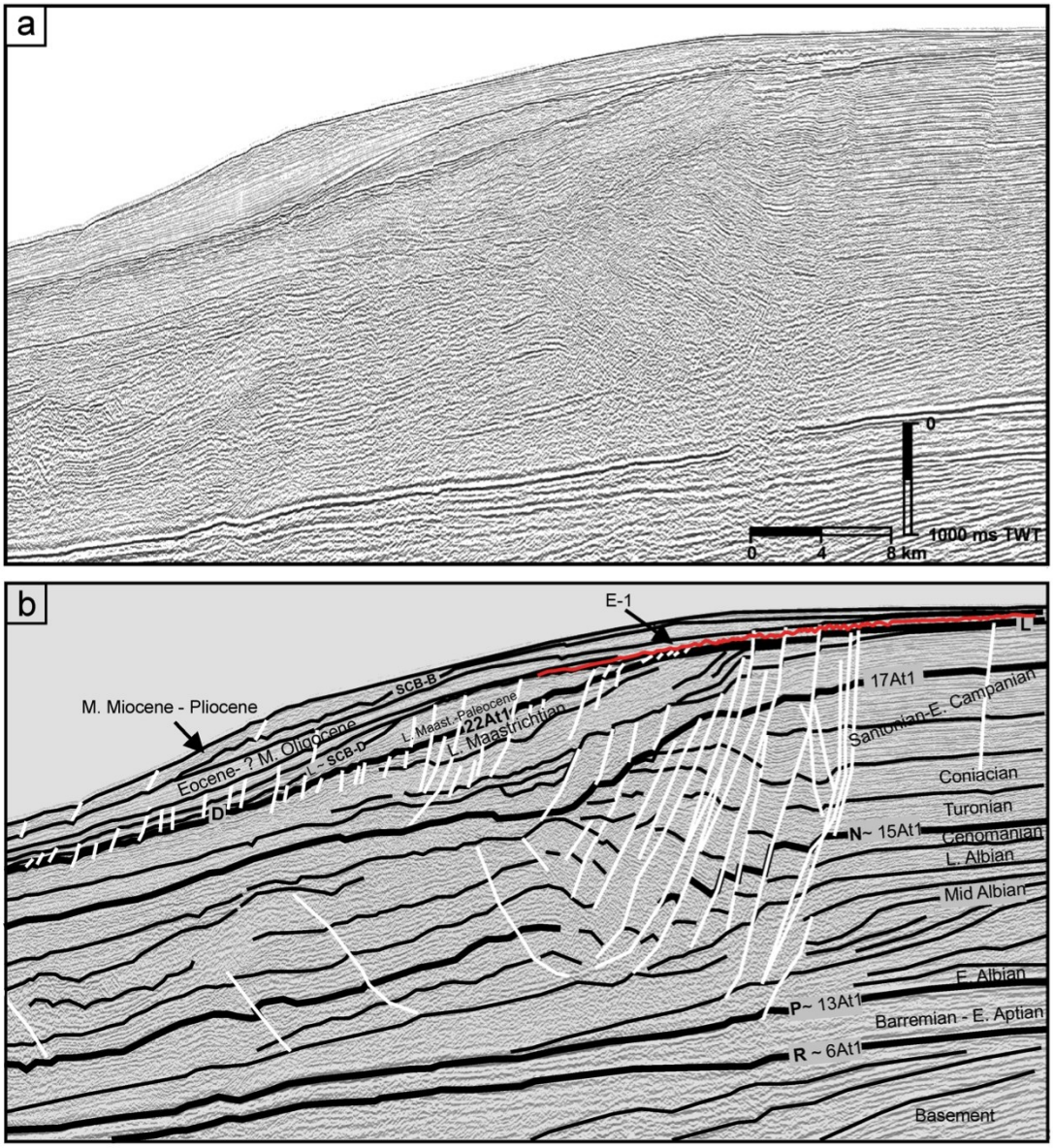

Figure 3-4: Detail of the gravity-faulted slope of Figure 3-3, showing late Maastrichtian and Cenozoic progradation and the location of the wavy reflector horizon E-1, (a) uninterpreted, (b) interpreted, thick black lines= major regional unconformity, white lines= faults. Some faults reach down into the Aptian/Albian source rock intervals.

3.3. Data and Methods

The seismic dataset consists of (1) 600 2D exploration seismic reflection profiles, acquired from 1976 to 2002 and covering an area of about 95000 km^2, and (2) an exploration 3D seismic reflection cube (Figure 3-1) covering an area of 1095 km^2 along the present day shelf break and upper slope, between 265 and 610 m water depth. The seismic cube is pre-stack time migrated and has a line spacing of 25 m and an average vertical resolution of 17 m, assuming average velocities of 1700 m/s for the Neogene and Eocene and 2000 m/s for Paleocene deposits (Bolli et al., 1978a; Bauer, 2000; Weigelt and Uenzelmann-Neben, 2004). These average velocities were used to calculate thicknesses in meters whenever mentioned in the text.

Lithologies and chronostratigraphy are based on initial reports from Leg 40 DSDP sites 360 and 361 (Bolli et al., 1978a) and well reports of 32 exploration wells, tied to the seismic lines. 2D and 3D data were loaded in the commercial seismic interpretation software Petrel 2011.1.2 from Schlumberger and five seismic horizons representing the main stratigraphic unconformities were mapped using guided auto-tracking and manual corrections.
The 3D seismic cube was further investigated using time-slices and seismic-attribute maps of dip-azimuth and variance extracted along the horizons. The latter is a coherence-type attribute used to image vertical discontinuities in the amplitude distribution (van Bemmel and Pepper, 2000).

3.4. Results

3.4.1. Slope seismostratigraphy

The five major horizons used in this study are the latest Cretaceous (Maastrichtian, ~67 Ma), the regional unconformity 22At1, a mid-Campanian unconformity (17At1) based on the stratigraphic framework of Brown et al. (1995) and a Lower-mid Eocene well marker based on biostratigraphy. A Mid--Cenozoic regional unconformity (SCB-B) and a Paleocene/Eocene reflector (SCB-D) from the study of Weigelt and Uenzelmann-Neben (2004) that are easily identified on 2D seismic were correlated with the 2D seismic in our study area. The nature of the “wavy" reflector named E-1 (Eocene-1) is the focus of this work.

3.4.1.1. Upper Cretaceous

From NE to SW across the shelf, the Upper Cretaceous succession (Cenomanian to mid-Campanian) is characterized by semi-continuous, parallel internal reflections, which are faulted and offset by listric faults and toe-thrusts in the distal areas (Figure 3-3). In the southern basin the average sediment thickness is 1100 ms two-way travel time (TWT) forming a prograding sequence, whereas in the northern basin the sediment thickness increases to more than 2300 ms TWT in the severely faulted shelf (Figure 3-4). Within the faulted section, high-amplitude reflections depict roll-over and growth structures in the Turonian- lower Campanian sediments. The lower portion of the Coniacian/Santonian is increasingly growth-faulted towards the west and northwest. The last movement along these fault planes occurred before the deposition of a sequence of elongated, margin parallel prograding slope wedges, located along the Upper Cretaceous shelf of the central Orange Basin. These bodies are characterized by chaotic and low amplitude internal reflections, and occur above unconformity 17At1. In the southern Orange Basin they consist of calcareous to non-calcareous claystones with thin silty and fine-grained sandstone layers. Similarly aged prograding slope wedges and mass transport complexes have also been reported along the Namibian margin of the Orange Basin (de Vera et al., 2010). Basinwards the Upper Cretaceous sediments have a more uniform thickness of 800 ms (TWT) and show parallel internal reflections.

3.4.1.2. Late Maastrichtian - Paleocene

These sediments are only identified below the present-day shelf-break as a middle-to-lower slope sediment wedge topped by reflector L of Gerrard and Smith (1982), and SCB-D of Weigelt and Uenzelmann-Neben (2004) (Figure 3-4). The sediment wedge onlaps unconformity 22At1 at the shelf break. It has an average thickness of 160 ms (TWT) in the south and 370 ms (TWT) in the northern Orange Basin, northwest of Childs Bank (Figure 3-5a), but thins out to 60 -90 ms TWT basinward, where it forms a thick band of strong reflectors with unconformity 22At1. Latest Maastrichtian sediments consist of deep-water chalks in the southern Orange Basin (McMillan, 2003). In the northern Orange Basin the late Maastrichtian/Paleocene sediments consist of claystones with sand- and shale-rich limestone stringers (SOEKOR internal reports).

3.4.1.3. Eocene - Mid-Miocene

Reflector D forms the base of a seismic unit composed of parallel continuous reflectors equivalent to units SCB-3 and SCB-4 of Weigelt and Uenzelmann-Neben (2004) that onlaps the paleo-shelf surface (Figure 3-3 and Figure 3-4). This unit is truncated by a severely slump scared Mid-Miocene unconformity (SCB-B). At the shelf break the unit's thickness varies between 100 ms TWT (85 m) and 300 ms TWT (255 m), thinning out landwards. Near Cape Canyon, it forms a margin parallel, narrow (~25 km wide) depocenter that extends 120 km north of Saldanha Bay along the paleo-shelf reaching 1700 ms TWT (1445 m) in thickness.
In the northern part of the study area, a characteristic wavy reflector "E-1" (Figure 3-4 and Figure 3-5c,d), was identified along the base of this unit, where the Maastrichtian-Paleocene wedge rapidly thickens. Nature and age of this horizon will be discussed later on. A set of early Eocene continuous reflectors onlap horizon E-1 and pinch out upslope towards the shelf break. In the northern Orange Basin, the Eocene sediments consist of claystones with sand- and shale-rich limestone stringers (SOEKOR internal reports). At DSDP site 361 early Eocene sediments are made up of carbonate-rich mudstone, but in the Kudu 9A-1 well, in the Orange Basin shelf, they consist of sandstones overlain by upper Eocene clays (Dingle et al., 1983).

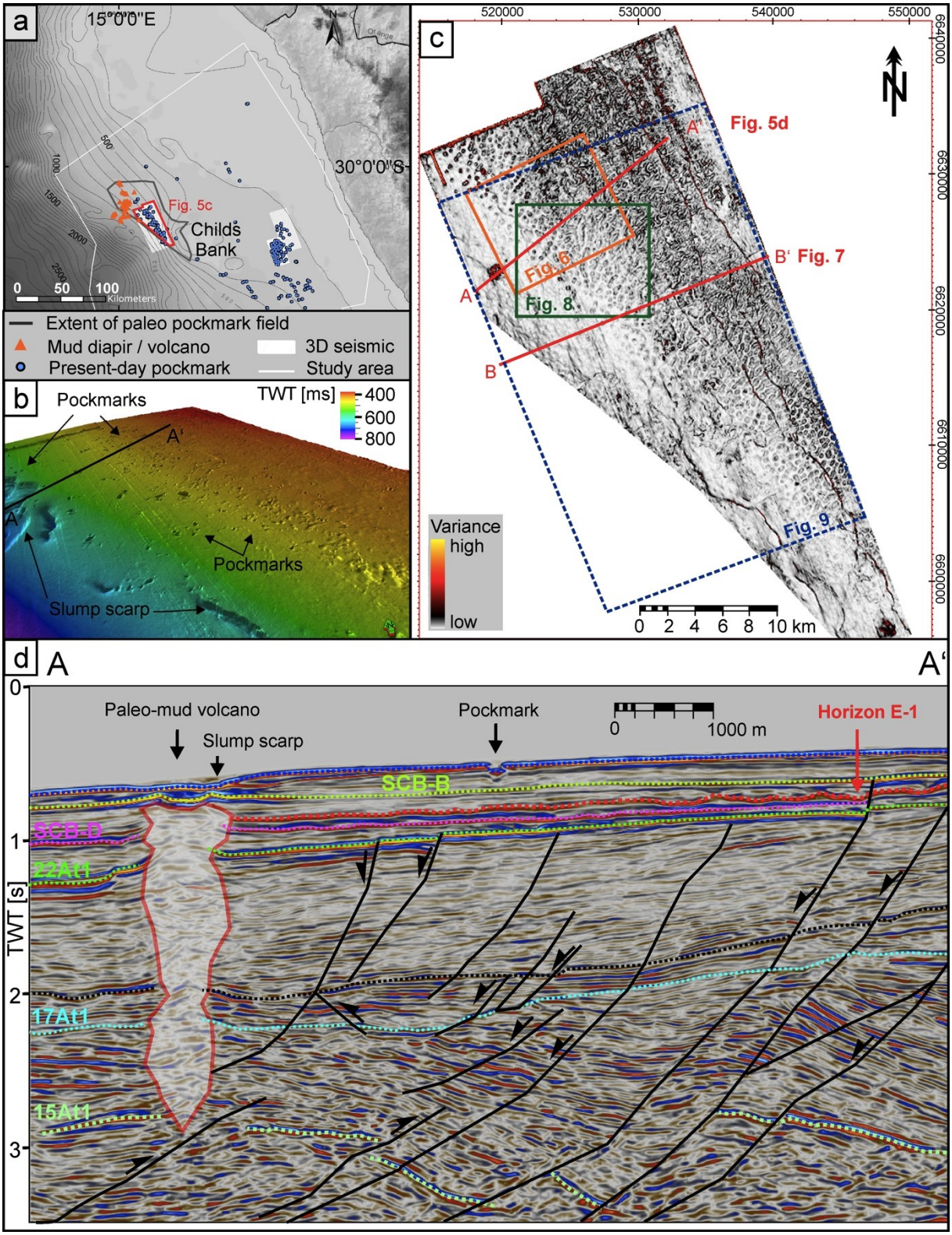

Figure 3-5: a) Location map of seafloor pockmarks, mud volcanoes, and early Eocene paleo-pockmarked surface. (b) Northward view of the seafloor in TWT contour at the shelf break showing present-day seafloor pockmarks. (c) Variance extracted along paleo-pockmark horizon E-1 showing circular and elongated depressions. Note the NE-SW alignment of the depressions and the NNW-SSE trend of reactivated Cretaceous faults (visualized in black to red colors). Location of cross-sections BB' in Figure 3-7 and of maps in Figure 3-6 and Figure 3-8 are plotted.

3.4.1.4. Mid-Miocene - Quaternary

This unit corresponds to units SCB-1 and SCB-2 of Weigelt and Uenzelmann-Neben (2004) and its base marks the basin-wide Mid-Cenozoic erosional unconformity (SCB-B). The basal part consists of weak, continuous reflectors frequently disturbed by slumps and channels. Within the top of the unit, an erosional unconformity can be identified along the shelf in the middle Orange Basin, south of Childs Bank. This unconformity truncates the underlying unit seaward. The overall thickness varies greatly across the basin. On the shelf, it is a thin cover hardly resolved by seismic data, whereas in the southern basin it thickens to 60 and 100 ms TWT on the shelf (51 and 85 m), and then thins out northwards. Thickness can locally reach up to 700 ms TWT (595 m) below the shelf. This unit was eroded along some areas below the shelf break, but was preserved further downslope, reaching an average thicknesses of 180- 350 ms TWT (153 - 298 m). Along the shelf in the northern Orange Basin we identified some sediment re-mobilization features, which occur above the Mid-Miocene unconformity and penetrate up to the seafloor. They correspond to mud volcanoes previously described by Ben-Avraham et al. (2002). These features form elongated structures situated above faults and do not occur further south along the shelf (Figure 3-6a).

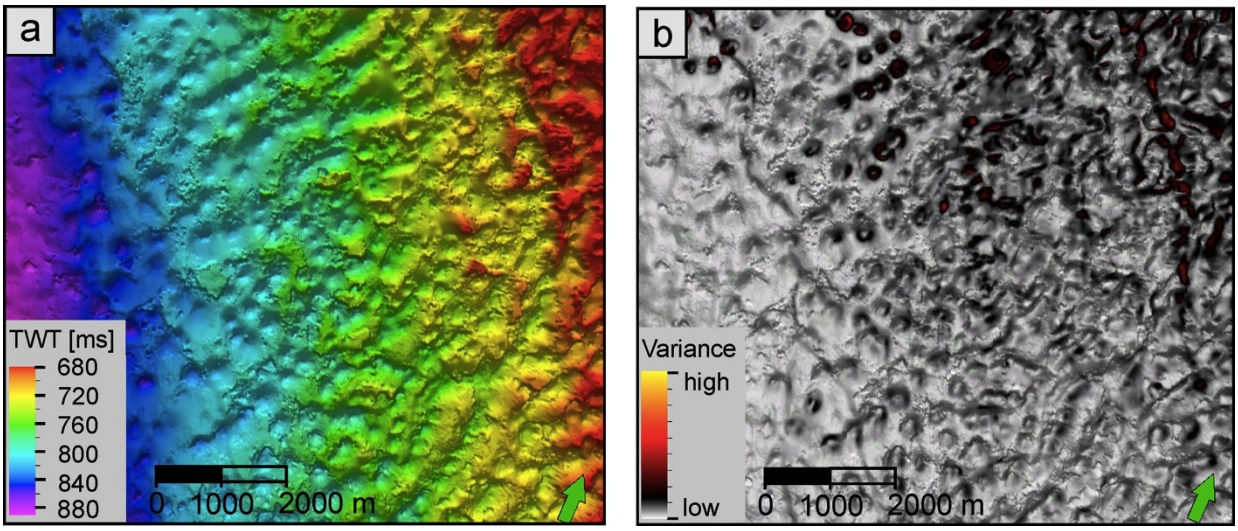

Figure 3-6: Paleo-pockmarks and NNE-SSW lineation trend on horizon E-1 as seen on (a) TWT contour and (b) variance map extracted along the horizon. Locations maps plotted in Figure 3-5, green arrow points north.

3.4.2. Present-day seafloor fluid escape features

Although this study focuses on Paleogene fluid flow features, it is worth mentioning the evidence of at least two Neogene episodes of fluid flow. A series of seafloor depressions were identified on 3D seismic subparallel to the present-day slope in water depths ranging from 225 to 450 m (Figure 3-7b). Their diameters and depths vary widely from 75 to 495 m and from 3.6 - 36 ms TWT (5 - 26 m), respectively. Based on their dimensions and their three-dimensional geometry, these features are interpreted as seafloor pockmarks produced by recent fluids seep from the subsurface. On 3D seismic the highest density of these pockmarks is observed above the Ibhubesi gas/condensate field (Figure 3-5a, eastern 3D seismic), which suggests a genetic relationship with the hydrocarbon “plumbing” system.

Similar features were also observed on the 2D seismic survey. By comparing their morphology and seismic character with those observed on the overlapping areas of the 3D seismic cube, pockmarks and their feeding chimneys can be identified on 2D vertical seismic sections (Figure 3-5a).

Mud volcanoes are prominent seafloor features that only occur in the northern Orange Basin (Figure 3-5a), also described by Ben-Avraham (2002) and Viola et al. (2005). They form sub-circular and elongated piercing structures with diameters varying from 590 to 6600 m reaching up to the present-day seafloor above late Cretaceous normal faults. Their enveloping surface either onlaps or lies conformably on reflector SCB-B with a maximum age of post mid-Miocene (~14Ma) for the initiation of mud volcanism. In Figure 3-5d the chaotic seismic reflections beneath the mud volcano are interpreted as the feeding fluid conduit (e.g. Løseth et al., 2009, Judd and Hovland, 2007), taking its root in an upper Cretaceous roll-over structure (Figure 3-5d).

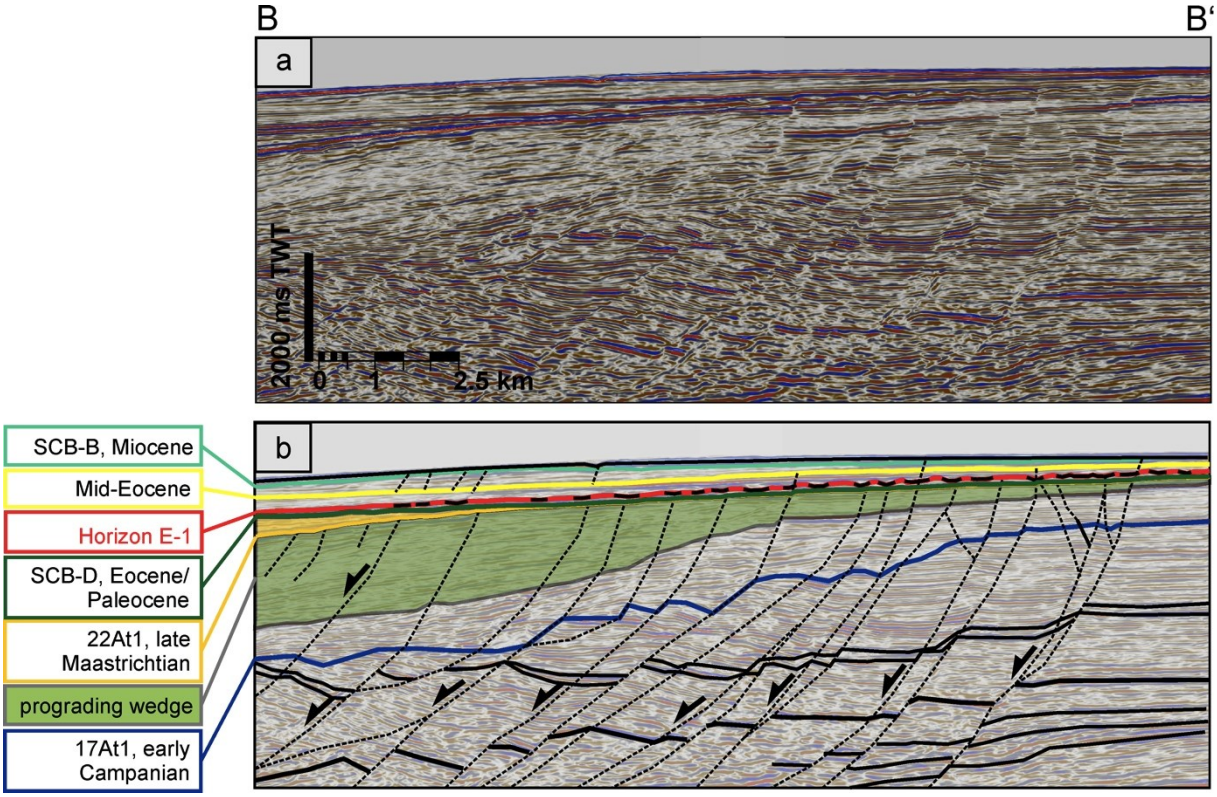

Figure 3-7: (a) Uninterpreted and (b) interpreted seismic crossline showing the structure of the shelf and Late Cretaceous to Cenozoic sediments. The pockmarks on horizon E-1 are located above faults. Pockmark density increases where the Late Campanian/Maastrichtian wedge (green area) pinches out. Locations of profile BB' is plotted in Figure 3-5.

3.4.3. Circular depressions on horizon E-1

Besides the above described present-day fluid flow and sediment mobilization structures, seismic interpretation also revealed the peculiar wavy morphology of horizon E-1 within Paleogene deposits along the shelf-break (Figure 3-5c, d). Horizon E-1 occurs within one distinct stratigraphic interval above reflector L, with a maximum age of latest Paleocene/early Eocene (~ 53 -56 Ma). A Mid-Eocene well marker (base Lutetian based on

biostratigraphy) located above horizon E-1 gives a minimum age of early Mid-Eocene (~48 Ma).

Horizon E-1 is continuous, except where it is offset by normal faults. This horizon was investigated in detail using time slices and seismic variance extracted along the reflector's positive amplitude phase. The 2D wavy morphology corresponds to circular depressions in 3D view (Figure 3-5c). They occur as individual features in NNE-SSW striking linear trends, and coalescing elongated structures. The wavy reflector, also be identified on 2D seismic, is continuous and can be mapped throughout an area of 2800 km^2 along the paleo-shelf break in the northern Orange Basin. The circular depressions range in diameter from 170 to 520 m, on average 294 m. Their depth varies from 6 to 42 ms TWT (~5 - 35 m). The individual pockmarks have an approximate density of 4.5/km^2. The overlying sediments are 160 - 318 ms TWT thick (140 - 270 m). Their density increases upslope and they merge with neighboring pockmarks to form linear arrangements of ten or more pockmarks, similar to the pockmark trains and gullies described on the present-day slope offshore Gabon (Pilcher and Argent, 2007). The pockmark lineaments are 2 - 5 km long and on average 290 m wide (Figure 3-6). Further upslope, at the paleo-shelf break, where the crests and troughs of horizon E-1 show the highest relief, the depressions form coalescing elongated structures, predominantly oriented NE-SW, and the distinction of individual pockmarks becomes difficult.

3.4.4. Late Cretaceous faults

The pockmarks are located above NNE-SSW oriented Upper Cretaceous listric normal faults, which are rooted in a mid- to late Albian décollement surface (Figure 3-4 and Figure 3-7). Extensional faulting was initiated during a phase of late Cretaceous denudation (Gallagher and Brown, 1999; Tinker et al., 2008a, 2008b) and was most severe during Coniacian to Campanian as indicated by the growth-structures and fault offsets. A last episode of fault movement, prior to the deposition of horizon E-1, is inferred from fault offsets of unconformity 22At1 (latest Maastrichtian). Additional coherency attribute analysis of the consolidated Upper Cretaceous succession reveals the presence of a fracture network (Figure 3-8). This fracture network follows the trend given by the large Cretaceous listric normal faults. Within this fracture network several NE-SW striking fractures coincide with the pockmark lineation trends. In one down-slope location individual paleo-pockmarks display a dextral curving arrangement that coincides with minor NNW-SSE oriented faults (Figure 3-8b, bottom left).

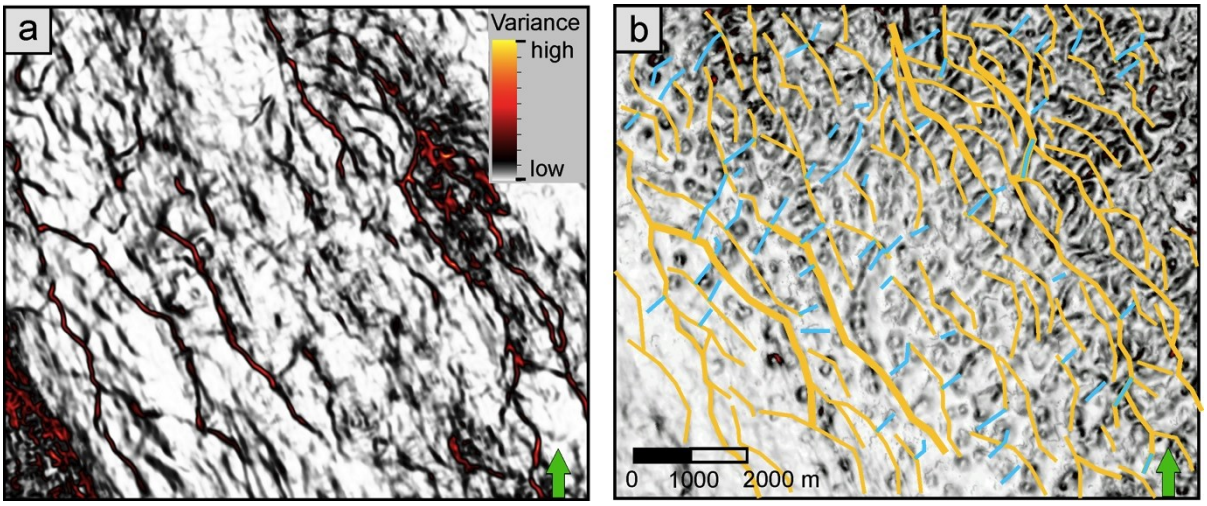

Figure 3-8: (a) Variance time-slice through the seismic reflections below the horizon E-1 showing large faults with higher offsets (red) and small discontinuities (black and dark grey) interpreted as fractures and (b) their relation to the paleo-pockmarks. Some NE-SW oriented fractures (light blue) seem to coincide with the pockmark lineation, the majority of the faults and fractures trend NW-SE (yellow). Locations maps plotted in Figure 3-5.

3.5. Discussion

3.5.1. Origin of paleo-pockmarks

The features on horizon E-1 are interpreted as buried paleo-pockmarks. They have similar sizes and depths when compared with other examples elsewhere (Pilcher and Argent, 2007; Judd and Hovland, 2007; Andresen et al., 2008) and references therein). Even their areal extent of 2800 km^2 is comparable to present-day pockmark fields covering up to 2800 km^2 offshore Gabon, and 20000 km^2 offshore eastern New Zealand as reported by Pilcher and Argent (2007) and Davy et al. (2010), respectively. Several fluid flow processes can lead to the formation of widespread seafloor depressions and pockmarks. In the context of this study, we refer as shallow fluid sources those located within or directly below the sedimentary unit containing pockmarked horizon E-1. These sources mainly include formation waters and biogenic gas. On the other hand, early and late Cretaceous source rocks and claystones, respectively, are considered as deep sources of thermogenic fluids.

3.5.1.1. Shallow fluid sources

Differential compaction and density inversion have been presented as formation mechanisms for giant hummocks and diapiric sediment structures in fine-grained low-density sediments overlain by high-density sandier muds (Davies et al., 1999; Vogt, 1997). Differential loading and eventual seal failure of overlaying cemented sediments can lead to continuous fluid expulsion from under-compacted underlying interval, forming troughs in successively younger sediment layers. Davies et al. (1999) mention cases where the hummock crests are underlain by polygonal fault systems, leading to a diapiric formation process. Although an extensive fault network exists below the pockmarked horizon E-1, there is no evidence for intrusive or diapiric processes below the paleo-pockmarks to explain

their relatively high relief. Concave continuous reflections are present as pockmark infill, whereas convex internal reflections are present within underlying sediments that constitute the high relief "ridge" of the pockmarks. This may be an indication of the high relief in the upslope pockmarks resulting from a density inversion process on a pre-existing relief, for example pockmarks, similar to load casts formation processes described by Owen (2003).
Biogenic methane production that could have led to massive fluid expulsion at the time of pockmark formation is not supported by any organic enrichment of the late Maastrichtian-Paleocene interval. According to SOEKOR well reports, these sediments are generally light-grey colored clays, which is not indicative of high organic matter contents.

3.5.1.2. Deep fluid sources

Lower Aptian black shales are thought to be the main contributor to the gas and condensate produced from the Kudu and Ibhubesi fields (Bray et al. 1998; Petroleum Agency SA, 2003; van der Spuy, 2005). The reservoirs are stratigraphic traps in Barremian/lower Aptian aeolian sandstones, and Albian and Cenomanian fluvial channel-fill sandstones (Jungslager, 1999; Petroleum Agency SA, 2003; van der Spuy, 2005). The organic-rich shales with sapropelitic and terrigenous organic matter can reach a cumulative thickness of 30 - 90 m in the Orange Basin. Well data show a thermal maturity corresponding to the dry gas window in the Cretaceous depocenter (VR_O > 1.5%, Petroleum Agency SA, 2003; Paton et al. 2007; Kuhlmann et al. 2011). Thermal maturity decreases to wet-gas and oil window maturity towards the west and southwest of the shelf break, in the area of the Cenozoic sediment wedge (van der Spuy, 2003; Paton et al. 2007; Kuhlmann et al. 2011). Their present-day maturity below the Cenozoic shelf-break of the northern Orange Basin is expected to be within the wet-gas to dry-gas range (van der Spuy, 2003, Kuhlmann et al., 2010, 2011). Some authors propose a main phase of hydrocarbon generation from this source rock during the Campanian due to rapid burial, and a second ongoing generation phase in the southern Orange Basin due to the progradation of the thick (more than 2000 m) Cenozoic wedge (Paton et al., 2007; Kuhlmann et al., 2011). Based on recent petroleum system modeling estimations by Kuhlmann et al. (2011) a similar trend can be assumed for the area of the paleo-pockmarked surface. In this area progradation of the late Maastrichtian wedge (1400 ms TWT, ~ 700 m) started earlier than in the south and continued with the deposition of the uppermost Maastrichtian/Paleocene slope wedge (max. 435 ms TWT, ~370 m). This could cause a Maastrichtian/Paleocene phase of rapid burial, increasing the temperature leading to maturation and expulsion of hydrocarbons from the underlying source rock(s).
A Cenomanian/Turonian aged organic-rich shale is another potential source rock and expected to change from a gas-prone facies on the proximal shelf to an oil-prone facies basinwards (Aldrich et al. 2003; van der Spuy, 2005). Basin modeling predicts this interval to be thermally immature within most of the southern Orange Basin, but increasing to oil-window maturity in the western-central basin (Kuhlmann, et al. 2011). The main phase of petroleum generation is proposed to have occurred during the Cenomanian to Campanian period, followed by a minor generation phase during the late Cretaceous/early Cenozoic,

driven by rapid shelf progradation due to margin tilting, erosion and possibly increased heat-flow due to volcanism. A similar process has been proposed by Kuhlmann et al. (2010, 2011) and Paton et al. (2007), for present-day gas leakage features observed in the southern basin, which would result from ongoing petroleum generation in the Cenozoic depocenters.

Another deep fluid source may be the pore fluids within the late Maastrichtian claystones of the rapidly prograding slope sediments. In the area under investigation they can reach a thickness of up to 640 ms TWT (704 m). In general, clays have a very high porosity of 75 -90% at the time of deposition, although it decreases exponentially during burial and dewatering (Long et al., 2011; Velde, 1996). Their pore space is usually water-saturated and during the first 500 m of burial the porosity is reduced by up to 40% (Velde, 1996, Judd and Hovland, 2007; Long et al., 2011). This process creates large quantities of water that need to be expelled either by diffuse migration through sediments or episodic flow (Velde, 1996). If these clays are rapidly buried, which is thought to be the case due to prograding shape of the slope wedge, disequilibrium compaction can lead to significant overpressure (Osborne and Swarbrick, 1997; Hustoft, et al., 2009; Long et al., 2011) and thus to sudden or episodic release of pore water.
Mud diapirs, which are generally rooted in upper Cretaceous strata, are proof that episodic fluid flow occurred during the Neogene. Viola et al. (2005) propose a similar timing and argue that flower structures, resulting from neotectonic activity in southern Africa, and the location of late Cretaceous normal faults control the diapirs' positions. This is a further indication, that paleo-fluid flow was directed along faults. Additionally, exploratory drilling in the study area encountered overpressure within lower Campanian claystones and also gas shows in sandstone layers, starting at depths below 1000 m to depths exceeding 4000 m. Hence, we propose that the paleo-fluids feeding the paleo-pockmark field consisted of pore fluids expelled from rapidly buried prograding slope sediments, and/or thermogenic hydrocarbons, predominantly gas, from the lower Aptian organic-rich shales.

3.5.2. Controls on pockmark location and lineation trends

Based on our observations, the NNE-SSW oriented paleo-pockmark arrangements correlate to the strikes of the late Cretaceous growth and listric normal faults. Figure 3-7 and Figure 3-8 demonstrate that the paleo-pockmarks are located above large listric normal faults. They can therefore be classified as fault-strike pockmarks similar to the examples shown by Pilcher and Argent (2007) offshore Gabon. In contrast to what has been reported elsewhere (i.e. Gabon, Pilcher and Argent 2007), further attribute analysis of the Upper Cretaceous succession and the uppermost Maastrichtian-Paleocene prograding sediment wedge did not reveal any channel-structures that could be related to the linear trend of the paleo-pockmarks.
The highest relief and density of the paleo-pockmarks occurs above fractured and growth-faulted late Cretaceous sediments where the Maastrichtian-Paleocene wedge thins out (Figure 3-9). This suggests that the highest fluid flux occurred in this particular area. Some

curvi-linear paleo-pockmark arrangements observed downslope further suggest that, in the absence of a fracture network, fluids flow along the large listric faults. Below the shelf-break where paleo-pockmark density decreases, upward fluid flow was inhibited due to the low-permeability of the thicker fine-grained uppermost Maastrichtian/Paleocene sediment wedge. All these observations suggest that the location of the paleo-pockmarks is fault-controlled. We propose that the bulk of the overpressured fluids migrated up-dip below the late Maastrichtian-Paleocene wedge within coarser-grained sediment layers until they encounter large listric faults or the flow-retarding overlying sediments pinch out. There, fluid pressures were high enough to penetrate the thinning flow barrier.

Contrary to the fault strike, the pockmark lineament trends are consistently oriented NNE-SSW and follow the southwestern dip direction of the paleo-slope with a characteristic knick-point where the paleo-slope dip increases. We propose two hypotheses that can lead to this observation: (1) erosion through downslope currents and (2) the formation of pockmark gullies according to Pilcher and Argent (2007).

The first hypothesis is supported by Uenzelmann-Neben et al. (2007)who studied Cenozoic sedimentation patterns around the South African margin based on seismic stratigraphy and inferred a Cenozoic oceanic circulation. They show that proto-Antarctic Bottomwater also flowed southwest along the northern Agulhas Ridge since the early Eocene and that the earliest erosional features attributed to this current are found in the southern Cape Basin. Thus the pockmark edges at the paleo shelf-break may have been eroded into NNE-SSW elongated features by downslope currents. Scouring by bottom currents systems has been reported to alter the initial circular to near-circular shape of pockmarks into elliptical pockmarks, where the ellipse's long axis corresponds to the current flow direction (e.g. the Danish and Norwegian North Sea and the South China Sea; (Bøe et al., 1998; Judd and Hovland, 2007; Sun et al., 2011)

The second hypothesis for the pockmarks' NNE-SSW orientation is a formation process similar to the pockmark trains and gullies described by Pilcher and Argent (2007) in the slope offshore Gabon. They propose a process in which linear arrays of pockmarks result from gravity slumping on unstable slopes. This process can be summarized as follows: it starts with slumping at the seafloor on the slope; single pockmarks form through upward fluid flow from slump-/fault-truncated carrier beds; as the pockmarks grow in size and number they coalesce into trains following the dip direction of the slope (Pilcher and Argent, 2007).

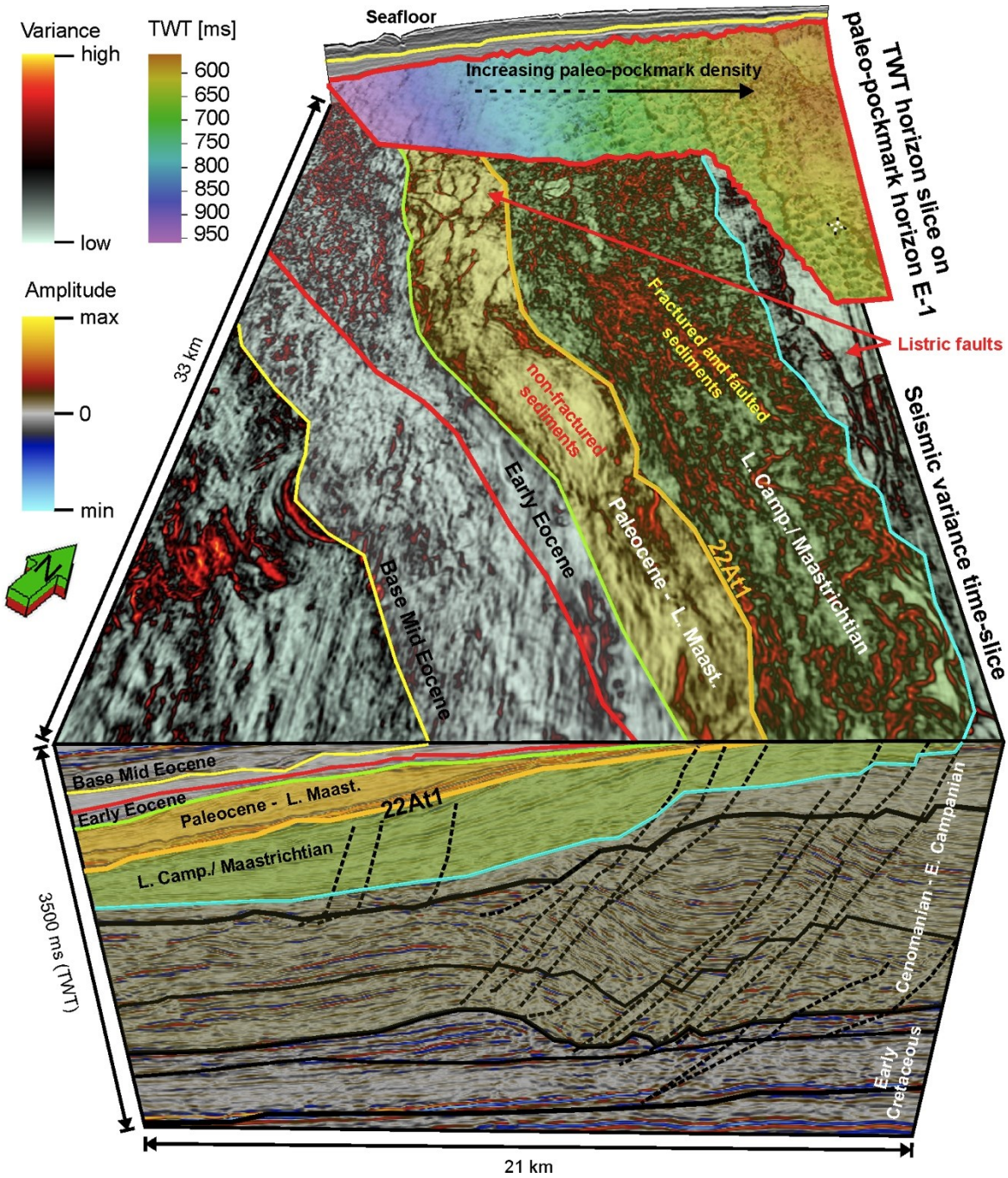

Figure 3-9: 3D view of the paleo-pockmarked horizon in relation to fault and fracture patterns of underlying sediments (for location see fig. 5c). The horizontal seismic variance time-slice depicts discontinuities caused by large listric faults and fractures within the sediments of the Late Maastrichtian (green overlay) and listric faults in the non-fractured Paleocene sediment wedges (orange overlay). The TWT horizon slice of paleo-pockmark horizon E-1 is outlined in red. Note the higher relief and density of paleo-pockmarks on horizon E-1 above the chaotic structure of the Late Campanian/Maastrichtian prograding wedge. The L-Maastrichtian/ Paleocene wedge pinch-out (orange transparency) coincides with the downslope occurrence of pockmarks on horizon E-1.

3.5.3. Geologic process related to the early Eocene fluid flow event

A model explaining the possible formation process of the identified paleo-pockmark field needs to account for both the fluid source and the process that led to a build-up of fluid overpressure and migration paths.

The Miocene-aged mud volcanoes and the present-day seafloor pockmarks in the proximity to the paleo-pockmark field are evidences for recurring pore fluid over-pressures in the slope of the northern Orange Basin. Ben-Avraham et al. (2002) and Viola et al. (2005) showed that large listric faults control the location of the post- mid Miocene mud volcanoes. Thermogenic gas is proposed to have contributed to the overpressure that initiated mud volcanism. Viola et al. (2005) further suggest that the neotectonic activity related to the Miocene margin uplift could be responsible for mud volcano formation. This underlines the important roles of thermogenic gas and deep faults in the "plumbing system" of the northern Orange Basin.

We propose that the early Eocene fluid escape event identified in this work resulted from a geologic process that started in the late Cretaceous and evolved as follows (Figure 3-10):

Late Cretaceous margin uplift and progradation:

The Santonian-Campanian margin uplift and tilting led to a destabilization of the slope creating large listric normal faults (Figure 3-10a, b). This initiated a phase of hydrocarbon generation from the Aptian source rocks (Paton et al., 2008; Kuhlmann et al., 2011). During the late Maastrichtian a fine-grained progradational sequence was deposited onto the slope (Figure 3-10c) and then overlain by a latest Maastrichtian/Paleocene clay-rich sedimentary wedge (Figure 3-10d). Their cumulative thickness at the paleo-slope can reach up to 1100 ms TWT (approx. 950 m). This sediment wedge is present only in the northern Orange Basin, because the main sediment supply during this time period was located at the present-day Orange River mouth (Dingle and Hendey, 1984).

Rapid burial and disequilibrium compaction:

The rapid deposition likely led to disequilibrium compaction of the clay-rich sediments and built-up of pore overpressure. Additionally, the rapid burial caused a Maastrichtian/early Cenozoic phase of source rock maturation in the paleo-pockmarked area. This assumption is supported by petroleum system modeling results (Kuhlmann et al., 2011). Therefore, thermogenic hydrocarbons were present at that time and would have played a decisive role in generating additional overpressure.

Early Eocene pockmark formation:

McMillan (2003) reports an Eocene margin uplift event and basinward subsidence of the continental shelf in the northern Orange Basin, where early Paleocene/Eocene igneous intrusions have been identified. This is supported by apatite (U-Th)/He measurements of deep inland boreholes (Dobson et al., 2011) which suggest a middle Eocene denudation onshore southwestern Africa. Together with the reported volcanism, these are clear

indications of tectonic activity during the time of paleo-pockmark formation. Hence, such basin-scale geologic processes can thus provide an external trigger for fluid flow from overpressured intervals during the early Eocene. Pore fluids and thermogenic gas then migrated up-dip below the Paleocene wedge and upward along the listric-fault planes creating pockmarks parallel to the fault strike.

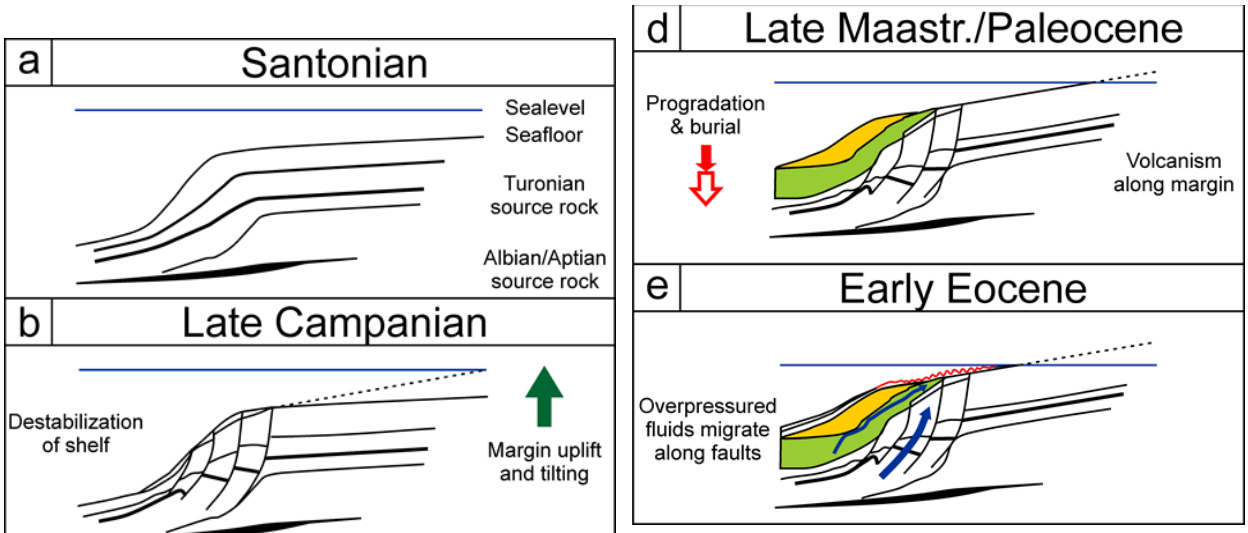

Figure 3-10: Conceptual model of the events leading to early Eocene fluid escape. (a) Progradation of Late Cretaceous sediments, (b) Late Cretaceous uplift, slope destabilization and gravity faulting of the shelf edge, (c) erosion on the shelf, rapid deposition and burial of Prograding slope wedge, (d) Paleocene wedge deposition, disequilibrium compaction of fine-grained sediments, and maturation of source rock generate overpressure, (e) overpressure leads to upward migration of pore fluids and gas below the Paleocene wedge and through the faulted shelf creating pockmarks along the shelf.

3.6. Conclusions

Our analysis of 3D and 2D seismic reflection data sets revealed the presence of a distinct early Eocene seismic horizon displaying circular and elongated depressions covering 2800 km^2 along the slope in the Orange Basin, on the southwest African margin. We interpret these depressions as a paleo-pockmark field produced by the release of pore fluids and thermogenic gas. They appear both as single pockmarks and pockmark trains aligned predominantly NNE-SSW. The pockmark trains occur at the paleo-shelf break and follow the Eocene slope's dip direction. We show that the location of the pockmarks is controlled by the underlying listric faults system of the Eocene paleo-slope.

The spatial and temporal occurrence of these paleo-pockmarks is associated to two episodes of fast sedimentation during late Maastrichtian to Paleocene in the northern Orange Basin, comprising a late Maastrichtian progradational slope wedge derived from fine-grained shelf-eroded material and a latest Maastrichtian to Paleocene aged sediment wedge. We present a model where pore fluid overpressure was generated by compaction disequilibrium of late Maastrichtian sediments, , further enhanced by source rock maturation and thermogenic gas expulsion resulting from rapid slope sedimentation during late Maastrichtian to Paleocene. The Paleocene-Eocene transition is known for its series of hyperthermal events characterized by excursions of the carbon isotope curve. The early Eocene widespread event of fluid and thermogenic gas escape identified in this work can be an example of the type of carbon-release processes occurring in hydrocarbon-prone sedimentary basins during this time.

The early Eocene paleo-pockmark field, the Miocene-aged mud volcanoes, and the present-day seafloor pockmarks are evidence for reoccurring pore fluid over-pressures in the slope of the northern Orange Basin and should be considered as a potential geohazard.

Acknowledgements

This research is part of the PhD project of A. Hartwig conducted at the Helmholtz Centre Potsdam German Research Centre for Geoscience (GFZ). We gratefully acknowledge funding by Forest Exploration International (South Africa) (PTY) Ltd. We thank Forest Exploration International (South Africa) (PTY) (Ltd), the Petroleum Oil and Gas Corporation of South Africa (Pty) (Ltd), Anschutz Overseas South Africa (Pty) (Ltd), and the Petroleum Agency SA for providing the data and for permission to publish our results. Z. Anka's position as Head of a Helmholtz-University Young Investigator Group is funded by the Helmholtz Association’s Initiative and Networking Fund. We are thankful for the comments and suggestions from Tony L. Albrecht, John P. Klein, editors Aurelian Gay and Christian Berndt, and two anonymous reviewers who helped to improve the manuscript.

4. Constraining Petroleum Generation and Migration in the Orange Basin, South Africa: A 3D basin modeling study

The contents of this chapter were prepared for submission to the international peer-reviewed journal “AAPG Bulletin” as follows:

Hartwig, A., Anka, Z., di Primio, R., 2014, Constraining Petroleum Generation and Migration in the Orange Basin, South Africa: A 3D basin modeling study. AAPG Bulletin, submitted

Abstract

A 3D basin model of the Orange Basin, offshore southwestern Africa, was constructed based on a large 2D seismic reflection industry dataset calibrated to well data. Our calibrated heat flow and erosion histories suggest a maximum heatflow of 96 mW/m^2 during early Cretaceous rifting and an exponential decrease to an average value of 52 mW/m^2 for the present day. Two periods of increased heatflow, by up to 8 mW/m^2, were identified during late Cretaceous/Paleocene and Mio-Pliocene in areas where the continental crust was affected by renewed lithospheric stretching, uplift and erosion.

The main phase of primary generation from Cretaceous source rocks in the basin occurred during mid. Cretaceous and late Cretaceous/Paleocene burial. A second phase of petroleum generation mainly driven by heatflow lasted from the latest Cretaceous/Paleocene until the end of the Miocene-Pliocene uplift.

The present-day active kitchen areas are located exclusively in the Cenozoic depocenters along the slope. In the northern Orange Basin, the lower Cretaceous source rocks are currently within the gas window, while Aptian and Cenomanian/Turonian (C/T) source rocks are within the oil window. In the southern Orange Basin all the Cretaceous source rocks are currently in the oil window.

The migration model confirms that the main carriers of the Orange Basin are Barremian to lower Aptian sandstones of the transitional sequence and Albian-to-Cenomanian fluvial sandstones of the early drift sequence. Petroleum accumulations are dominated by gas and condensate.

The greatest risk for reproducing Ibhubesi accumulations in the 3D model is the seal. Albian fluvial channels were only filled when their trapping efficiency was improved by introducing an Albian claystone seal into the model. Without this seal, smaller accumulations were exclusively formed in Cenomanian channels below the C/T source rock. Drainage area analysis of the petroleum accumulations in the Ibhubesi area indicates that stratigraphic traps were filled by early Cenozoic times, and that hydrocarbon losses due to spilling or leakage through the seal are greatest during times of margin uplift and erosion.

Keywords: basin modeling, Ibhubesi, South Atlantic, petroleum system, Kudu, gas condensate

4.1. Introduction

The Orange Basin (OB) is located offshore southwestern Africa (Fig. 1). On the shelf, the basin contains a thick Cretaceous rift-drift sequence and a thin Cenozoic cover, which develops into a series of prograding wedges at the shelf break (Weigelt and Uenzelmann-Neben, 2004; Paton et al., 2008). Up to date, 38 exploration wells were drilled and led to the discovery of the Kudu and Ibhubesi gas fields proving the existence of a Deep Gas and an Albian Gas play, respectively (Petroleum Agency SA, 2012). The Deep Gas Play consists of gas generated from Barremian-to-Aptian-aged source rocks that are stratigraphically trapped in Barremian-aged aeolian sandstones, with proven reserves of 1.38 trillion cubic feet (tcf) in the Kudu field (~ 39.1 billion m^3; Tullow Oil, 2007). The Albian Gas Play has Aptian-to-Albian-sourced gas and condensate which is trapped in Albian and Cenomanian-aged fluvial channel sandstones. Well tests in the Ibhubesi field showed that individual compartments contain between 28 - 520 billion cubic feet (bcf) of gas and condensate (~0.79 - 14.73 billion m^3) with total gas reserves of 1.15 tcf (32.56 billion m^3, Berge et al., 2002). Further potential for hydrocarbon accumulations exists in syn-rift grabens and Cretaceous turbidites in the deep water Orange Basin (Petroleum Agency SA, 2012).

Evidence of recent and present-day fluid and gas leakage processes, such as "sniffer" anomalies near the seafloor (Jungslager, 1999), seabed pockmarks and seismic chimneys (Ben-Avraham et al., 2002; Paton et al, 2007; Boyd et al., 2011; Kuhlmann et al., 2010), and also mud diapirs (Ben-Avraham et al., 2002; Viola, et al. 2005) have been identified on 2D seismic surveys in the Orange Basin. Pockmarks above the Ibhubesi field and in the slope of the Orange Basin (Hartwig et al., 2012a), as well as the frequent gas shows encountered during drilling in lower Cretaceous sediments suggest a recent phase of hydrocarbon generation and migration (Fig. 1). Nonetheless, the locations of the recent and/or active oil and gas kitchen as well as the hydrocarbon migration pathways remain unconstrained due to the limited amount of data that is available for the Cenozoic evolution of the basin.

Previous modeling studies by Davies and van der Spuy (1992, 1D model,) of the Kudu wells, and of the southern Orange Basin by Paton et al. (2007, 2D model), Boyd et al. (2011, 2D model), and Kuhlmann et al. (2011, 3D petroleum system model,) address the timing of petroleum maturation and generation. All these studies indicate that the main phase of hydrocarbon generation and migration occurred during the late Cretaceous, which may have continued into the early Cenozoic in the Kudu area (Davies and Van der Spuy, 1992). Paton et al. (2007) and Kuhlmann et al. (2011) further proposed active petroleum generation in the Cenozoic depocenter of the deepwater southern Orange Basin. Kuhlmann et al. (2011) suggest long-distance migration from the present-day kitchen in the deepwater areas to explain hydrocarbon leakage sites in the near-shore basin.

The 3D basin model presented in this contribution was developed not only to unify earlier modeling studies (e.g. Paton et al. 2007, Kuhlmann et al., 2011), but also to include more recent age constraints for the Cenozoic sequence (e.g. Weigelt and Uenzelmann-Neben, 2004; Hartwig et al., 2012a) and results from a 3D crustal modeling study (Hirsch et al., 2010) in order to refine the basin's burial and thermal history. New aspects of our study

include the larger extension of the 3D basin model, which covers the entire South African Orange Basin from Saldanha Bay in the south to the Namibian border in the north (Figure 4-1) and includes the proximal rift-grabens and the distal Cenozoic deepwater depocenters. Furthermore, new compositional kinetic models, based on equivalents from DSDP site 361 in the Cape Basin from Hartwig et al., (2012b), were used to simulate source rock maturation and petroleum generation for the Cretaceous source rocks. The simulation of 3D hydrocarbon migration dynamics and filling history of the Ibhubesi area was refined using fault planes and conceptual channel maps derived from the seismic-data interpretation and the work of Brown et al. (1995).

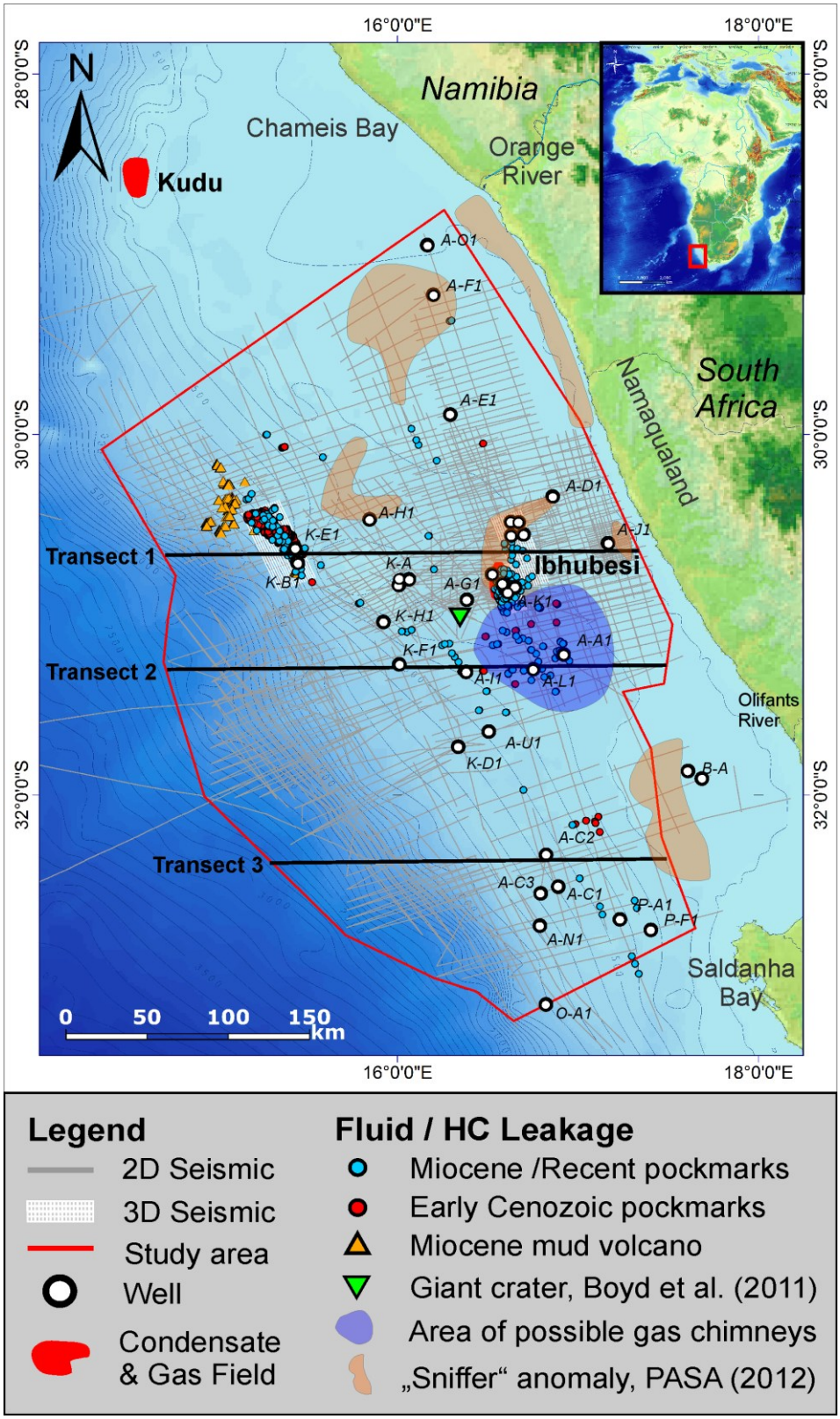

Figure 4-1: Location of the Orange Basin offshore South Africa with a general overview of the study area, the seismic reflection dataset analyzed, and the 3D basin model coverage, superimposed on bathymetry. Locations of fluid and hydrocarbon leakage indicators are shown according to Boyd et al. (2011), Petroleum Agency SA (2012), and Hartwig et al. (2012a).

4.2. Geologic setting and petroleum system elements

The Orange Basin is located on the southwest African continental passive margin. The basin fill consists of more than 8 km thick synrift and drift sequences related to the opening of the South Atlantic, which started in the late Jurassic (Gerrard and Smith 1982) (Figure 4-2). The margin evolution, basin structure, and sedimentary history are documented in previous works for both the Cretaceous (e.g. McMillan (2003), Séranne and Anka (2005), Paton et al. (2008), Hirsch et al. (2010), de Vera et al. (2010), Kuhlmann et al, (2010) and references therein) and the Cenozoic successions (Weigelt and Uenzelmann-Neben (2004), Wigley and Compton (2006)).

Rifting was initiated during the middle to late Jurassic, at about 160 Ma. It resulted in the formation of north-northwest trending rift and half-grabens on continental crust subparallel to the present-day southwest African coast, such as the A-J half graben (Gerrard and Smith 1982, Muntingh 1993; Broad et al., 2006). Syn-rift sediments are at least of Hauterivian age and were dated in the A-J half graben, but deeper sediments may be as old as Jurassic (see Fig. 1; Petroleum Agency SA, 2012). They consist of continental sandstones intercalated with lacustrine shales, conglomerates, and volcaniclastics (Broad et al., 2006). The initial opening of the South Atlantic and emplacement of oceanic crust began in the early Cretaceous (Blaich et al., 2009; Franke et al., 2010) and was accompanied by extensive volcanism forming a transitional crust with a thick seaward dipping reflector (SDR) wedge (Gladczenko et al., 1998). The unusually wide (up to 200 km) transitional crust underneath the Orange Basin depocenter displays gently westward dipping seismic reflectors. They are interpreted to consist of rapidly emplaced subaerial flood basalts (Bauer et al., 2000) that are intercalated with continental clastics at the SDR/flood basalt pinch-out along the continental crust (Gerrard and Smith, 1982; Dingle et al., 1983). The continent-ocean boundary and onset of true oceanic crust is located west of the SDRs and roughly coincides with the present-day base of slope.

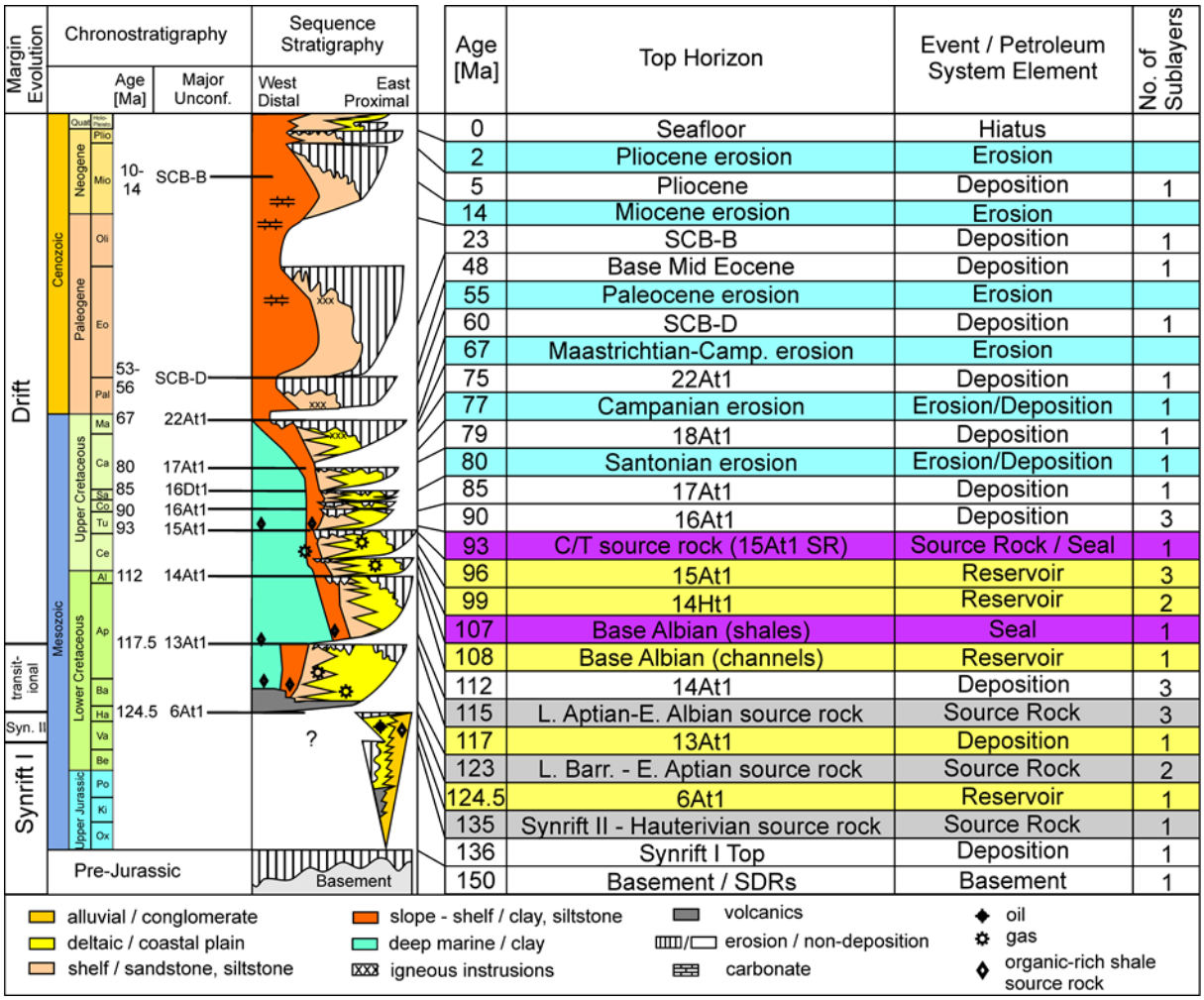

Figure 4-2: General chronostratigraphy of the Orange Basin (left, modified from Hartwig et al., 2012a) and horizons defined in the 3D model input (right). Note that horizons, affected by erosion have modified top horizon ages due to the modeling setup of the modeling software. See text for details.

The rift sequence is truncated by the break-up unconformity 6At1 (Muntingh and Brown, 1993) of late Hauterivian to early Barremian age (McMillan, 2003) (Figure 4-2). Up to 2000 m of rift-to-drift transitional sequence, consisting of fluvial and marine sand- and siltstones, were deposited on a ramp-like margin during Barremian to early Aptian times. This sequence contains early Aptian aged organic-rich black shales from the first marine transgression.

A middle Aptian-aged unconformity 13At1 marks the beginning of open oceanic conditions. It is overlain by transgressive organic-rich shales that were deposited under anoxic conditions (Herbin et al. 1987; Jungslager, 1999; van der Spuy, 2003). The mid-Albian to Cenomanian deposits consist of deltaic and fluvio-marine sediments with a cumulative thickness exceeding 3500 m (Gerrard and Smith, 1982; McMillan, 2003). At the top of this sequence, organic-rich shales of a marine condensed section have been reported (Aldrich et al. 2003; McMillan, 2003) and are associated with a Cenomanian/Turonian hiatus in the Orange Basin (15At1). This interval is overlain by an aggradational sequence of Coniacian to late Santonian/early Campanian age (Muntingh, 1993; McMillan, 2003; Paton et al., 2008). Late Cretaceous margin uplift, westward tilting (Gallagher, 1999; McMillan, 2003; Kounov et al., 2009) and subsequent erosion of the inner shelf (Wigley and Compton, 2006) led to the

deposition of Campanian-Maastrichtian progradational sequences onto an already unstable shelf (Broad et al., 2006). This resulted in intense normal faulting of the Cenomanian-Campanian succession and the formation of growth- and roll-over structures along the northern slope of the basin (Gerrard and Smith, 1982; Brown et al., 1995, de Vera et al., 2010). These structures are not seen in the southern Orange Basin (Paton et al., 2008). The end of Cretaceous sedimentation is marked by a late Maastrichtian - early Paleocene unconformity that truncates Albian and Cenomanian sediments on the inner shelf and Campanian to Maastrichtian sediments on the middle to outer shelf (Gerrard and Smith 1982, Paton et al., 2008). Additionally, there is substantial evidence for late Cretaceous/early Cenozoic igneous activity on- and offshore the southwestern African margin (Phillips et al., 2000; Verwoerd and de Beer, 2006; Moore et al., 2008). Ages of igneous intrusions along the Namaqualand coast and the southern Cape range from 77 to 59 Ma (Phillips et al., 2000; Verwoerd and de Beer, 2006; Moore et al., 2008) showing a trend of progressively younger volcanic activity towards the west coast (Dingle et al., 1983; Phillips et al., 2000). Moore et al. (2008) propose a second minor episode of Eocene-Oligocene alkaline volcanism for the Klinghardt province (30- 40 Ma) and Chameis Bay pipes (30 and 50 Ma) offshore southern Namibia (see Figure 4-1).

In general, Cenozoic sediments form a thin cover (50 to 250 m) on the proximal domains of the continental shelf and an aggradational wedge along the steep slope, with thicknesses of up to 1000 m and 1700 m in the northern and southern Orange Basin, respectively. During the Paleogene the main sediment supply entered the Orange Basin in the vicinity of the present-day Olifants River (Dingle and Hendey, 1984), forming an up to 1500 m thick prograding sequence affected by growth-faults and toe-thrusts along the southern slope (Séranne and Anka, 2005; Paton et al., 2008; de Vera et al., 2010).

The Paleogene – Neogene transition is marked by a regional erosional unconformity with characteristic submarine slides and slump scars (e.g.: unconformity SCB-B of Weigelt and Uenzelmann-Neben, 2004; Wigley and Compton, 2006). This event coincides with a phase of mid. Miocene tectonic uplift (Dingle et al., 1983; Partridge and Maud, 2000; Séranne and Anka, 2005). The erosion event removed most of the Paleogene and early Neogene deposits onshore the west coast (Partridge and Maud, 2000). The bulk of the Neogene Orange River discharge entered the basin in the area of the present-day Orange River mouth (de Wit, 1999; Dingle and Hendey, 1984). Neogene deposits consist of shallow marine (Dingle, 1973; Partridge and Maud, 2000) biogenic sediments (e.g. Bolli et al., 1978a; Dingle et al., 1983; Wigley and Compton, 2006). Numerous large Pliocene slumps have been identified along the continental slope and may have been caused be renewed uplift and erosion during the Pliocene (Partridge et al., 2006; Dingle et al., 1983). Offshore Pliocene deposits form a scattered, very thin cover and are truncated by several erosional unconformities. Larger sediment accumulations are restricted to small deltas of the Orange and Olifants rivers (Dingle et al., 1983; Wigley and Compton, 2006).

4.2.1. Source rocks

There are three source rock intervals within the Cretaceous synrift and drift sediments of the Orange Basin:

An Hauterivian oil-prone lacustrine shale found in the synrift sediments of the isolated A-J Graben (Jungslager, 1999; Petroleum Agency SA, 2012). Jungslager (1999) suggests that similar organic-rich shale intervals may be present in other rift grabens along the continental margin.

Barremian to early Albian aged black shales, which represent the main source rock interval, deposited in anoxic marine environments of the nascent South Atlantic (van der Spuy, 2003; Hartwig et al., 2012b and references therein). Anoxia was most severe during the first marine incursion lasting from Barremian to early Aptian times. This transitional sequence contains oil and gas prone organic-rich marine shales, proven to exist in the Kudu area, the southern distal Orange Basin, and at DSDP site 361 in the Cape Basin (Davies and van der Spuy, 1990; McMillan, 2003; van der Spuy, 2003). During the late Aptian and early Albian bottom water ventilation increased due to the widening of the South Atlantic. The early drift deposits contain intercalated wet-gas and gas-prone marine shales known from exploration wells and DSDP site 361 (Adekola et al., 2012; Akinlua et al., 2010; Hartwig et al., 2012b; van der Spuy, 2003 and references therein).

A Cenomanian/Turonian-aged marine condensed section, which contains oil- and gas-prone organic-rich shales (Aldrich et al, 2003; Adekola et al., 2012). Similar time-equivalent source rocks deposited during the Oceanic Anoxic Event (OAE) are known to occur throughout the South Atlantic (Herbin et al., 1987; Bray et al., 1998; Burwood, 1999; Hartwig et al. 2012b)

4.2.2. Reservoir and seal rocks

Continental sandstones of the synrift sequence provide potential reservoirs for structural and stratigraphic traps in the rift grabens. In the A-J1 well, oil shows were encountered in sandstones interbedded with Hauterivian-aged lacustrine source rocks (Jungslager, 1999).

Aeolian sandstones of the transitional phase, such as the Barremian sandstones of the Kudu gas field, may occur regionally in the northern Orange Basin (van der Spuy, 2003; Petroleum Agency SA, 2012). In the Kudu field, they form a stratigraphic trap at the featheredge of the SDR sequence, consisting of medium-grained aeolian and fine- to medium- grained fluvial sandstones intercalated with basalts and volcaniclastics (Wickens and McLachlan, 1990).

The Albian and Cenomanian succession contains extensive (up to 1500m thick) fluvio-deltaic sandstones and incised-valley fill sandstones (McMillan, 2003), which account for the majority of gas shows in exploration wells located in the Cretaceous depocenter (such as the A-F, A-G, A-K wells, see Figure 4-1: PASA, 2012; Jungslager, 1999), although the sandstone reservoir quality is often reduced by silica and chlorite cementation (Fadipe et al., 2011). Potential traps are stratigraphic with low relief and sometimes fault-bounded. Up to date, the best reservoir properties and gas flow rates are found in Middle Albian to Cenomanian aged fluvial channel sandstones of the Ibhubesi gas/condensate field (Jungslager, 1999; Petroleum Agency SA, 2012).

Further reservoir potential may exist in sand-rich deepwater turbidite channel/lobe deposits of the Upper Cretaceous succession, either in the form of stratigraphic or structural traps in the extensional growth-fault and compressional toe-thrust domain of the slope (Jungslager, 1999).
Regional sealing rocks are generally Lower and Upper Cretaceous transgressive shales and a thick claystone sequence of middle Turonian to late Coniacian age (see Figure 4-2).

4.3. 3D Model input and calibration

4.3.1. Depth maps

The 3D basin model comprises the offshore Orange Basin in water depths between 100-2850 m from Alexander Bay and the Namibian border in the north to Saldanha Bay in the south and has a surface area of 95.600 km^2 (Figure 4-1). The modeling software used for this study is the commercially available PetroMod 3D v.2011.1.1 package (Schlumberger).
The model layers are defined by 17 depths maps with a grid resolution of 500 x 500 m derived from the seismic interpretation of an extensive 2D exploration seismic-reflection dataset. The seismic horizons were interpreted according to the sequence stratigraphic framework of Muntingh and Brown (1993) and Brown et al. (1995) for the late Jurassic and Cretaceous basin fill and according to Weigelt and Uenzelmann-Neben (2004) and Hartwig et al. (2012a) for the Cenozoic (Figure 4-2). The model's lower boundary is defined by the rifted continental crust in the east and a transitional crust consisting of subaerial flood basalts and SDRs to the west. The ages of horizons, erosional unconformities, and depositional hiati are based on the biostratigraphy for the Orange Basin from McMillan (2003), which is in better agreement with the International Stratigraphic Chart of Ogg et al. (2008) than the chronostratigraphic ages provided by Broad et al. (2006). Each layer, as defined by the horizons, represents one continuous depositional event in the model. Several layers were split into sublayers to incorporate the variability of source rock intervals and the vertical lithologic changes within depositional sequences (Figure 4-3, Transect 1).

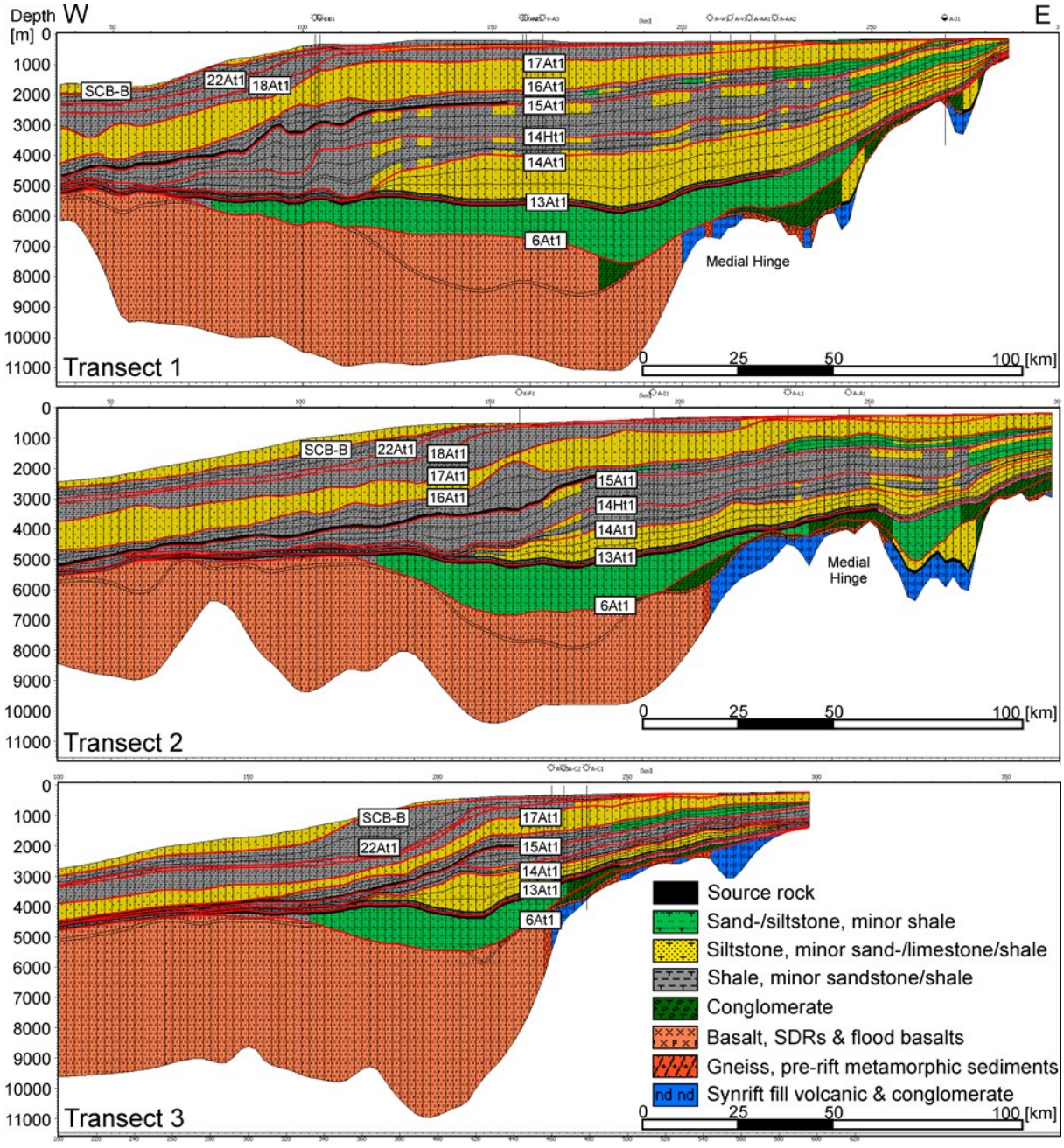

Figure 4-3: E-W transects and projected wells extracted from the 3D basin model depicting the present-day margin geometry and a simplified view of the layers assigned lithologies (for location see Fig. 1). Note that the thickness of the Cretaceous sequences increases from south to north, while the Cenozoic sequences' thickness decreases in the same direction.

4.3.2. Faults

Three fault families were identified on the seismic profiles:

1) Listric extensional faults: along the shelf edge which offset the upper Cretaceous sequences with a décollement surface within the upper Albian shales in the north and upper Cretaceous and lower Cenozoic sequences in the south.

2) Compressional faults: in the lower slope of the northern Orange Basin affecting upper Cretaceous sequences.

3) Syn-rift graben-bounding normal faults: along the eastern basin margin that offset the Cretaceous sequences.

The three fault families were incorporated into the model as gridded faults planes. They are based on the fault stick interpretation of 38 faults that represent the regional trends and are traceable over tens of kilometers on 2D and 3D seismic data. Fault kinematics was not modeled, as they were rather modeled as either open or closed permeability paths, in order to determine their role as potential fluid conduits for vertical migration or as trapping sites for hydrocarbons. Hence, faults were considered to be open during time periods of active fault movement identified from the seismic data (i.e. the late Cretaceous shelf collapse and Neogene reactivation). Conversely, they were defined as closed during periods of tectonic quiescence (i.e. no net movement of faults identified on seismic). This latter scenario will be addressed as the "initial model" in the discussion. For sensitivity analysis two additional models, with either open or closed faults for the entire simulation time span, were simulated and are discussed as "open scenario" and "closed scenario", respectively.

4.3.3. Lithofacies definition

Lithologies for each model layer were assigned using facies maps. The lithologic properties, such as density, porosity, permeability, heat conductivity, and radiogenic heat production are predefined based on the extensive lithology database of the used software. The sequences lateral facies variations are based on the lithologic descriptions from well reports and the literature (Dingle et al., 1983; Gerrard and Smith, 1982; McMillan, 2003; Weigelt and Uenzelmann-Neben, 2004; Wigley and Compton, 2006) (Figure 4-3). Four facies maps including conceptual channels were constructed for the mid. and upper Albian, Cenomanian, and Turonian layers in order to test their potential as carrier beds and stratigraphic traps (Figure 4-4). The maps of the Albian/ lower Cenomanian are based on the location of large incised valleys from the seismic interpretation, which have been in part reported also by Brown et al. (1995). Layers with varying siltstone, sandstone, and shale content separate the channel sublayers from each other.

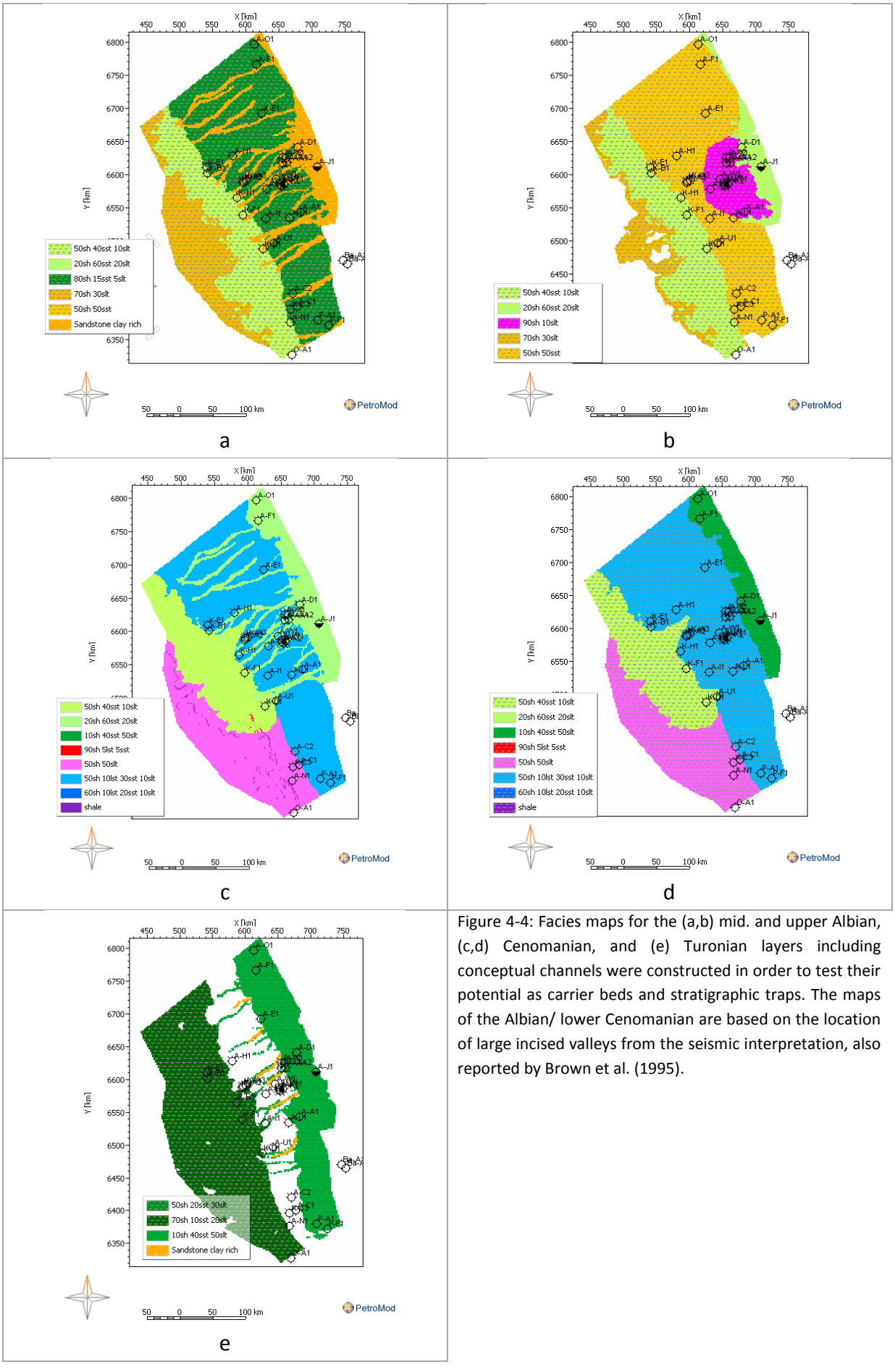

Figure 4-4: Facies maps for the (a,b) mid. and upper Albian, (c,d) Cenomanian, and (e) Turonian layers including conceptual channels were constructed in order to test their potential as carrier beds and stratigraphic traps. The maps of the Albian/ lower Cenomanian are based on the location of large incised valleys from the seismic interpretation, also reported by Brown et al. (1995).

4.3.4. Source rock definition and petroleum generation kinetics

The source rocks' thickness, initial Total Organic Carbon (TOC) and Hydrogen Index (HI) were defined based on the data from Adekola et al. (2012) Davies and van der Spuy (1990) Jungslager (1999) and van der Spuy (2003). A summary of the source rock definitions is given in Table 4-1. Petroleum generation kinetics were assigned from compositional kinetic models of Hartwig et al. (2012b) based on immature Aptian/Albian, and Cenomanian/ Turonian source rock samples from DSDP site 361. Bulk kinetic models were used during the thermal model calibration. Hydrocarbon migration was modeled using a four-component kinetic model with source rock tracking and secondary cracking (restricted to methane generation). The four components are: (1) C_1 (dry gas), (2) C_2-C_5 (wet gas), (3) C_6-C_{14} (light oil), and (4) C_{15}+ (black oil). Thickness maps of the source rock intervals were generated according to the trend given by well intersections and implemented as individual layers parallel to the top horizon of the corresponding sequence.

Table 4-1: Source rock description

Source rock	TOC [%]	HI [mg/g]	Kergogen Type	Max. Thickness [m]	Kinetic model
Upper Hauterivian lacustrine synrift II	10	750	Type I	100	Alaskan Tasmanite Type I (Di Primio and Horsfield, 2006)
Barremian - early Aptian marine/deltaic	8	550	Type II/III	100	Late Aptian Type II/III DSDP 361 no. 15 (Hartwig et al., 2012b)
Late Aptian - early Albian deltaic	8	150	Type III	50	Late Aptian Type III DSDP 361 no. 19 (Hartwig et al., 2012b)
Late Aptian - early Albian marine	8	550	Type II	50	Early Albian Type II DSDP 361 no. 10 (Hartwig et al., 2012b)
Cenomanian/Turonian Type II	5	200	Type II	90	Turonian Type II DSDP 530A no. 1 (Hartwig et al., 2012b)
Cenomanian/Turonian Type III/IV	3	100	Type III/IV	90	Tertiary Coal (Di Primio and Horsfield, 2006)

4.3.4.1. Upper Hauterivian lacustrine synrift source rock (Synrift II)

The synrift source rock of the A-J1 half-graben has been reported as a 60 m thick lacustrine shale with a TOC content of 10% and a Hydrogen Index (HI) of 600 mg HC/g TOC (Jungslager, 1999). A SOEKOR report describes organic matter as a mixture of algal Type I and detrital Type III kerogen. The penetrated source rock interval is 60 to 140 m thick, with TOC up to 12% and HIs varying between 500 and 1150 mg HC/g TOC. The extent and occurrence of syn-rift source rocks in other grabens is largely unconstrained. The upper Hauterivian organic-

rich shales of the A-J well correspond to high amplitude reflections on the seismic. Such reflectors are also imaged in other grabens and may be distinguished from similarly-imaged igneous material by means of magnetic surveys (Jungslager, 1999). Where drilled, the igneous graben fills have a relatively higher magnetic signature than the A-J half-graben. This assumption is supported by the existence of a synrift lacustrine source rock in the graben structure targeted by the A-F well (pers. commun. D. v.d. Spuy), that is also characterized by a low magnetic anomaly. Based on this observation, the hypothetical occurrence of synrift source rocks was used to construct facies maps of this interval (exemplarily shown Figure 4-5a). This source rock was modeled with a maximum thickness of 100 m, 10% TOC, HI of 750 mg HC/g TOC and the compositional kinetic model of a Type I kerogen from di Primio and Horsfield (2006).

4.3.4.2. Barremian - lower Aptian marine/deltaic source rock

This source rock interval has only been encountered in the distal wells of the southern (O-A1 and A-C wells) and northern (Kudu wells) Orange Basin (Davies and van der Spuy, 1990; Jungslager, 1999; van der Spuy, 2003) where they contain predominately wet-gas prone organic matter with thin intercalations of oil-prone organic matter (Figure 4-5b). Drilled thicknesses are in the range of a few meters up to 40 m in the south and up to 100 m in the Kudu area, with a present-day TOC up to 4% and maximum HI of 200 mg HC/g TOC at vitrinite reflectance ranging from 0.9 - 2.0 % R_O (Davies and van der Spuy, 1990; van der Spuy, 2003; Adekola et al., 2012). Hence, the original TOC might have been as high as 8% (van der Spuy, 2003). Therefore, the source rock was modeled with 8% TOC and a HI = 550 mg HC/g TOC, using the kinetic model based on late Aptian Type II/III kerogen from DSDP site 361 measured by Hartwig et al. (2012b).

4.3.4.3. Upper Aptian - lower Albian marine/deltaic source rock

The upper Aptian/Albian organic-rich black shales have been sampled or identified using gamma-ray logs throughout the distal part of the Orange Basin. Their cumulative thickness generally varies between 40 and 90 m, but can reach up to 150 m (van der Spuy, 2003). They contain predominately gas-prone Type III kerogen with a present-day TOC of 2-3% and HI < 200 mg HC/g TOC (Adekola et al. 2012). At DSDP site 361, the upper Aptian and lower Albian succession consists of 350 m of alternating siltstones and organic-rich black shales. The black shales have an estimated cumulative thickness of up to 200 m. Hartwig et al. (2012b) report that the majority of the black shale intervals contain gas-prone Type III kerogen with up to 5% TOC and HI < 150 mg HC/g TOC. From the recovered cores in that site, only 40% of the black shales contain oil-prone Type II or Type II/III kerogen with up to 8% TOC and an HI ranging from 300 to 550 mg HC/ g TOC. The upper Aptian- lower Albian source rock interval was subdivided into three sublayers with a maximal cumulative thickness of 150 m. The kinetic model of an Aptian Type III kerogen from DSDP 361 with 8% TOC and an HI of 150 mg HC/g TOC was assigned to the basal sublayer, which is overlain by a siltstone sublayer (Figure 4-5c and d). The uppermost third source rock sublayer was assigned a mixed Type II/III

kerogen kinetic model from DSDP 361 with 8% TOC and a HI of 550 mg HC/ g TOC in order to account for the presence of higher-quality marine organic matter in some black -shale horizons (Hartwig et al., 2012b).

4.3.4.4. Cenomanian/Turonian (C/T) marine condensed section

Several exploration wells encountered terrestrial organic-matter enriched claystones in the Cenomanian/Turonian marine condensed section with TOC contents generally below 2%. At DSDP site 361 the Turonian section contains a very poor Type III/IV kerogen as well (Hartwig et al., 2012b). However, in the A-F well in the northern Orange Basin the overall source rock quality seems to improve as it contains up to 5% TOC with HIs between 100 and 470 mg HC/g TOC, indicating oil-prone Type II kerogen (Adekola et al., 2012). Aldrich et al. (2003) and van der Spuy (2005) propose that a similar organic-matter quality may be expected in the distal Orange Basin (Figure 4-5e). Based on these observations, two different facies were assigned to this source rock: (1) a Type III/IV kerogen with 3% TOC and HI of 100 mg HC/g TOC using the kinetics of a Tertiary Coal from di Primio and Horsfield (2006) for the proximal and southern Orange Basin shelf and (2) a Type II kerogen kinetic model from the Turonian of DSDP site 530A of Hartwig et al. (2012a) with 5% TOC and HI of 200 mg HC/g TOC for the northern shelf and slope.

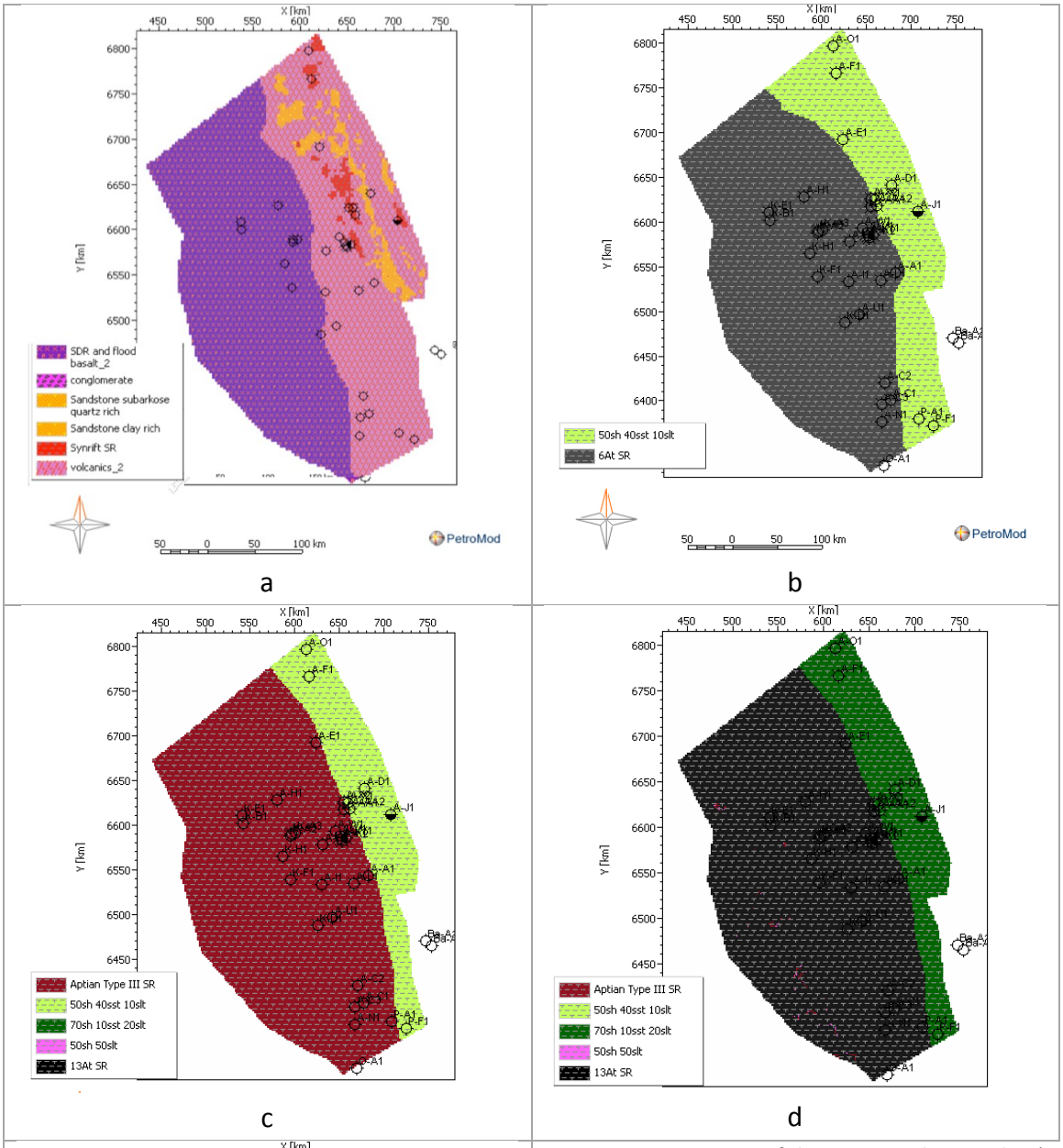

Figure 4-5: Facies maps of the source rock intervals: a) Synrift II layer; b) Barremian Aptian layer; c) Aptian/Albian Type III source rock layer; d) Aptian/Albian and Albian Type II source rock layer; e) Turonian/Cenomanian source rock layer.

4.3.5. Boundary conditions

For thermal modeling the upper and lower boundary conditions are defined by the sediment-water interface temperatures (SWIT) and the basal heatflow (Hantschel and Kauerauf, 2009). The thermal calibration of the model was conducted in several steps. First, a basic paleo heat flow trend based on the thermal model of Hirsch et al. (2010) was assigned (Figure 4-6). This model was in part tested and validated with the 3D basin model of Kuhlmann et al. (2011) for the southern Orange Basin. Erosion magnitudes and maps were constructed (Figure 4-7) based on the seismic interpretation as discussed below. The thermal model was then calibrated against vitrinite reflectance (VR) and corrected borehole temperature data from 28 exploration wells in the study area. In a second and third step, lateral variations in erosion and basal heat flow were included to account for local differences in the VR trends. The local variations were in turn correlated with geologic events reported in the literature.

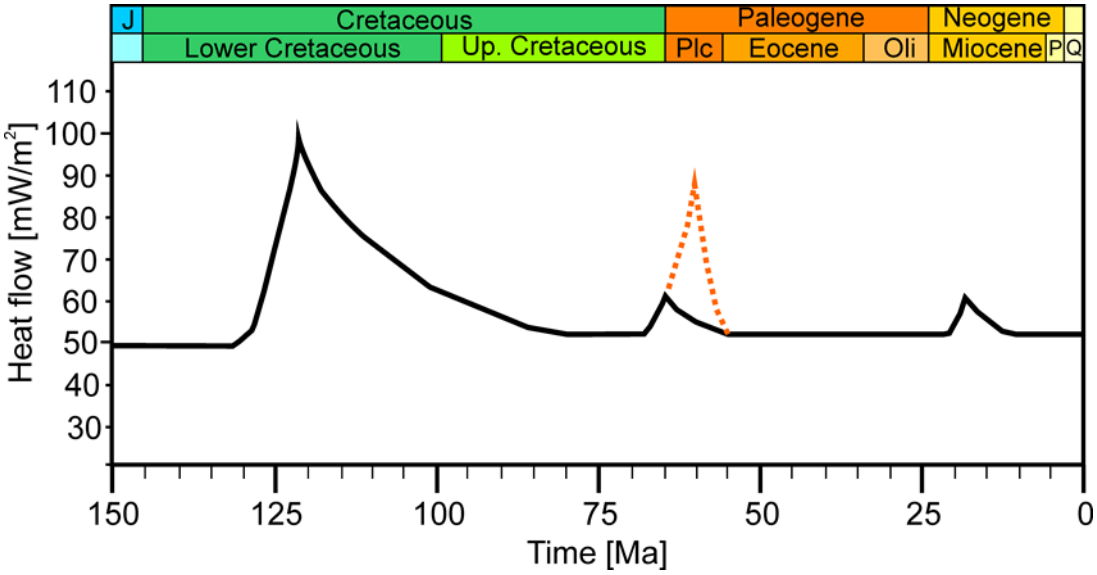

Figure 4-6: Heat flow trend (black line) used in this study based on Hirsch et al. (2010) with a variable early Cenozoic heat flow "spike" (orange dashed line) for the southern study area due to volcanic activity.

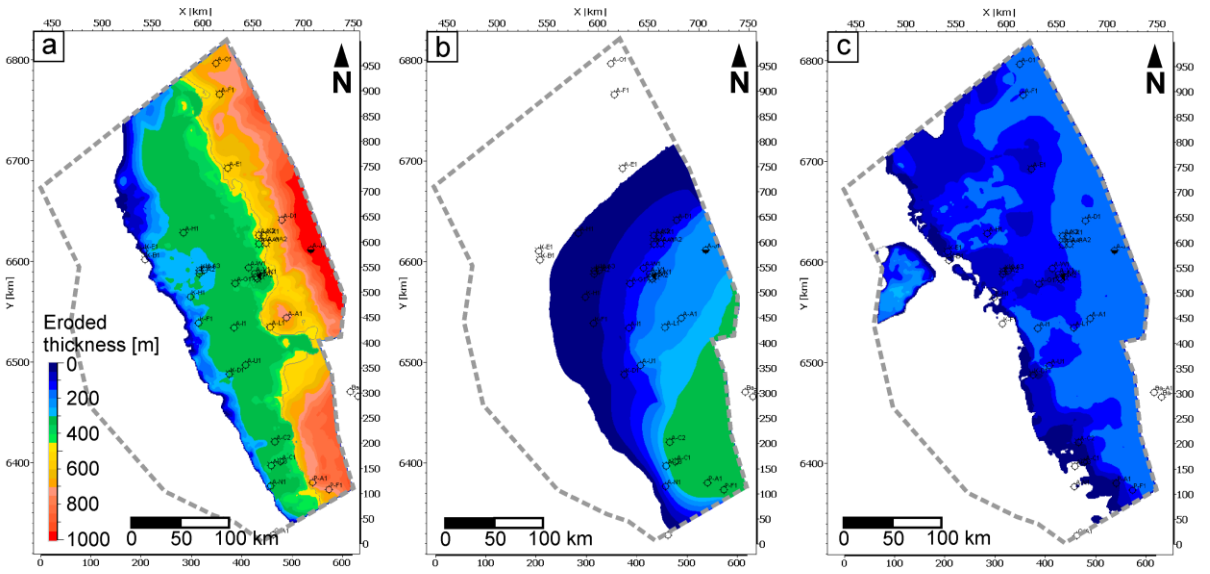

Figure 4-7: Cumulative erosion of a) Late Cretaceous, b) Paleocene, and c) Mio-Pliocene layers. Note the Pliocene-aged slumping event in 4c. The total study area is outlined in grey dashed lines.

4.3.5.1. Sediment-water interface temperature (SWIT) and paleobathymetry

The SWIT was assigned with an automatic tool from the modeling software based on an average surface temperature history by Wygrala (1989). In combination with present-day latitude as input, this tool calculates the SWIT based on the paleo-water depth and the paleo-latitude (Hantschel and Kauerauf, 2009), thus providing a temperature constraint for the model top.

Paleobathymetry maps were reconstructed for each time step from the shelf-break geometry observed in the seismic dataset and the regional sea-level trend reported in the literature (Dingle et al., 1983; McMillan, 2003; Wigley and Compton, 2006). Depositional environments of the southern Orange Basin were taken from Kuhlmann et al. (2011) and Paton et al. (2007) and extrapolated to the north of the basin.

4.3.5.2. Heat flow

The best calibration with present-day surface heat flow values (Goutorbe et al., 2008) and borehole temperatures was achieved when assigning an average present-day basal heat flow of 52 mW/m^2. Hirsch et al. (2010) provide a heat flow scenario that takes into account two departures from the uniform stretching model of McKenzie (1978). One departure is due to the emplacement of a high-velocity body during the synrift phase ("underplating"), which gives maximum heat flow values of 96 mW/m^2 during the rift phase, and is up to 50 mW/m^2 higher than the background value from the uniform stretching model (Hirsch et al., 2010). A second departure represents two phases of crustal thinning that induced the late Cretaceous/Paleocene and Miocene uplift and erosion events. The heat flow during these times was increased slightly by up to 8 mW/m^2 (Figure 4-6). The highest heat flow values were found to correlate with the areas of maximum erosion (Hirsch et al., 2010). The paleo

heat flow maps were then constructed based on a uniform stretching heat flow trend with the above-mentioned deviations (Figure 4-8).

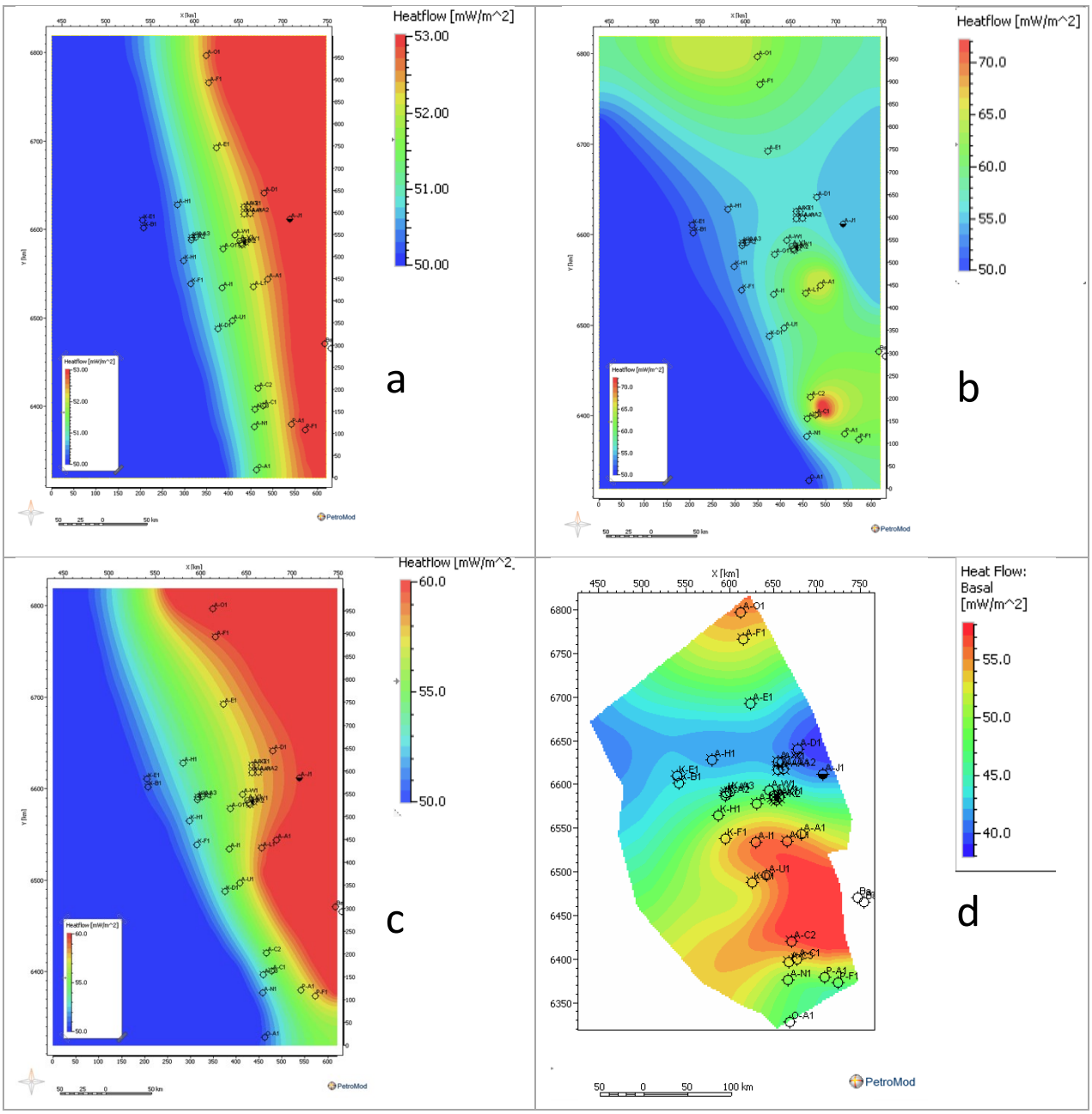

Figure 4-8: Basal heatflow maps for the (a) post-rift Cretaceous uplift, (b) Cenozoic volcanism, (c) Cenozoic uplift events, and (d) present-day.

4.3.6. Erosion

Our seismic interpretation is in agreement with previous studies of the Orange Basin (Brown L. F. et al., 1995; Kuhlmann et al., 2010; Séranne and Anka, 2005), which show two major phases of erosion and/or sediment bypass, most likely related to lithospheric stretching (Hirsch et al., 2010). One of these episodes lasted from the Santonian to Paleocene and the second from the late Oligocene/early Miocene to Pliocene. The late Cretaceous and Miocene erosion phases had a significant impact on the thermal history of

the Orange Basin and therefore need to be included to explain the present-day observed sediment maturity (Hirsch et al., 2010; Kuhlmann et al., 2011). For this study, these two main phases have been sub-divided into several minor events according to their seismic record and are included in the modeling process.

Gallagher and Brown (1999) and Raab et al. (2005) showed that the first phase of rapid denudation onshore South Africa began at about 83 Ma (latest Santonian) and lasted until 60 Ma (early Paleocene). The onset coincides with an observed episode of slope collapse and shelf erosion (unconformity 17At1) followed by progradation of lower Campanian sediments. These events were modeled as the simultaneous erosion of the Santonian-Coniacian and lower Campanian layers on the inner-to-middle shelf and concomitant deposition along the slope from 80 to 75 Ma. Eroded thickness ranges from 0 m on the outer and central shelf to 650 m on the inner shelf along the coast. During the late Maastrichtian to Paleocene (67 – 60 Ma) onshore denudation continued and was accompanied by a regional sea-level fall (Dingle et al., 1983) creating the prominent unconformity 22At1. Eroded thicknesses range from 0 m along the shelf break to 350 m for the greater part of the shelf. Our estimated maximal cumulative erosion of 1000 m during the late Cretaceous (Figure 4-7a) is in very good agreement with erosion magnitudes proposed by Paton et al. (2008) and Kuhlmann et al. (2011). Onshore erosion was significantly higher, Gallagher and Brown (1999) suggests up to 2 km for the Namibian and South African margin, which provided the sediment volumes that constitute the upper Cretaceous progradational sequences (Guillocheau et al., 2012; Rouby et al., 2009; Tinker et al., 2008a).

The reconstructions of Neogene erosional events is less constrained due to the thin Cenozoic sedimentary cover on the shelf (< 250 m), but Cenozoic denudation is assumed to be less significant than the Cretaceous one (Kounov et al., 2009). In order to better constrain our seismic data-derived estimations of eroded thickness, we used present-day heights, above the sea level, of onshore Cenozoic outcrops. Onshore Paleocene/early Eocene outcrops near Buntfeldschuh are up to 160m above sea level and Miocene outcrops occur up to 90 m above present-day sea level as marine terraces along the Namaqualand coast (Dingle et al., 1983; Partridge and Maud, 2000; Roberts et al., 2006). Based on this method, we reconstructed a Miocene (23 - 14 Ma) erosion event of up to 80 m of Paleogene sediments and a Pliocene (5 - 2 Ma) erosion event that removed up to 100 m of pre-Pliocene sediments on the middle and inner shelf. The eroded thickness of the Miocene and Pliocene events (Figure 4-7c) should be considered as minimum estimates as Corbett (1996, their Fig. 11) and Wigley and Compton (2006, their Fig. 1) suggest a minimum original thickness of approximately 200 and 160 m for Oligocene and Miocene sediments, respectively, in the outer shelf of the northern Orange Basin, which are missing on the inner shelf due to erosion. Additionally, cumulative Neogene erosion may have been as high as 540 m on the inner shelf (Hirsch et al., 2010). Finally, a depositional hiatus was assigned during the Quaternary (2 - 0 Ma, Figure 4-2) to reflect the very low sediment input.

4.3.7. Thermal calibration

The above described heat flow and erosion scenarios give a good thermal calibration to present-day borehole temperatures and surface heat flow measurements of the entire Orange Basin, as well as a very good calibration of VR trends for the northern and central basin. The VR curves for southern wells still indicate a higher maturity than those predicted by the model. Hirsch et al. (2010) made a similar observation, and suggest higher amounts of erosion than can be reconstructed from seismic data alone.

Such an erosion event may have occurred during the Paleocene. McMillan (2003) mentions a Paleocene phase of uplift for the Agulhas Arch, to the south of the study area. This may have been related to igneous activity, which has not been reported for the northern study area. There is ample evidence for on- and offshore igneous intrusions along the South African margin during that time period. Offshore examples are the Agulhas Arch and the A-C well areas in south of the Orange Basin and the Chameis Bay pipes offshore Namibia (Gerrard and Smith, 1982; Moore et al., 2008). Further, Gallagher and Brown (1999) mention a minimum denudation of 100 m near onshore alkaline pipes. Dobson et al. (2011) made a similar observation; they report a phase of Eocene onshore denudation in southern Namibia that may tentatively be associated to the emplacement of igneous intrusions, such as the Chameis Bay alkaline pipes. Based on these reports we assumed that additional erosion occurred in areas of early Cenozoic igneous activity. This allows reconstructing a Paleocene erosion event that provides a better thermal calibration for the southern basin. On average, an additional 350 m of erosion are required to calibrate the VR trends (Figure 4-7b). As a result, maximum Cenozoic erosion amounts to 540 m for the south, which is in good agreement with the values proposed by Hirsch et al. (2010) and Kuhlmann et al. (2011).

This calibration with erosion events left two areas with VR trends higher than predicted by the model, namely the A-L and A-A well area and the A-C well area. In those cases, the difference in modeled versus observed maturity could not be explained by erosion alone. Gerrard & Smith (1982) and Dingle et al. (1983) have mentioned that igneous intrusions occurred in these two areas. A similar situation has been described for the Bredasdorp Basin to the south, where organic geochemical data and burial history models were used to show that local maturity anomalies result from an early Cenozoic hot-spot transit and hydrothermal charge due to large slumps (Davies, 1997). Local heat flow "spikes" of up to 70 and 90 mW/m^2 were assigned for the A-L/A-A and A-C igneous activity areas respectively, during the late Paleocene (58 Ma). This assumption gives the best thermal model calibration to the VR trends (Figure 4-9). Maturity studies of the Delaware Basin in west Texas, USA, have also demonstrated that igneous intrusions can cause a three-fold increase in heatflow resulting anomalously high source rock maturity on a very local scale (Barker and Pawlewicz, 1987).

The wells located along the slope of the Orange Basin show a "bump" in their VR trends for the late Santonian to early Maastrichtian when compared to underlying sediments. The values are consistently between 0.5 and 0.65% R_O. This is likely due to the reworking of Turonian-Coniacian aged organic matter eroded from the shelf and onshore coastal margin.

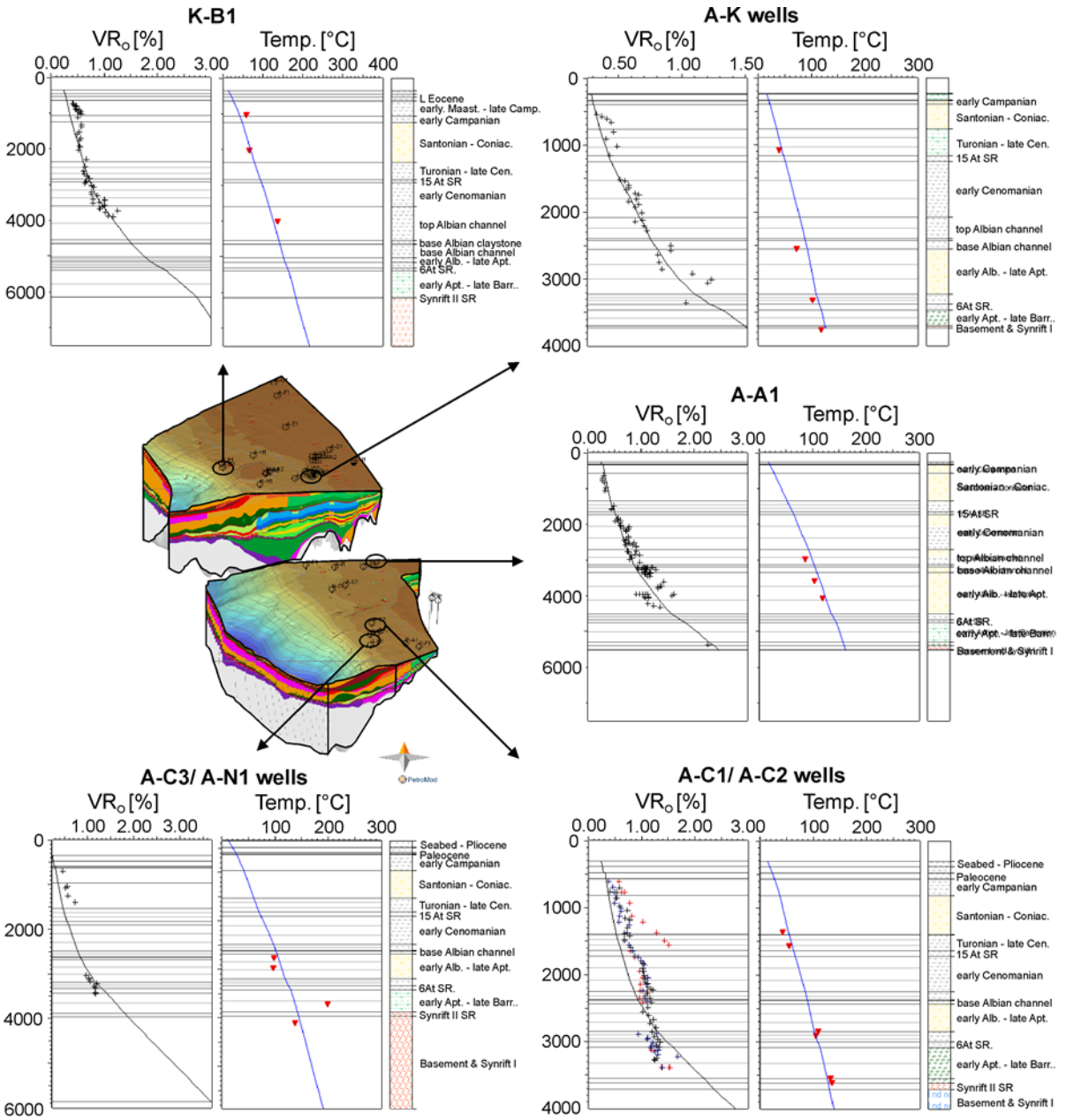

Figure 4-9: Calibration of thermal model against vitrinite reflectance and temperature data at different well locations in the northern and southern sectors of the basin.

4.3.8. Migration modeling

Hydrocarbon migration was modeled using the Hybrid Method (Darcy flow and Flowpath - PetroMod 2011.1.1). Based on a pre-defined permeability threshold, usually 10^{-2}mD at 30% porosity, the model's cells are treated as either a carrier (and reservoir, i.e. sandstone) or a low permeability facies (i.e. silt and shale) (Hantschel and Kauerauf, 2009). Darcy flow is calculated in low permeability layers where three-phase flow (water, oil, gas) is modeled at very small time intervals taking capillary pressure, buoyancy, and friction into account to provide a very accurate migration model. The Flowpath method (ray tracing) is used for flow in carrier rocks and assumes instant petroleum migration, which is mainly buoyancy controlled (Hantschel and Kauerauf, 2009). The Flowpath calculations define drainage areas

for every accumulation and quantify petroleum losses through the seal, along faults, and across spill points within the carrier system.

On the other hand, The Invasion-Percolation (IP) method provides an alternative to the Darcy-based Hybrid method, because it significantly reduces calculation times for large basin models and therefore allows using a higher grid resolution. The IP approach is buoyancy driven and assumes instant flow during each time step until a capillary balance is reached (Hantschel and Kauerauf, 2009). In this approach, the generation and expulsion of petroleum from the source rock control the timing of migration. Migration pathways are calculated through a connectivity analysis of each cell in the model, based on absolute permeability and capillary entry pressure (Kroeger et al., 2009). The main advantage of IP over the Hybrid Method, however, is the use of one migration calculation method for the entire model, especially across cells with large permeability differences, which are found at the reservoir-seal boundaries of incised channels in low-permeability rocks. The biggest drawback of IP in comparison to the Hybrid Method is the rough estimate for the timing of migration and that modeled migration pathways are not reproducible in detail.

Both, the Hybrid and IP method use a simplified percolation calculation to simulate flow along faults and seal bypass at the top of an accumulation (Hantschel and Kauerauf, 2009). Petroleum migration was simulated several times taking into account the results of previous models to achieve an optimization of temperature and pressure calculations.

4.4. Results & Discussion

The studies of Paton et al. (2007) and Kuhlmann et al. (2011), in the southern Orange Basin, discussed the timing of generation for the Barremian to Aptian and Turonian source rocks in detail (the latter only in Kuhlmann et al., 2011). Additionally, both studies postulate a potential for present-day generation in the area of Cenozoic progradation in the deepwater Orange Basin. Since our 3D model supports their results concerning the timing of generation, we will focus our results and discussion on the potential present-day and recent kitchen areas, as well as the petroleum migration dynamics in the study area.

4.4.1. Timing of generation and present-day maturity

4.4.1.1. Synrift source rock

The present-day oil window (0.6 - 1.3%VR_O) for the synrift source rock ranges from 2000 to 4000 m depth along the eastern basin margin (Figure 4-10a). Since the existence of a synrift source rock, except within the A-J half-graben, is not yet proven, the following results on the basin-wide timing of petroleum generation are purely theoretical. Generally, the onset of primary generation occurred by late Aptian times. The timing of peak oil generation (~50% transformation ration (TR)), on the other hand, is very variable depending on the rift-graben location relative to the early Cretaceous depocenter. In the most distal rift-grabens 50% and 100% TR are reached during the late Albian and Cenomanian, respectively. In contrast, in the

proximal rift-grabens where the source rock is currently within the oil window, 50% TR starts to be reached during the Paleocene (Figure 4-10c), getting progressively younger with decreasing depth towards the coast. In the deepest part of the A-J half-graben, for example, peak primary petroleum generation was reached during the Miocene (Figure 4-10d).

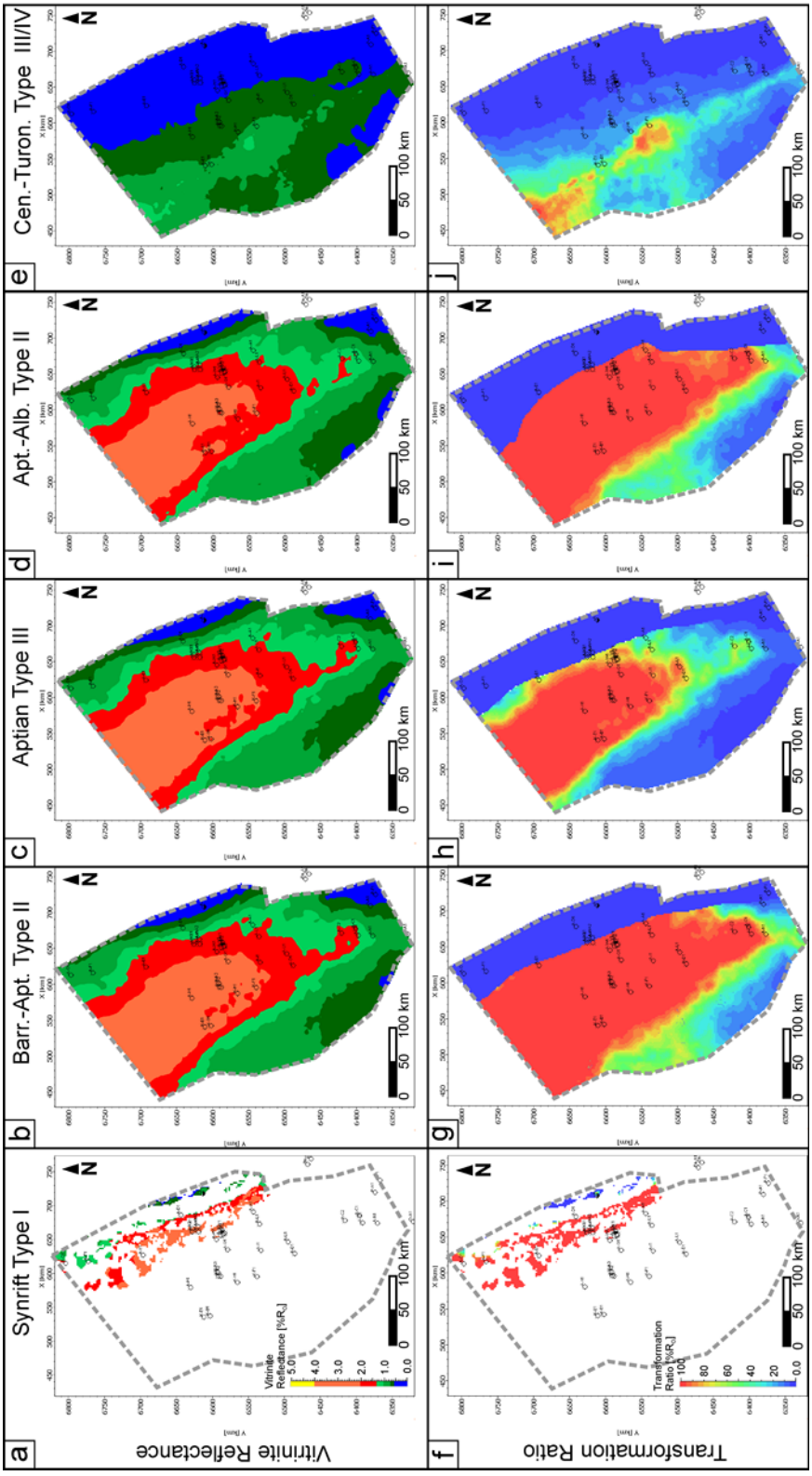

Figure 4-10: Modeled present-day thermal maturity shown as vitrinite reflectance and (f–j) present-day transformation ratio (TR) maps of the defined source rocks. Synrift source rock characteristics (a, f) are shown only for potential synrift structures. The Aptian-Albian Type III kerogen source rock (c, h) has significantly lower TR than the lower Cretaceous Type II kerogens and thus a remaining primary hydrocarbon generation potential in the Cretaceous depocenter

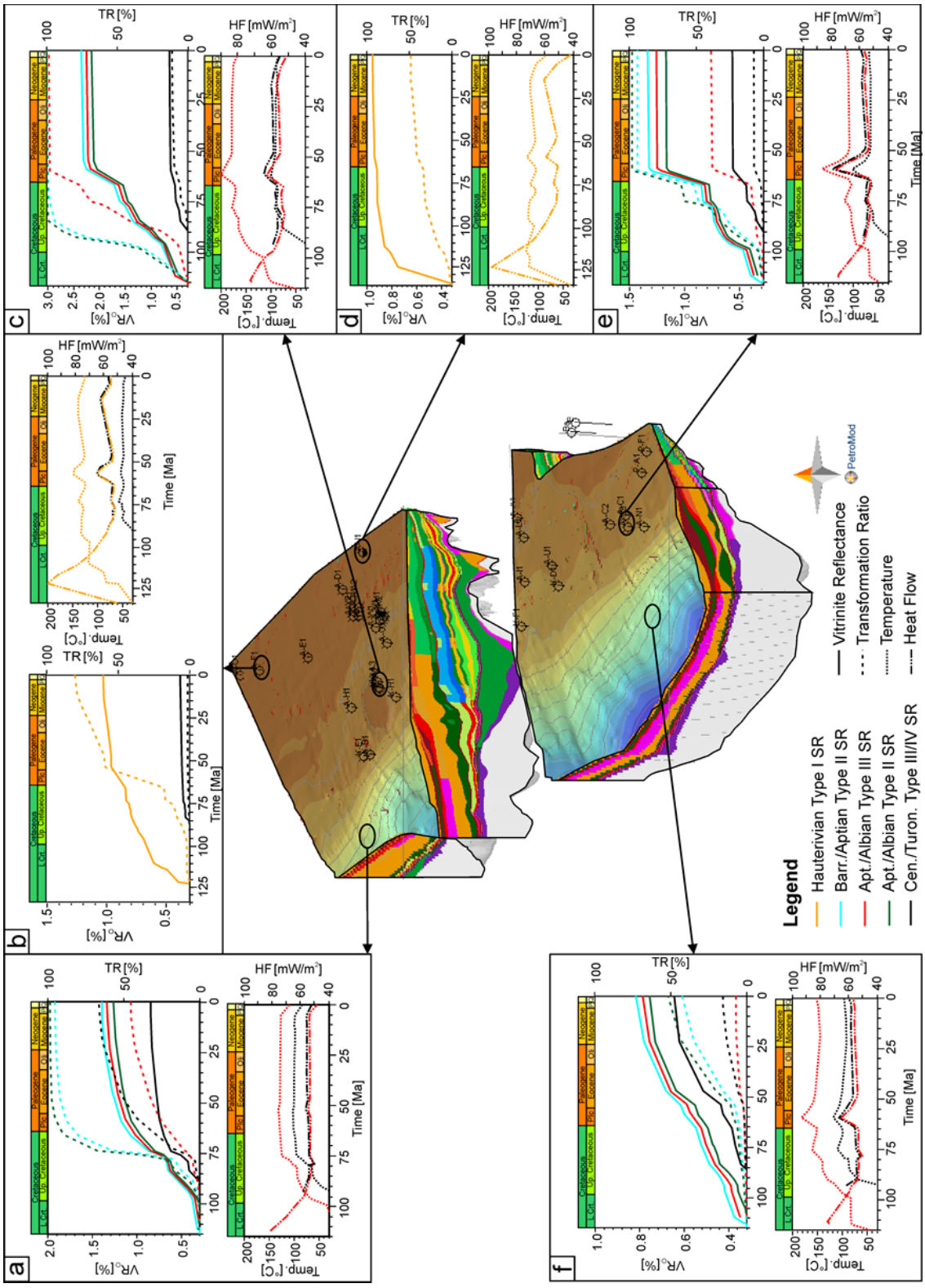

Figure 4-11: 1D time extractions showing the evolution of vitrinite reflectance, transformation ratio for all potential source rocks at different locations and layer temperature and heat flow for selected source rock intervals. Present-day kitchen areas in the western deepwater part are controlled by Cenozoic burial and characterized by an ongoing l increasing TRs (a, f). In contrast, the recent kitchen areas along the eastern coastal margin with potential synrift source rocks (b, d) are predominately controlled by paleo-heat flow. Primary generation in the Cretaceous depocenter ended during the latest Cretaceous/ early Paleocene, which is represented by TRs of 100% at those times (c, e).

4.4.1.2. Barremian to early Albian aged source rocks

In terms of present-day thermal maturity the Barremian to early Albian aged source rocks are overmature (>2.0% VR_O) in the basin center and within the wet-gas/late oil window (1.0 - 2.0 %VR_O) below the shelf-break (Figure 4-10b). Maturities between 0.6 - 1.0% VR_O, corresponding to the main phase of oil generation, are predicted for the distal deepwater area and in the southernmost Orange Basin. The onset of petroleum generation (10% TR at 0.6% VR_O) in the Cretaceous depocenter occurred during the late Albian to Cenomanian (Figure 4-11c). The main phase of oil generation (>50% TR at 0.8% VR_O) from oil- and wet-gas prone marine Type II and mixed Type II/III kerogens started in the basin`s depocenter during the late Cenomanian (95Ma) and propagated westwards with the prograding Turonian-Santonian sequences until 75 Ma. The end of primary petroleum generation (>95% TR at 1.25% VR_O) from the marine kerogen types was generally reached at the Maastrichtian/Paleocene transition. However, a potential for primary generation remains in areas where oil-window maturities exist, namely the areas of Cenozoic sediment progradation. There, modeled time-extractions suggest ongoing source rock maturation and hence petroleum generation since the late Cretaceous, though at significantly lower rates (Figure 4-11a, f)

The terrestrially influenced Aptian Type III kerogen source rock shows a delay in its transformation trend due to a higher thermal stability of the organic matter (Hartwig et al. 2012a). The main phase of petroleum generation (50%TR at 1.1% VR_O) from this source rock in the basin center started in the early Campanian (Figure 4-11c) propagating westward with a delay of 15 - 20 Ma relative to the Type II and II/III source rocks. Thus, in the area corresponding to the present-day slope, peak petroleum generation (~50% TR) probably occurred during the Cretaceous-Paleocene transition (Figure 4-11e). Areas with present-day potential for primary generation are characterized by present-day TRs < 80% (Figure 4-10h). They are generally found at burial depths of less than 4500 m. Recent generation in the deepwater Orange Basin is burial-driven, while the last phase of generation in the Cretaceous depocenter on the shelf was heatflow-driven due to the Miocene uplift event (Figure 4-11b, c). The Type III kerogen source rock's TR increased continuously by 5% from the Paleocene to the mid Miocene within the Cretaceous depocenter and is currently in the gas window. In the Cenozoic depocenters along the slope the source rock's TR increased by up to 20% until present-day and is currently in the oil window (Figure 4-10g - i, Figure 4-11a, f). This differentiation between Type II and thermally more stable Type III kerogens source rock intervals was not included in the previous modeling studies of the Orange Basin. Hence, the areas with a potential for recent primary generation on the shelf were not considered.

4.4.1.3. Cenomanian/Turonian (C/T) source rock

At present-day the C/T source rock is thermally immature (< 0.6% VR_O) in the proximal Orange Basin (Figure 4-10e). It is in the early-to-late oil window (0.6 - 1.3% VR_O) near the present-day slope in centers of Cenozoic sedimentation. The onset of petroleum generation (10% TR) generally occurred during the Paleocene and Eocene (Figure 4-11). Significant TRs

above 50% are only reached in areas of the growth-faulted slope of the northern Orange Basin (Figure 4-10j). The recent and present-day kitchen areas for the C/T source rock are located in the Cenozoic depocenters, where the TR increased continuously by up to 20% since the Paleocene.

4.4.2. Migration and Accumulation

The primary aim of the migration modeling was to understand under which conditions the Ibhubesi gas field is reproduced in the 3D basin model. Secondary objectives were to investigate the role of channels and faults during hydrocarbon migration as well as the petroleum migration dynamics in the present-day kitchen areas.

The majority of the Orange basin gas shows were encountered in the incised valley-fills and sand-rich Albian intervals (Jungslager, 1999) and in the transitional sequence directly below Aptian source rocks (Jungslager, 1999; Schmidt, 2004; SOEKOR internal reports). The 3D migration models (both Hybrid and IP) show that the highest petroleum saturations are consistently located in the transitional sequence and in the structural highs of the Albian and Cenomanian sandstones.

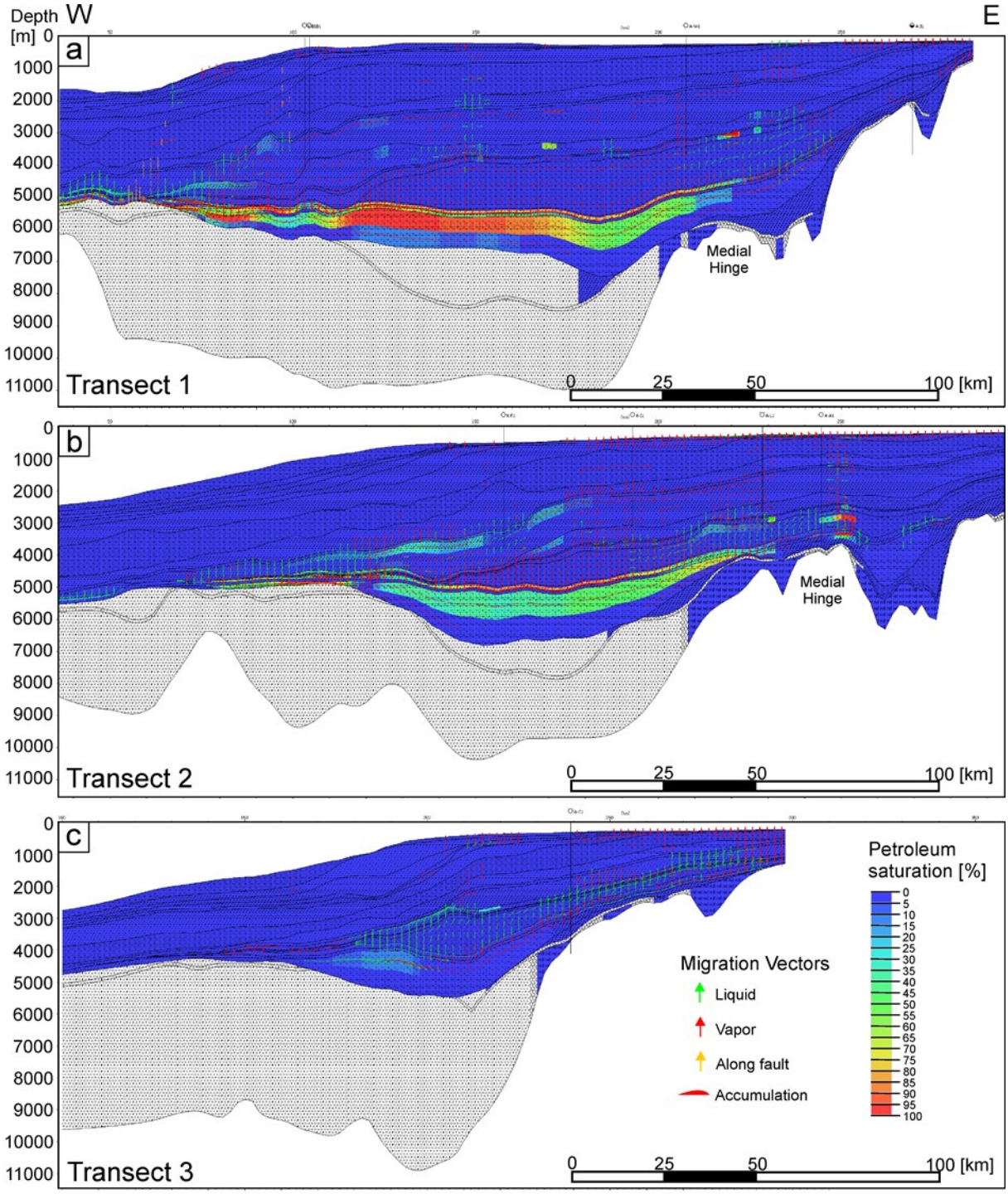

Figure 4-12: Modeled petroleum saturation, hydrocarbon accumulations, and migration vectors extracted from the 3D Hybrid migration basin model along a W-E transects (for location see Figure 4-1). Lateral migration occurs within Lower Cretaceous sand-rich sequences and channels, which are the main carrier systems. Note that the early Cretaceous source rocks act as seals for downward-expelled hydrocarbons, creating accumulations in the transitional sequence such as the Kudu field offshore Namibia. The Ibhubesi-type accumulations in Albian channel sandstones (Transect 1) were recreated by incorporating a shale-rich layer at mid-Albian level. Recent- and present-day generated hydrocarbons in the western deepwater areas migrate up-dip into roll-over structures and subtle anticlines. Vertical hydrocarbon migration occurs above structural closures and anticlines and at seafloor outcrops of lower Cretaceous sequences along the eastern margin, where "sniffer" anomalies have also been reported (see Figure 4-1).

The upper Barremian-lower Aptian sandstones of the transitional sequence are charged by downward-expelled petroleum generated from the lower Aptian source rocks, which also acts as a regional seal (Figure 4-12). Similar observations were also made by Schmidt (2004) on a 2D model of the Namibian margin across the Kudu gas field, where the main Barremian aeolian and coastal sandstone reservoirs are directly overlain by the early Aptian source rock (Jungslager, 1999; Schmidt, 2004; Wickens and McLachlan, 1990). Thus, our migration model supports the assumption that the transitional sequence provides a regional carrier for hydrocarbons, as proposed by Jungslager (1999).

Upward-expelled petroleum generally migrates vertically through the Albian and Cenomanian sand-rich intervals until it reaches the (organic-rich) C/T condensed section and the thick Coniacian to Campanian aged claystones, as indicated by the migration vectors (Fig. 9). These sequences provide an important regional seal on the shelf below which petroleum migrates laterally towards the coast. As soon as the sand and silt content of the upper Cretaceous increases, hydrocarbons migrate vertically and leak to the seafloor. Thus, the migration model reproduces leakage to the seafloor in areas of present-day "sniffer" anomalies (Figure 4-12b, compare with Figure 4-1) reported by Jungslager (1999) and Petroleum Agency SA (2012) and gas seeps and chimneys as described by Kuhlmann et al. (2010) and Boyd et al., (2011). The most widespread hydrocarbon loss occurs where the lower Cretaceous is truncated due to erosion, forming subcrops under Plio-Pleistocene sediment cover. Vertical migration up to the seafloor further occurs above subtle structural highs, especially along the medial hinge line in the proximal OB and above roll-over structures and along faults in the OB slope. There the hydrocarbon column heights are sufficient to overcome the capillary entry pressure of the regional seal. Such leakage processes may well be very similar to those that led to the formation of an extensive Eocene paleo-pockmark field in the northern OB slope (Hartwig et al., 2012a).

The petroleum saturation of the Albian and Cenomanian intervals depict that the conceptual channels have higher saturations than the surrounding rocks. In conjunction with the migration vectors of the 2D transects (Figure 4-12) they allow to interpret the channels as potential carriers for up-dip migrating petroleum from the present-day kitchen areas.
Our initial model also produced higher petroleum saturations within the Cenomanian channels than in the mid and top Albian channels. The Turonian channels, on the other hand, did not show any saturation higher than the surrounding claystones.
However, the main mid Albian channel reservoirs of the Ibhubesi gas-condensate field (Jungslager, 1999) showed very low petroleum saturations (< 5%). The highest saturations, up to 40%, were found in the Cenomanian channels. Additionally, the model did not show any significant hydrocarbon accumulations in the channels. Jungslager (1999) mentions that the highest flow rates of the A-K1 well (initial Ibhubesi discovery well) were measured off-structure in stratigraphically-trapped channel sandstones with high porosities up to 20%. Similar porosities averaging around 15% were reproduced within the channel sandstones of

our model. The surrounding sand-claystone lithologies of the model show average porosities between 5 and 8 %. The A-K1 well report and Fig. 8 of Jungslager (1999) mention claystones (partially organic-rich, SOEKOR unpublished) that are intercalated with the reservoir sandstones. Further, Fadipe et al. (2011) conducted a study on the effects of diagenesis and cementation processes in reservoir sandstones from the Ibhubesi field. They conclude that primary porosity is frequently reduced by silica cement and mechanical compaction. The intercalated shales and silica-cemented sandstones may thus act as a local seal, which was not included in the initial model definition. We improved the trapping efficiency by introducing a sandstone-free silty shale sublayer above the mid Albian channels with a maximum thickness of 40 m. Such claystone intervals occur as part of estuarine deposits in the early Cretaceous Orange delta. The ensuing migration model produced gas and condensate accumulations in the mid Albian channels and higher petroleum saturations in both mid and top Albian channels, than in the Cenomanian channels (Figure 4-13). This shows that the intercalated shales dramatically increase the trapping efficiency in the stratigraphically trapped Albian channel sands. The seal helps to direct migrating hydrocarbons into subtle structures. In absence of such a local seal, early Cretaceous-sourced petroleum migrates vertically and is dispersed throughout the lower Cretaceous sediments.

The synrift and basal transitional sediments in and above the rift grabens usually consist of conglomerates with intercalated volcaniclastics and continental or marine sandstones, respectively. With these lithologic definitions in the model, most of the petroleum expelled from the synrift source rock migrate up-dip towards the graben edge where it enters the sand-rich transitional sequence. From there it follows the previously outlined migration paths of Aptian/Albian-sourced petroleum. Again, the sealing capacity of synrift and early transitional sediments is crucial. The tested oil of the A-J graben was produced from sandstones that are intercalated with the source rock (Jungslager, 1999). Therefore, it is very likely that the lacustrine shales act both as source and seal. This situation is partially reproduced by the 3D model, which predicts that the synrift source rock of the A-J graben has present-day petroleum saturations of up to 7%. This may be interpreted as unexpelled petroleum. If a sealing lithology is assigned to the break-up unconformity above the A-J graben, low-API synrift-sourced petroleum accumulates in stratigraphic pinch-out traps at the graben flanks and in synrift truncation traps below the break-up unconformity.

Both the Hybrid and the IP model predict petroleum accumulations in the Albian channels, in the transitional sequence along the rifted basement, and potentially in synrift pinch-outs. Additionally, the IP model also predicts accumulations in potential basin-floor fans of late Aptian to Cenomanian age and in late Cretaceous growth- and roll-over structures. Jungslager (1999) and van der Spuy (2003) have proposed these hypothetical plays before. The Hybrid model does not reproduce them because its accumulations are limited to the carrier beds, which have a higher permeability than the defined threshold value for Flowpath calculations (2.01 log mD at 30% porosity). Instead, they show up as areas with high petroleum saturations (Figure 4-14).

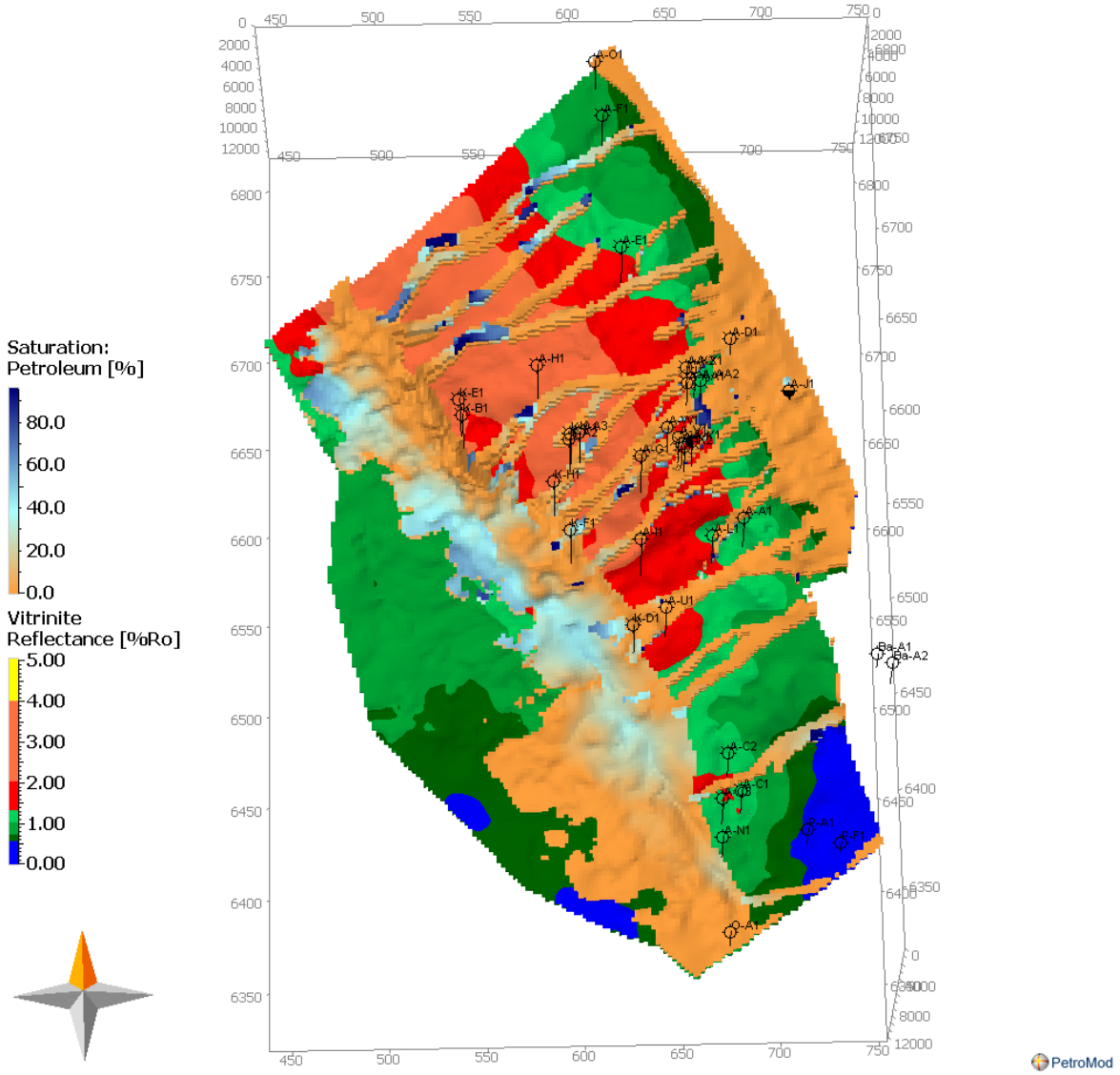

Figure 4-13: 3D view of modeled petroleum saturation within the conceptual Albian channels and deepwater sediments as calculated by the Hybrid method (blue tones denote high values). The vitrinite reflectance of the Aptian source rock layers is shown below the Albian channel layers. The recent and present-day deepwater kitchen areas charge the deepwater sediments as propose in Figure 4-12.

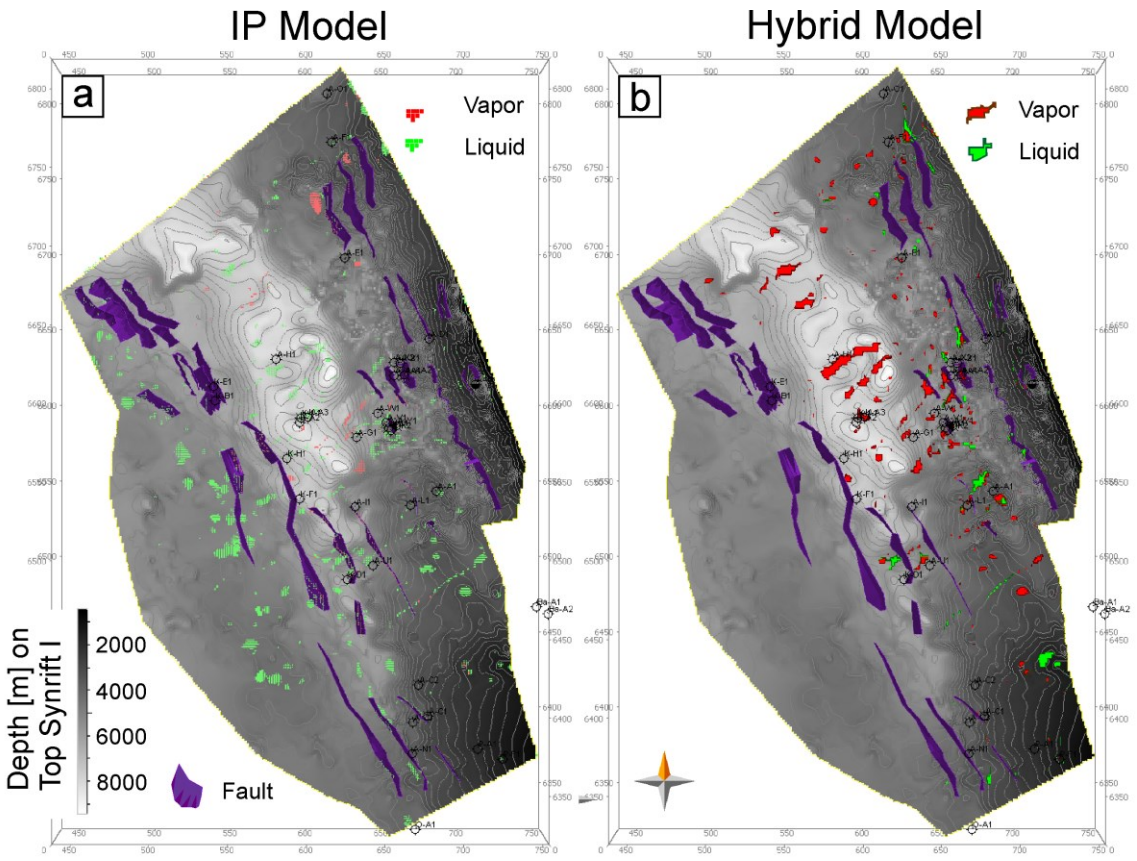

Figure 4-14: Hydrocarbon accumulations as predicted for the main carriers by a) the IP method and b) the Hybrid method (see text for details). Hybrid model accumulations generally have higher vapor contents than IP- model accumulations. The IP method generates liquid HC accumulations in sand-rich basinfloor fans in the western deepwater OB. These areas correlte to areas with higher petroleum saturations calculated by the Hybrid method (Figure 4-13)

4.4.3. Petroleum system evolution

The petroleum system charts of the Cretaceous and Cenozoic depocenters (Figure 4-15) summarize the Orange Basin's evolution with respect to hydrocarbon generation.

The charts provide a summary for the present-day shelf and slope, which is closely related to the Cretaceous and Cenozoic depocenters, respectively.

The early Cretaceous source rocks are intercalated with Aptian to Albian aged clastic reservoir facies. Primary generation from marine source rocks started before a regional seal, consisting of upper Cretaceous clays, was consolidated. Therefore, a high risk exists for marine-sourced black oils not having been trapped. Seals for Albian and Cenomanian channels were consolidated by latest Cretaceous times, thus creating efficient stratigraphic traps, such as those found in the Ibhubesi field. This timing coincides with maximum burial and primary generation of condensate and gas from thermally more stable terrestrially influenced marine deltaic source rocks (Type III kerogen). The onset of secondary cracking reactions in marine source rocks generated additional gas during latest Cretaceous to early Cenozoic times. Latest Cretaceous/early Cenozoic and Miocene-Pliocene episodes of margin uplift, tilting, and erosion are the greatest risk for preservation of hydrocarbon accumulations in the proximal Cretaceous depocenter of the OB.

Early Cretaceous basinfloor fans are the potential reservoir facies of the deepwater OB. They may create stratigraphic traps that are intercalated with Barremian to Aptian/Albian marine

and deltaic source rocks. Primary generation from marine Type II source rocks in the deepwater Orange Basin was burial-driven and began with the progradation of the northern OB shelf during the Cenomanian to Campanian. These thick claystone sequences provided a regional seal. Ensuing faulting and shelf collapse during latest Cretaceous margin uplift may have formed additional structural traps. Continuous sedimentation during the Cenozoic, albeit at lower rates than during the late Cretaceous, led to the onset of primary generation from the thermally more stable Aptian/Albian type III kerogens and the C/T marine source rock. Hydrocarbon generation is still going on at present-day.

A change in the fluvial drainage pattern during the late Cretaceous to Paleogene caused a southward shift of the main depocenter from the vicinity of the present-day Orange River to the area of the Oliphants River (Dingle and Hendey, 1984). Thus influencing the onset of petroleum generation in the southern deepwater OB. Primary generation from lower Cretaceous marine source rocks started during the latest Cretaceous. The Cenozoic shelf progradation provided a thick claystone sequence that acts as a regional seal. Faulting and shelf collapse of this Cenozoic sequences generally did not affect potential early Cretaceous reservoir intervals. Renewed deepwater sediment input during the Neogene drives continuous hydrocarbon generation from Cretaceous source rocks to the present-day

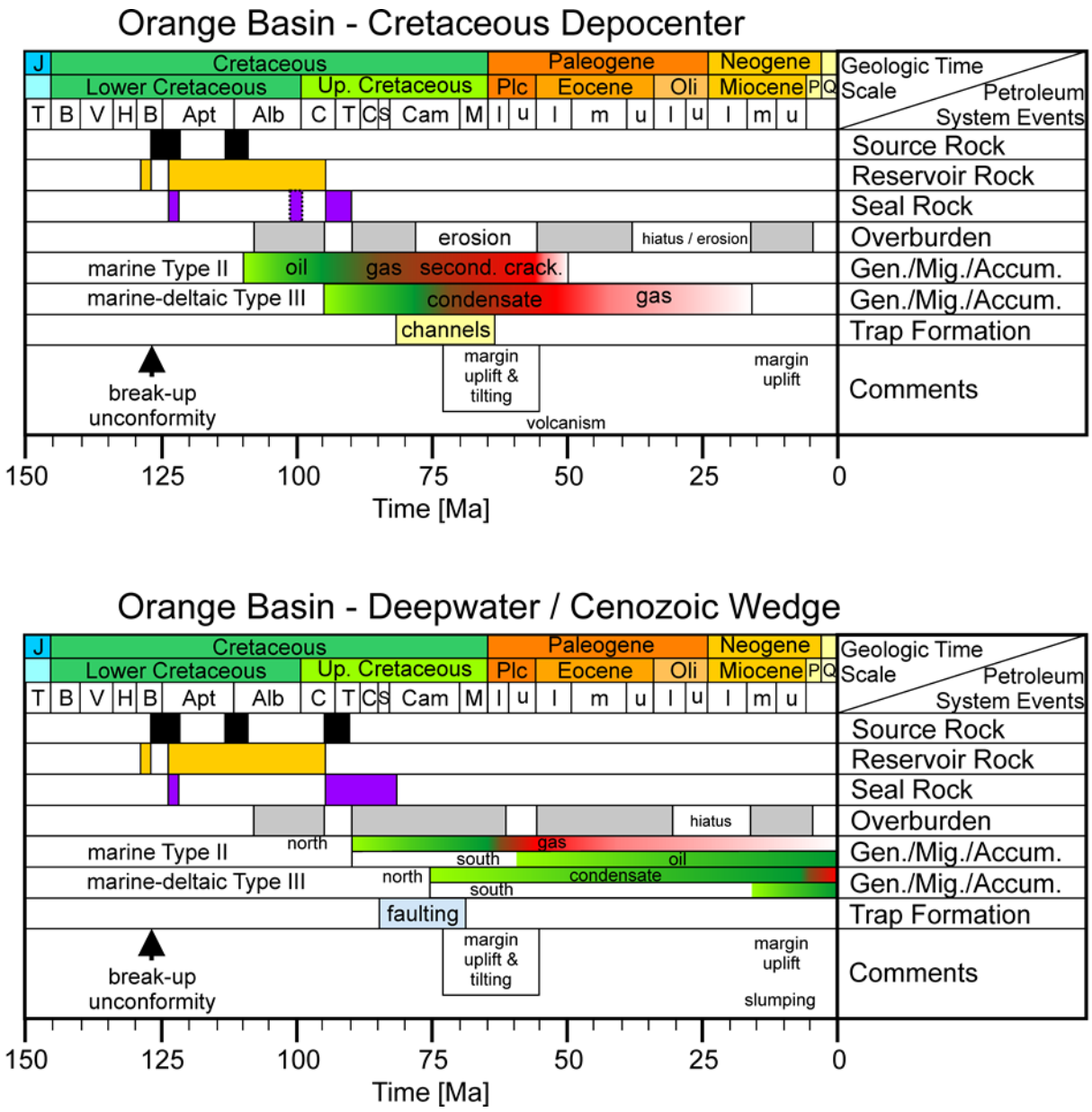

Figure 4-15: Petroleum system elements chart for the Cretaceous depocenter and the deepwater Cenozoic wedge in the Orange Basin.

4.4.4. Ibhubesi filling history

The filling history of the Ibhubesi field can be reconstructed from the Hybrid migration model under the assumption that the petroleum accumulations in the sandstone facies of the conceptual Albian channels are analogues to the Albian channel reservoirs of the Ibhubesi field. It should be kept in mind that the scale difference of the migration model reservoir cells (2000 x 2000 x ~250 m grid resolution, length x width x height) to the approximated maximum extent of an Ibhubesi reservoir (5000 x 500 x 25 m) and the uncertainties on source rock thickness and extent only allow a qualitative interpretation.

The timing, relative amounts of accumulated and lost hydrocarbons, and individual source rock contributions are discussed first for the "open scenario" and then for the "initial model" for accumulations in the vicinity of Ibhubesi wells (Figure 4-16). The present-day petroleum in the reservoirs is predicted to occur as a vapor phase, sometimes with a small liquid leg, with an average API of 62° at surface conditions. The condensate from Ibhubesi well drill-stem tests has an average API varying from 49 to 59° (Forest Exploration International internal report).

The accumulations in the "open model" are purely stratigraphic traps in subtle anticlines. They formed during the early Cenomanian with the onset of hydrocarbon expulsion from marine Aptian and Albian source rocks. The first major episode of hydrocarbon loss occurs during the first phase of Santonian margin uplift and westward tilting. This is expressed by large amounts of liquid hydrocarbons lost due to spilling (Figure 4-17a, b). The final episode of late Cretaceous margin uplift drives a second episode of spilling and loss along faults. During this time the reservoirs received continuous recharge with liquid petroleum until the Paleocene, when primary generation from the marine source rocks ends. The late Cretaceous/Cenozoic transition also marks the onset of secondary cracking in Aptian-Albian marine source rocks and simultaneous primary generation of gas and condensate from the Aptian Type III source rock. During the Cenozoic, the overall liquid volume decreases until the present-day. The migration of gaseous hydrocarbons into the closures, on the other hand, increases and continues until the Pliocene, the main contributors being the Aptian Type III kerogen source rock and secondary cracking processes. The overall volume of the accumulations, however, stays more or less constant because the traps of our model are filled to spill since the early Cenozoic. Excess petroleum is spilled and migrates up-dip into other accumulations or is eventually lost along faults or as top or side outflow. The vapor amounts lost through the seal are minor, when compared to the other two mechanisms. The youngest episode of spilling coincides with the Miocene-Pliocene phase of erosion. Since the Pliocene, the shelf received very low sediment supply and therefore petroleum generation due to burial ended in the Ibhubesi area. Thus, spilling of hydrocarbons drastically decreases and leakage along faults becomes the main hydrocarbon loss risk, which is supported by the seismic chimneys and seafloor pockmarks interpreted on seismic surveys of the OB slope (Boyd et al., 2012; Hartwig et al., 2012a; Kuhlmann et al., 2010).

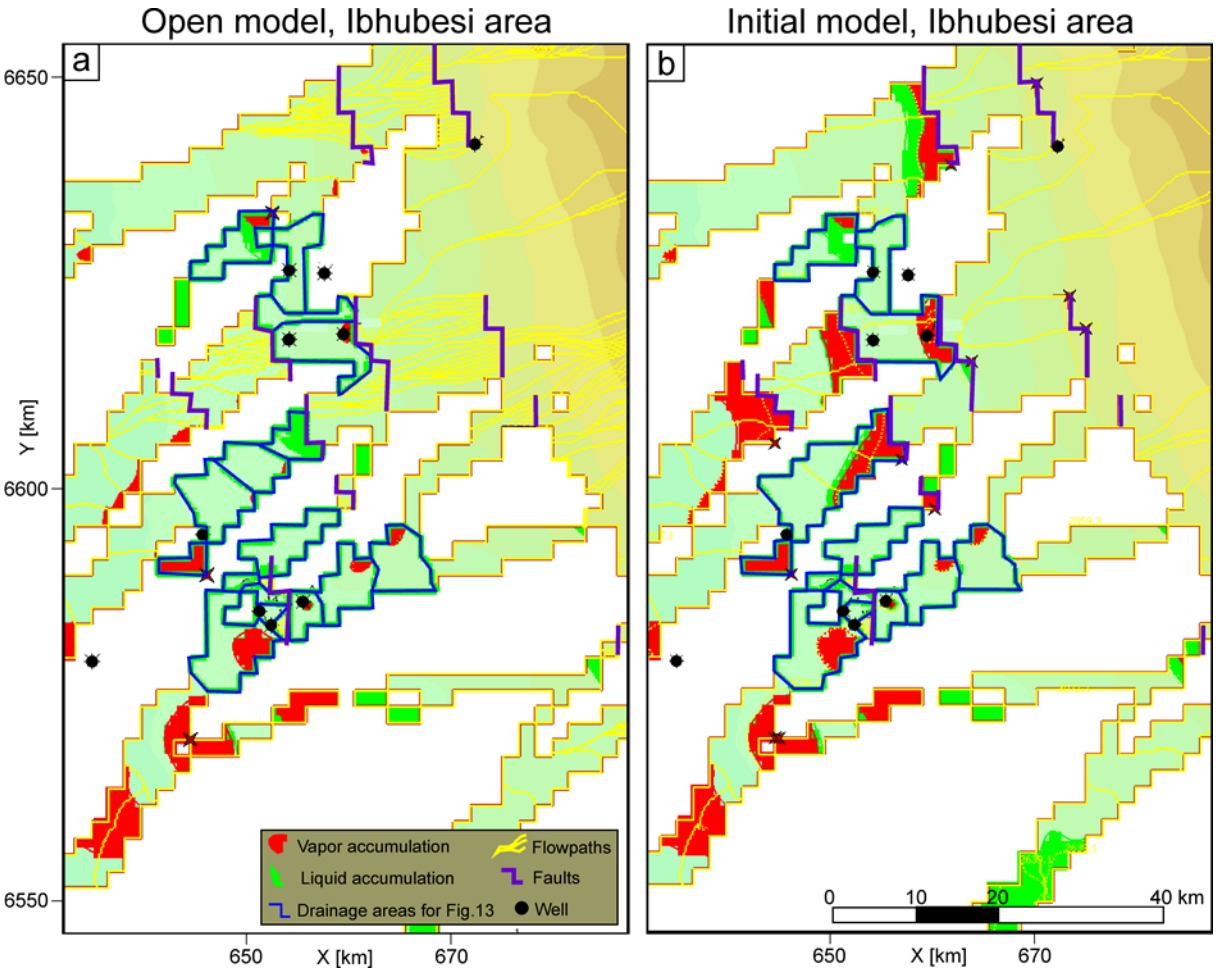

Figure 4-16: Predicted hydrocarbon accumulations in the Ibhubesi area from the (a) “open model” with open faults and (b) the “initial model” with variable fault properties. The blue outline marks drainage areas used for calculating hydrocarbon losses through time (Figure 4-17.) See text for details.

The filling history trend for the Ibhubesi area of the "initial model" is very similar to the "open scenario". Nonetheless, the overall volume of hydrocarbons that flow through the drainage area in the "initial model" is larger by a factor of 1.5 and the relative amounts of accumulated petroleum are also larger due to the structural trapping at faults. The main difference between the two models lies in the dominant mechanism of hydrocarbon loss.

Whereas spilling and leakage along faults are the dominant mechanisms in the "open scenario", losses through the seal dominate the "initial model", especially during phases of burial (Figure 4-17c, d). Closed faults create barriers for spilled hydrocarbons that migrate up-dip. As a result, the fluid pressure in fault-bounded accumulations exceeds the capillary entry pressure of the seal and hydrocarbons leave the carrier. The effects of margin uplift are well demonstrated in the sudden increase of reservoir spilling in the "initial model" as trap closure decreases through tilting.

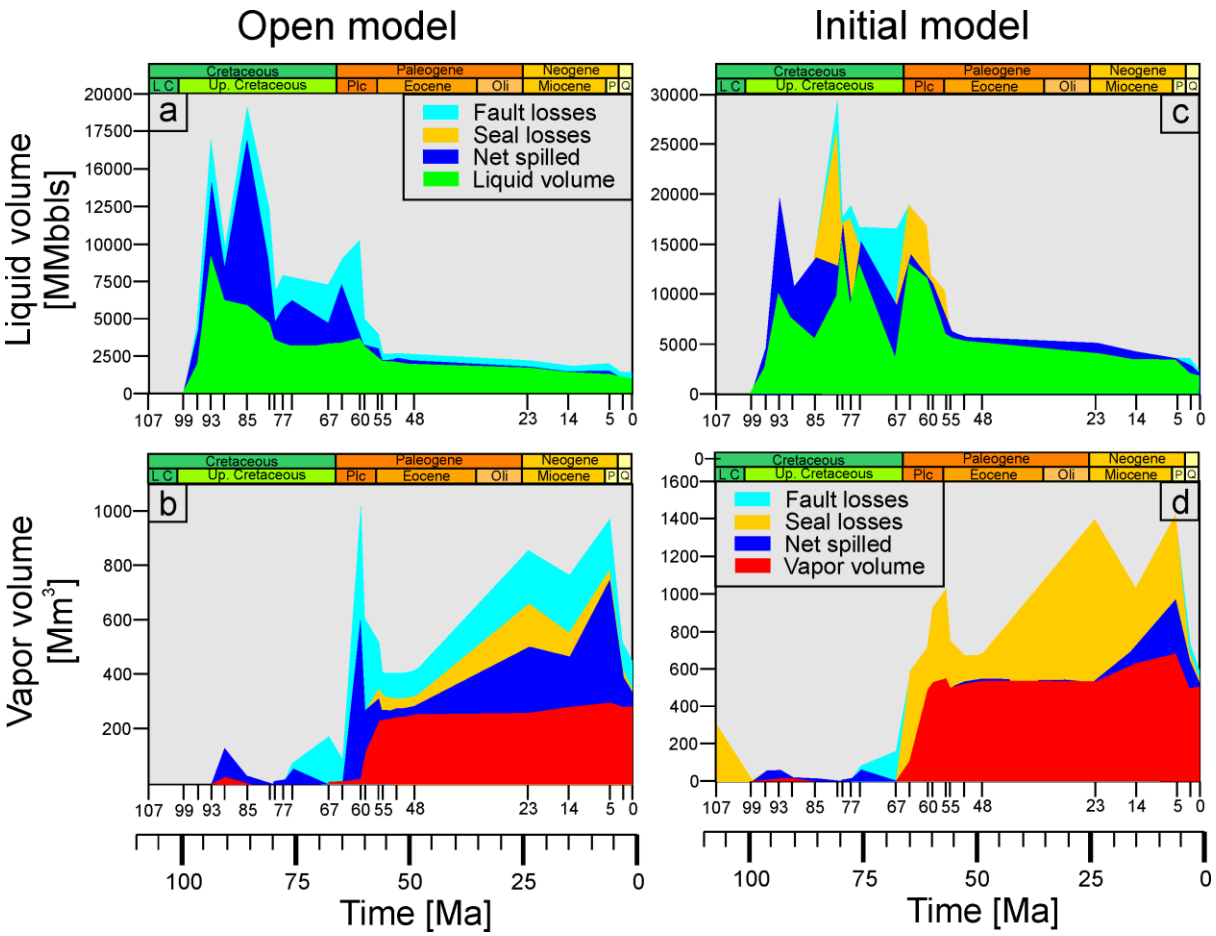

Figure 4-17: Liquid and vapor hydrocarbon losses for the Ibhubesi area as calculated from the open fault scenario ("open model") (a, b) and the initial scenario with open faults during tectonically active periods and closed faults for tectonically quiet periods ("initial model") (c, d). In both models, the highest losses occur during phases of margin uplift. The Ibhubesi reservoirs are filled to spill since the early Cenozoic. If faults are closed (c, d), leakage occurs mainly through the seal.

4.4.4.1. The role of faults during migration

In the case of the Ibhubesi field it has been proposed that gas migrated from the source rock along faults into the reservoirs (Ben-Avraham et al., 2002). Seismic interpretation studies from the Orange Basin have also shown that indicators for past and present-day fluid and hydrocarbon leakage, such as mud volcanoes and pockmarks, are usually associated with deep-seated faults (e.g.: Ben-Avraham et al., 2002; Boyd et al., 2012; Hartwig et al., 2012a; Kuhlmann et al., 2010; Viola et al., 2005). In terms of the simple fault-property model used in this study, this implies that faults have to be defined as being open during times of leakage or reservoir charge, i.e. acting as fluid conduits. In the Hybrid and IP migration methods, flow along an open fault only occurs if the pressure exerted by the petroleum in the adjoining cells is higher than the capillary entry pressure of the fault (Hantschel and Kauerauf, 2009).

A filling of sandstone reservoirs along the faults, as is proposed for the Ibhubesi field, could not be reconstructed with the "open scenario". Instead, the faults that cut across channels near the Ibhubesi field help to drain potential accumulations. In contrast to the "open scenario", the impermeable faults in the "initial model" and the "closed scenario" create

significantly more structural traps for up-dip migrating petroleum in the Albian and Cenomanian channels, which are eventually filled and leak through the seal. The simple fault definition of this model, however, is not sufficient to test a fault that acts both as seal for the reservoir and also as conduit for migrating petroleum from deeper source rocks. A more refined model using shale-gauge-ratios or fault-capillary pressure variability might be able to address more accurately the role of faults during reservoir filling.

The studies of Berge et al. (2002, Fig. 2 and 6 therein) and Jungslager (1999, Fig. 7 therein) show that seismic amplitude anomalies related to gas-charged sands of the Ibhubesi field exist on both sides of a major fault, though not directly at the fault's plane. Thus supporting the observation from seismic studies of the Orange Basin (e.g.: Ben-Avraham et al., 2002; Hartwig et al., 2012a) that clearly show the association of faults to hydrocarbon leakage indicators, such as pockmarks above the Ibhubesi area. Cartwright et al. (2007) described this type of seal-bypass system, although the actual process that leads to a focused flow at the fault remains controversial (Bjørlykke et al., 2005; Cartwright et al., 2007; Hantschel and Kauerauf, 2009). According to Clayton and Hay (1994) and Bjørlykke et al. (2005) the fault planes located below 1000 m depth or in subsiding basins are generally closed for fluid flow, either due to cementation along the shear zone or because of vertical stress much higher than the horizontal due to the high overburden pressure. However, faults may be open for fluid flow below 1000 m depth in compressional settings or if hydraulic overpressure keeps a fault open. Clayton and Hay (1994) propose that leakage at faults occurs due to capillary or fracture failure in the seal at the top of a fault-bound accumulation, rather than through the fault's shear zone. In this manner, hydrocarbons may leak vertically from one accumulation to the next structural trap along the fault until reaching the fault's end. At shallow depth, generally less than 1000 m, fault planes may act as fluid conduits again (Clayton and Hay, 1994), which would explain the reported association of seafloor pockmarks with faults. This is the dominant seal-bypass mechanism in the "initial model". Furthermore, our models show that regardless of the three fault scenarios, the greatest hydrocarbon losses from reservoirs occurred during times of margin uplift, namely the late Cretaceous/Paleocene and the Miocene-Pliocene. These modeling results correlate well to the observed time intervals for past hydrocarbon leakage identified on seismic data, such as early Eocene paleo-pockmarks and Miocene mud volcanoes in the northern OB (Ben-Avraham et al., 2002; Viola et al., 2005; Hartwig et al., 2012b), and Pliocene to recent pockmarks above the Ibhubesi field (Jungslager, 1999; Hartwig et al., 2012b).

4.5. Conclusions

An integrated basin-wide 3D model of the Orange Basin, offshore southwestern Africa, was constructed based on a large 2D exploration seismic dataset and calibrated to well data. Our calibration of the thermal model suggests a maximum heatflow of 96 mW/m^2 during rifting and an exponential decrease to an average value of 52 mW/m^2 for the present day, with two periods of increased heatflow by up to 8 mW/m^2 in areas where the continental crust was

affected by renewed lithospheric stretching during late Cretaceous/Paleocene and Mio-Pliocene. The cumulative maximum erosion during the two phases of lithospheric stretching and ensuing margin uplift are 1000 m and 540 m, respectively. Regions where vitrinite reflection trends indicate higher paleo-temperatures correspond to locations of reported early Cenozoic igneous activity.

In the A-J graben, primary generation from the Hauterivian-aged synrift Type I source rock began in the Cretaceous and the present-day TR of 50% was reached during the Miocene.
Application of the kinetic model of Hartwig et al. (2012b) demonstrates that the onset of primary generation from Aptian Type III-kerogen source rocks occurs with a delay of 20 Ma in comparison to early Cretaceous marine Type II and II/III kerogens source rocks. The main phase of primary generation from Barremian to Albian aged Type II and II/III and the Aptian Type III source rocks in the basin center occurred during the mid Cretaceous and the late Cretaceous/Paleocene, respectively. A second heatflow-controlled phase of petroleum generation from these source rocks lasted from the latest Cretaceous/Paleocene until the end of the Mio-Pliocene uplift.
Regions with a present-day potential for primary generation from the Type III-kerogen source rock are found at burial depths of less than 4500 m, characterized by TRs of less than 80%.
The present-day kitchen areas are located in the Cenozoic depocenters along the slope (Fig. 12, Deepwater / Cenozoic Wedge). In the northern areas of the basin, the lower Cretaceous Type II and II/III source rocks are currently within the gas window, Aptian Type III kerogen and Cenomanian/Turonian Type II/III kerogen source rocks are within the oil window. In the southern basin, both the lower Cretaceous and a potential C/T source rocks are currently in the oil window.

The migration model confirms that the main carriers of the Orange Basin are Barremian to early Aptian sandstones of the transitional sequence and Albian to Cenomanian fluvial sandstones of the early drift sequence. Petroleum accumulations are dominated by gas and condensate. Secondary cracking reactions in early Cretaceous marine source rocks and primary gas/condensates from Aptian Type III source rocks were the main contributors to present-day accumulations along the eastern basin margin.
The greatest risk for reproducing the Ibhubesi accumulations is the seal. Albian fluvial channels were only filled when their trapping efficiency was improved by introducing an Albian claystone seal into the model. In the absence of this Albian seal, smaller accumulations were exclusively formed in Cenomanian channels below the C/T source rock.
Drainage area analysis of petroleum accumulations in the Ibhubesi area was conducted on two migration models with different fault properties. These models indicate that stratigraphic traps may have been filled to spill since the early Cenozoic and that hydrocarbon losses due to spilling ("open scenario") and leakage through the seal ("initial model" and "closed scenario") are highest during times of margin uplift and erosion.

Acknowledgements

This research is part of the PhD project of A. Hartwig conducted at the Helmholtz Centre Potsdam (GFZ) German Research Centre for Geoscience. We gratefully acknowledge funding by Forest Exploration International (South Africa) (PTY) Ltd. We thank Forest Exploration International (South Africa) (PTY) (Ltd), PetroSA (Pty) (Ltd), Anschutz Overseas South Africa (Pty) (Ltd), and the Petroleum Agency SA for providing the data and for permission to publish our results. Z. Anka position is funded by a Helmholtz-University Young Investigator Group grant from the Helmholtz Association's Initiative and Networking Fund. We are thankful for the discussions with Tony L. Albrecht, John P. Klein, and Dave van der Spuy.

5. Complementary results and interpretations on the hydrocarbon migration dynamics and the early South Atlantic margin evolution

In the course of this study a vast amount of additional data were made available by Forest Exploration International Pty. Ltd. SA, the Petroleum Agency SA, and PetroSA in the form of reprocessed 2D deep-seismic reflection profiles optimized for imaging basement structures, as well as biomarker and isotope measurements conducted on hydrocarbons recovered from drill stem test and sidewall core extracts. The interpretations are presented in the following sub-chapters.

Additionally, interpretations and findings on the seaward dipping reflector (SDR) morphology in the Orange Basin were done in collaboration with Hannes Koopmann from the Federal Institute for Geosciences and Natural Resources (Bundesanstalt für Geowissenschaften und Rohstoffe, BGR) who studies the continental margin evolution offshore South Africa for his PhD thesis. The results from this collaboration are published in Koopmann et al. (2014).

Additional data is also available from mass balance calculations of the flow simulations conducted with the PetroMod 2011 software. These are interpreted and discussed within the framework of the MOM project, previously described in Chapter 3, in an attempt to put transient hydrocarbon leakage from sedimentary basins into a global climate perspective on a geologic time scale.

5.1. Interpretation of light hydrocarbons and $d^{13}C$ stable isotope data from extracted rock samples and reservoir fluids from the Orange Basin

Forest Oil Exploration conducted organic geochemical analysis on some of their wells. The data come from whole oil condensate samples collected from Ibhubesi well drill-stem tests (DST) of different reservoir compartments, extracted OM samples of cuttings and core from the proximal A-F1 shelf well and the distal shelf-break wells K-B1 and K-E1, and published data of the Kudu wells reported in Schmidt et al. (2004).

The $C_{27}/C_{28}/C_{29}$ iso-steranes were measured for the K-B1 and K-E1 wells located at the Cretaceous shelf-break. The ternary plot can give insights into the depositional facies (Hunt, 1996; Peters et al., 2005). It indicates shallow marine to open marine conditions with mixed planktonic and land plant precursors for the K-B1 and K-E1 wells (Figure 5-1). The biomarkers of shale extracts from the Kudu wells and Aptian Bredasdorp basin source rocks that were examined by Davies and Van der Spuy (1993) plot into the same region. This indicates that the hydrocarbons found in the K-B1 and K-E1 wells were sourced from the Aptian marine type II/III source rock.

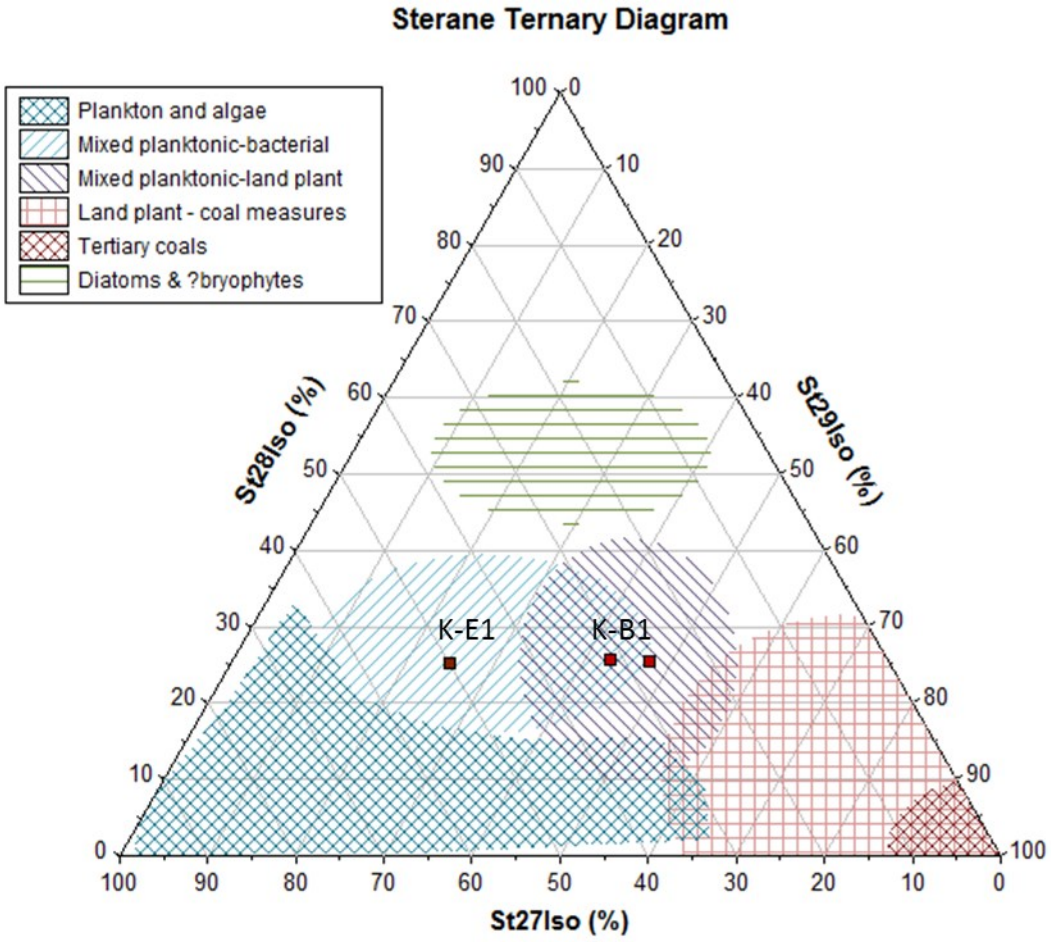

Figure 5-1: Iso-sterane diagram for K-B1 and K-E1 well samples.

a

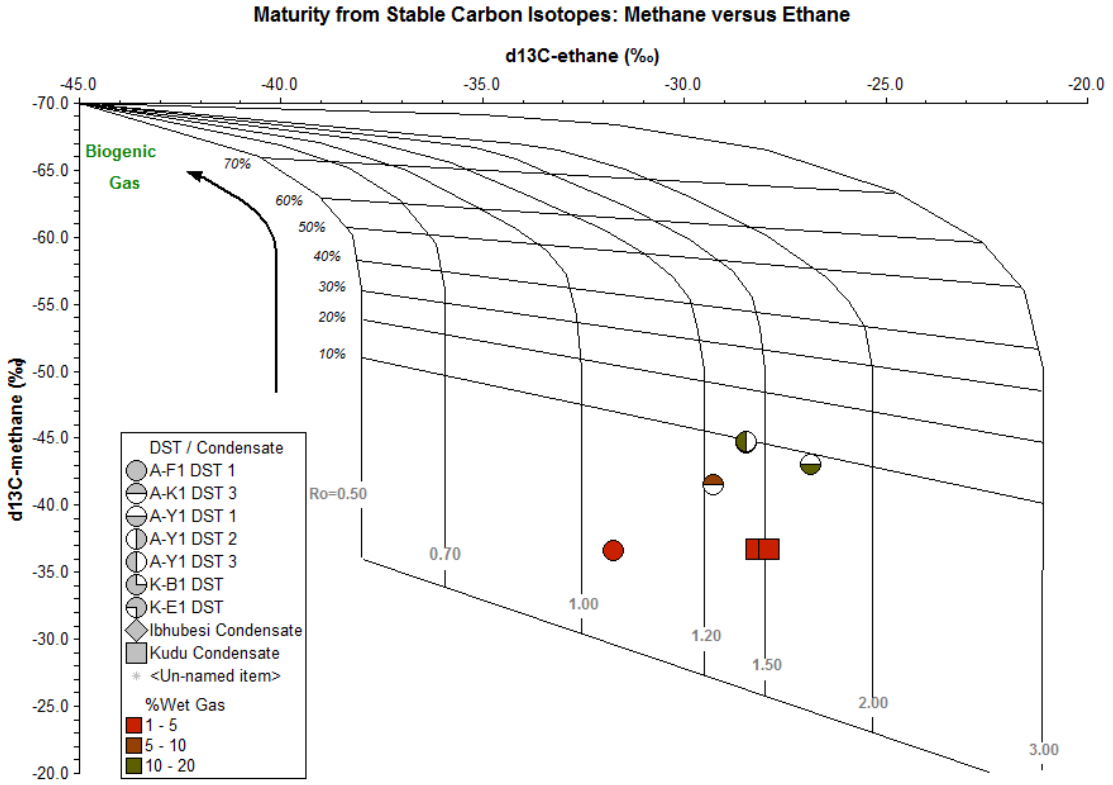

b

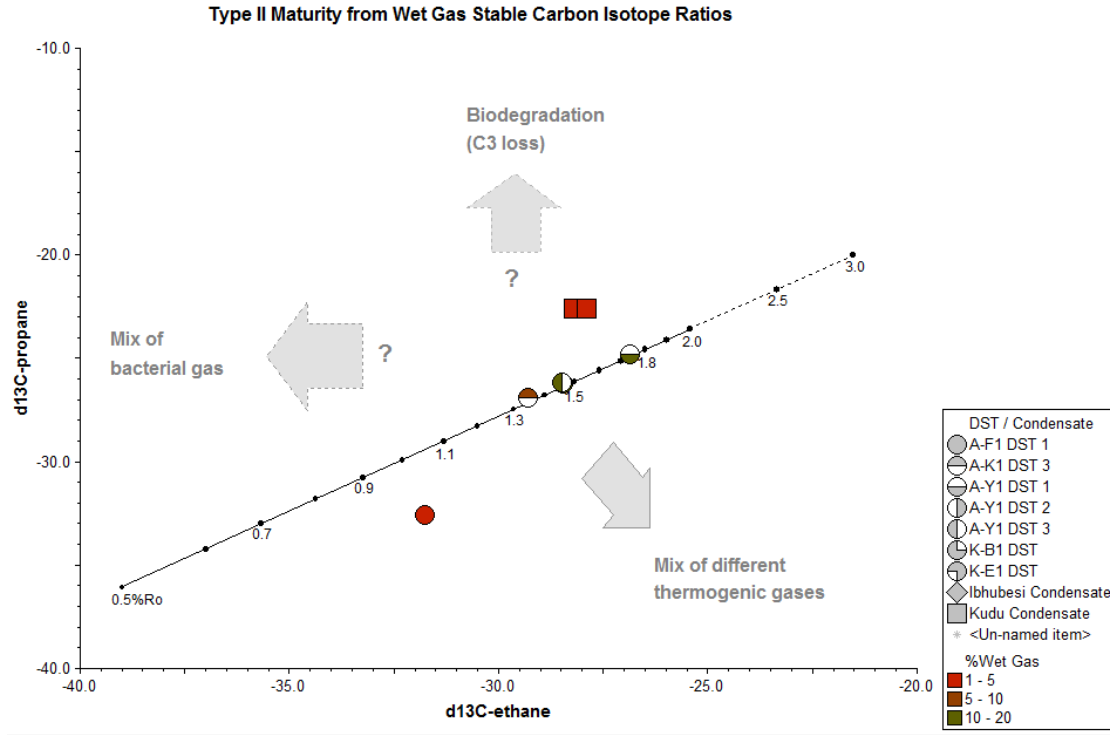

Figure 5-2: Maturity from $d^{13}C$ isotope measurements of Kudu, Ibhubesi reservoir fluids, and A-F1 well extract; a) $d^{13}C$ methane vs. $d^{13}C$ ethane; b) $d^{13}C$ ethane vs. $d^{13}C$ propane.

The $d^{13}C$ stable carbon isotope values of methane, ethane, and propane can be used to characterize hydrocarbon gases (Hunt, 1996; Laughrey and Baldassare, 1998; Schoell, 1983). The values may, however, be influenced by evaporative fractionation during migration or in the reservoir, the residence time in the reservoir, and multiple phases of petroleum charging of a reservoir, leading to an underestimation of maturity or mixing of gases from different sources (Laughrey and Baldassare, 1998; Schoell, 1983).

The plots of methane against ethane and ethane against propane for the Ibhubesi and Kudu condensates indicate condensate to dry gas maturity of the source rock at the time of petroleum generation. The equivalent range of vitrinite reflectance would be 1.2 – 1.8 % VR_O (Figure 5-2). The A-F1 well sample indicates a source that was in the late oil window, approx. 1.0% R_O, at the time of generation.

Plotting $d^{13}C$ methane values against gas wetness ($C_1/\Sigma C_{1-4}$, Laughrey and Baldassre, 1998) indicates that the samples from the Ibhubesi field are condensate- and possibly oil-associated (Figure 5-3). Laughrey and Baldassre (1998) mention that these types of gases may have formed during oil-generation or were associated with oils in reservoir but have since migrated to a new reservoir and retained their original isotope signature. Plotting the iso-butane/butane ratio versus gas wetness implies that the condensate may be derived from a mixed Type II/III kerogen. The Kudu condensate on the other hand may be characterized as thermal gas condensate (Figure 5-4). According to Laughrey and Baldassre (1998), this plot region describes condensate and gas generated or formed by secondary cracking at high maturities. The fate of the oil cannot be answered using these graphs. The results of Hartwig et al. (submitted; Chapter 4) suggest that any generated oil in the Ibhubesi area has undergone secondary cracking. This is supported by previous studies (e.g. Davies and van der Spuy, 1990; Schmidt, 2004). Thus, the condensate and dry gas from Kudu and Ibhubesi reservoir compartments are most likely a mixed product of secondary oil cracking and primary products of petroleum generation from a mixed gas-prone, predominately terrestrial source rock. Davies and van der Spuy (1990) note an absence of any bitumen in Kudu reservoirs side-wall cores. In the light of the modeling results (Chapter 4), this is interpreted as an indication for secondary cracking of unexpelled oil in the source rock rather than the reservoir.

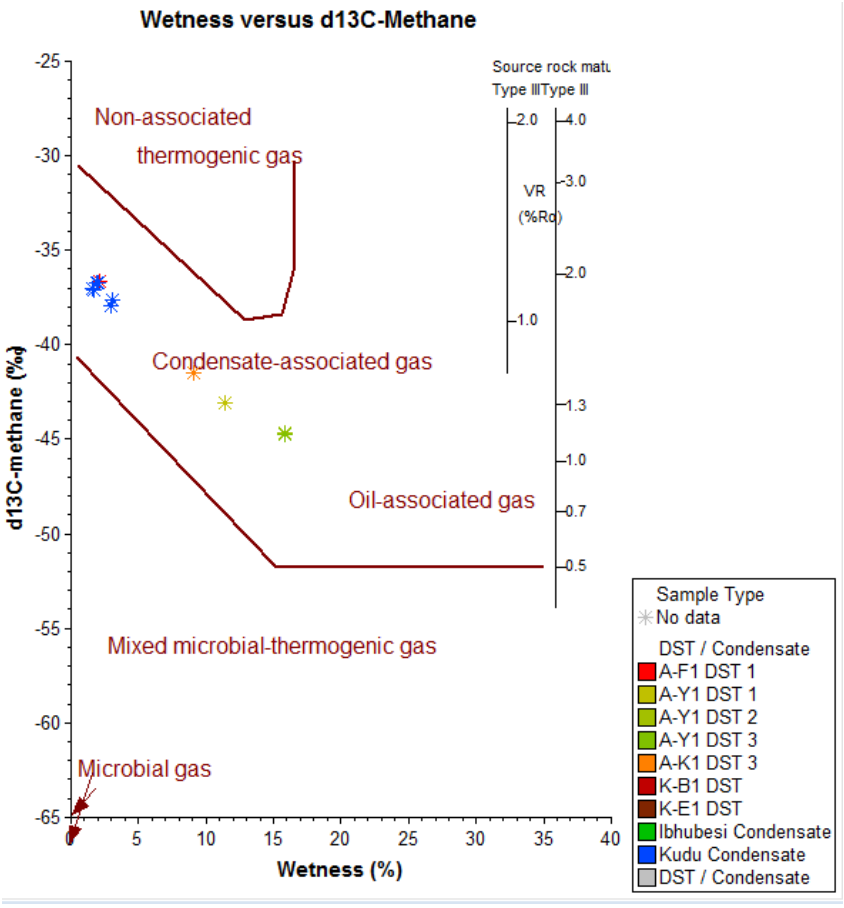

Figure 5-3: Gas-type from d^{13}C methane and gas wetness according to Laughrey and Baldassre (1998).

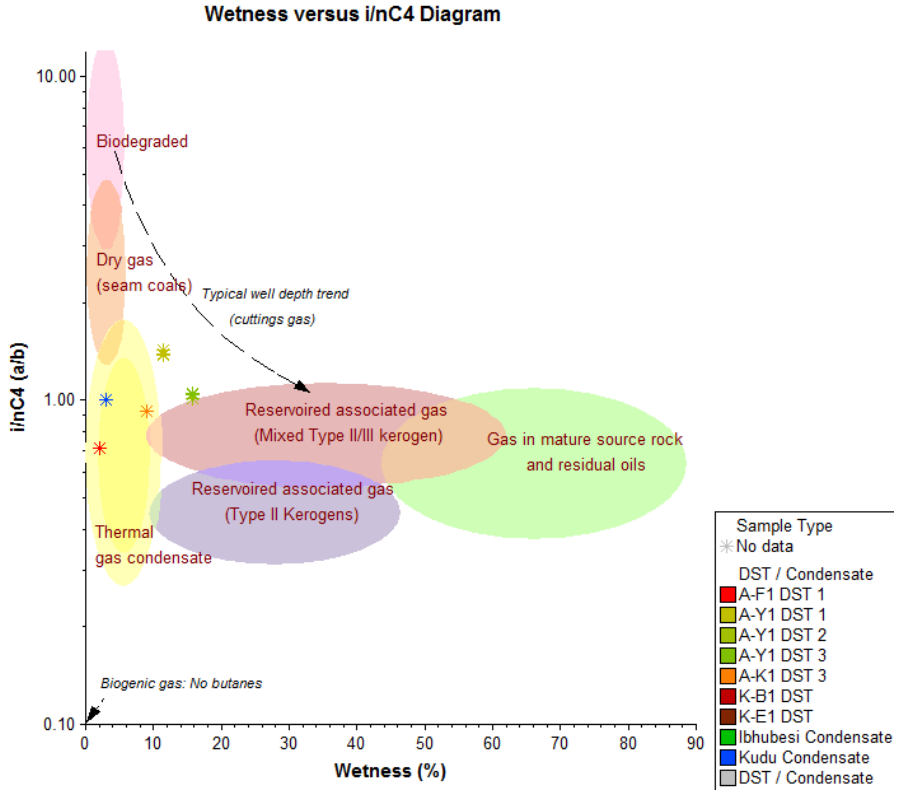

Figure 5-4: Gas type derived from iso-butane/butane ratio vs. gas wetness according to Laughrey and Baldassre (1998).

The Thompson plot is based on an empirical relationship of heptane and iso-heptane ratios that correlate to source rock type and maturity (Peters et al., 2005; Thompson, 1983). The Ibhubesi samples follow the aromatic (type III kerogen) trend line closely (Figure 5-5). Schmidt (2004) made a similar observation about the Kudu condensate and postulated that the condensate migrated laterally from a more proximal terrestrial-influenced source facies into the Kudu reservoir. The above-mentioned maturity of the Ibhubesi condensate and A-F1 well extract, as well as their aromaticity, make the Aptian type III organic-rich shale a very likely source rock for these hydrocarbons. According to the modeling results of Hartwig et al. (submitted Chapter 4) the Aptian source rocks had the corresponding maturity and remaining generation potential at those locations during its late stage of petroleum generation in the late Cretaceous to early Cenozoic. The studies and 1D burial models by Davies and van der Spuy (1990 and 1992) demonstrate the presence of an oil- and wet-gas prone early Aptian marine source rock and an older Barremian-Aptian gas-prone source rock that is absent south of the Kudu area. These authors postulate that the oil- and condensate was generated by the marine source rock during the late Cretaceous and early Cenozoic and migrated up-dip or was lost to the surface during the margin tilting tectonic phase. Any remaining petroleum and extractable organic matter in the marine source shales and tight siltstone layers would have undergone secondary cracking leading to the dry gas accumulations (Davies and Van der Spuy, 1992; Davies and van der Spuy, 1990; Schmidt, 2004). This scenario is supported by my 3D modeling results (Chapter 4), which predict a drastic change from liquid to predominately gas-filled reservoirs during the Cretaceous-Cenozoic transition. This is due to spilling and leakage of marine-sourced liquid petroleum during margin tilting, followed by secondary cracking of oil and recharge with light hydrocarbons and gas from the mixed marine-terrestrial source.

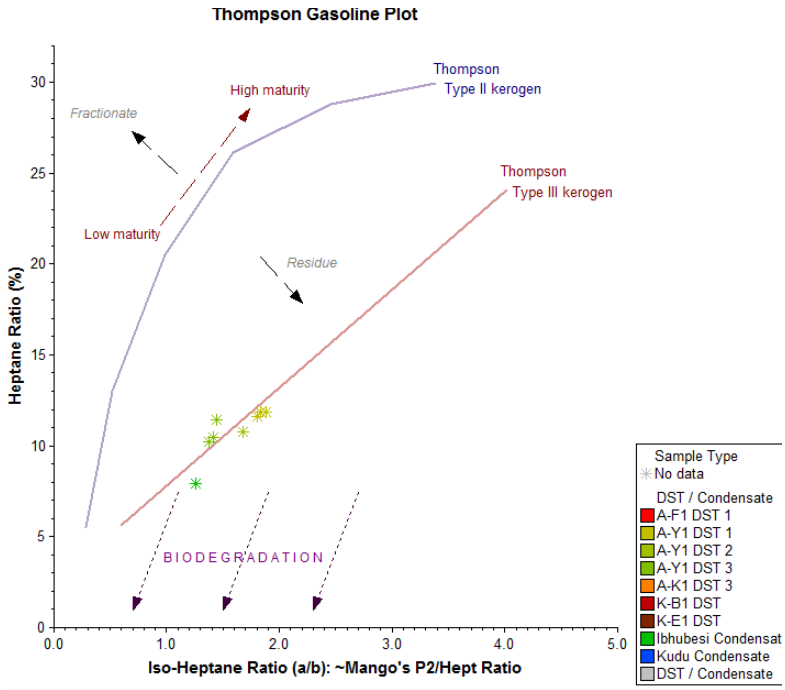

Figure 5-5: Thompson diagram to help determine source and relative maturity of light hydrocarbons.

5.2. Additional seismic interpretation results on synrift structures in the Orange Basin and new insights into the South Atlantic margin evolution and segmentation

The Petroleum Agency SA and PetroSA reprocessed several 2D seismic surveys to enhance the imaging of basement and rift structures, at max. depths of 5000 ms TWT in the northern Orange Basin. The interpretations of the basement structures not only helped to define the extent of the rift grabens and an economic basement for basin modeling purposes, but also to identify basement structures that give new insights into the rift evolution of the South Atlantic margin. Up to date, the evolution of the rift system that developed during the early break-up of Gondwana is not well constrained. The results presented below help to tie observations that were made on the conjugate margin of South America to the South African margin. New findings on the SDR morphology along the Orange Basin went into the interpretations presented by Koopmann et al. (2012) and published by Koopmann et al. (2014) that document new findings on SDR emplacement and margin segmentation along the South Atlantic margin. These results are outlined below.

The geologic evolution of the continental margin basins along the South Atlantic can be subdivided into synrift, rift-to-drift transition, and drift phases that were related to the progressive opening of the South Atlantic (Beglinger et al., 2012; Davison, 1999; Marcano et al., 2013; Torsvik et al., 2009).

The break-up of Gondwana was accompanied by Triassic to Jurassic intra-continental rifting, forming north-south trending grabens and half-grabens along the present-day southwest African margin (Coward et al., 1999; Gerrard and Smith, 1982; Karner and Driscoll, 1999). The conjugate Argentine margin, on the other hand, hosts east-west and northwest-southeast trending rift structures (Autin et al., 2013; Loegering et al., 2013; Marcano et al., 2013). This hints at a complex South Atlantic pre-rift evolution that involved NW-SE extension (Franke et al., 2006; Loegering et al., 2013) and the reactivation of Paleozoic basement structures on both sides of the incipient South Atlantic rift (Autin et al., 2013; Kounov et al., 2013).

The South Atlantic can be divided into southern and central segments that are separated by the Rio Grande Rise – Walvis Ridge (e.g. Torsvik et al. 2009; Blaich et al., 2009; Marcano et al., 2013). The existence of an evaporite rift-to-drift transitional sequence characterizes the central segment (Hudec and Jackson, 2004; Séranne and Anka, 2005; Torsvik et al., 2009; Beglinger et al., 2012), of which there is not any evidence in the southern segment. The southern segment is characterized by the existence of a prominent SDR wedge (Bauer et al., 2000; Franke et al., 2006; Gladczenko et al., 1997; Jackson et al., 2000) that can be subdivided into several sequences (Koopmann et al., 2012; Koopman et al., 2013 submitted), evidence for extensive volcanism along the margin during the final rift phase (Gladczenko et al., 1997). Onshore evidence are the large igneous province (LIP) of the Paraná-Etendeka flood basalts that erupted within a short time period 133-130 Ma and the accompanying

NW-SE and margin parallel trending dike swarms (Jackson et al., 2000; Torsvik et al., 2009). They can be linked to the Gough and Tristan da Cunha hotspots via their plume trails that formed the Rio Grande Rise – Walvis Ridge, respectively (Gladczenko et al., 1997; Jackson et al. 2000; Blaich et al., 2009; Torsvik et al., 2009). The presence of SDRs in the central segment has been inferred for the Brazilian margin, but they appear to be absent on the conjugate margin (Torsvik et al., 2009).

5.2.1. New findings on the South Atlantic margin segmentation in the Orange Basin

In an effort to define a base for the basin model an attempt was made to map the rift-onset unconformity. This interpretation contributed to the studies and publications of Maystrenko et al. (2013) and Koopmann et al. (2014) listed below:

Maystrenko, Y.P., Scheck-Wenderoth, M., Hartwig, A., Anka, Z., Watts, A.B., Hirsch, K.K., Fishwick, S., 2013. Structural features of the Southwest African continental margin according to results of lithosphere-scale 3D gravity and thermal modelling. Tectonophysics 604, 104–121.

Koopmann, H., Franke, D., Schreckenberger, B., Schulz, H., Hartwig, A., Stollhofen, H., di Primio, R., 2013. Segmentation and volcano-tectonic characteristics along the SW African continental margin, South Atlantic, as derived from multichannel seismic and potential field data. Marine and Petroleum Geology 50, 22-39.

The location of synrift graben and half-graben structures of the metamorphic basement were mapped and reported in previous studies (e.g. Gerrard and Smith 1982; Dingle et al. 1983). They trend north-northwest and are subparallel to the present-day coastline (Broad et al., 2006; Gerrard and Smith, 1982; Muntingh, 1993). Gerrard and Smith (1982) named the rift-onset unconformity horizon “T”, which forms the basal reflector of the synrift graben and can be correlated E-W from the coastline to the medial hinge line (sometimes called the Inner High) on 2D exploration seismic data. West of the medial hinge, the rift-onset unconformity dips steeply and is usually not well imaged on exploration seismic. Horizon T forms a westward-thickening synrift wedge with the overlying break-up unconformity. Gerrard and Smith (1982) and Dingle et al. (1983) mention that the rift-onset unconformity rises up towards the Outer High, where the synrift package appears to thin and pinch-out westwards. Wherever horizon “T” could be identified on 2D and 3D exploration seismic, it was mapped for this study and used as economic basement for the basin model along the eastern margin. There it represents the rifted metamorphic basement of the continental crust.

The initial opening of the South Atlantic was accompanied by extensive volcanism forming a transitional crust west of the medial hinge line with a thick SDR wedge to the west (Gladczenko et al., 1998) of the Orange Basin. The unusually wide (up to 200 km) transitional crust underneath the basin depocenter displays gently westward dipping seismic reflectors.

They are interpreted to consist of rapidly emplaced subaerial flood basalts (Bauer et al., 2000) that pinch-out along the continental crust (Gerrard and Smith, 1982; Dingle et al., 1983). Within the framework of this thesis' basement interpretation, the SDR morphology was mapped in detail (Figure 5-6). These findings are reported in Koopmann et al. (2012) and Koopmann et al. (2013). They identified at least four subsequent phases of SDR wedge emplacement during rifting. The undulating morphology of the SDR boundaries is interpreted as variations in extruding magma volumes and differences in post-rift margin subsidence (Koopmann et al., 2014). The observations on SDR morphology and occurrence further helped to characterize the margin segmentation and allow new insights into the South Atlantic rift evolution. Based on this Koopmann et al. (2012) and Koopmann et al. (2013) identified four greater margin segments from the Agulhas-Falkland Fracture Zone in the south to the Walvis Ridge in the north. Their greater segment I is magma poor and stretches from the Agulhas-Falkland Fracture Zone to offshore Cape Town. In contrast, their greater segment II, which coincides with the north-south extent of the Orange Basin depocenter and hosts extensive SDR sequences, is indicative of voluminous volcanism during rifting. Similar observations are reported for the conjugate Argentinian margin by Franke et al. (2010).

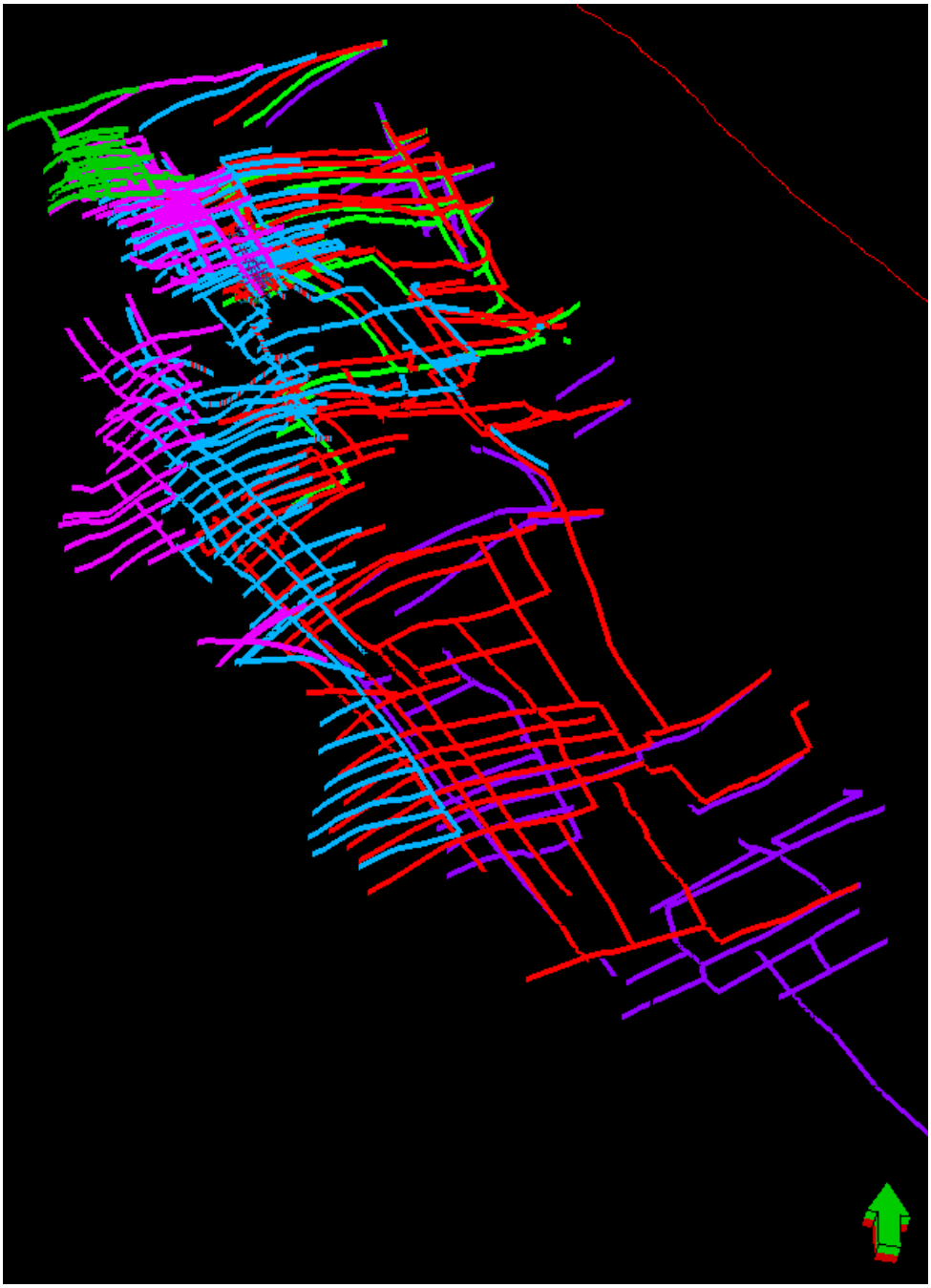

Figure 5-6: Oblique view of the Orange Basin margin showing the SDR interpretation with its distinct concave-down morphology. The different wedges are signified by different colors and can be correlated along the margin. The offshore end marks the limit of seismic coverage. The SDR order is best visualized by the northernmost seismic interpretation along the South African-Namibian border. Note the undulating morphology of individual SDR boundaries, which is a result of differential subsidence and variations in magma volumes.

A new and very distinct observation is the left lateral offset and apparent north dipping of the SDRs in the northern Orange Basin. This challenges the current simple SDR emplacement model, in which SDR flows are orthogonal to the spreading axis and subjected to homogeneous subsidence (Koopmann et al., 2013). The SDR offset occurs along an ancient fault zone that may be linked to the Gariep Fold Belt (Koopmann et al., 2013). This zone of weakness is also in the vicinity of the early Eocene pockmark field, the Miocene mud

volcanoes and a very prominent slump west of Childs Bank (Dingle, 1980), which is visible on bathymetry maps (Figure 3-5a) and of possible Pliocene age.

Greater segment II correlates well with the findings of Maystrenko et al. (2013). Their 3D crustal model captures the extent of a high-density crustal body below the SDR wedges and the Cretaceous-Cenozoic depocenters from the southern Orange Basin to the Walvis Ridge. The presence of this high-density and high-velocity body was also proposed by previous 2D modeling studies (Bauer et al., 2000; Gladczenko et al., 1998; Hirsch et al., 2009). These high-density crustal bodies are often associated to mafic magmatic material that was emplaced during rifting, also referred to as underplating (Maystrenko et al., 2013; Hirsch et al., 2009; Bauer et al., 2000). The preliminary SDR and refraction seismic interpretations of Koopmann et al. (2013), as well as the available modeling results of Maystrenko et al. (2013) at the time of the 3D basin model construction, were used to approximate the location of the continent-ocean boundary, i.e. the occurrence of true oceanic crust.

5.2.2. Synrift basement structures in the Orange Basin

This 2D seismic interpretation of the basement revealed NW-SE trending basement structures on the rift-onset unconformity, west of the medial hinge line. Especially in the south these structures can be mapped up to 60 km west of the medial hinge line where subaerial flood basalts and post-rift sediment cover are comparatively thin (Figure 5-7). The NW-SE trending basement structures are interpreted to be closely related, or even a continuation of Paleozoic zones of weakness of the Cape Fold Belt.

Tankard et al. (2009) mention Paleozoic (Ordovician) NW-trending rift structures and pull-apart basins in the Saldanha area of the Cape Fold Belt. These are related to the Cango and Worcester fault zones that are inferred to have formed by dextral movement along the Pan-African fold belt. This phenomenon can also be observed on the conjugate margin (Tankard et al., 2009). Thus it is inferred that Paleozoic NW-trending rift structures are present in the metamorphic basement of the offshore Orange Basin as well.

The Namibian margin may be taken as an analogue for this. There, Gladczenko et al. (1998) reported pre-Jurassic rift basins that occur below the Cretaceous rift deposits. The authors suggest, that these structures are directly linked to the Damara Fold Belt and its lineaments, which can also be traced beneath the northern Orange Basin (Bauer et al. 2000)

Similar structural trends are observed on the conjugate South Atlantic margin in the Salado and Colorado Basin, Argentina, and are interpreted to result from N-S extension along the Paleozoic basement fabric (Autin et al., 2013; Dingle, 1980; Loegering et al., 2013). Loegering et al. (2013) and Autin et al., (2013) clearly identified NW-SE trending fault zones that control the location of early synrift depocenters.

Several authors (e.g. Franke et al., 2006, Tankard et al., 2009; Autin et al., 2013) have proposed dextral movement during the early phase of Gondwana rifting, which causes dextral movement during the break-up of Gondwana and a reactivation of NW trending fault zones in the Paleozoic basement.

Since the Colorado and Orange Basin are conjugate margins and were likely subjected to the same tectonic stresses, there must be a common origin of these structures. The metamorphic basement of the Orange Basin was already subjected to extensional tectonics during the late Jurassic synrift I phase (Broad et al., 2006; Light et al., 1993), when the Outeniqua Basin of southern Africa and the Malvinas and Falkland Basin of South America had already begun to open (Macdonald et al., 2003). In fact, this allows connecting the NW-SE structures of the Outeniqua Basin along the Cape Fold Belt with the NW-SE basement structures mapped in the Orange Basin and the NW-SE trending Eastern and Central synrift segments of the Colorado Basin as defined by Autin et al. (2013).

Further investigations are needed to confirm, whether these NW-SE trending structures played any role in the formation and location of the Inner and Outer basement highs of the Orange Basin.

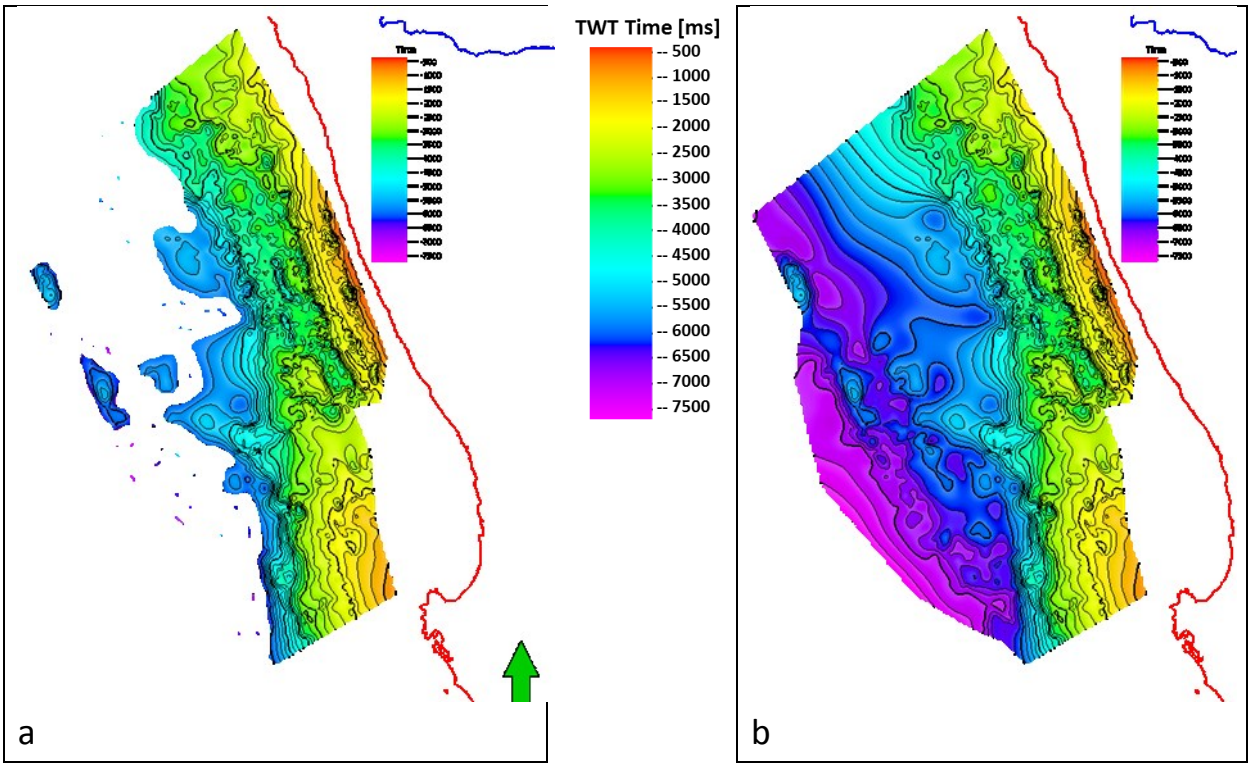

Figure 5-7: TWT on acoustic basement. The interpretation shows the location of coast parallel synrift graben in the metamorphic basement and a NW trending basement high in central study area, interpreted as a remnant of the early rift phase. Similar trending basement structures also occur along the conjugate margin. (a) Basement features that were identified across several 2D seismic lines. (b) Interpolated top of economic basement map. This map was gridded using all basement reflections, even if they were not identified on the next 2D seismic line.

5.3. A new approach to the evaluation of paleo- and present-day hydrocarbon leakage dynamics using 3D basin models

5.3.1. Hydrocarbon loss calculations

The author refrains from making any quantitative analysis of hydrocarbon leakage using the basin modeling results, because the source rock richness and distribution is not well enough constrained for the Orange Basin. The modeling results are based on the bulk source rock and basin evolution inputs of the basin modeling study described in Chapters 2 and 4, and are interpreted in the framework of Chapters 3 and 4.

Two aspects regarding the hydrocarbon migration and leakage dynamics need to be evaluated. First, how does the timing of the main phase of hydrocarbon generation compare with top-outflow rates? Secondly, when did the main phases of hydrocarbon accumulation in reservoirs occur versus the main phases of hydrocarbon leakage? A great part of this has already been addressed in Chapter 4. At this point the results from five different hydrocarbon flow simulations will be compared using PetroMod 2011 calculations for hydrocarbons accumulated in reservoir and model top-outflow. It is assumed that top-outflow captures thermogenic hydrocarbon leakage at the sediment-surface interface at all scales for each modeled time-step.

The five different flow simulations come from three models that used the Hybrid method (Darcy + Flowpath) simulation for an open, closed, and initial (variable timing of open and closed) fault scenario, and two models simulated with the Invasion Percolation method (IP) for the open and initial fault scenario. The initial fault model is most likely the closest representation of the geologic behavior of the faults in the Orange Basin. The fault property assumptions are based on the results of seismic interpretation and a review of the literature on the margin evolution and the timing of tectonic activity. The open and closed scenarios represent end-members in the role of faults during migration, which were discussed in Chapter 4.

For the Hybrid models, the main phases of accumulation in reservoirs are (1) the early late Cretaceous, which corresponds to the main phase of petroleum generation in the Cretaceous OB depocenter, and (2) the latest Cretaceous/Paleocene, an episode of shelf erosion and margin tilting that resulted in burial and source rock maturation along and beyond the shelf edge (Figure 5-8). The second phase of hydrocarbon accumulation in reservoirs is not as pronounced in the IP models, resulting in a net-loss from reservoirs (Figure 5-8). The main phases of top-outflow in the open and closed fault Hybrid models occur (i) during the early Cretaceous when a regional seal was not yet in place, (ii) during the late Cretaceous faulting and shelf collapse, when vertical migration paths are added to the model, and (iii) during the latest Cretaceous/Paleocene margin tilting and erosion. In the closed-fault Hybrid model top-outflow occurs predominately during margin tilting. The initial variable-fault Hybrid model, of course, captures the top-outflow losses due to both faulting and margin tilting during the late Cretaceous and early Cenozoic. Defining ages for fault

activity, allowing them to act as fluid conduits during certain tectonic phases, introduces another variable to the timing of losses.

The open and initial variable-fault IP models show a slightly different picture. Outflow at the top is greatest during periods of hydrocarbon generation and during fault activation in the early late Cretaceous and latest Cretaceous/Paleocene. This apparent synchronization of hydrocarbon generation and immediate loss are due to the assumption of instantaneous hydrocarbon migration during each time-step in IP flow modeling. The early Cretaceous top-outflow event appears to be relatively smaller.

In all but the initial Hybrid model, hydrocarbon accumulation and top-outflow are generally synchronized due to either the end-member Hybrid scenario or the IP simplification. Thus the timing of hydrocarbon generation and tilting of carrier beds are the main control on the timing of leakage in these model scenarios.

It follows that the relative timing of hydrocarbon leakage can only be investigated with the initial variable-fault Hybrid model, as described in Chapter 4. The two main phases of reservoir charging correspond to the two main phases of petroleum generation (Figure 5-8). These are (1) the Cenomanian-Santonian phase of petroleum generation in the Cretaceous depocenter and (2) during the latest Cretaceous/Paleocene phase of petroleum generation along the shelf and the deepwater Orange Basin. Loss at the sediment-surface interface (top-outflow) is delayed until the next important tectonic event. The largest increases in top-outflow occur during the early Albian and the early Eocene. The late Cretaceous top-outflow event is only the third important event in this model. Interestingly, the early Eocene event is concomitant with a major fluid flow and paleo-leakage event reported by Hartwig et al. (2012a, Chapter 3). This early Eocene paleo-pockmark field at the shelf-break of the northern OB has been interpreted as a result of thermogenic gas and over-pressured pore fluids being expelled to the surface along faults. Thus, the model lends further support to these interpretations. The Paleocene-Eocene is also a time of active tectonics in the basin, characterised by fault reactivation, on- and offshore volcanism, and a shift in sedimentation patterns from the northern to the southern Orange Basin as mentioned in Chapters 3 and 4.

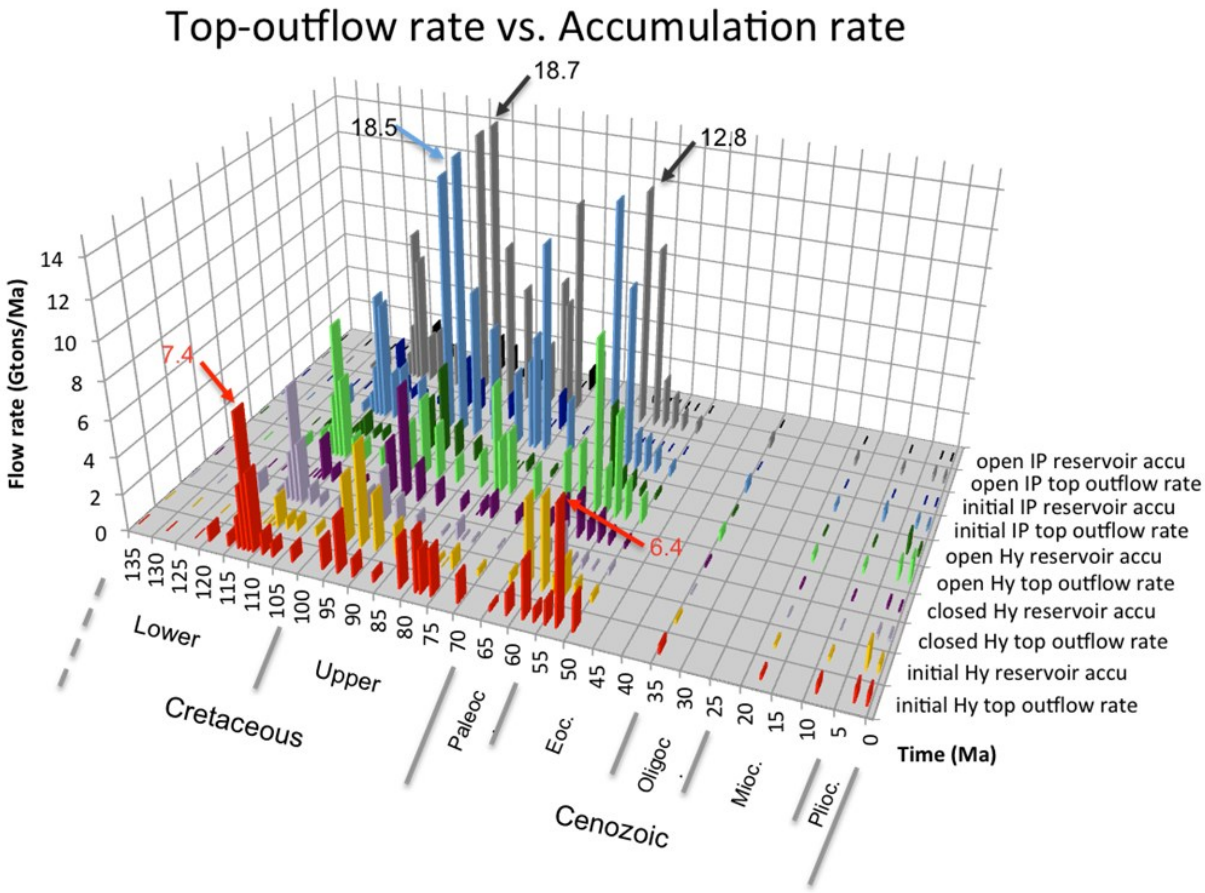

Figure 5-8: Estimated Hydrocarbon top-outflow and accumulation rates for each time step of the Hybrid (Hy) and Invasion Percolation (IP) models using various fault property scenarios.

5.3.2. Paleo and present-day hydrocarbon leakage as calibration tools for 3D basin models

3D basin models are used to make predictions on subsurface accumulations and thus, indirectly simulate hydrocarbon losses as well. Hence, past and present-day fluid flow features, their surface and subsurface expressions, especially if resulting from thermogenic hydrocarbon leakage, can be used for model calibration. In fact, the study of surface seeps should be used for all flow simulation studies. Such data should be readily available since seep studies are a traditional exploration tool that reduces the exploration risk (Hunt, 1996; Judd and Hovland, 2007). The present-day seafloor fluid flow features shown by Hartwig et al. (2012a, Chapter 3) were compared to the flow modeling results presented in Chapter 4 and discussed therein. At basin scale, the areas of observed and modeled hydrocarbon leakage correlate well to one another. This is an indication that hydrocarbon migration dynamics at this scale can be adequately addressed for the Orange Basin with the present 3D basin model. Also previous petroleum system modeling studies were able to reproduce these present-day fluid flow and potential hydrocarbon leakage sites of the Orange Basin by means of 2D and 3D basin models (Boyd et al., 2012; Kuhlmann et al., 2010; Paton et al., 2007).

The use of paleo-fluid flow features is largely constrained by the scale and data quality, which document the event. Several authors (Andresen and Huuse, 2011; Andresen, 2012; Anka et al., 2013; Gay et al., 2006a; Imbert and Ho, 2012) have demonstrated that it is possible to constrain such paleo-leakage to a mechanism and time period. Using 2D basin modeling techniques Naeth et al. (2005) and Anka et al. (2013) have also been able to correlate fluid flow features with the structural elements of the basin and the predicted migration pathways from modeling. In this study, an attempt is made to use both present-day and paleo-leakage sites to test the validity of a thermogenic hydrocarbon-sourced fluid flow for past and present-day events using a 3D basin model. The 3D modeling approach provides a 3-dimensional full-physics solution for hydrocarbon migration. This allows the modeler to constrain the source, timing, direction, and magnitude of hydrocarbon migration in the context of the basin evolution. To the author's knowledge the modeling of and calibration to interpreted paleo-leakage events using 3D basin modeling techniques has not been attempted to date.

For instance, it is assumed that a causal relationship exists between the early Eocene pockmark field interpreted from seismic (presented in Chapter 3) and the modeled early Eocene hydrocarbon-loss event (presented in Chapter 4 and section 6.1.). On one hand, Hartwig et al. (2012a, Chapter 3) argue that the exact paleo-fluid flow triggering mechanism is not completely understood, but may be related to tectonic uplift and an active hydrocarbon kitchen at that time. The initial variable-fault Hybrid model further indicates that fault reactivation played a decisive role in the hydrocarbon migration dynamics of the Orange Basin. Under these circumstances, hydrocarbon leakage is predicted to occur during the early Eocene and roughly in the same location where the paleo pockmark field is observed. However, since the relative timing of basin events in the 3D basin model depends on the input ages and fault property definitions, there is a risk of circular logic. Nonetheless, all model scenarios (Hybrid and IP, -open, -closed, -initial) indicate that the latest Cretaceous-Paleocene transition was a phase of active petroleum generation accompanied by secondary cracking reactions, and all models reproduced a major Paleocene-Eocene hydrocarbon loss event independent of fault properties (Figure 5-8). Therefore, as a result of this study, a relationship between the location of the latest Cretaceous/Paleocene active kitchen and the Paleocene/early Eocene leakage site can be established.

The initial variable-fault Hybrid model seems to capture the basin evolution and relative timing of tectonic events better than any of the other four models. Since 4-component kinetic models were used in this study, the model's top-outflow rates can be further subdivided into oil and gas phases (Figure 5-9). This indicates that gas (C1-C5 components) was the dominant phase of leaking hydrocarbons. Overall, this lends further support to three of the assumptions made in Chapter 3: (1) hydrocarbons were actively generated prior to the leakage event, (2) the involved leaking fluids contained thermogenic gas, and (3) tectonic activity either in the form of margin tilting or fault reactivation influenced the timing of the leakage event and acted as a focusing mechanism. Other paleo-leakage events, such as the Miocene mud volcanoes (Ben-Avraham et al. 2002; Viola et al., 2005), which occur in the same area as the early Eocene paleo-pockmark field, are clearly related to the large fault

system (Viola et al., 2005; Boyd et al., 2012). The modeled time steps for the Miocene, however, do not display any large leakage events during this time. This may result from the low temporal resolution for that time period. It could also be argued that the Miocene mud volcanoes were created through a different mechanism other than petroleum generation-related overpressure, and hence it would not show up on the mass balance calculations of the models. However, the current study cannot resolve this issue. The most recent episode of hydrocarbon leakage, interpreted to have taken place during the Pliocene and present-day, is represented in the open and initial variable fault Hybrid model (compare with Chapter 3 and 4). This episode led to the formation of pockmarks that were identified on 3D exploration seismic of the present-day seafloor (see Chapter 3).

Nevertheless, similar paleo-fluid flow events will have to be investigated in basin settings with less geologic uncertainties than in the Orange Basin. This could help to confirm the reliability of 3D basin model calculations regarding paleo hydrocarbon leakage events.

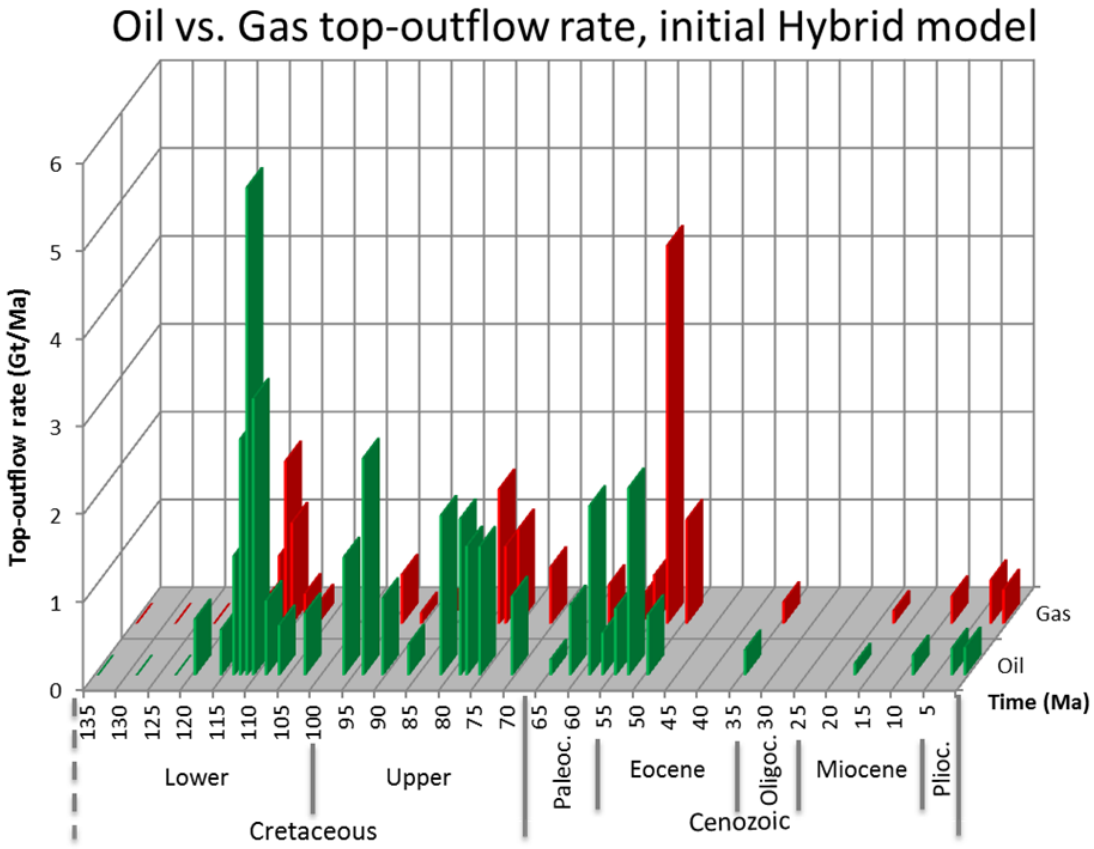

Figure 5-9: Oil (green) vs. gas (red) top-outflow rates from the initial variable-fault property Hybrid model. Oil outflow rates are highest before the regional seal is consolidated, whilst the highest gas outflow rates are reached during the early Eocene after the onset of secondary cracking (compare with Figure 4-15).

5.3.3. The Paleocene-early Eocene paleo-leakage event in the Orange Basin from a global paleo-climate perspective

Kroeger and Funnell (2012) mention two possible mechanisms that could have led to an increased rate of hydrocarbon generation in sedimentary basins during the late Cretaceous-early Cenozoic transition: (1) an increase of sedimentation rates during the late Cretaceous-Paleocene that led to higher hydrocarbon generation rates as reported by Klemme and Ulmishek (1991), and (2) the synchronization of hydrocarbon generation across basins due to higher Paleocene-Eocene sediment surface temperatures. Following the discussion of the modeling results presented in the previous section, hydrocarbon generation and leakage phases during the Cretaceous and Paleocene/Eocene in the Orange Basin, respectively, were linked to sedimentation rates and tectonic activity. If higher Paleocene-Eocene surface temperatures (e.g. Kroeger and Funnell, 2012; Svensen et al., 2004; Zeebe et al., 2009) were taken into account, the overall modeled amount of generated hydrocarbons is expected to increase accordingly. This scenario would have the largest effect on the source rocks of the lower slope and deep-water Orange Basin, which were going through the early-to-late oil window during that time (see chapter 4).

A follow-up study should investigate in more detail the effect of an increased surface temperature on hydrocarbon generation and leakage rates in the Orange Basin. This could be accompanied by end-member testing of source rock richness. The current model configuration assumes a relatively rich suite of source rocks with an initial HI of 550 mg/g and an initial TOC of 8%. These values are based on core measurements of Hartwig et al. (2012b) and literature data (Davies and Van der Spuy, 1992; Jungslager, 1999; Schmidt, 2004).

In order to evaluate the significance of the identified Paleocene-Eocene leakage event from a global climate perspective, the top-outflow rates from the open fault IP and the initial variable fault Hybrid model were calculated. The basic assumptions are: (1) the source rock descriptions of both models represent a rich end-member scenario; (2) the open fault IP model is an end-member leakage scenario, as it produced the highest leakage rates of any model; (3) the initial variable fault Hybrid model is the best representation of timing of geologic events; and (4) the top-outflow represent an average value for both macro and micro, cumulative seepage rates. As mentioned above, there are two major leakage events, (i) an early Upper Cretaceous event due to an absence of a regional seal and (ii) the Paleocene-Eocene leakage due to margin tilting possibly accompanied by fault reactivation. The open fault IP model yields leakage rates of 1.87 x 10-2 teragram/year (Tg/yr; = 18.7 gigatons/million years (Gt/Ma)) and 1.28 x 10-2 Tg/yr (= 12.8 Gt/Ma) for the early Upper Cretaceous and Paleocene-Eocene events, respectively. The initial variable fault Hybrid model yields 7.4 x 10^{-3} Tg/yr (= 7.4 Gt/Ma) and 6.7 x 10^{-3} Tg/yr (= 6.7 Gt/Ma) respectively.

The above values do not take oxidization or solution processes into account that occur within the first few hundred meters of the water column and in the shallow subsurface. Thus, the actual contribution of methane from the subsurface to the atmosphere is likely lower (Kroeger et al., 2011). In comparison, the calculated annual peak leakage rates for the

Orange Basin fall within the 10^{-2} to 10^{-3} Tg/yr leakage rate range calculated for the Western Canada Sedimentary Basin (WCSB) and the Central Graben (CG) of the North Sea (Berbesi et al., 2014).

In order to put the leakage rates into a global perspective, it is assumed that methane is the main component of the leaked hydrocarbons. Thus, the average peak leakage rates for thermogenic methane from the Orange Basin, the WCSB, and the CG are about five magnitudes lower than the present-day annual methane exchange rates of 500-600 Tg/yr (Etiope, 2009; Judd and Hovland, 2007; Kroeger et al., 2011; O'Connor et al., 2010; Westbrook et al., 2009). They are also four magnitudes lower than the current estimates for cumulative annual leakage from submarine seeps in the order of 20 Tg/yr (Judd and Hovland, 2007; Etiope, 2009). Large uncertainties are associated to such estimates, thus the values for annual global onshore and offshore methane leakage rates vary between 40 – 60 Tg/yr (Etiope, 2009; Etiope et al., 2009; Kroeger et al., 2011; Milkov, 2004). The values reported by Etiope (2009) are primarily based on flux measurements at macro seep sites (mud volcanoes, active pockmarks, etc.), which may cause a bias towards high values, whereas the basin model calculations represent average values for macro and micro seepage across an entire basin. Since the peak leakage rates for the OB, WCSB, and CG are also associated to periods of peak generation, it seems unlikely that it could affect global climate. In either case, the leakage rates of thermogenic hydrocarbons from sedimentary basins are minor on a global scale, when compared to greenhouse gas emissions from wetlands (92 – 237 Tg/yr,), and anthropogenic sources (75 – 110 Tg/yr, Judd and Hovland, 2007; Kroeger et al., 2011; O'Connor et al., 2010). A focusing mechanism for migrating thermogenic methane is required to achieve the higher leakage rates, as suggested by Berbesi et al. (2013). Effective focusing of migration has been shown to occur along faults (Cartwright et al., 2007; Etiope, 2009; Hartwig et al., 2012a; Hunt, 1996; Judd and Hovland, 2007; Løseth et al., 2009; Ostanin et al., 2012; Westbrook et al., 2009).

One aspect that is generally not considered in petroleum system flow simulations is a meta-stable methane repository, such as methane hydrate occurrence. Methane hydrate accumulations contain biogenic and thermogenic gas (Majorowicz et al., 2012; Milkov, 2004), which was generated and bound over long periods of time. Due to their ability to store and suddenly release significant volumes of gas accumulated through transient leakage, methane hydrates appear to be more significant on a paleo- and present-day global climate perspective than the transient leakage from sedimentary basins discussed above (Berbesi et al., 2014; Buffett and Archer, 2004; Dickens et al., 1997, 1995; Kroeger et al., 2011). Westbrook et al. (2009) estimate, that warming by 1°C during the recent years, may have led to the release of 20 Tg/yr of methane in the Svalbard area alone. Davy et al. (2010) estimated that the sudden destabilization of methane hydrates during glacial-interglacial transitions may have led to the formation of giant gas escape features with diameters of up to several kilometers. One such feature could potentially release up to 7 Tg of methane at once (Davy et al., 2010). Similarly, Imbert et al. (2012) reported Paleocen-Eocene-aged "fossil hydrate pockmarks" offshore northwestern Australia. Imbert et al. (2012) propose a thermogenic origin for the methane and discuss their interpretation in the context of

potential climatic feedback mechanism during the PETM. This emphasizes the importance of taking methane hydrate formation, dissociation, and focused fluid flow into account when investigating potential feedback mechanisms between thermogenic gas leakage from sedimentary basins and global climate change (Berbesi et al., 2014; Imbert and Ho, 2012; Kroeger et al., 2011; Majorowicz et al., 2012).

Future studies should investigate peak and average hydrocarbon leakage rates across different basins settings, in order to estimate the amount of time it takes to build up a climatically significant amount of methane hydrate, globally or regionally, similar to the studies by Kroeger and Funnel (2012) and Berbesi et al. (2013). Further, a comparison of these masses with potentially catastrophic dissociation rates of such reservoirs is required. A significant amount would be in the order of 1500 – 4000 Gt of biogenic and thermogenic carbon (Bowen, 2013; Dunkley Jones et al., 2010; Kroeger et al., 2011; Zeebe et al., 2009) needed to explain the $d^{13}C$ carbon isotopic excursion observed during the PETM. A starting point would be to identify sedimentary basins that experienced peak hydrocarbon generation during the latest Cretaceous-early Cenozoic transition and show evidence of Cenozoic paleo-leakage events such as the Orange Basin (Hartwig et al., 2012a), or offshore Australia (Imbert and Ho, 2012; Kroeger and Funnell, 2012). 3D basin modeling studies can help calculating average leakage rates prior, during, and after such events. If enough data on the area of leakage is available, hypothetical methane hydrate build-up rates and volumes can be calculated to put each basin into a global perspective. Given enough temporal (chronostratigraphic) resolution of seismic data, it may even be possible to locate regions that exhibit a quasi-simultaneous occurrence of paleo-leakage features across several basins.

6. Integration & Summary

The aim of this study was to characterize the hydrocarbon migration dynamics in the Orange Basin through time and to investigate its potential impact on global climate on a geologic time scale. One of the major challenges of this study was to identify the location of the recent and active hydrocarbon kitchen in the basin and to compare the petroleum migration modeling results to known occurrences of hydrocarbon leakage in the basin.

6.1. Interpretation of the relative timing of paleo-fluid flow events using a refined Cenozoic chronostratigraphy

The basin scale seismic interpretation study was conducted to refine the chronostratigraphic interpretation for the Cenozoic sediments from the shelf break to the deepwater Orange Basin and correlating them with onshore events. This was achieved through integration of the current chronostratigraphic interpretation of the Orange Basin shelf and literature regarding the Cenozoic onshore margin evolution with interpretations from the IODP drilling program using 2D and 3D exploration seismic data sets.

The interpretation captures some of the major tectonic events of the Cenozoic. These are the major margin tilting events during the late Cretaceous and Mio-Pliocene, and subtle uplifting during the Paleogene, which may tentatively be correlated to an episode of early Cenozoic on- and offshore volcanism. The chronostratigraphic framework was applied to constrain the relative age of paleo-fluid flow features that were interpreted on seismic during this and previous studies.

Thus, a distinct seismic horizon with circular depressions was identified on the 3D and 2D seismic reflection data sets and assigned an early Eocene age. These depressions are interpreted as paleo-pockmarks. This is the first time that paleo-leakage features are identified in the Orange Basin. The paleo-pockmarks cover an area of more than 2800 km^2 along the slope of the northern Orange Basin and appear both as single pockmarks and predominantly NNE-SSW aligned pockmark trains. The pockmark trains occur at the paleo-shelf break and follow the Eocene paleo-slope's dip direction. Their location is controlled by the underlying listric faults system of the Eocene paleo-slope. It is proposed here that the spatial and temporal occurrence of these paleo-pockmarks is associated to two episodes of fast sedimentation during late Maastrichtian to Paleocene in the northern Orange Basin. It was hypothesized, that the formation was a result of pore fluid overpressure due to disequilibrium compaction during burial, which was further enhanced by maturation of the source rock and thermogenic gas expulsion. The full physics 3D basin model and the evaluation of the top-outflow rates lend additional support to the latter part of this hypothesis.

Studying the role of the faults as active fluid conduits, however, proved to be difficult. The 3D seismic attribute analysis was able to highlight the fault-to-pockmark correlation regarding their location. Furthermore, the modeling results imply a flow rate enhancing

effect of the faults. But due to the low sedimentation rates during the early Cenozoic, extensive shelf erosion, and frequent fault reactivation, the actual fluid pathways could not be identified on seismic. This leaves an uncertainty with respect to the role of overpressure as initiating mechanism for fluid flow. It is possible that an unidentified non-overpressure related factor contributed to the pockmark formation, such as the lithologic composition. On the other hand, the Miocene mud volcanoes seem to be rooted above the Turonian shale sequence and occur along the same faults as the early Eocene pockmark field. This observation provides credibility for the proposed overpressure occurrence during the early Eocene. The early Eocene paleo-pockmark field, the Miocene-aged mud volcanoes, and the present-day seafloor pockmarks are evidence for reoccurring pore fluid over-pressures in the slope of the northern Orange Basin and should be considered as a potential geohazard.

6.2. Basement structures along the South African continental margin

The new findings regarding NW-SE structural trends of the basement are perhaps not so significant from a petroleum exploration point of view, but they shed new light on the early rift evolution during the break-up of Gondwana. It is proposed, that they are a continuations of Paleozoic structures of the Pan African Fold Belt, similar to those found offshore the Damara Fold Belt in Namibia and on the conjugate South American margin in the Colorado and Salado Basins. These findings in the Orange Basin lend additional support to the theory, that early rifting during the break up of Gondwana resulted in reactivation and dextral movement along Paleozoic zones of structural weakness.
Similar prominent basement-controlled offsets were discovered within the SDR sequence of the Orange Basin. The seismic basement interpretation, on SDR wedge morphology in specific, further contributed interpretations to studies that led to new insights on the characteristics of the margin segmentation and SDR emplacement, as well as the crustal structure along the South African margin.

6.3. Source rock characteristics of Cretaceous organic-rich black shales and mudstones from the South Atlantic margin

The geologic and tectonic evolution of the nascent South Atlantic during the early to late Cretaceous exerted a strong control on source rock richness. The source rock characterization study of the DSDP wells 361, 530A, and 364, demonstrates how the bulk properties, such as richness and quality of the Cretaceous black shales and mudstones, improve northward along the South Atlantic margin. This is depicted in the bulk kinetic models and petroleum type prediction from artificial maturation experiments conducted on the thermally immature black shale and mudstone samples.
The kerogen type improves from a (sometimes sulfur-enriched) terrestrially influenced Type II and Type III in the Cape Basin to a predominately Type II to Type IIS north of the Walvis Ridge and in the Angola Basin. The investigated Turonian aged black shale from the Cape

Basin is a poor Type III/IV source rock. At DSDP sites 364 and 530A the Turonian to Coniacian black shales have a very good oil-prone marine source rock potential with high HI and TOC contents. The organofacies trends correlate well with the evolution of the South Atlantic. This depicts the generally more favorable conditions for organic matter preservation in the restricted carbonate-rich and periodically silled oceanic basins north of the Walvis Ridge-Rio Grande Rise, when compared to the siliciclastic-rich Cape Basin. The Cape Basin generally experienced shorter periods of oxygen deficiency during the Cretaceous, mainly due to better bottom-water ventilation and connection to the open Oceans after the Falkland Plateau had cleared the tip of the South African continent by the mid Cretaceous.

The bulk kinetic models show, that major differences in activation energy distribution are caused by variations in the organic matter type. The organic sulfur content has a minor effect in reducing kerogen stability, except in Type IIS kerogen.

The Cretaceous source rocks of the southwest African margin generate mainly low GOR black oils of paraffinic-naphthenic-aromatic petroleum types with some potential for high sulfur heavy oils in the Angola Basin. The offshore Kwanza Basin contains black shales with a potential for wax-rich petroleum with high GOR at high maturity. The terrestrially influenced Aptian and Albian black shale intervals exhibit a potential for gas and condensate generation at high maturities.

To the best of our knowledge, this study provides the first compositional kinetic description for Cretaceous source rocks from the southwest African margin.

Previous research emphasized on the richness of the oil-prone source rocks in the Cape Basin. In fact, this study suggests, that the greater portion of the Aptian and Albian source rock samples of the Cape Basin contain a mixed Type II/III kerogen and an abundance of terrestrial organic matter, thus being more gas- and condensate-prone. The results on the $d^{13}C$ isotope data from drill stem tests and extracted samples of the northern Orange Basin, presented in Chapter 5 suggest a significant contribution of gas and condensate sourced form terrestrial organic matter to present day reservoirs. This observation motivated the incorporation of various source rock intervals into the basin model.

6.4. Modeling hydrocarbon migration dynamics in the Orange Basin

The 3D model of the Orange Basin was constructed based on a large 2D exploration seismic dataset and calibrated to well data. Our calibration of the thermal model suggests a heatflow of 96 mW/m^2 during rifting and an exponential decrease to average values of 52 mW/m^2 for the present day, with two periods of increased heatflow by up to 8 mW/m^2. The increased heat flow was applied to areas where the continental crust was affected by renewed lithospheric stretching during late Cretaceous/Paleocene and Mio-Pliocene. The cumulative maximum erosion during the two phases of lithospheric stretching and ensuing margin uplift are 1000 m and 540 m, respectively. Regions where vitrinite reflection trends indicate higher paleo-temperatures correspond to locations of reported early Cenozoic igneous activity.

In the A-J graben, primary generation from the Hauterivian-aged synrift Type I source rock began in the Cretaceous and the present-day TR of 50% was reached during the Miocene.
Application of the kinetic models from Chapter 2 demonstrates that the onset of primary generation from Aptian Type III-kerogen source rocks occurs with a delay of 20 Ma in comparison to early Cretaceous marine Type II and II/III source rocks. The main phase of primary generation from Barremian to Albian aged Type II and II/III and the Aptian Type III source rocks in the basin center occurred during the mid-Cretaceous and the late Cretaceous/Paleocene, respectively. A second heatflow-controlled phase of petroleum generation from these source rocks lasted from the latest Cretaceous/Paleocene until the end of the Mio-Pliocene uplift.
Regions with a present-day potential for primary condensate and wet gas generation from the Type III kerogen-rich source rock are found at burial depths of less than 4500 m, characterized by TRs of less than 80%.
The present-day kitchen areas are located in the Cenozoic depocenters along the slope. In the northern areas of the basin, the lower Cretaceous Type II and II/III source rocks are currently in the gas window, Aptian Type III kerogen and Cenomanian/Turonian Type II/III kerogen source rocks are in the oil window. In the southern basin, both the lower Cretaceous and a potential C/T source rock are currently in the oil window.
The migration model confirms that the main carriers of the Orange Basin are Barremian to early Aptian sandstones of the transitional sequence and Albian to Cenomanian fluvial sandstones of the early drift sequence. Petroleum accumulations are dominated by gas and condensate. Secondary cracking reactions in early Cretaceous marine source rocks and primary gas/condensates from Aptian Type III source rocks were the main contributors to present-day accumulations along the eastern basin margin. The $d^{13}C$ isotope data is in agreement with these findings.
The greatest control for reproducing the Ibhubesi accumulations is the seal. Albian fluvial channels were only filled when their trapping efficiency was improved by introducing an Albian claystone seal into the model. In the absence of this Albian seal, smaller accumulations were exclusively formed in Cenomanian channels below the C/T source rock.
Drainage area analysis of petroleum accumulations in the Ibhubesi area was conducted on two migration models with different fault properties. These models indicate that stratigraphic traps may have been filled to spill since the early Cenozoic and that hydrocarbon losses due to spilling ("open scenario") and leakage through the seal ("initial model" and "closed scenario") are highest during times of margin uplift and erosion.

6.5. Hydrocarbon leakage on a geologic time scale

A comparative evaluation of hydrocarbon leakage using calculated top outflow rates was conducted on five model iterations with varying flow models and fault properties. In general, hydrocarbon leakage to the surface was greatest following the main phases of petroleum generation. At the time when the early Cretaceous source rocks enter the early oil window, the Upper Cretaceous regional seals where not yet deposited. This causes the first major

surface leakage event. After the regional seals are consolidated, an intermediate phase of surface leakage occured following the late Cretaceous margin tilting event and slope collapse (faulting). A second major phase of surface leakage occured during the Paleocene to early Eocene. This is a time period of active tectonics, signified by fault reactivation, on- and offshore volcanism, and a shift in sedimentation patterns from the northern to the southern Orange Basin. The active hydrocarbon kitchen was also located along the shelf during this time, due to the rapid progradation of the late Cretaceous shelf. The migration models further confirm that gaseous and light hydrocarbons were the main components of the migrating petroleum during early Cenozoic. All these factors support the seismic interpretation of the early Eocene paleo pockmark field. The Paleocene-Eocene transition is known for its series of hyper-thermal events characterized by excursions of the carbon isotope curve. The early Eocene widespread event of fluid and thermogenic gas escape identified in this work can be an example of the type of carbon-release processes occurring in hydrocarbon-prone sedimentary basins during this time.

The modeling results emphasize the correlation of hydrocarbon leakage phases to the tectonic evolution of the margin. They further demonstrate that paleo and present-day hydrocarbon leakage can be adequately reproduced with a 3D basin model. This supports the value of the 3D modeling approach for the study of paleo- and present day hydrocarbon leakage.

On a global scale, the modeled transient hydrocarbon leakage amounts of 10^{-2} to 10^{-3} Tg/yr during peak out-flow events compares well to those of other sedimentary basins. These magnitudes are marginal when compared to other present-day methane contributors to the atmosphere, such as wetlands and anthropogenic sources.

7. Outlook

To date, the Orange Basin is still underexplored with only one commercially producing field, the Kudu gas-condensate field. The diverse datasets available for this study are not consistently available throughout the basin. Most of the available data were collected for either specific prospects or with a low-sample density across the margin. Nevertheless they allowed exploring different approaches to solve the questions at hand. This integrated approach is the way forward for future studies.

A systematic coring or sampling of Cenozoic aged sediments down to the Cretaceous-Cenozoic unconformity at the shelf break along the margin and the slope would help tying IODP drilling results to thin Cenozoic cover on the shelf. In addition, $d^{13}C$ isotope measurements could help gain insights into climatic conditions before and after the proposed Eocene leakage event. This type of study could also be tied to the acquisition of shallow seismic to image the upper 500 m of the sediments. Such higher frequency seismic is better at imaging gas and fluid leakage features in the shallow sub surface than exploration seismic that is optimized for deep targets. Ideally, such a seismic study would also target the mud volcanoes in the northern Orange Basin. In combination with a seep and subsurface sampling study this could help constrain the origin and ages of the structures, as well as their time periods of activity.

A continuous effort to conduct biomarker and isotope studies on extract samples and seafloor seeps of the Orange Basin would help unravel the migration dynamics in the basin, as well as provide constraints on source rock maturity and contributions to reservoir fluids. All of the above can be used to reduce uncertainties and add calibration points to the basin modeling study. The basin model can be refined with bulk density and porosity data derived from core-calibrated well log models of Orange Basin exploration wells. This can help reduce the uncertainties for the 3D pressure and temperature calculations, which are very important for migration simulations, as well as provide better constraints on sublayer lithologies.

The investigations on the crustal structure, break-up kinematics, and synrift volcanisms were not the focus of this study. Therefore further investigations are necessary to confirm these findings and the acquisition of additional seismic data and collaboration with other disciplines that are specified for this purpose should be considered. This type of collaboration proved to be fruitful in the course of this study. An onshore-offshore correlation study on the age, origin, and direction of movement of the dominating basement lineaments from the southern Orange Basin across the Cape Fold Belt and into the Outeniqua Basin could serve as a reconnaissance study to unravel the early rift evolution of southern Africa. The literature contains a wealth of information on outcrop studies conducted in the Cape Fold Belt, but few of these studies have made an attempt to tie their findings on the Triassic-Jurassic onshore evolution to recent offshore seismic interpretations.

The next attempts to study hydrocarbon leakage on a geologic time scale using basin modeling techniques should focus on basin settings where maximum burial occurred during the recent past (for example the Neogene) or in basins with an active oil kitchen. That would reduce the effect of geologic uncertainties for migration simulations for the recent past. Ideally, that study area has known paleo and/or active leakage sites that have been studied and mapped. One problem with many surface hydrocarbon seep studies is that the hydrocarbon source is unknown, or rather not accounted for in the study. Therefore biomarker and isotope studies should be included to distinguish thermogenic from biogenic gas, and to identify the main contributing source rock. The key lies in calibrating the predicted top outflow rates to flux measurements at the surface. Thus linking surface seeps to their source, and evaluating surface rates to generation-, expulsion-, and migration rates.
A basin model top outflow calibration to known surface leakage rates should include a sensitivity study that focuses on the model resolution versus the mass balance calculations utilizing an area of interest (AOI) model. Hydrocarbon leakage is generally a local phenomenon, a result of several geologic factors that may vary considerably across a few kilometers. Hence leakage rates can vary considerably from site to site. This is not well represented in the top-outflow rate calculations. One way to address this would be with a high-resolution AOI model, set up as a model-in-model configuration for the leakage site that it is being calibrated to. This would allow using basin-scale source rock generation, expulsion, and migration inputs, as well as varying the resolution of the AOI from the basin scale (500 x 500m) to that of 3D seismic (25 x 25 m) or even higher. At that resolution, single large pockmark occurrences can be addressed. The goal being to simulate sudden focused fluid flow, rather than transient leakage. Such an approach could establish an optimum range in model resolution for migration and hydrocarbon leakage modeling, using Hybrid (Darcy and Flowpath) or IP methods. To take this one step further, methane hydrate formation and dissociation kinetics could be introduced into an AOI model. This is to test whether sufficient amounts of thermogenic gas are available in a specific basin setting to form clathrates, which, if destabilized, may result in a sudden release of large amounts of methane into the hydro- and atmosphere. To my knowledge, simulating such an event has not been tested in a basin model.

Abbreviations

°C	degree Celsius
°K	degree Kelvin
^{12}C	Carbon-12 stable isotope
^{13}C	Carbon-13 stable isotope
1D	one-dimensional
2D	two-dimensional
3D	three-dimensional
A	[s^{-1}] pre-exponential factor for Arrenhius equation
API°	oil density at 15°C as defined by the American Petroleum Institute: $API° = (\frac{141.5}{oil\ density}) - 131.5$
bcf	billion cubic feet
Bo	oil formaiton factor
BSR	bottom simulating reflector
C/T	Cennomanian/Turonian
CH_4	methane
CLD	chain length distribution
cm	centimeter
CO_2	carbon dioxide
$d^{13}C$	delta Carbon 13 stable istotope ratio, $d^{13}C = \left(\frac{\left(\frac{^{13}C}{^{12}C}\right)_{sample}}{\left(\frac{^{13}C}{^{12}C}\right)_{standard}} - 1\right) * 1000‰$
DSDP	Deep Sea Drilling Project
e.g.	exempli gratia = for example
Ea	activation energy
g	gram
GC	gas-chromatography
GOR	gas-oil-ratio
Gt	gigaton
HI	hydrogen index HI = (S2/TOC)*100%
IODP	International Ocean Drilling Project
IP	Invasion Percolation
k	reaction rate constant
km	kilometer
km^2	square kilometer
LIP	large igneous province
m	meter
m^2	square meter
m^3	cubic meter
Ma	million years ago
mD	milidarcy

mg	miligram
min	minute
mm	milimeter
MPa	mega Pascal
ms	milisecond
MSSV	micro-scaled sealed vessel
mW	miliwatt
My	million years
OAE2	oceanic anoxic event 2
OB	Orange Basin
OI	oxygen index OI= (S3/TOC)*100%
OM	organic matter
P-N-A	paraffinic-naphtenic-aromatic
PETM	Paleocene-Eocene Thermal Maxiumum
P_{sat}	saturation pressure
PVT	pressure volume temperature
Py-GC	pyrolysis-gas chromatography
S1	amount of free hydrocarbons measured during Rock Eval pyrolysis
S2	amount of generated hydrocarbons measured during Rock Eval pyrolysis
S3	amount of carbon dioxide measured during Rock Eval pyrolysis
SDR	seaward dipping reflector
Sm^3	standard cubic meter at 15.6°C and 101.325 kilo Pascal
SWIT	sediment-water interface temperature
tcf	trillion cubic feet
Tg	teragram
T_{max}	S2 peak temperature measured in °C during Rock Eval pyrolysis
TOC	total organic carbon weight %
TR	transformation ratio
TVD	true vertical depth
TWT	two-way travel time
VR	vitrinite reflectance
VR_O	vitrinite reflectance in oil
yr	year

References

Adekola, S.A., Akinlua, A., Mangelsdorf, K., 2012. Organic geochemical evaluation of Cretaceous shale samples from the Orange Basin, South Africa. Applied Geochemistry 27, 1633–1642.

Akinlua, A., Adekola, S.A., Swakamisa, O., Fadipe, O.A., Akinyemi, S.A., 2010. Trace element characterisation of Cretaceous Orange Basin hydrocarbon source rocks. Applied Geochemistry 25, 1587–1595.

Al-Hajeri, M.M., Al Saeed, M., Derks, J., Fuchs, T., Hantschel, T., Kauerauf, A., Neumaier, M., Schenk, O., Swientek, O., Tessen, N., Welte, D., Wygrala, B., Kornpihl, D., Peters, K., 2009. Basin and Petroleum System Modeling. Oilfield Review 21, 14–29.

Aldrich, J., Zilinski, R., Edman, J., Leu, W., Berge, T., Corbett, K., 2003. Documentation of a New Petroleum System in the South Atlantic, in: AAPG Annual Convention Salt Lake City 2003. Salt Lake City, Utah, p. 90013.

Allen, P.A., Allen, J.R., 2013. Basin Analysis: Principles and application to petroleum play assessment, 3rd ed. Blackwell Publishing Ltd, Oxford.

Amante, C., Eakins, B.W., 2009. ETOPO1 1 Arc-Minute Global Relief Model: Procedures, Data Sources and Analysis, NOAA Technical Memorandum NESDIS NGDC-24. NOAA.

Andresen, K.J., 2012. Fluid flow features in hydrocarbon plumbing systems: What do they tell us about the basin evolution? Marine Geology 332-334, 89–108.

Andresen, K.J., Huuse, M., 2011. “Bulls-eye” pockmarks and polygonal faulting in the Lower Congo Basin: Relative timing and implications for fluid expulsion during shallow burial. Marine Geology 279, 111–127.

Andresen, K.J., Huuse, M., Clausen, O.R., 2008. Morphology and distribution of Oligocene and Miocene pockmarks in the Danish North Sea – implications for bottom current activity and fluid migration. Basin Research 20, 445–466.

Andresen, K.J., Huuse, M., Schodt, N.H., Clausen, L.F., Seidler, L., 2011. Hydrocarbon plumbing systems of salt minibasins offshore Angola revealed by three-dimensional seismic analysis. AAPG Bulletin 95, 1039–1065.

Anka, Z., Ondrak, R., Kowitz, A., Schødt, N., 2013. Identification and numerical modelling of hydrocarbon leakage in the Lower Congo Basin: Implications on the genesis of km-wide seafloor mounded structures. Tectonophysics 604, 153–171.

Anka, Z., Séranne, M., 2004. Reconnaissance study of the ancient Zaire (Congo) deep-sea fan. (ZaiAngo Project). Marine Geology 209, 223–244.

Anka, Z., Séranne, M., Lopez, M., Scheck-Wenderoth, M., Savoye, B., 2009. The long-term evolution of the Congo deep-sea fan: A basin-wide view of the interaction between a

giant submarine fan and a mature passive margin (ZaiAngo project). Tectonophysics 470, 42–56.

Anka, Z., Séranne, M., Primio, R. di, 2010. Evidence of a large upper-Cretaceous depocentre across the Continent-Ocean boundary of the Congo-Angola basin. Implications for palaeo-drainage and potential ultra-deep source rocks. Marine and Petroleum Geology 27, 601–611.

Autin, J., Scheck-Wenderoth, M., Loegering, M.J., Anka, Z., Vallejo, E., Rodriguez, J.F., Dominguez, F., Marchal, D., Reichert, C., di Primio, R., Götze, H.-J., 2013. Colorado Basin 3D structure and evolution, Argentine passive margin. Tectonophysics.

Bacon, M., Simm, R., Redshaw, T., 2009. 3-D Seismic Interpretation. Cambridge University Press, Cambridge.

Baristeas, N., Anka, Z., di Primio, R., Rodriguez, J.F., Marchal, D., Dominguez, F., 2012. Distribution of hydrocarbon leakage indicators in the Malvinas Basin, offshore Argentine continental margin. Marine Geology 332-334, 56–74.

Barker, C.E., Pawlewicz, M.J., 1987. The effects of igneous intrusions and higher heat flow on the thermal maturity of Leonardian and younger rocks, western Delaware basin, Texas, in: Cromwell, D.W., Mazzullo, L. (Eds.), Glass Mountains Guidebook. Permian Basin Section, Society of Economic Paleontologist and Mineralogists, Midland, Texas, pp. 69–83.

Bauer, K., Neben, S., Schreckenberger, B., Emmermann, R., Hinz, K., Fechner, N., Gohl, K., Schulze, A., Trumbull, R.B., Weber, K., 2000. Deep structure of the Namibia continental margin as derived from integrated geophysical studies. Journal of Geophysical Research 105, 25829.

Beglinger, S.E., Doust, H., Cloetingh, S., 2012. Relating petroleum system and play development to basin evolution: West African South Atlantic basins. Marine and Petroleum Geology 30, 1–25.

Ben-Avraham, Z., Smith, G., Reshef, M., Jungslager, E.H.A., 2002. Gas hydrate and mud volcanoes on the southwest African continental margin off South Africa. GSA Bulletin 30, 927–930.

Berbesi, L.A., di Primio, R., Anka, Z., Horsfield, B., Wilkes, H., 2014. Methane leakage from evolving petroleum systems: Masses, rates and inferences for climate feedback. Earth and Planetary Science Letters 387, 219–228.

Berge, T.B., Aminzadeh, F., de Groot, P.F., Oldenziel, T., 2002. Seismic inversion successfully predicts reservoir, porosity, and gas content in Ibhubesi Field, Orange Basin, South Africa. Leading Edge 1, 338–348.

Berndt, C., Bünz, S., Clayton, T., Mienert, J., Saunders, M., 2004. Seismic character of bottom simulating reflectors: examples from the mid-Norwegian margin. Marine and Petroleum Geology 21, 723–733.

Bjørlykke, K., Høeg, K., Faleide, J.I., Jahren, J., 2005. When do faults in sedimentary basins leak? Stress and deformation in sedimentary basins; examples from the North Sea and Haltenbanken, offshore Norway. AAPG Bulletin 89, 1019–1031.

Blaich, O.A., Faleide, J.I., Tsikalas, F., Franke, D., León, E., 2009. Crustal-scale architecture and segmentation of the Argentine margin and its conjugate off South Africa. Geophyscial Journal International 178, 85–105.

Bøe, R., Rise, L., Ottesen, D., 1998. Elongate depressions on the southern slope of the Norwegian Trench (Skagerrak): morphology and evolution. Marine Geology 146, 191–203.

Bolli, H.M., Ryan, W.B.F., Foresman, J.B., Hottman, W.E., Kagami, H., Longoria, J.F., McKnight, B.K., Melguen, M., Natland, J., Decima-Proto, F., Siesser, W.G., 1978a. 4. Angola continental margin - sites 364 and 365, Initial Reports of the Deep Sea Drilling Project. National Science Foundation, Washington.

Bolli, H.M., Ryan, W.B.F., Foresman, J.B., Hottman, W.E., Kagami, H., Longoria, J.F., McKnight, B.K., Melguen, M., Natland, J., Decima-Proto, F., Siesser, W.G., Proto-Decim, F., 1978b. 2. Cape basin continental rise - sites 360 and 361, Initial Reports of the Deep Sea Drilling Project. National Science Foundation, Washington (U.S. Government Printing Office).

Bordenave, M.L., 1993. Applied Petroleum Geochemistry. Éditions Technip, Paris.

Boreham, C.J., Horsfield, B., Schenk, H.J., 1999. Predicting the quantities of oil and gas generated from Australian Permian coals, Bowen Basin using pyrolytic methods. Marine and Petroleum Geology 16, 165–188.

Bowen, G.J., 2013. Up in smoke: A role for organic carbon feedbacks in Paleogene hyperthermals. Global and Planetary Change 109, 18–29.

Bowen, G.J., Zachos, J.C., 2010. Rapid carbon sequestration at the termination of the Palaeocene-Eocene Thermal Maximum. Nature Geoscience 3, 866–869.

Boyd, D., Anka, Z., di Primio, R., Kuhlmann, G., de Wit, M., 2012. Passive margin evolution and controls on natural gas leakage in the Orange Basin, South Africa. South African Journal of Geology 114, 415–432.

Bray, R., Lawrence, S., Swart, R., 1998. Source rock, maturity data inidcate potential off Namibia. Oil and Gas Journal 96, 84–89.

Broad, D.S., Jungslager, E.H.A., McLachlan, I.R., Roux, J., 2006. Offshore Mesozoic basins, in: Johnson, M.R., Anhaeusser, C.R., Thomas, R.J. (Eds.), The Geology of South Africa. Geological Society of South Africa, Johannesburg, Council for Geoscience, Pretoria, Johannesburg, Pretoria, pp. 553–571.

Brown Jr., L.F., Benson, J.M., Brink, G.J., Doherty, S., Jollands, A., Jungslager, E.H.A., Keenan, J.H.G., Muntingh, A., van Wyk, N.J.S., 1995. Sequence Stratigraphy in Offshore South African Divergent Basins. AAPG Studies in Geology 41.

Buffett, B., Archer, D., 2004. Global inventory of methane clathrate: sensitivity to changes in the deep ocean. Earth and Planetary Science Letters 227, 185–199.

Burwood, R., 1999. Angola: source rock control for Lower Congo Coastal and Kwanza Basin petroleum systems. Geological Society of London, Special Publication 153, 181–194.

Bustin, R.M.M., Cameron, A.R.R., Grieve, D.A.A., Kalkreuth, W.D.D., 1985. Coal Petrology its Principles, Methods, and Applications, second rev. ed. Geological Association of Canada, Victoria.

Carozza, D.A., Mysak, L.A., Schmidt, G.A., 2011. Methane and environmental change during the Paleocene-Eocene thermal maximum (PETM): Modeling the PETM onset as a two-stage event. Geophysical Research Letters 38, L05702.

Carruthers, D., Ringrose, P., 1998. Secondary oil migration: oil-rock contact volumes, flow behaviour and rates. Geological Society of London, Special Publication 144, 205–220.

Cartwright, J., Huuse, M., Aplin, A., 2007. Seal bypass systems. AAPG Bulletin 91, 1141–1166.

Cathles, L.M., Su, Z., Chen, D., 2010. The physics of gas chimney and pockmark formation, with implications for assessment of seafloor hazards and gas sequestration. Marine and Petroleum Geology 27, 82–91.

Chaloner, W.G., 2005. The palaeobotanical work of Marie Stopes. Geological Society of London, Special Publication 241, 127–135.

Clayton, C.J., Hay, S.J., 1994. Gas migration mechanisms from accumulation to surface. Bulletin Geologic Society Denmark 41, 12–23.

Cole, D., Stewart, S.A., Cartwright, J.A., 2000. Giant irregular pockmark craters in the Palaeogene of the Outer Moray Firth Basin, UK North Sea. Marine and Petroleum Geology 17, 563–577.

Cole, G.A., Requejo, A.G., Ormerod, D., Yu, Z., Clifford, A., 2000. Petroleum geochemical assessment of the Lower Congo Basin, in: Mello, M.R., Katz, B.J. (Eds.), Petroleum Systems of South Atlantic Margins. pp. 325–339.

Corbett, I.B., 1996. A review of diamiferous marine deposits of western southern Africa. Africa Geoscience Review 3, 157–174.

Coward, M.P., Purdy, E.G., Ries, A.C., Smith, G.D., 1999. The distribution of petroleum reserves in basins of the South Atlantic margins, in: Bate, R.H., Clure, V.S. (Eds.), The Oil and Gas Habitats of the South Atlantic. Geologic Society, London, pp. 101–131.

Davies, C.P.N., 1997. Unusual biomarker maturation ratio changes through the oil window, a consequence of varied thermal history. Organic Geochemistry 27, 537–560.

Davies, C.P.N., van der Spuy, D., 1990. Chemical and optical investigations into the hydrocarbon source potential and thermal maturity of the Kudu 9A-2 and 9A-3 boreholes. Communications of the Geological Survey of Namibia 6, 49–58.

Davies, C.P.N., Van der Spuy, D., 1992. The Kudu wells: Source rocks, maturation, generation and timing of migration, in: Southwestern African Continental Margin: Evolution and Physical Charactersitics. Windhoek, Namibia.

Davies, C.P.N., Van der Spuy, D., 1993. The Kudu wells: Results of a biomarker study related to burial history modelling. Communications of the Geological Survey of Namibia 8, 45–56.

Davies, R., Cartwright, J., Rana, J., 1999. Giant hummocks in deep-water marine sediments: Evidence for large-scale differential compaction and density inversion during early burial. Geology 27, 907.

Davison, I., 1999. Tectonics and hydrocarbon distribution along the Brazilian South Atlantic margin. Geological Society of London, Special Publication 153, 133–151.

Davy, B., Pecher, I., Wood, R., Carter, L., Gohl, K., 2010. Gas escape features off New Zealand: Evidence of massive release of methane from hydrates. Geophysical Research Letters 37, L21309.

De Vera, J., Granado, P., McClay, K., 2010. Structural evolution of the Orange Basin gravity-driven system, offshore Namibia. Marine and Petroleum Geology 27, 223–237.

De Wit, M., 1999. Post-Gondwana drainage and the development of diamond placers in western South Africa. Economic Geology 94, 721–740.

Deroo, G., Herbin, J.P., Huc, A.Y., 1984. 30. Organic geochemsitry of cretaceous black shales from deep sea drilling project site 530, leg 75, eastern south Atlantic, DSDP report, Leg 75.

Di Primio, R., Dieckmann, V., Mills, N., 1998. PVT and phase behaviour analysis in petroleum exploration. Organic Geochemistry 29, 207–222.

Di Primio, R., Horsfield, B., 1996. Predicting the generation of heavy oils in carbonate/evaporitic environment using pyrolsis methods. Organic Geochemistry 24, 999–1016.

Di Primio, R., Horsfield, B., 2006. From petroleum-type organofacies to hydrocarbon phase prediction. AAPG Bulletin 90, 1031–1058.

Di Primio, R., Horsfield, B., Fuhrmann, A., 2005. Predicting gas composition and its effect on petroleum phase behaviour during secondary migration, in: AAPG Annual Convention 2005. Calgary, Alberta, Canada.

Di Primio, R., Skeie, J.E., 2004. Development of a compositional kinetic model for hydrocarbon generation and phase equilibria modelling: a case study from Snorre Field, Norwegian North Sea. Geological Society of London, Special Publication 237, 157–174.

Dickens, G.R., Castillo, M.M., Walker, J.C.G., 1997. A blast of gas in the latest Paleocene: Simulating first-order effects of massive dissociation of oceanic methane hydrate. Geology 25, 259–262.

Dickens, G.R., O'Neil, J.R., Rea, D.K., Owen, R.M., 1995. Dissociation of oceanic methane hydrate as a cause of the carbon isotope excursion at the end of the Paleocene. Paleoceanography 10, 965–971.

Dieckmann, V., Keym, M., 2006. A new approach to bridge the effect of organofacies variations on kinetic modelling and geological extrapolations. Organic Geochemistry 37, 728–739.

Dieckmann, V., Schenk, H.J., Horsfield, B., Welte, D.H., 1998. Kinetics of petroleum generation and cracking by programmed-temperature closed-system pyrolysis of Toarcian Shales. Fuel 77, 23–31.

Dingle, R. V, 1980. Large allochthonous sediment masses and their role in the construction of the continental slope and rise off southwestern Africa. Marine Geology 37, 333–354.

Dingle, R. V, Hendey, Q.B., 1984. Late mesozoic and tertiary sediment supply to the eastern Cape Basin (SE Atlantic) and palaeo-drainage systems in southwestern Africa. Marine Geology 56, 13–26.

Dingle, R. V, Siesser, W.G., Newton, A.R., 1983. Mesozoic and Tertiary Geology of Southern Africa. A.A. Balkema, Rotterdam.

Dingle, R. V., 1973. The geology of the continental shelf between Luderitz and Cape Town (Southwest Africa), with special reference to Tertiary strata. Journal of the Geologic Society London. 129, 337–362.

Dobson, K., Brown, R., Macdonald, R., Gallagher, K., Stuart, F., 2011. Constraining the Cenozoic evolution of South Africa using (U-Th)/ He thermochronology : the influence of dynamic topography at a passive margin, in: EGU General Assembly 2011. Vienna, Austria, p. 4915.

Dunkley Jones, T., Ridgwell, A., Lunt, D.J., Maslin, M.A., Schmidt, D.N., Valdes, P.J., 2010. A Palaeogene perspective on climate sensitivity and methane hydrate instability. Philosophical Transactions of the Royal Society A: Physical, Mathematical and Engineering 368, 2395–415.

Eglinton, T.I., Schenck, P.A., Sinninghe Damsté, J.S., De Leeuw, J.W., 1989. Organic sulphur in macromolecular sedimentary organic matter: I. Structure and origin of sulphur-containing moieties in kerogen, asphaltenes and coal as revealed by flash pyrolysis. Geochimica et Cosmochimica Acta 53, 873–889.

Eglinton, T.I., Sinninghe Damste, J.S., Kohnen, M.E.L., de Leeuw, J.W., Larter, S.R., Patience, R.L., 1990. Analysis of Maturity-Related Changes in the Organic Sulfur Composition of Kerogens by Flash Pyrolysis-Gas Chromatography, in: Geochemistry of Sulfur in Fossil Fuels. American Chemical Society, pp. 529–565.

Emery, K.O., Uchupi, E., Philips, J.D., Bowin, C.O., Simpson, E.S.W., 1975. Continental margin off western Africa; Cape St. Francis (South Africa) to Walvis Ridge (South-West Africa). AAPG Bulletin 59, 3–59.

Espitalié, J., 1987. Use of Tmax as a Maturation Index for Different Types of Organic Matter. Comparison with Vitrinite Reflectance, in: Burrus, J. (Ed.), Thermal Modelling in Sedimentary Basins. Gulf Publishing Company, Houston, Texas, pp. 475–496.

Etiope, G., 2009. Natural emissions of methane from geological seepage in Europe. Atmos. Environ. 43, 1430–1443.

Etiope, G., Ciccioli, P., 2009. Earth's Degassing: A Missing Ethane and Propane Source. Science 323, 478.

Etiope, G., Feyzllaye, A., Baciu, C.L., 2009. Terrestrial methane seeps and mud volcanoes: a global perspective of gas origin. Marine and Petroleum Geology 26, 333–334.

Fadipe, O.A., Carey, P.F., Akinlua, A., Adekola, S.A., 2011. Provenance, diagenesis and reservoir quality of the lower cretaceou sandstone of the Orange Basin, South Africa. South African Journal of Geology 114, 433–448.

Falkowski, P., Scholes, R.J., Boyle, E., Canadell, J., Canfield, D., Elser, J., Gruber, N., Hibbard, K., Hogberg, P., Linder, S., Mackenzie, F.T., Moore III, B., Pedersen, T., Rosenthal, Y., Seitzinger, S., Smetacek, V., Steffen, W., 2000. The global carbon cycle : a test of our knowledge of Earth as a system. Science 290, 291.

Foresman, J.B., 1978. 11. Organic geochemistry DSDP LEG 40, continental rise of southwest Africa, Initial reports of the Deep Sea Drilling Project. National Science Foundation, Washington (U.S. Government Printing Office).

Forster, A., Kuypers, M.M.M., Turgeon, S.C., Brumsack, H.-J., Petrizzo, M.R., Sinninghe Damsté, J.S., 2008. The Cenomanian/Turonian oceanic anoxic event in the South Atlantic: New insights from a geochemical study of DSDP Site 530A. Palaeogeography Palaeoclimatology Palaeoecology 267, 256–283.

Franke, D., Ladage, S., Schnabel, M., Schreckenberger, B., Reichert, C., Hinz, K., Paterlini, M., de Abelleyra, J., Siciliano, M., 2010. Birth of a volcanic margin off Argentina, South Atlantic. Geochemistry, Geophysics, Geosystems 11.

Franke, D., Neben, S., Schreckenberger, B., Schulze, A., Stiller, M., Krawczyk, C.M., 2006. Crustal structure across the Colorado Basin, offshore Argentina. Geophyscial Journal International 165, 850–864.

Gallagher, K., Brown, R., 1999. Denudation and uplift at passive margins: the record on the Atlantic Margin of southern Africa. The Royal Society Journal 357, 835–859.

Gay, A., Lopez, M., Berndt, C., Séranne, M., 2007. Geological controls on focused fluid flow associated with seafloor seeps in the Lower Congo Basin. Marine Geology 244, 68–92.

Gay, A., Lopez, M., Cochonat, P., Levaché, D., Sermondadaz, G., Seranne, M., 2006a. Evidences of early to late fluid migration from an upper Miocene turbiditic channel revealed by 3D seismic coupled to geochemical sampling within seafloor pockmarks, Lower Congo Basin. Marine and Petroleum Geology 23, 387–399.

Gay, A., Lopez, M., Cochonat, P., Séranne, M., Levaché, D., Sermondadaz, G., 2006b. Isolated seafloor pockmarks linked to BSRs, fluid chimneys, polygonal faults and stacked Oligocene-Miocene turbiditic palaeochannels in the Lower Congo Basin. Marine Geology 226, 25–40.

Gay, A., Lopez, M., Ondreas, H., Charlou, J.L., Sermondadaz, G., Cochonat, P., 2006c. Seafloor facies related to upward methane flux within a Giant Pockmark of the Lower Congo Basin. Marine Geology 226, 81–95.

Gerrard, I., Smith, G.C., 1982. Post-Paleozoic Succession and Structure of the Southwestern African Continental Margin. Stud. Cont. margin Geol. AAPG Memoir 34.

Gilbert, D., 1978. 35. Organic Facies Variations in the Mesozoic South Atlantic, Initial Report of the Deep Sea Drilling Project Vol. 40. Government Printing Office, Washington.

Gladczenko, T.P., Hinz, K., Eldholm, O., Meyer, H., Neben, S., Skogseid, J., 1997. South Atlantic volcanic margins. Journal of the Geologic Society London. 154, 465–470.

Gladczenko, T.P., Skogseid, J., Eldhom, O., 1998. Namibia volcanic margin. Marine Geophysical Research. 20, 313–341.

Goutorbe, B., Lucazeau, F., Bonneville, A., 2008. The thermal regime of South African continental margins. Earth and Planetary Science Letters 267, 256–265.

Guillocheau, F., Rouby, D., Robin, C., Helm, C., Rolland, N., Le Carlier de Veslud, C., Braun, J., 2012. Quantification and causes of the terrigeneous sediment budget at the scale of a continental margin: a new method applied to the Namibia-South Africa margin. Basin Research 24, 3–30.

Haacke, R.R., Westbrook, G.K., Hyndman, R.D., 2007. Gas hydrate, fluid flow and free gas: Formation of the bottom-simulating reflector. Earth and Planetary Science Letters 261, 407–420.

Hantschel, T., Kauerauf, A.I., 2009. Fundamentals of Basin and Petroleum Systems Modeling. Springer-Verlag Berlin Heidelberg.

Haq, B.U., Hardenbol, J., Vail, P.R., 1987. Chronology of fluctuating sea levels since the triassic. Science 235, 1156–67.

Hardenbol, J., Thierry, J., Farley, M.B., Jacquin, T., Graciansky, P.C. de, Vail, P.R., 1998. Mesozoic and Cenozoic Sequence Chronostratigraphic Chart, in: Graciansky, P.C. de, Hardenbol, J., Jacquin, T., Vail, P.R. (Eds.), Mesozoic and Cenozoic Sequence Stratigraphy of European Basins. Society of Sedimentary Geology.

Hartwig, A., Anka, Z., di Primio, R., 2012a. Evidence of a widespread paleo-pockmarked field in the Orange Basin: An indication of an early Eocene massive fluid escape event offshore South Africa. Marine Geology 332-334, 222–234.

Hartwig, A., di Primio, R., Anka, Z., Horsfield, B., 2012b. Source rock characteristics and compositional kinetic models of Cretaceous organic rich black shales offshore southwestern Africa. Organic Geochemistry 51, 17–34.

Hasiotis, T., Papatheodorou, G., Kastanos, N., Ferentinos, G., 1996. A pockmark field in the Patras Gulf (Greece) and its activation during the 14/7/93 seismic event. Marine Geology 130, 333–344.

Hay, W.W., Sibuet, J.-C., 1984. 2. Site 530 southeastern corner of the Angola Basin, Initial Report of the Deep Sea Drilling Project Vol. 75. Government Printing Office, Washington.

Head, I.M., Jones, D.M., Larter, S.R., 2003. Biological activity in the deep subsurface and the origin of heavy oil. Nature 426, 344–52.

Heggland, R., 1998. Gas seepage as an indicator of deeper prospective reservoirs. A study based on exploration 3D seismic data. Marine and Petroleum Geology 15, 1–9.

Herbin, J.P., Müller, C., Graciansky, P.C. de, Jacquin, T., Magniez-Jannin, F., Unternehr, P., 1987. Cretaceous Anoxic Events in the South Atlantic. Revista Brasileira de Geociecias 17, 92–99.

Higgins, J.A., Schrag, D.P., 2006. Beyond methane: Towards a theory for the Paleocene-Eocene Thermal Maximum. Earth and Planetary Science Letters 245, 523–537.

Hirsch, K.K., Bauer, K., Scheck-Wenderoth, M., 2009. Deep structure of the western South African passive margin - Results of a combined approach of seismic, gravity and isostatic investigations. Tectonophysics 470, 57–70.

Hirsch, K.K., Scheck-Wenderoth, M., van Wees, J.-D., Kuhlmann, G., Paton, D.A., 2010. Tectonic subsidence history and thermal evolution of the Orange Basin. Marine and Petroleum Geology 27, 565–584.

Horsfield, B., 1989. Practical criteria for classifying kerogens: Some observations from pyrolysis-gas chromatography. Geochimica et Cosmochimica Acta 53, 891–901.

Horsfield, B., 1997. The Bulk Composition of First-Formed Petroleum in Source Rocks, in: Welte, D.H., Horsfield, B., Baker, D.R. (Eds.), Petroleum and Basin Evolution. Springer Verlag, Berlin, Heidelberg, pp. 337–402.

Horsfield, B., Disko, U., Leistner, F., 1989. The micro-scale simulation of maturation: outline of a new technique and its potential applications. Geologische Rundschau 78, 361–374.

Hovland, M., Svensen, H., Forsberg, C.F., Johansen, H., Fichler, C., Fosså, J.H., Jonsson, R., Rueslåtten, H., 2005. Complex pockmarks with carbonate-ridges off mid-Norway: Products of sediment degassing. Marine Geology 218, 191–206.

Hudec, M.R., Jackson, M.P.A., 2004. Regional restoration across the Kwanza Basin, Angola: Salt tectonics triggered by repeated uplift of a metastable passive margin. AAPG Bulletin 88, 971–990.

Hunt, J.M., 1996. Petroleum Geochemistry and Geology, 2nd ed. W. H. Freeman and Company, New York.

Imbert, P., Ho, S., 2012. Seismic-scale funnel-shaped collapse features from the Paleocene–Eocene of the North West Shelf of Australia. Marine Geology 332-334, 198–221.

Jackson, M.P.A., Cramez, C., Fonck, J.-M., 2000. Role of subaerial volcanic rocks and mantle plumes in creation of South Atlantic margins: implications for salt tectonics and source rocks. Marine and Petroleum Geology 17, 477–498.

Judd, A.G., Hovland, M., 2007. Seabed Fluid Flow. Cambridge University Press, Cambridge.

Jungslager, E.H.A., 1999. Petroleum habitats of the Atlantic margin of South Africa. Geological Society of London, Special Publication 153, 153–168.

Karner, G.D., Driscoll, N.W., 1999. Tectonic and stratigraphic development of the West African and eastern Brazilian Margins: insights from quantitative basin modelling. Geological Society of London, Special Publication 153, 11–40.

Kassold, S., Schulz, M., Wilkes, H., Haberer, R.M., Naumann, R., Plessen, B., Hartmann, J., 2008. interactions in a Jurassic oil reservoir : Heidrun field , Haltenbanken area (Norway), in: EGU General Assembly 2008. Vienna, Austria.

Keym, M., Dieckmann, V., Horsfield, B., Erdmann, M., Galimberti, R., Kua, L.-C., Leith, L., Podlaha, O., 2006. Source rock heterogeneity of the Upper Jurassic Draupne Formation, North Viking Graben, and its relevance to petroleum generation studies. Organic Geochemistry 37, 220–243.

Kiel, S., 2009. Global hydrocarbon seep-carbonate precipitation correlates with deep-water temperatures and eustatic sea-level fluctuations since the Late Jurassic. Terra Nova 21, 279–284.

Killops, S.D., Killops, V.J., 2005. Introduction to Organic Geochemistry, 2nd ed. Wiley-Blackwell, Oxford.

King, L.H., Maclean, B., 1970. Pockmarks on the Scotian shelf. GSA Bulletin 81, 3141–3148.

Klemme, H.D., Ulmishek, G.F., 1991. Effetive Petroleum Source Rocks of the World: Stratigraphic Distribution and Controlling Depositional Factors. AAPG Bulletin 73, 1809–1851.

Koopmann, H., Franke, D., Schreckenberger, B., Schulz, H., Hartwig, A., Stollhofen, H., di Primio, R., 2014. Segmentation and volcano-tectonic characteristics along the SW African continental margin, South Atlantic, as derived from multichannel seismic and potential field data. Marine and Petroleum Geology 50, 22–39.

Koopmann, H., Hartwig, A., Schulz, H., Schreckenberger, B., Franke, D., 2012. New findings on the aspect of margin segmentation along the South African margin, in: EGU General Assembly 2012. Vienna, Austria.

Kounov, A., Viola, G., de Wit, M., Andreoli, M.A.G., 2009. Denudation along the Atlantic passive margin: new insights from apatite fission-track analysis on the western coast of South Africa. Geological Society of London, Special Publication 324, 287–306.

Kounov, A., Viola, G., Dunkl, I., Frimmel, H.E., 2013. Southern African perspectives on the long-term morpho-tectonic evolution of cratonic interiors. Tectonophysics.

Kroeger, K.F., di Primio, R., Horsfield, B., 2009. Hydrocarbon flow modeling in complex structures (Mackenzie Basin, Canada). AAPG Bulletin 93, 1209–1234.

Kroeger, K.F., di Primio, R., Horsfield, B., 2011. Atmospheric methane from organic carbon mobilization in sedimentary basins - the sleeping giant? Earth Science Review 107, 423–442.

Kroeger, K.F., Funnell, R.H., 2012. Warm Eocene climate enhanced petroleum generation from Cretaceous source rocks: A potential climate feedback mechanism? Geophysical Research Letters 39, L04701.

Kuhlmann, G., Adams, S., Anka, Z., Campher, C., di Primio, R., Horsfield, B., 2011. 3D petroleum system modellin within a passive margin setting, Orange Basin, block 3/4, offshore South Africa - Implications for gas generation migration and leakage. South African Journal of Geology 114, 387–414.

Kuhlmann, G., Adams, S., Campher, C., van der Spuy, D., di Primio, R., Horsfield, B., 2010. Passive margin evolution and its controls on natural gas leakage in the southern Orange Basin, blocks 3/4, offshore South Africa. Marine and Petroleum Geology 27, 973–992.

Kusznir, N.J., Roberts, a. M., Morley, C.K., 1995. Forward and reverse modelling of rift basin formation. Geological Society of London, Special Publication 80, 33–56.

Laughrey, C.D., Baldassare, F.J., 1998. Geochemistry and Origin of Some Natural Gases in the Plateau Province , Central Appalachian Basin , Pennsylvania and Ohio. AAPG Bulletin 82, 317–335.

Lehne, E., Dieckmann, V., 2007. Bulk kinetic parameters and structural moieties of asphaltenes and kerogens from a sulphur-rich source rock sequence and related petroleums. Organic Geochemistry 38, 1657–1679.

Leite da Costa, J., Schirmer, T.W., Laws, B.R., 2001. Lower Congo Basin, deep-water exploration province, offshore West Africa, in: Downey, M.W., Threet, J.C., Morgan, W.A. (Eds.), Petroleum Provinces of the Twenty-First Century: AAPG Memoir 74. pp. 517–530.

Liebetrau, V., Eisenhauer, A., Linke, P., 2010. Cold seep carbonates and associated cold-water corals at the Hikurangi Margin, New Zealand: New insights into fluid pathways, growth structures and geochronology. Marine Geology 272, 307–318.

Light, M.P.R., Maslanyj, M.P., Banks, N.L., 1992. New geophysical evidence for extensional tectonics on the divergent margin offshore Namibia. Geological Society of London, Special Publication 68, 257–270.

Light, M.P.R., Maslanyj, M.P., Greenwood, R.J., Banks, N.L., 1993. Seismic sequence stratigraphy and tectonics offshore Namibia. Geological Society of London, Special Publication 71, 163–191.

Ligtenberg, H., Connolly, D., 2003. Chimney detection and interpretation, revealing sealing qualityof faults, geohazards, charge of and leakage from reservoirs. Journal of Geochemical Exploration 78-79, 385–387.

Linke, P., Sommer, S., Rovelli, L., McGinnis, D.F., 2010. Physical limitations of dissolved methane fluxes: The role of bottom-boundary layer processes. Marine Geology 272, 209–222.

Loegering, M.J., Anka, Z., Autin, J., di Primio, R., Marchal, D., Rodriguez, J.F., Franke, D., Vallejo, E., 2013. Tectonic evolution of the Colorado Basin, offshore Argentina, inferred from seismo-stratigraphy and depositional rates analysis. Tectonophysics.

Loncke, L., Mascle, J., Fanil Scientific, P., 2004. Mud volcanoes, gas chimneys, pockmarks and mounds in the Nile deep-sea fan (Eastern Mediterranean): geophysical evidences. Marine and Petroleum Geology 21, 669–689.

Long, H., Flemings, P.B., Germaine, J.T., Saffer, D.M., 2011. Consolidation and overpressure near the seafloor in the Ursa Basin, Deepwater Gulf of Mexico. Earth and Planetary Science Letters 305, 11–20.

Løseth, H., Gading, M., Wensaas, L., 2009. Hydrocarbon leakage interpreted on seismic data. Marine and Petroleum Geology 26, 1304–1319.

Løseth, H., Wensaas, L., Arntsen, B., Hanken, N.-M., Basire, C., Graue, K., 2011. 1000 m long gas blow-out pipes. Marine and Petroleum Geology 28, 1047–1060.

Lourens, L.J., Sluijs, A., Kroon, D., Zachos, J.C., Thomas, E., Röhl, U., Bowles, J., Raffi, I., 2005. Astronomical pacing of late Palaeocene to early Eocene global warming events. Nature 435, 1083–7.

Macdonald, D., Gomez-Perez, I., Franzese, J., Spalletti, L., Lawver, L., Gahagn, L., Dalziel, I., Thomas, C., Trewin, N., Hole, M., Paton, D., 2003. Mesozoic break-up of SW Gondwana: implications for regional hydrocarbon potential of the southern South Atlantic. Marine and Petroleum Geology 20, 287–308.

Magoon, L.B., Dow, W.G., 1994. The Petroleum System, in: Magoon, L.B., Dow, W.G. (Eds.), The Petroleum System - from Source to Trap AAPG Memoir 60. Tulsa, Oklahoma, pp. 3–24.

Mahlstedt, N., Horsfield, B., 2012. Metagenetic methane generation in gas shales I. Screening protocols using immature samples. Marine and Petroleum Geology 31, 27–42.

Majorowicz, J., Safanda, J., Osadetz, K., 2012. Inferred gas hydrate and permafrost stability history models linked to climate change in the Beaufort-Mackenzie Basin, Arctic Canada. Climate of the Past 8, 667–682.

Marcano, G., Anka, Z., di Primio, R., 2013. Major controlling factors on hydrocarbon generation and leakage in South Atlantic conjugate margins: A comparative study of Colorado, Orange, Campos and Lower Congo basins. Tectonophysics 133.

Maslin, M., Owen, M., Day, S., Long, D., 2004. Linking continental-slope failures and climate change: Testing the clathrate gun hypothesis. Geology 32, 53–56.

Maystrenko, Y.P., Scheck-Wenderoth, M., Hartwig, A., Anka, Z., Watts, A.B., Hirsch, K.K., Fishwick, S., 2013. Structural features of the Southwest African continental margin according to results of lithosphere-scale 3D gravity and thermal modelling. Tectonophysics 604, 104–121.

McKenzie, D., 1978. Some remarks on the development of sedimentary basins. Earth and Planetary Science Letters 40, 25–32.

McMillan, I.K., 2003. Foraminiferally defined biostratigraphic episodes and sedimentation pattern of the Cretaceous drift succession (Early Barremian to Late Maastrichtian) in seven basins on the South African and southern Namibian continental margin. South African Journal of Science 99, 537–576.

Mello, M.R., Gaglianone, P.C., Brassell, S.C., Maxwell, J.R., 1988a. Geochemical and biological marker assessment of depositional environments using Brazilian offshore oils. Marine and Petroleum Geology 5, 205–223.

Mello, M.R., Katz, B.J., 2000. Petroleum Systems of South Atlantic Margins. AAPG Memoir 73.

Mello, M.R., Koutsoukos, E.A.M., Hart, M.B., Brassell, S.C., Maxwell, J.R., 1989. Late cretaceous anoxic events in the Brazilian continental margin. Organic Geochemistry 14, 529–542.

Mello, M.R., Telnaes, N., Gaglianone, P.C., Chicarelli, M.I., Brassell, S.C., Maxwell, J.R., 1988b. Organic geochemical characterisation of depositional palaeoenvironments of source rocks and oils in Brazilian marginal basins. Organic Geochemistry 13, 31–45.

Meyers, P.A., 1984. 6. Organic Geochemistry of Sediments from the Angola Basin and the Walvis Ridge: A Synthesis of Studies from Deep Sea Drilling Project Leg 75, Initial Report of the Deep Sea Drilling Project. U.S. Government Printing Office, Washington.

Milkov, A. V, 2004. Global estimates of hydrate-bound gas in marine sediments: how much is really out there? Earth Science Review 66, 183–197.

Milkov, A. V, 2011. Worldwide distribution and significance of secondary microbial methane formed during petroleum biodegradation in conventional reservoirs. Organic Geochemistry 42, 184–207.

Moore, A.E., Blenkinsop, T., Cotterill, F., 2008. Controls on post-Gondwana alkaline volcanism in Southern Africa. Earth and Planetary Science Letters 268, 151–164.

Moss, J.L., Cartwright, J., 2010a. 3D seismic expression of km-scale fluid escape pipes from offshore Namibia. Basin Research 22, 481–501.

Moss, J.L., Cartwright, J., 2010b. The spatial and temporal distribution of pipe formation, offshore Namibia. Marine and Petroleum Geology 27, 1216–1234.

Muntingh, A., 1993. Geology, prospects in Orange basin offshore western South Africa. Oil and Gas Journal 106–109.

Muntingh, A., Brown L. F., J., 1993. Sequence Stratigraphy of Petroleum Plays, Post-Rift Cretaceous Rocks (Lower Aptian to Upper Maastrichtian), Orange Basin, Western Offshore, South Africa, in: Weimar, P., Posamentier, H. (Eds.), Siliciclastic Sequence Stratigraphy, Recent Developments and Applications; AAPG Memoir 58. The American Association of Petroleum Geologists, Tulsa, Oklahoma, U.S.A., pp. 71–98.

Muscio, G.P.A., Horsfield, B., 1996. Neoformation of Inert Carbon during the Natural Maturation of a Marine Source Rock: Bakken Shale, Williston Basin. Energy & Fuels 10, 10–18.

Naeth, J., Primio, R., Horsfield, B., Schaefer, R.G., Shannon, P.M., Bailey, W.R., Henriet, J.P., 2005. Hydrocarbon seepage and carbonate mound formation: a basin modelling study from the Porcupine Basin (offshore Ireland). Journal of Petroleum Geology 28, 147–165.

Nürnberg, D., Müller, R.D., 1991. The tectonic evolution of the South Atlantic from Late Jurassic to present. Tectonophysics 191, 27–53.

O'Connor, F.M., Boucher, O., Gedney, N., Jones, C.D., Folberth, G.A., Coppell, R., Friedlingstein, P., Collins, W.J., Chappellaz, J., Ridley, J., Johnson, C.E., 2010. Possible role of wetlands, permafrost, and methane hydrates in the methane cycle under future climate change: A review. Reviews of Geophysics 48, RG4005.

Ogg, J.G., Ogg, G., Gradstein, F.M., 2008. The Concise Geologic Time Scale. Cambridge University Press, Cambridge.

Orr, W.L., 1986. Kerogen/asphaltene/sulfur relationships in sulfur-rich Monterey oils. Advances in Petroleum Geochemistry 10, 499–516.

Ostanin, I., Anka, Z., di Primio, R., Bernal, A., 2012. Identification of a large Upper Cretaceous polygonal fault network in the Hammerfest basin: Implications on the reactivation of regional faulting and gas leakage dynamics, SW Barents Sea. Marine Geology 332-334, 109–125.

Owen, G., 2003. Load structures: gravity-driven sediment mobilization in the shallow subsurface. Geological Society of London, Special Publication 216, 21–34.

Partridge, T.C., Maud, R.R., 2000. Macro-Scale Geomorphic Evolution of Southern Africa, in: Partridge, T.C., Maud, R.R. (Eds.), The Cenozoic of Southern Africa. Oxford University Press, New York, pp. 3–18.

Paton, D.A., di Primio, R., Kuhlmann, G., van der Spuy, D., Horsfield, B., 2007. Insights into the Petroleum System Evolution of the southern Orange Basin, South, Africa. South African Journal of Geology 110, 261–274.

Paton, D.A., van der Spuy, D., di Primio, R., Horsfield, B., 2008. Tectonically induced adjustment of passive-margin accommodation space; influence on the hydrocarbon potential of the Orange Basin, South Africa. AAPG Bulletin 92, 589–609.

Pepper, A.S., Corvi, P.J., 1995. Simple kinetic models of petroleum formation. Part I: oil and gas generation from kerogen. Marine and Petroleum Geology 12, 291–319.

Peters, K.E., Magoon, L.B., Lampe, C., Hosford Scheirer, A., Lillis, P.G., Gautier, D.L., USGS, 2007. A Four-Dimensional Petroleum System Model for the San Joaquin Province, California, Petroleum Systems and Geologic Assessment of Oil and Gas in the San Joaquin Basin Province, California. USGS.

Peters, K.E., Walters, C.C., Mankiewicz, P.J., 2006. Evaluation of kinetic uncertainty in numerical models of petroleum generation. AAPG Bulletin 90, 387–403.

Peters, K.E., Walters, C.C., Moldowan, J.M., 2005. The Biomarker Guide: Biomarkers and isotopes in the environment and human history, Volume 1. Cambridge University Press.

Pether, J., Roberts, D.L., Ward, J.D., 2000. Deposits of the West Coast, in: Partridge, T.C., Maud, R.R. (Eds.), The Cenozoic of Southern Africa. Oxford University Press, Oxford.

Petroleum Agency SA, 2012. Exploration opportunities in South Africa [WWW Document]. URL http://www.petroleumagencysa.com/Libraries/Promotion_Images/14_Final_WPC_Qatar_2011fa.sflb.ashx (accessed 8.10.12).

Phillips, D., Kiviets, G.B., Biddulph, M.G., Madav, M.K., 2000. Cenozoic Volcanism, in: Partridge, T.C., Maud, R.R. (Eds.), The Cenozoic of Southern Africa. Oxford University Press, New York, p. 373.

Pilcher, R., Argent, J., 2007. Mega-pockmarks and linear pockmark trains on the West African continental margin. Marine Geology 244, 15–32.

Raab, M.J., Brown, R.W., Gallagher, K., Weber, K., Gleadow, A.J.W., 2005. Denudational and thermal history of the Early Cretaceous Brandberg and Okenyenya igneous complexes on Namibia's Atlantic passive margin. Tectonics 24, TC3006.

Raynaud, J.F., Robert, P., 1978. 6. Microscopical survey of organic matter from DSDP sites 361, 362, and 364, DSDP report, Leg 40.

Reynolds, J.G.O., Burnham, A.K., 1995. Comparison of kinetic analysis of source rocks and kerogen. Organic Geochemistry 23, 11–19.

Ridgwell, A., Edwards, U., 2007. Geological Carbon Sinks, in: Reay, D., Smith, K., Grace, J. (Eds.), Greenhouse Gas Sinks. CAB International, Wallingford, CT, pp. 74–97.

Roberts, D.L., Botha, G.A., Maud, R.R., Pether, J., 2006. Coastal Cenozoic Deposits, in: Johnson, M.R., Anhaeusser, C.R., Thomas, R.J. (Eds.), The Geology of South Africa. Geological Society of South Africa, Johannesburg, Pretoria, pp. 605–628.

Rouby, D., Bonnet, S., Guillocheau, F., Robin, C., Biancotto, F., Dauteuil, O., Braun, J., 2009. Sediment supply to the Orange sedimentary system over the last 150 My: An evaluation from sedimentation/denudation balance. Marine and Petroleum Geology 26, 782–794.

Ruhl, M., Bonis, N.R., Reichart, G.-J., Sinninghe Damsté, J.S., Kürschner, W.M., 2011. Atmospheric carbon injection linked to end-Triassic mass extinction. Science 333, 430–4.

SA, P.A., 2003. South African Exploration Opportunities. South African Agency for Promotion of Petroleum Exploration and Exploitation, Parow, Cape Town, Parow, Cape Town.

Schaeffer, P., Reiss, C., Albrecht, P., 1995. Geochemical study of macromolecular organic matter from sulfur-rich sediments of evaporitic origin (Messinian of Sicily) by chemical degradations. Organic Geochemistry 23, 567–581.

Schenk, H.J., Di Primio, R., Horsfield, B., 1997a. The conversion of oil into gas in petroleum reservoirs. Part 1: Comparative kinetic investigation of gas generation from crude oils of lacustrine, marine and fluviodeltaic origin by programmed-temperature closed-system pyrolysis. Organic Geochemistry 26, 467–481.

Schenk, H.J., Horsfield, B., Krooss, B., Schaefer, R.G., Schwochau, K., 1997b. Kinetics of Petroleum Formation and Cracking, in: Welte, D.H., Horsfield, B., Baker, D.R. (Eds.), Petroleum and Basin Evolution. Springer-Verlag, Berlin Heidelberg, pp. 231–270.

Schiefelbein, C.F., Zumberge, J.E., Cameron, N.C., Brown, S.W., 2000. Geochemical comparison of crude oil along the South Atlantic margins. AAPG Memoir 73, 15–26.

Schmidt, S., 2004. The Petroleum Potential of the Passive Continental Margin of South-Western Africa- A Basin Modelling Study. Fak. für Georesourcen und Mater. Rheinisch-Westfälische Technische Hochschule Aachen.

Schoell, M., 1983. Genetic Characterization of Natural Gases. AAPG Bulletin 12, 2225–2238.

Séranne, M., Anka, Z., 2005. South Atlantic continental margins of Africa: A comparison of the tectonic vs climate interplay on the evolution of equatorial west Africa and SW Africa margins. Journal of African Earth Science 43, 283–300.

Séranne, M., Nzé Abeigne, C.-R., 1999. Oligocene to Holocene sediment drifts and bottom currents on the slope of Gabon continental margin (West Africa): Consequences for sedimentation and southeast Atlantic upwelling. Sedimentary Geology 128, 179–199.

Siesser, W.G., Dingle, R. V, 1981. Tertiary Sea-Level Movements around Southern Africa. The Journal of Geology 89, 523–536.

Stainforth, J.G., 2009. Practical kinetic modeling of petroleum generation and expulsion. Marine and Petroleum Geology 26, 552–572.

Sun, Q., Wu, S., Hovland, M., Luo, P., Lu, Y., Qu, T., 2011. The morphologies and genesis of mega-pockmarks near the Xisha Uplift, South China Sea. Marine and Petroleum Geology 28, 1146–1156.

Svensen, H., Planke, S., Corfu, F., 2010. Zircon dating ties NE Atlantic sill emplacement to initial Eocene global warming. Journal of the Geologic Society London. 167, 433–436.

Svensen, H., Planke, S., Malthe-Sørenssen, A., Jamtveit, B., Myklebust, R., Rasmussen Eidem, T., Rey, S.S., 2004. Release of methane from a volcanic basin as a mechanism for initial Eocene global warming. Nature 429, 542–5.

Swart, R., 2009. Hydrate occurrences in the Namibe Basin, offshore Namibia. Geological Society of London, Special Publication 319, 73–80.

Tankard, A., Welsink, H., Aukes, P., Newton, R., Stettler, E., 2009. Tectonic evolution of the Cape and Karoo basins of South Africa. Marine and Petroleum Geology 26, 1379–1412.

Tegelaar, E.W., Noble, R. a., 1994. Kinetics of hydrocarbon generation as a function of the molecular structure of kerogen as revealed by pyrolysis-gas chromatography. Organic Geochemistry 22, 543–574.

Thompson, K.F.M., 1983. Classification and thermal history of petroleum based on light hydrocarbons. Geochimica et Cosmochimica Acta 47, 303–316.

Tinker, J., de Wit, M., Brown, R., 2008a. Linking source and sink: Evaluating the balance between onshore erosion and offshore sediment accumulation since Gondwana break-up, South Africa. Tectonophysics 455, 94–103.

Tinker, J., de Wit, M., Brown, R., 2008b. Mesozoic exhumation of the southern Cape, South Africa, quantified using apatite fission track thermochronology. Tectonophysics 455, 77–93.

Tissot, B.P., Pelet, R., Ungerer, P., 1987. Thermal history of sedimentary basins, maturation indices, and kinetics of oil and gas generation. AAPG Bulletin 71, 1445–1466.

Tissot, B.P., Welte, D.H., 1984. Petroleum Formation and Occurence. Springer Verlag, Berlin.

Torsvik, T.H., Rousse, S., Labails, C., Smethurst, M.A., 2009. A new scheme for the opening of the South Atlantic Ocean and the dissection of an Aptian salt basin. Geophyscial Journal International 177, 1315–1333.

Uenzelmann-Neben, G., Schluter, P., Weigelt, E., 2007. Cenozoic oceanic circulation within the South African gateway: indications from seismic stratigraphy. South African Journal of Geology 110, 275–294.

Van de Meent, D., Brown, S.C., Philp, R.P., Simoneit, B.R.T., 1980. Pyrolysis-high resolution gas chromatography and pyrolysis gas chromatography-mass spectrometry of kerogens and kerogen precursors. Geochimica et Cosmochimica Acta 44, 999–1013.

Van der Spuy, D., 2003. Aptian source rocks in some South African Cretaceous basins. Geological Society of London, Special Publication 207, 185–202.

Van der Spuy, D., 2005. Prospectivity of the Northern Orange Basin, offshore South, in: 18th World Petroleum Congress. 2005 World Petroleum Congress, Johannesburg, South Africa.

Van Wees, J.D., van Bergen, F., David, P., Nepveu, M., Beekman, F., Cloetingh, S., Bonté, D., 2009. Probabilistic tectonic heat flow modeling for basin maturation: Assessment method and applications. Marine and Petroleum Geology 26, 536–551.

Vasseur, G., Luo, X., Yan, J., Loggia, D., Toussaint, R., Schmittbuhl, J., 2013. Flow regime associated with vertical secondary migration. Marine and Petroleum Geology 45, 150–158.

Velde, B., 1996. Compaction trends of clay-rich deep sea sediments. Marine Geology 133, 193–201.

Verwoerd, W.J., de Beer, C.H., 2006. Cretaceous and Teritary igneous events, in: Johnson, M.R., Anhaeusser, C.R., Thomas, R.J. (Eds.), The Geology of South Africa. The Geological

Society of South Africa, Johannesburg, Council for Geoscience, Pretoria, Johannesburg, Pretoria, pp. 573–583.

Viola, G., Andreoli, M., Ben-Avraham, Z., Stengel, I., Reshef, M., 2005. Offshore mud volcanoes and onland faulting in southwestern Africa: neotectonic implications and constraints on the regional stress field. Earth and Planetary Science Letters 231, 147–160.

Vogt, P.R., 1997. Hummock fields in the Norway Basin and Eastern Iceland Plateau: Rayleigh-Taylor instabilities? Geology 25, 531–534.

Weigelt, E., Uenzelmann-Neben, G., 2004. Sediment deposits in the Cape Basin: Indications for shifting ocean currents? AAPG Bulletin 88, 765–780.

Welte, D.H., Horsfield, B., Baker, D.R., 1997. Petroleum and Basin Evolution. Springer Verlag, Berlin, Heidelberg.

Westbrook, G.K., Thatcher, K.E., Rohling, E.J., Piotrowski, A.M., Pälike, H., Osborne, A.H., Nisbet, E.G., Minshull, T.A., Lanoisellé, M., James, R.H., Hühnerbach, V., Green, D., Fisher, R.E., Crocker, A.J., Chabert, A., Bolton, C., Beszczynska-Möller, A., Berndt, C., Aquilina, A., 2009. Escape of methane gas from the seabed along the West Spitsbergen continental margin. Geophysical Research Letters 36, L15608.

Wickens, H. de V, McLachlan, I.R., 1990. The stratigraphy and sedimentology of the reservoir interval of the Kudu 9A-2 and 9A-3 boreholes. Communications of the Geological Survey of Namibia 6, 9–22.

Wigley, R.A., Compton, J.S., 2006. Late Cenozoic evolution of the outer continental shelf at the head of the Cape Canyon, South Africa. Marine Geology 226, 1–23.

Wilhelms, A., Larter, S.R., Head, I., Farrimond, P., di-Primio, R., Zwach, C., 2001. Biodegradation of oil in uplifted basins prevented by deep-burial sterilization. Nature 411, 1034–1037.

Wygrala, B.P., 1989. Integrated study of an oil field in the southern Po basin, northern Italy. Forschungszentrum Jülich reports.

Yassir, N., 2003. The role of shear stress in mobilizing deep-seated mud volcanoes: geological and geomechanical evidence from Trinidad and Taiwan. Geological Society of London, Special Publication 216, 461–474.

Zachos, J., Pagani, M., Sloan, L., Thomas, E., Billups, K., 2001. Trends, rhythms, and aberrations in global climate 65 Ma to present. Science 292, 686–93.

Zachos, J.C., Dickens, G.R., Zeebe, R.E., 2008. An early Cenozoic perspective on greenhouse warming and carbon-cycle dynamics. Nature 451, 279–283.

Zeebe, R.E., Zachos, J.C., 2013. Long-term legacy of massive carbon input to the Earth system: Anthropocene versus Eocene. Philosophical Transactions of the Royal Society A: Physical, Mathematical and Engineering 371.

Zeebe, R.E., Zachos, J.C., Dickens, G.R., 2009. Carbon dioxide forcing alone insufficient to explain Palaeocene-Eocene Thermal Maximum warming. Nature Geoscience 2, 576–580.

Zimmerman, H.B., Boersma, A., McCoy, F.W., 1987. Carbonaceous sediments and palaeoenvironment of the Cretaceous South Atlantic Ocean. Geological Society of London, Special Publication 26, 271–286.

Appendix

DSDP sample compilation and laboratory results

G007867	DSDP sample info and GFZ Rock-Eval data	
No sample picture	Sample info	G007867
	Location	Walvis Ridge
	Leg	75
	Site	530
	Hole	A
	Core	95
	Section	5
	Top [cm]	9.0
	Bot [cm]	10.0
	Depth [mbsf]	1014.09
	S1 (mg/g)	0.16
	S2 (mg/g)	0.58
	S3 (mg/g)	1.5
	Tmax (°C)	407
	PP (mg/g)	0.74
	PI (wt ratio)	0.22
	HI (mg HC/g TOC)	64
	OI (mg CO2/g TOC)	165
	TOC (%)*	0.91
	Chrono-stratigraphic Age	lower Turonian ?
	Lithology (from DSDP reports)	green claystone, black shale
Open Pyrolysis GC		
No measurements for open pyroysis, bulk kinetics, and compositional kinetics were conducted on this sample.		

*: TOC from Leco

G007868	DSDP sample info and GFZ Rock-Eval data	
No sample picture	Sample info	G007868
	Location	Walvis Ridge
	Leg	75
	Site	530
	Hole	A
	Core	95
	Section	CC
	Top [cm]	41.0
	Bot [cm]	42.0
	Depth [mbsf]	1014.41
	S1 (mg/g)	1.87
	S2 (mg/g)	96.67
	S3 (mg/g)	11.53
	Tmax (°C)	407
	PP (mg/g)	98.54
	PI (wt ratio)	0.02
	HI (mg HC/g TOC)	721
	OI (mg CO2/g TOC)	86
	TOC (%)*	13.4
	Chrono-stratigraphic Age	lower Turonian ?
	Lithology (from DSDP reports)	green claystone, black shale

Open Pyrolysis GC

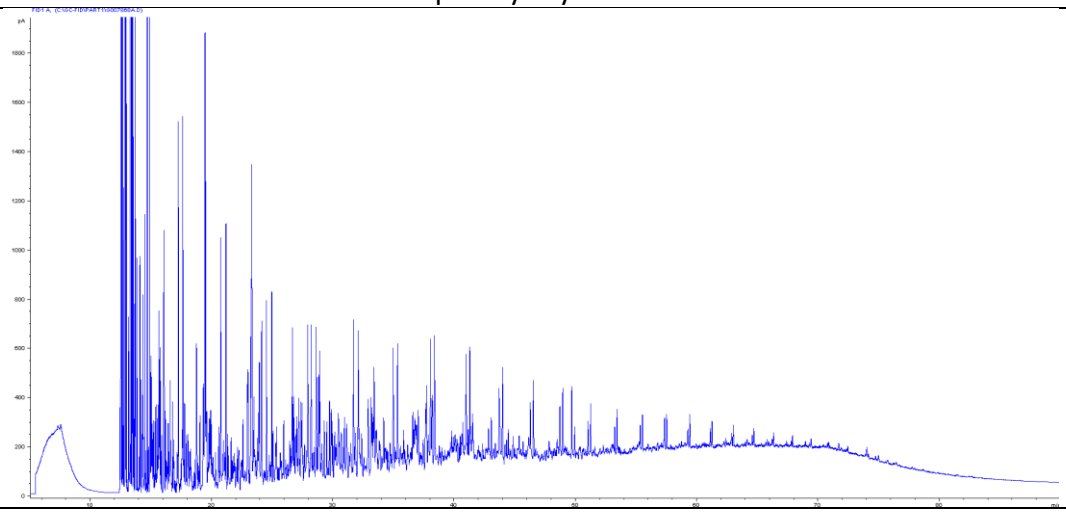

Bulk kinetics

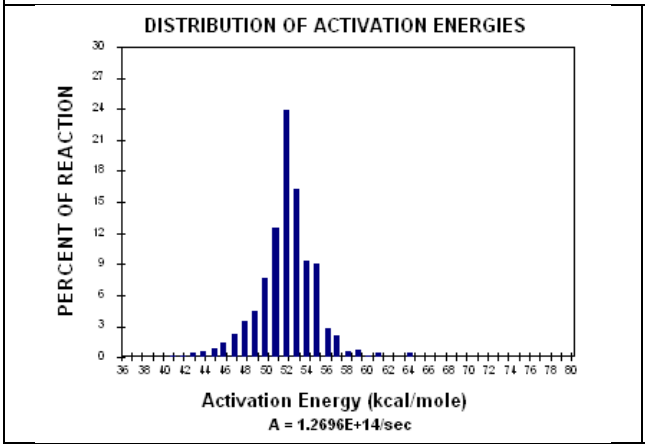

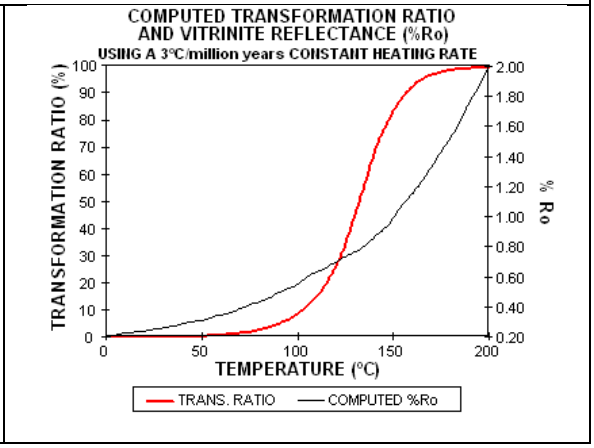

GC at 10% transformation ratio

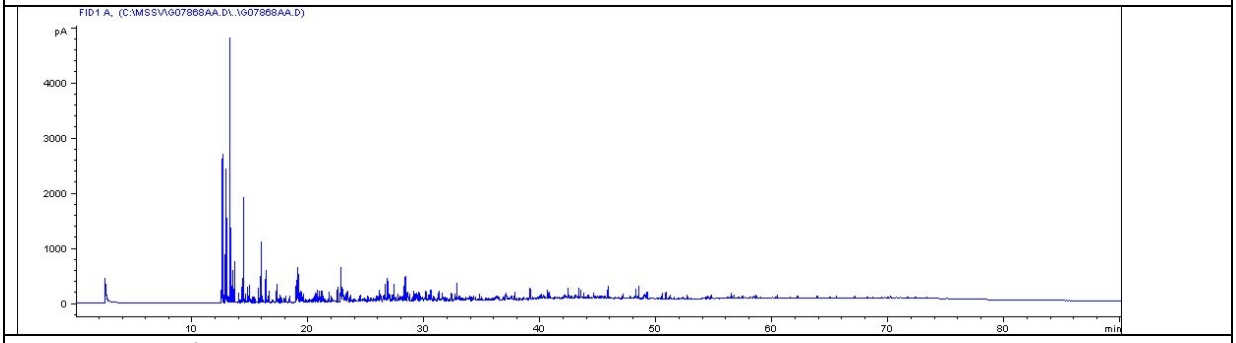

GC at 30% transformation ratio

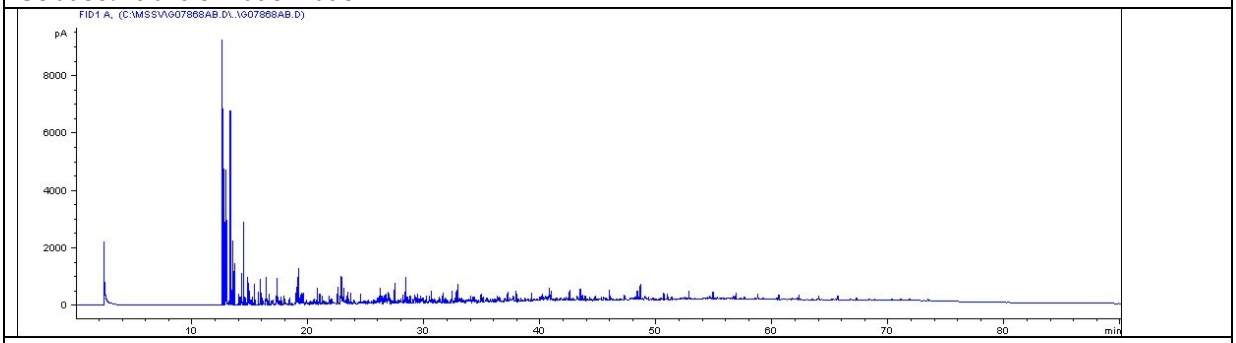

GC at 50% transformation ratio

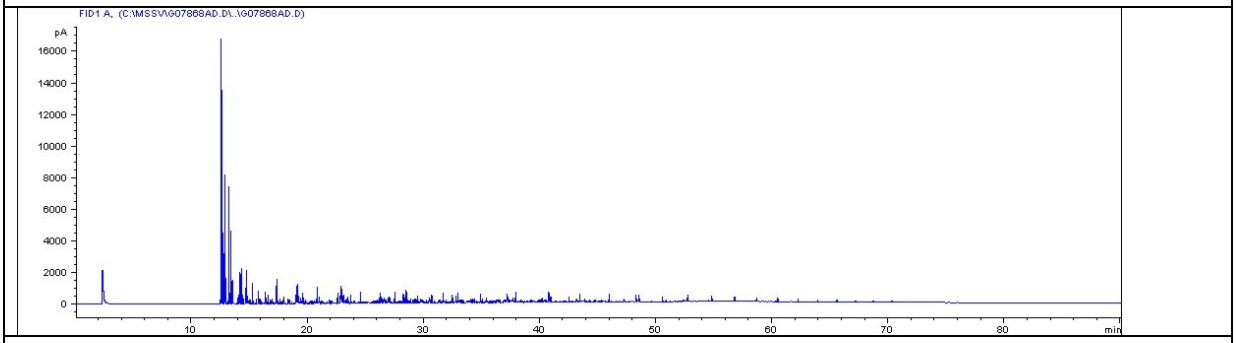

GC at 70% transformation ratio

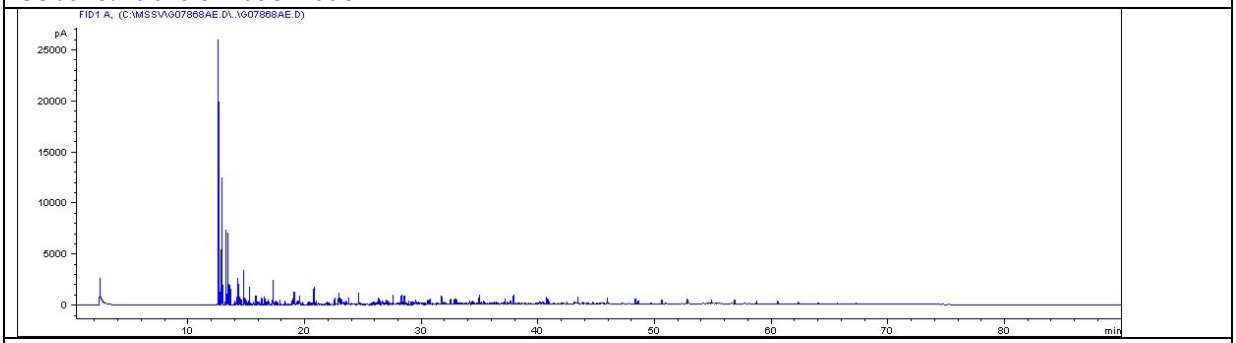

GC at 90% transformation ratio

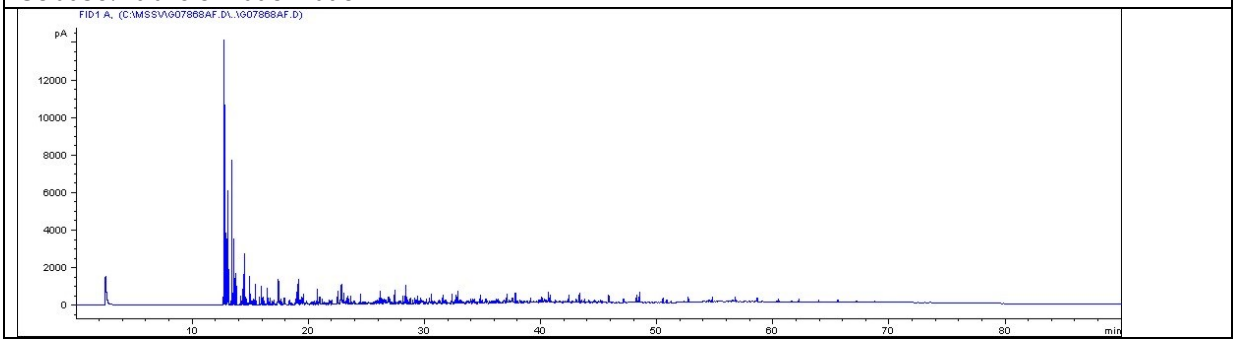

G007869	DSDP sample info and GFZ Rock-Eval data	
No sample picture	Sample info	G007869
	Location	Walvis Ridge
	Leg	75
	Site	530
	Hole	A
	Core	97
	Section	4
	Top [cm]	27.0
	Bot [cm]	28.0
	Depth [mbsf]	1030.77
	S1 (mg/g)	0.67
	S2 (mg/g)	53.63
	S3 (mg/g)	6.1
	Tmax (°C)	410
	PP (mg/g)	54.3
	PI (wt ratio)	0.01
	HI (mg HC/g TOC)	506
	OI (mg CO2/g TOC)	58
	TOC (%)*	10.6
	Chrono-stratigraphic Age	Albian
	Lithology (from DSDP reports)	claystone, black shale
Open Pyrolysis GC		
Open pyrolysis GC not available. No measurements compositional kinetics were conducted on this sample.		

Bulk kinetics

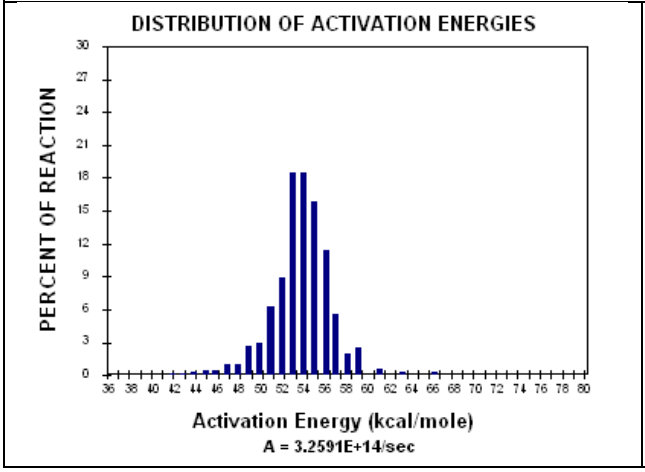

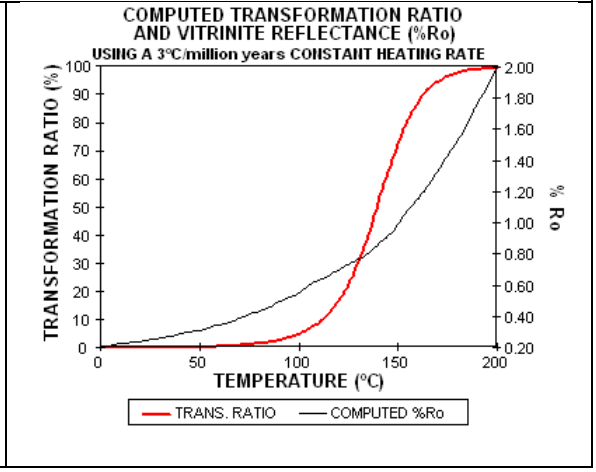

G007870	DSDP sample info and GFZ Rock-Eval data	
No sample picture	Sample info	G007870
	Location	Walvis Ridge
	Leg	75
	Site	530
	Hole	A
	Core	97
	Section	4
	Top [cm]	79.0
	Bot [cm]	80.0
	Depth [mbsf]	1031.29
	S1 (mg/g)	0.21
	S2 (mg/g)	13.51
	S3 (mg/g)	2.12
	Tmax (°C)	415
	PP (mg/g)	13.72
	PI (wt ratio)	0.02
	HI (mg HC/g TOC)	225
	OI (mg CO2/g TOC)	35
	TOC (%)*	6.01
	Chrono-stratigraphic Age	Albian
	Lithology (from DSDP reports)	claystone, black shale
Open Pyrolysis GC		
Open pyrolysis GC not available. No measurements for bulk kinetics and compositional kinetics were conducted on this sample.		

G007871	DSDP sample info and GFZ Rock-Eval data	
No sample picture	Sample info	G007871
	Location	Walvis Ridge
	Leg	75
	Site	530
	Hole	A
	Core	98
	Section	3
	Top [cm]	55.0
	Bot [cm]	56.0
	Depth [mbsf]	1038.55
	S1 (mg/g)	0.25
	S2 (mg/g)	12.79
	S3 (mg/g)	2.98
	Tmax (°C)	411
	PP (mg/g)	13.04
	PI (wt ratio)	0.02
	HI (mg HC/g TOC)	196
	OI (mg CO2/g TOC)	46
	TOC (%)*	6.51
	Chrono-stratigraphic Age	Albian
	Lithology (from DSDP reports)	claystone, mudstone, black shale

Open Pyrolysis GC

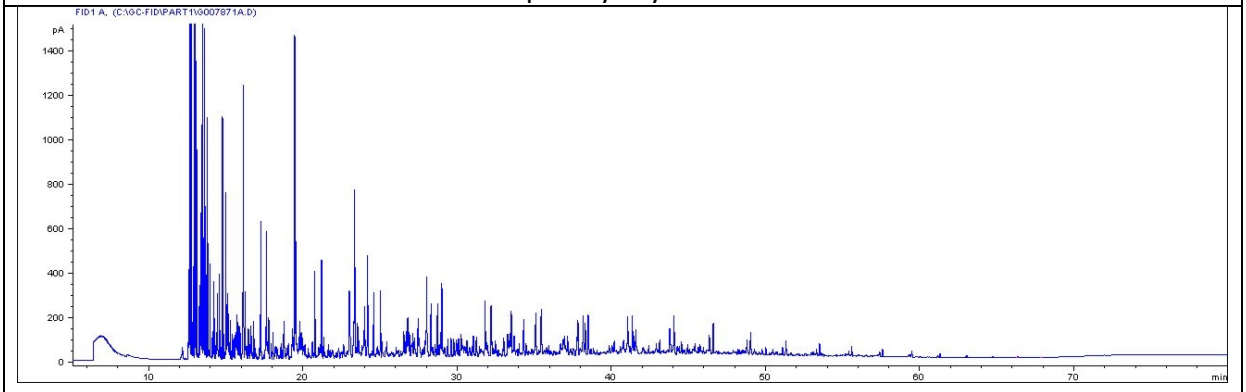

No measurements for compositional kinetics were conducted on this sample.

Bulk kinetics

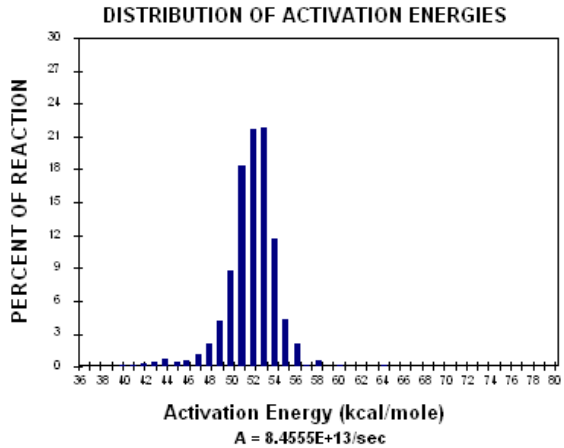

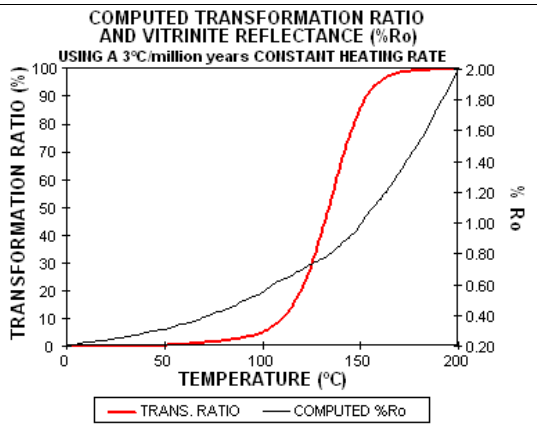

G007872	DSDP sample info and GFZ Rock-Eval data	
No sample picture	Sample info	G007872
	Location	Walvis Ridge
	Leg	75
	Site	530
	Hole	A
	Core	101
	Section	5
	Top [cm]	55.0
	Bot [cm]	56.0
	Depth [mbsf]	1068.55
	S1 (mg/g)	0.04
	S2 (mg/g)	0.27
	S3 (mg/g)	0.85
	Tmax (°C)	417
	PP (mg/g)	0.31
	PI (wt ratio)	0.13
	HI (mg HC/g TOC)	59
	OI (mg CO2/g TOC)	187
	TOC (%)*	0.45
	Chrono-stratigraphic Age	Albian
	Lithology (from DSDP reports)	mudstone, marlstone, black shale

Open Pyrolysis GC

Open pyrolysis GC not available.

No measurements for bulk kinetics and compositional kinetics were conducted on this sample.

G007873	DSDP sample info and GFZ Rock-Eval data	
	Sample info	G007873
	Location	Walvis Ridge
	Leg	75
	Site	530
	Hole	A
	Core	104
	Section	3
	Top [cm]	9.0
	Bot [cm]	10.0
	Depth [mbsf]	1088.09
	S1 (mg/g)	0.09
	S2 (mg/g)	4.49
	S3 (mg/g)	1.45
	Tmax (°C)	428
	PP (mg/g)	4.58
	PI (wt ratio)	0.02
	HI (mg HC/g TOC)	175
	OI (mg CO2/g TOC)	57
	TOC (%)*	2.56
	Chrono-stratigraphic Age	Albian
	Lithology (from DSDP reports)	grey siltstone, black shale, green limestone

Open Pyrolysis GC

Open pyrolysis GC not available.

No measurements for compositional kinetics were conducted on this sample.

Bulk kinetics

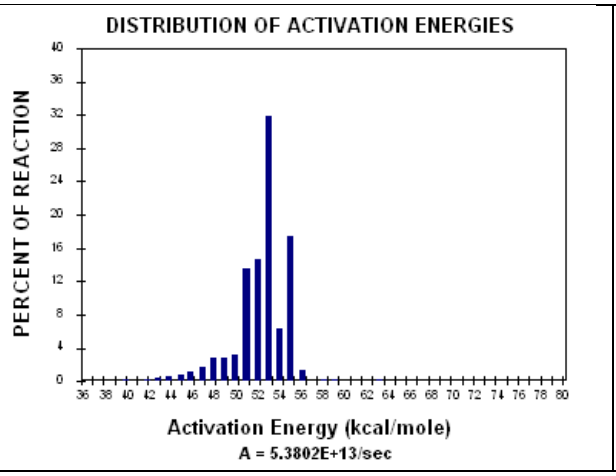

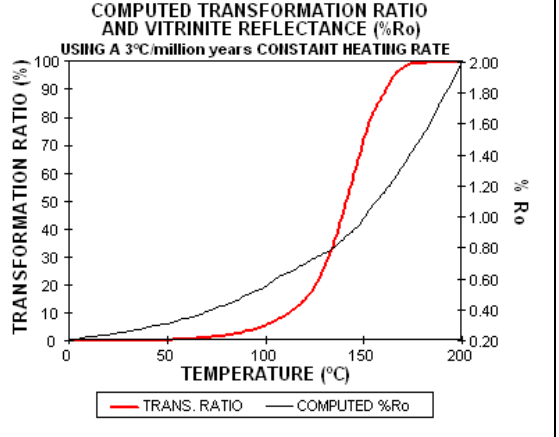

G007874	DSDP sample info and GFZ Rock-Eval data	
	Sample info	G007874
	Location	Walvis Ridge
	Leg	75
	Site	530
	Hole	A
	Core	104
	Section	3
	Top [cm]	99.0
	Bot [cm]	100.0
	Depth [mbsf]	1088.99
	S1 (mg/g)	0.15
	S2 (mg/g)	7.44
	S3 (mg/g)	1.69
	Tmax (°C)	413
	PP (mg/g)	7.59
	PI (wt ratio)	0.02
	HI (mg HC/g TOC)	144
	OI (mg CO2/g TOC)	33
	TOC (%)*	5.15
	Chrono-stratigraphic Age	Albian
	Lithology (from DSDP reports)	grey siltstone, black shale, green limestone

Open Pyrolysis GC

Open pyrolysis GC not available.

No measurements for bulk kinetics and compositional kinetics were conducted on this sample.

G007875	DSDP sample info and GFZ Rock-Eval data	
	Sample info	G007875
	Location	Walvis Ridge
	Leg	75
	Site	530
	Hole	A
	Core	105
	Section	3
	Top [cm]	85.0
	Bot [cm]	86.0
	Depth [mbsf]	1097.85
	S1 (mg/g)	0.49
	S2 (mg/g)	27.52
	S3 (mg/g)	2.11
	Tmax (°C)	405
	PP (mg/g)	28.01
	PI (wt ratio)	0.02
	HI (mg HC/g TOC)	385
	OI (mg CO2/g TOC)	30
	TOC (%)*	7.14
	Chrono-stratigraphic Age	Albian
	Lithology (from DSDP reports)	siltstone, limestone, black shale

Open Pyrolysis GC

Open pyrolysis GC not available.

No measurements for bulk kinetics and compositional kinetics were conducted on this sample.

G007876	DSDP sample info and GFZ Rock-Eval data	
	Sample info	G007876
	Location	Walvis Ridge
	Leg	75
	Site	530
	Hole	A
	Core	105
	Section	3
	Top [cm]	126.0
	Bot [cm]	127.0
	Depth [mbsf]	1098.26
	S1 (mg/g)	0.14
	S2 (mg/g)	7.81
	S3 (mg/g)	1.34
	Tmax (°C)	409
	PP (mg/g)	7.95
	PI (wt ratio)	0.02
	HI (mg HC/g TOC)	180
	OI (mg CO2/g TOC)	31
	TOC (%)*	4.33
	Chrono-stratigraphic Age	Albian
	Lithology (from DSDP reports)	siltstone, limestone, black shale

Open Pyrolysis GC

Open pyrolysis GC not available.

No measurements for bulk kinetics and compositional kinetics were conducted on this sample.

G007877	DSDP sample info and GFZ Rock-Eval data	
	Sample info	G007877
	Location	Orange Basin
	Leg	40
	Site	361
	Hole	--
	Core	24
	Section	2
	Top [cm]	98.0
	Bot [cm]	99.0
	Depth [mbsf]	812.98
	S1 (mg/g)	0.08
	S2 (mg/g)	0.37
	S3 (mg/g)	1.03
	Tmax (°C)	417
	PP (mg/g)	0.45
	PI (wt ratio)	0.18
	HI (mg HC/g TOC)	23
	OI (mg CO2/g TOC)	65
	TOC (%)*	1.58
	Chrono-stratigraphic Age	Turonian
	Lithology (from DSDP reports)	shale

Open Pyrolysis GC

Open pyrolysis GC not available.

No measurements for bulk kinetics and compositional kinetics were conducted on this sample.

G007878	DSDP sample info and GFZ Rock-Eval data	
	Sample info	G007878
	Location	Orange Basin
	Leg	40
	Site	361
	Hole	--
	Core	28
	Section	5
	Top [cm]	75.0
	Bot [cm]	76.0
	Depth [mbsf]	1007.25
	S1 (mg/g)	1.22
	S2 (mg/g)	39.91
	S3 (mg/g)	2.29
	Tmax (°C)	406
	PP (mg/g)	41.13
	PI (wt ratio)	0.03
	HI (mg HC/g TOC)	510
	OI (mg CO2/g TOC)	29
	TOC (%)*	7.82
	Chrono-stratigraphic Age	lower Albian
	Lithology (from DSDP reports)	shale, carbonaceous

Open Pyrolysis GC

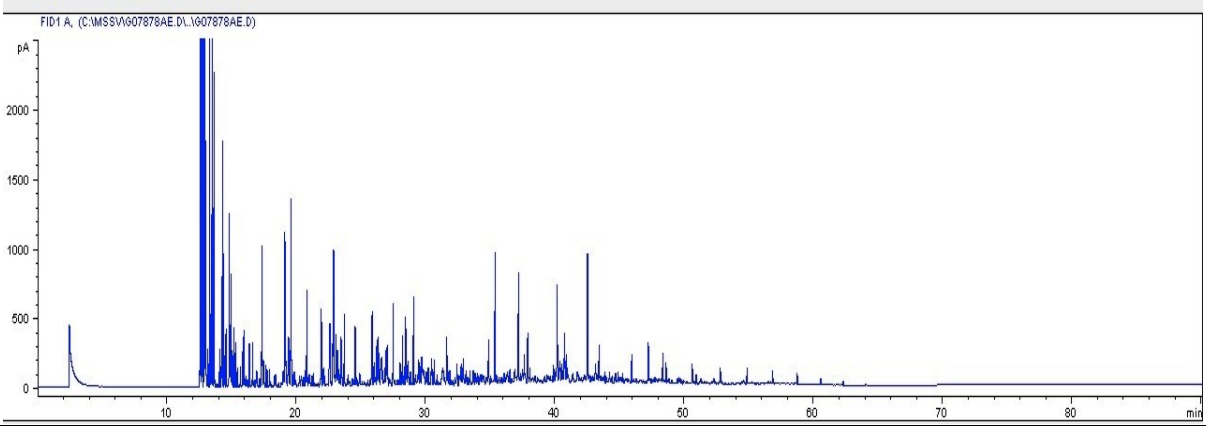

Bulk kinetics

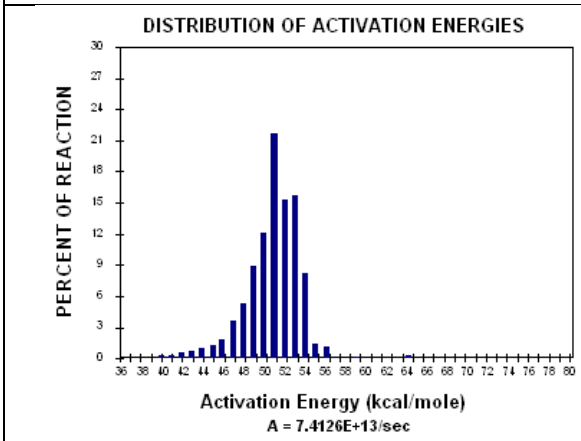

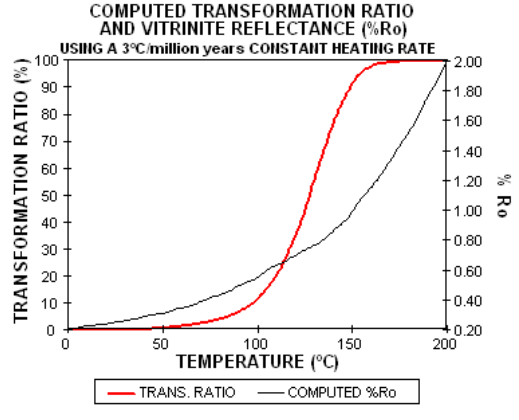

GC at 10% transformation ratio

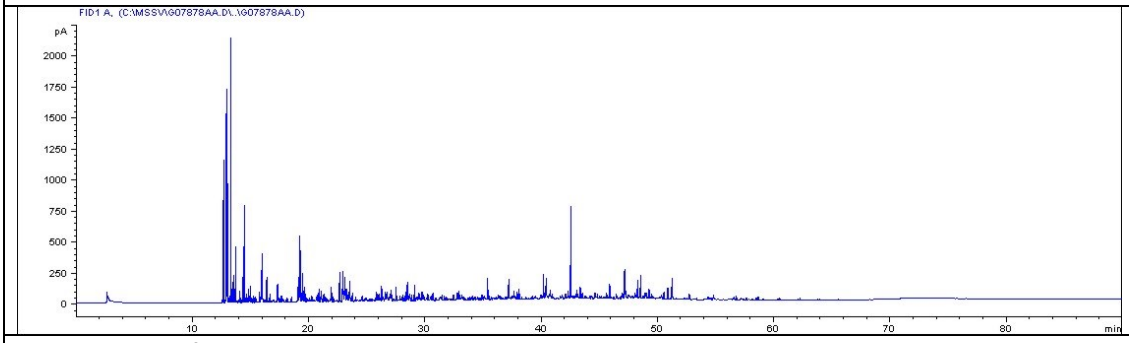

GC at 30% transformation ratio

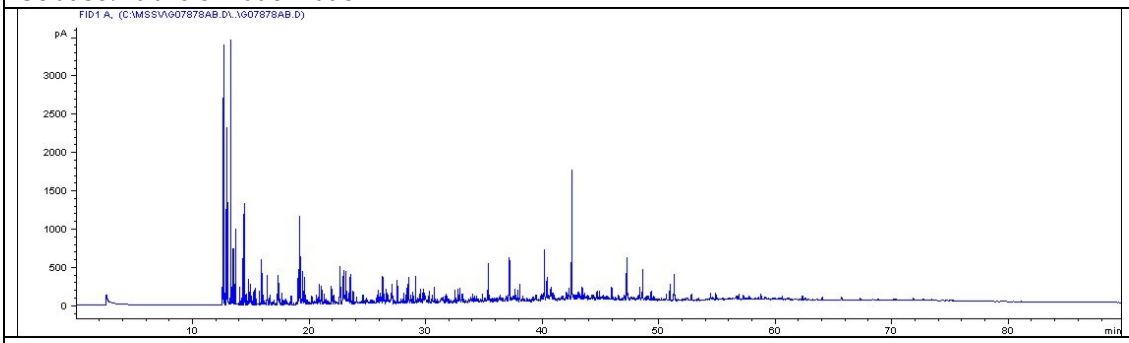

GC at 50% transformation ratio

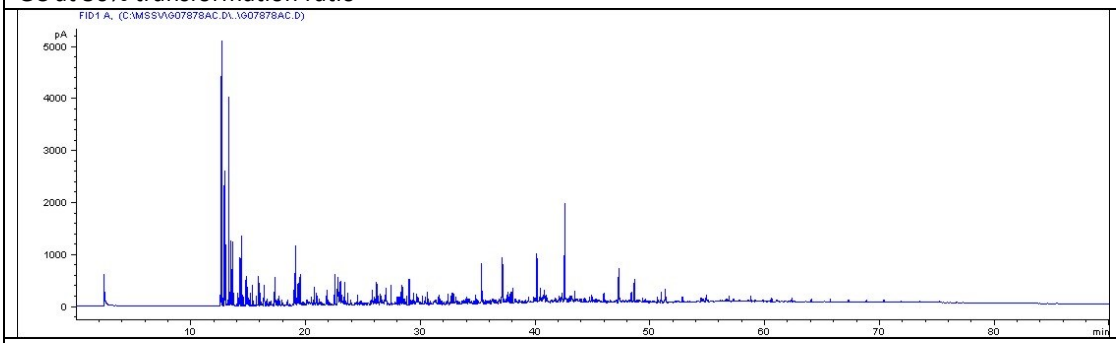

GC at 70% transformation ratio

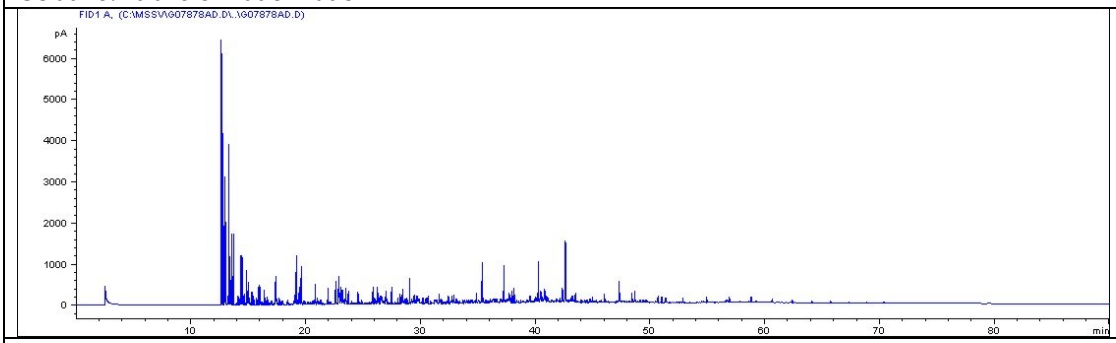

GC at 90% transformation ratio

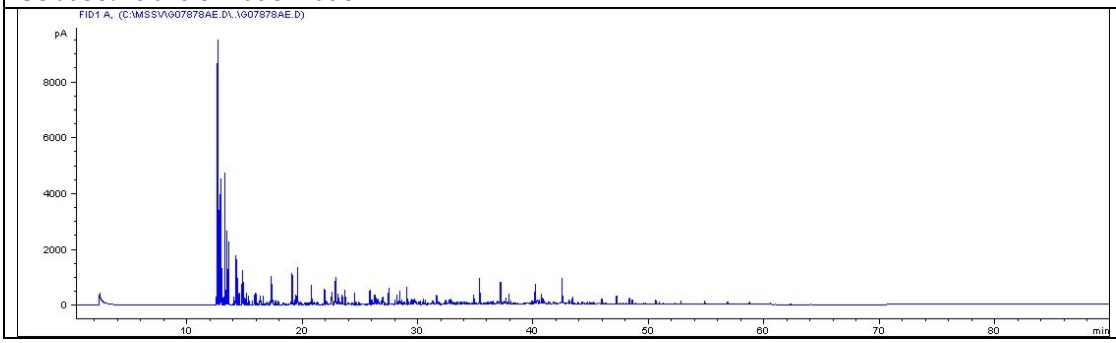

G007879	DSDP sample info and GFZ Rock-Eval data	
	Sample info	G007879
	Location	Orange Basin
	Leg	40
	Site	361
	Hole	--
	Core	28
	Section	5
	Top [cm]	137.0
	Bot [cm]	138.0
	Depth [mbsf]	1007.87
	S1 (mg/g)	0.67
	S2 (mg/g)	18.68
	S3 (mg/g)	1.49
	Tmax (°C)	405
	PP (mg/g)	19.35
	PI (wt ratio)	0.03
	HI (mg HC/g TOC)	365
	OI (mg CO2/g TOC)	29
	TOC (%)*	5.12
	Chrono-stratigraphic Age	lower Albian
	Lithology (from DSDP reports)	shale, carbonaceous

Open Pyrolysis GC

Open pyrolysis GC not available.

No measurements for compositional kinetics were conducted on this sample.

Bulk kinetics

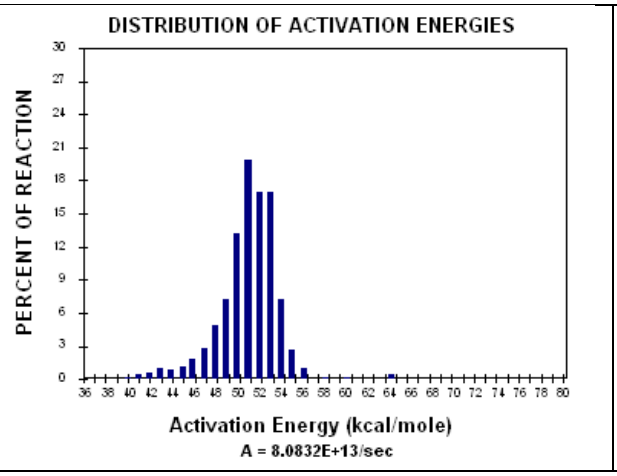

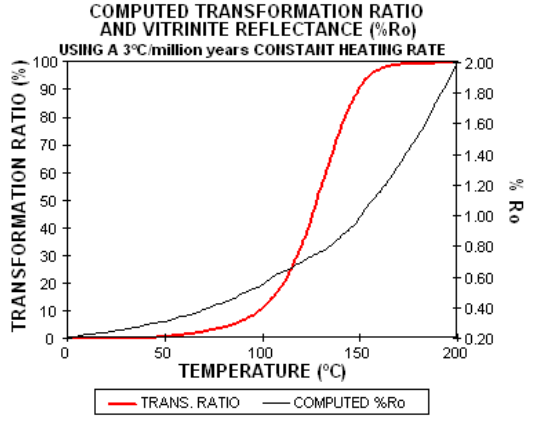

G007880	DSDP sample info and GFZ Rock-Eval data	
	Sample info	G007880
	Location	Orange Basin
	Leg	40
	Site	361
	Hole	--
	Core	29
	Section	2
	Top [cm]	50.0
	Bot [cm]	51.0
	Depth [mbsf]	1031.00
	S1 (mg/g)	0.17
	S2 (mg/g)	2.56
	S3 (mg/g)	1.79
	Tmax (°C)	414
	PP (mg/g)	2.73
	PI (wt ratio)	0.06
	HI (mg HC/g TOC)	63
	OI (mg CO2/g TOC)	44
	TOC (%)*	4.09
	Chrono-stratigraphic Age	lower Albian
	Lithology (from DSDP reports)	shale, carbonaceous

Open Pyrolysis GC

Open pyrolysis GC not available.

No measurements for bulk kinetics and compositional kinetics were conducted on this sample.

G007881	DSDP sample info and GFZ Rock-Eval data	
	Sample info	G007881
	Location	Orange Basin
	Leg	40
	Site	361
	Hole	--
	Core	29
	Section	2
	Top [cm]	112.0
	Bot [cm]	113.0
	Depth [mbsf]	1031.62
	S1 (mg/g)	0.16
	S2 (mg/g)	3.19
	S3 (mg/g)	1.37
	Tmax (°C)	416
	PP (mg/g)	3.35
	PI (wt ratio)	0.05
	HI (mg HC/g TOC)	83
	OI (mg CO2/g TOC)	36
	TOC (%)*	3.84
	Chrono-stratigraphic Age	lower Albian
	Lithology (from DSDP reports)	shale, carbonaceous

Open Pyrolysis GC

Open pyrolysis GC not available.

No measurements for bulk kinetics and compositional kinetics were conducted on this sample.

G007882	DSDP sample info and GFZ Rock-Eval data	
	Sample info	G007882
	Location	Orange Basin
	Leg	40
	Site	361
	Hole	--
	Core	32
	Section	6
	Top [cm]	36.0
	Bot [cm]	37.0
	Depth [mbsf]	1066.86
	S1 (mg/g)	0.16
	S2 (mg/g)	3.45
	S3 (mg/g)	1.39
	Tmax (°C)	416
	PP (mg/g)	3.61
	PI (wt ratio)	0.04
	HI (mg HC/g TOC)	67
	OI (mg CO2/g TOC)	27
	TOC (%)*	5.14
	Chrono-stratigraphic Age	upper Aptian
	Lithology (from DSDP reports)	mudstone

Open Pyrolysis GC

Open pyrolysis GC not available.

No measurements for bulk kinetics and compositional kinetics were conducted on this sample.

G007883	DSDP sample info and GFZ Rock-Eval data	
	Sample info	G007883
	Location	Orange Basin
	Leg	40
	Site	361
	Hole	--
	Core	33
	Section	3
	Top [cm]	50.0
	Bot [cm]	51.0
	Depth [mbsf]	1070.5
	S1 (mg/g)	0.88
	S2 (mg/g)	45.06
	S3 (mg/g)	3.57
	Tmax (°C)	419
	PP (mg/g)	45.94
	PI (wt ratio)	0.02
	HI (mg HC/g TOC)	554
	OI (mg CO2/g TOC)	44
	TOC (%)*	8.13
	Chrono-stratigraphic Age	Aptian
	Lithology (from DSDP reports)	shale

Open Pyrolysis GC

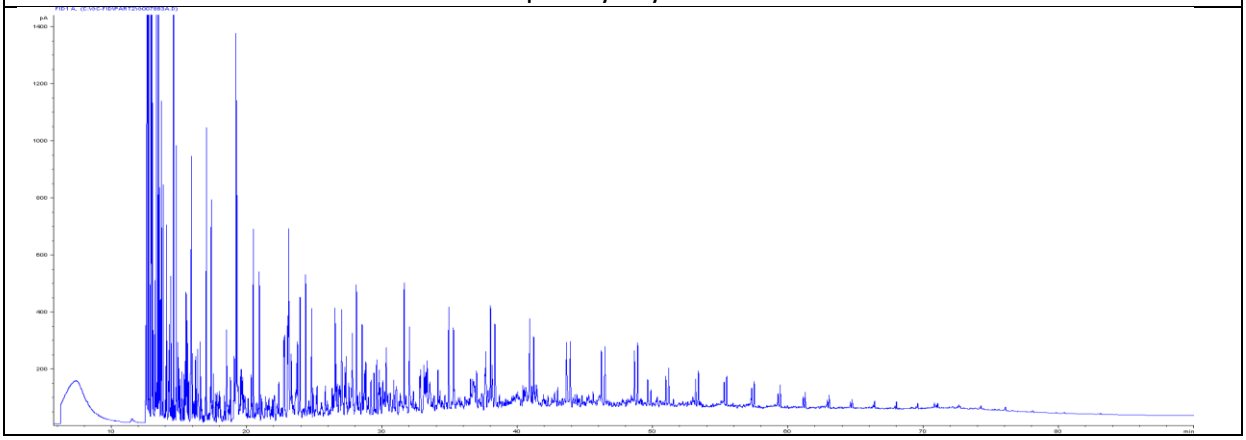

Bulk kinetics

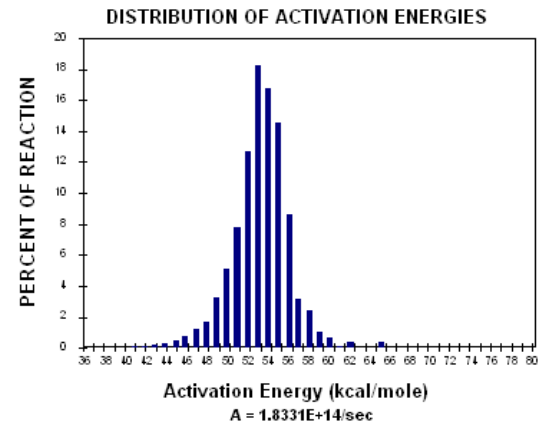

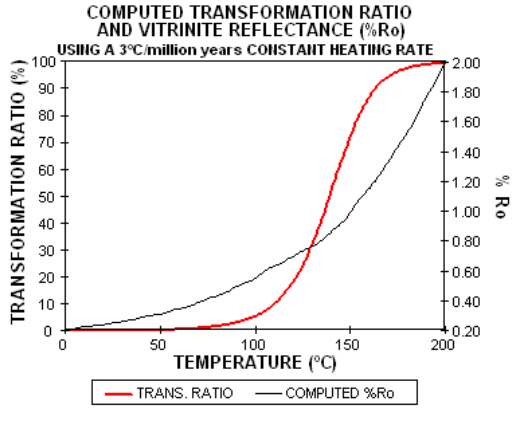

GC at 10% transformation ratio

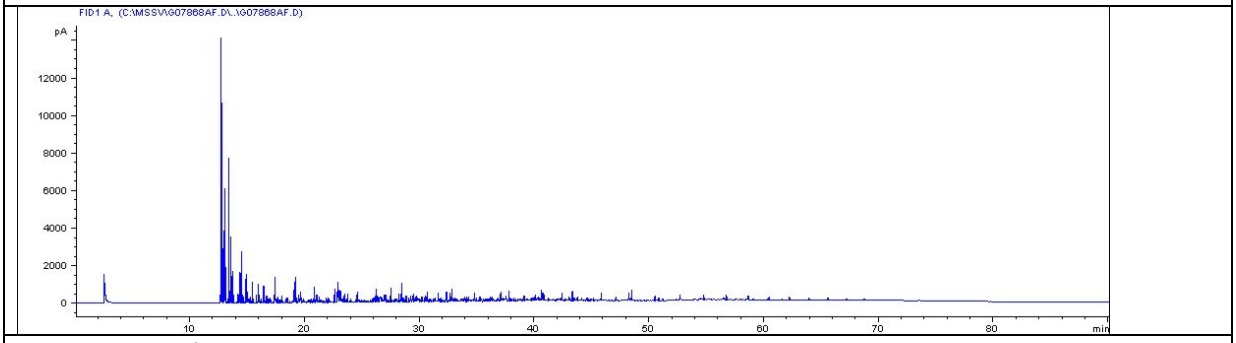

GC at 30% transformation ratio

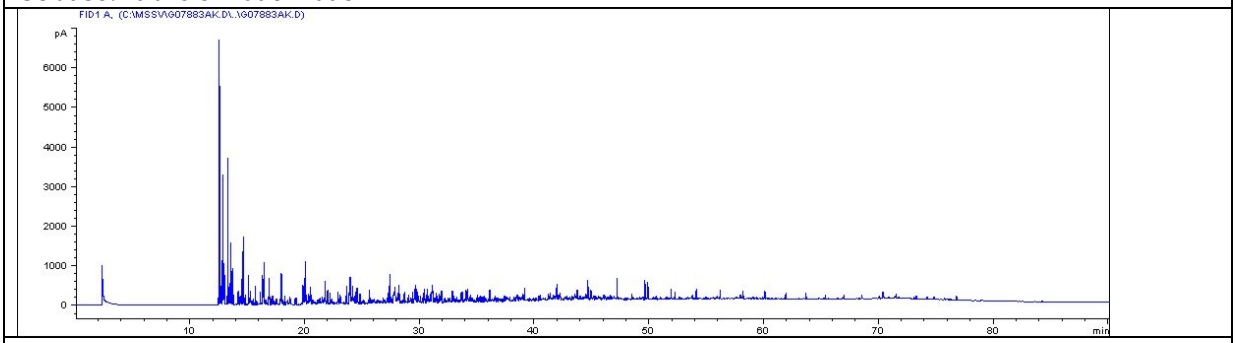

GC at 50% transformation ratio

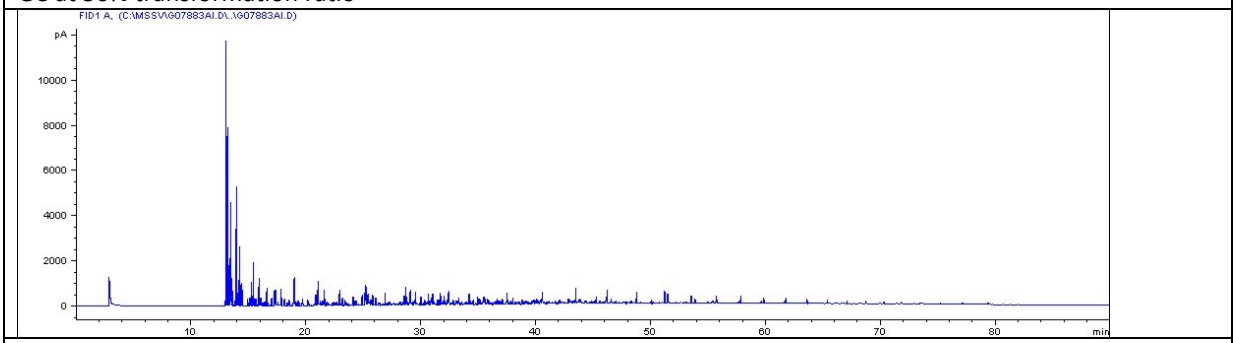

GC at 70% transformation ratio

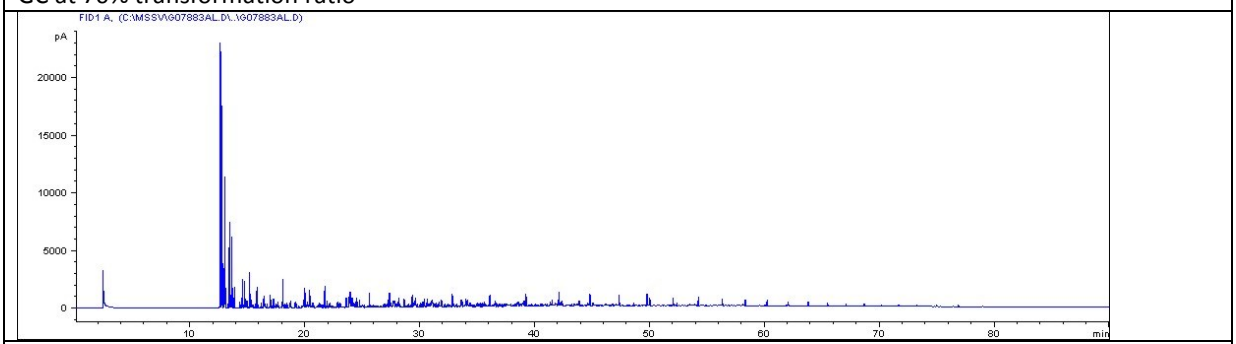

GC at 90% transformation ratio

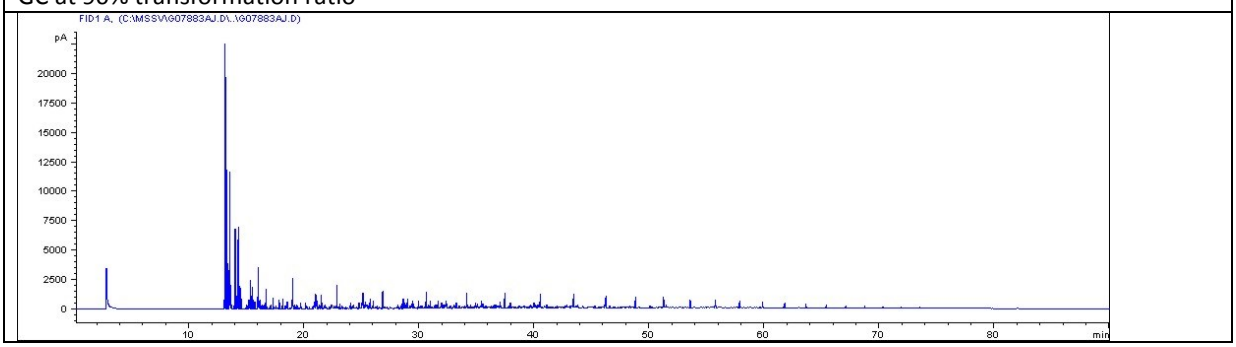

G007884	DSDP sample info and GFZ Rock-Eval data	
	Sample info	G007884
	Location	Orange Basin
	Leg	40
	Site	361
	Hole	--
	Core	36
	Section	2
	Top [cm]	67.0
	Bot [cm]	68.0
	Depth [mbsf]	1097.67
	S1 (mg/g)	0.19
	S2 (mg/g)	1.76
	S3 (mg/g)	1.59
	Tmax (°C)	414
	PP (mg/g)	1.95
	PI (wt ratio)	0.1
	HI (mg HC/g TOC)	37
	OI (mg CO2/g TOC)	33
	TOC (%)*	4.8
	Chrono-stratigraphic Age	Aptian
	Lithology (from DSDP reports)	shale, carbonaceous

Open Pyrolysis GC

Open pyrolysis GC not available.

No measurements for bulk kinetics and compositional kinetics were conducted on this sample.

G007885	DSDP sample info and GFZ Rock-Eval data	
	Sample info	G007885
	Location	Orange Basin
	Leg	40
	Site	361
	Hole	--
	Core	37
	Section	1
	Top [cm]	75.0
	Bot [cm]	76.0
	Depth [mbsf]	1105.75
	S1 (mg/g)	1.11
	S2 (mg/g)	21.83
	S3 (mg/g)	4.68
	Tmax (°C)	412
	PP (mg/g)	22.94
	PI (wt ratio)	0.05
	HI (mg HC/g TOC)	315
	OI (mg CO2/g TOC)	68
	TOC (%)*	6.92
	Chrono-stratigraphic Age	Aptian
	Lithology (from DSDP reports)	shale

Open Pyrolysis GC

Open pyrolysis GC not available.

No measurements for compositional kinetics were conducted on this sample.

Bulk kinetics

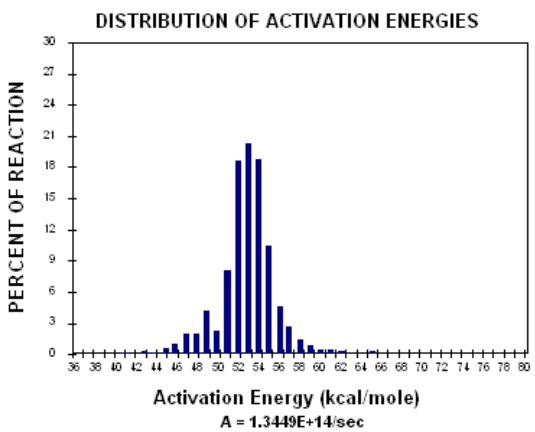

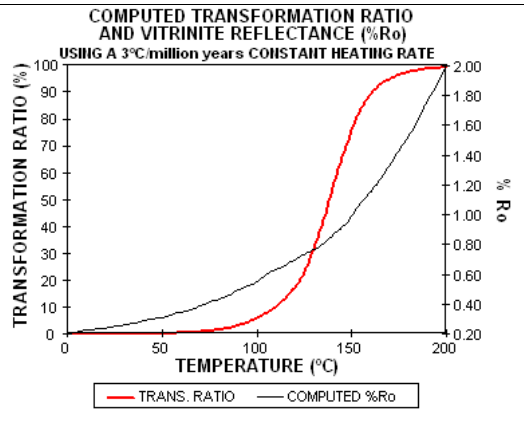

G007886	DSDP sample info and GFZ Rock-Eval data	
	Sample info	G007886
	Location	Orange Basin
	Leg	40
	Site	361
	Hole	--
	Core	37
	Section	1
	Top [cm]	140.0
	Bot [cm]	141.0
	Depth [mbsf]	1106.4
	S1 (mg/g)	0.29
	S2 (mg/g)	2.33
	S3 (mg/g)	2.31
	Tmax (°C)	409
	PP (mg/g)	2.62
	PI (wt ratio)	0.11
	HI (mg HC/g TOC)	37
	OI (mg CO2/g TOC)	36
	TOC (%)*	6.35
	Chrono-stratigraphic Age	Aptian
	Lithology (from DSDP reports)	shale

Open Pyrolysis GC

Open pyrolysis GC not available.

No measurements for bulk kinetics and compositional kinetics were conducted on this sample.

G007887	DSDP sample info and GFZ Rock-Eval data	
	Sample info	G007887
	Location	Orange Basin
	Leg	40
	Site	361
	Hole	--
	Core	40
	Section	4
	Top [cm]	126.0
	Bot [cm]	127.0
	Depth [mbsf]	1148.76
	S1 (mg/g)	0.83
	S2 (mg/g)	5.06
	S3 (mg/g)	2.24
	Tmax (°C)	401
	PP (mg/g)	5.89
	PI (wt ratio)	0.14
	HI (mg HC/g TOC)	97
	OI (mg CO2/g TOC)	43
	TOC (%)*	5.22
	Chrono-stratigraphic Age	Aptian
	Lithology (from DSDP reports)	shale

Open Pyrolysis GC

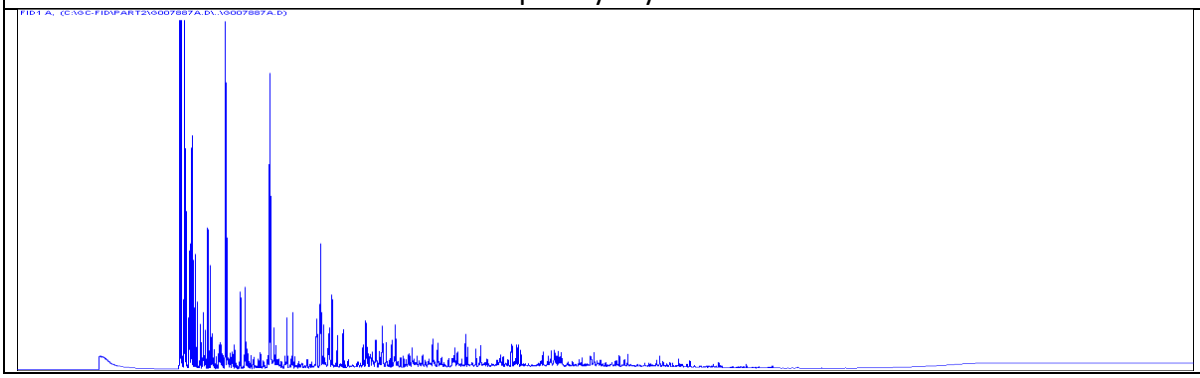

Bulk kinetics

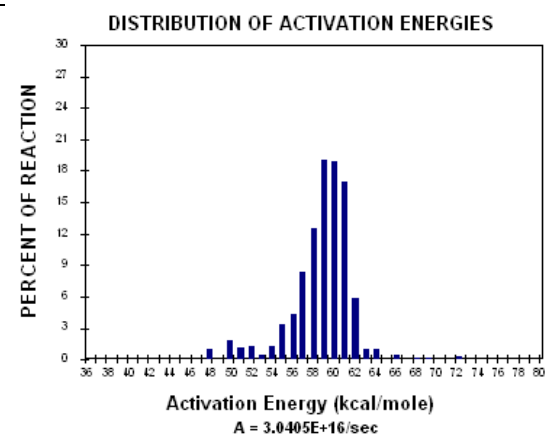

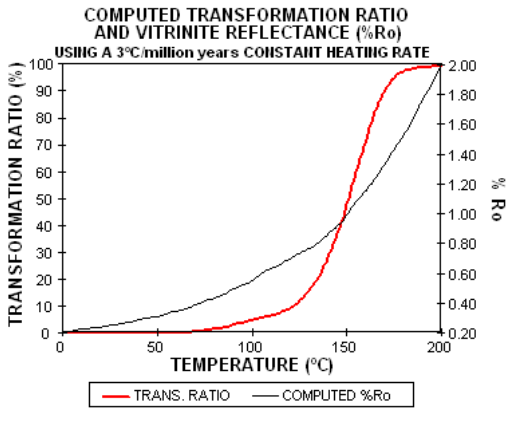

G007888	DSDP sample info and GFZ Rock-Eval data		
	Sample info	G007888	
	Location	Orange Basin	
	Leg	40	
	Site	361	
	Hole	--	
	Core	47	
	Section	1	
	Top [cm]	136.0	
	Bot [cm]	137.0	
	Depth [mbsf]	1267.86	
	S1 (mg/g)	0.19	0.19
	S2 (mg/g)	1.09	1.21
	S3 (mg/g)	1.19	1.43
	Tmax (°C)	411	414
	PP (mg/g)	1.28	1.4
	PI (wt ratio)	0.15	0.14
	HI (mg HC/g TOC)	28	31
	OI (mg CO2/g TOC)	30	36
	TOC (%)*	3.93	3.93
	Chrono-stratigraphic Age	Aptian	
	Lithology (from DSDP reports)	shale, carbonaceous, sandy	

Open Pyrolysis GC

Open pyrolysis GC not available.

No measurements for bulk kinetics and compositional kinetics were conducted on this sample.

G007889	DSDP sample info and GFZ Rock-Eval data		
	Sample info	G007889	
	Location	Angola Basin	
	Leg	40	
	Site	364	
	Hole	*	
	Core	21	
	Section	4	
	Top [cm]	133.0	
	Bot [cm]	134.0	
	Depth [mbsf]	602.48	
	S1 (mg/g)	0.89	0.89
	S2 (mg/g)	46.32	48.95
	S3 (mg/g)	6.9	6.99
	Tmax (°C)	409	409
	PP (mg/g)	47.21	49.84
	PI (wt ratio)	0.02	0.02
	HI (mg HC/g TOC)	459	485
	OI (mg CO2/g TOC)	68	69
	TOC (%)*	10.1	10.1
	Chrono-stratigraphic Age	upper Coniacian	
	Lithology (from DSDP reports)	marly chalk and mudstone	

Open Pyrolysis GC

Open pyrolysis GC not available.

No measurements for bulk kinetics and compositional kinetics were conducted on this sample.

G007890	DSDP sample info and GFZ Rock-Eval data	
	Sample info	Angola Basin
	Location	40
	Leg	364
	Site	*
	Hole	23
	Core	1
	Section	137.0
	Top [cm]	138.0
	Bot [cm]	645.37
	Depth [mbsf]	3.45
	S1 (mg/g)	112.38
	S2 (mg/g)	8.98
	S3 (mg/g)	407
	Tmax (°C)	115.83
	PP (mg/g)	0.03
	PI (wt ratio)	764
	HI (mg HC/g TOC)	61
	OI (mg CO2/g TOC)	14.7
	TOC (%)*	low. Con. - up. Turon.
	Chrono-stratigraphic Age	marly chalk
	Lithology (from DSDP reports)	Angola Basin

Open Pyrolysis GC

Open pyrolysis GC not available.

No measurements for bulk kinetics and compositional kinetics were conducted on this sample.

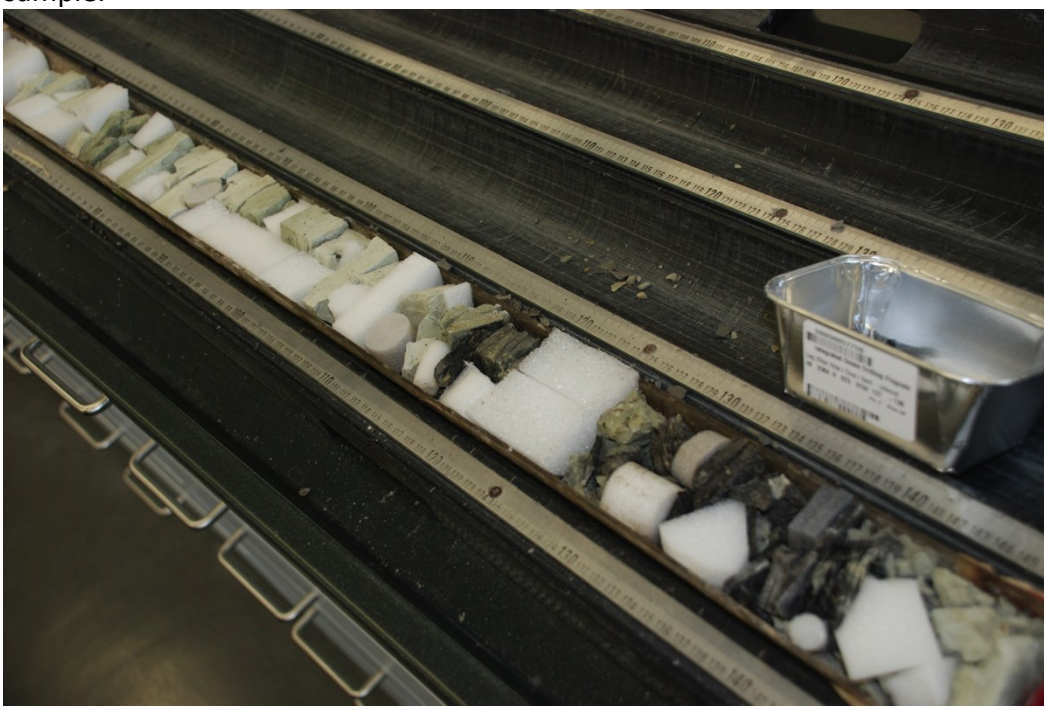

Core image showing organic-rich marly chalk interbedded between white marls.

G007891	DSDP sample info and GFZ Rock-Eval data	
	Sample info	G007891
	Location	Angola Basin
	Leg	40
	Site	364
	Hole	*
	Core	23
	Section	3
	Top [cm]	128
	Bot [cm]	129
	Depth [mbsf]	648.28
	S1 (mg/g)	1.32
	S2 (mg/g)	92.24
	S3 (mg/g)	7.62
	Tmax (°C)	413
	PP (mg/g)	93.56
	PI (wt ratio)	0.01
	HI (mg HC/g TOC)	769
	OI (mg CO2/g TOC)	64
	TOC (%)*	12
	Chrono-stratigraphic Age	low. Con. - up. Turon.
	Lithology (from DSDP reports)	marly chalk

Open Pyrolysis GC

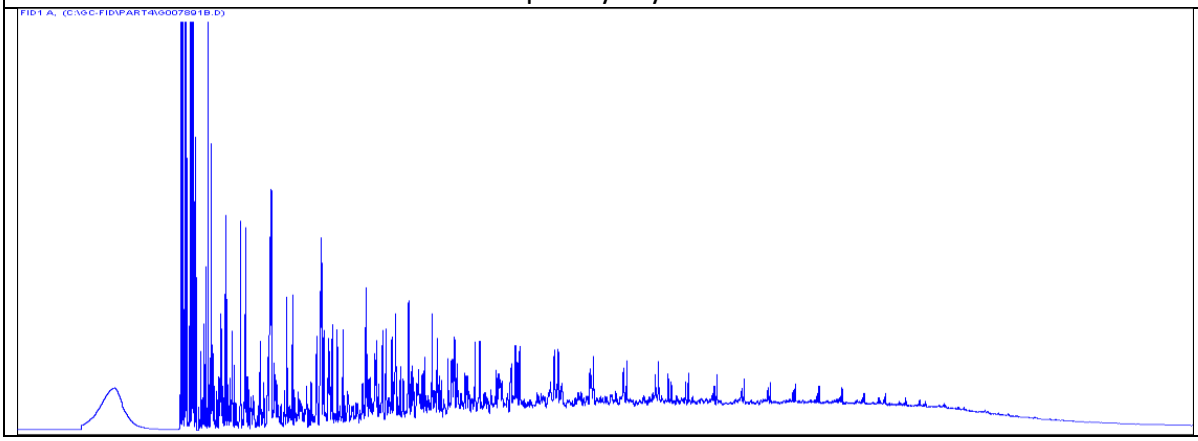

Bulk kinetics

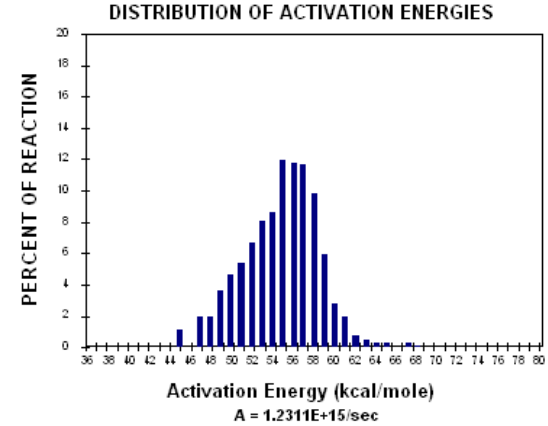

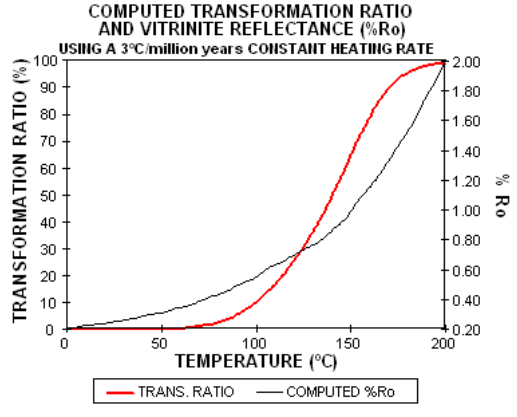

GC at 10% transformation ratio

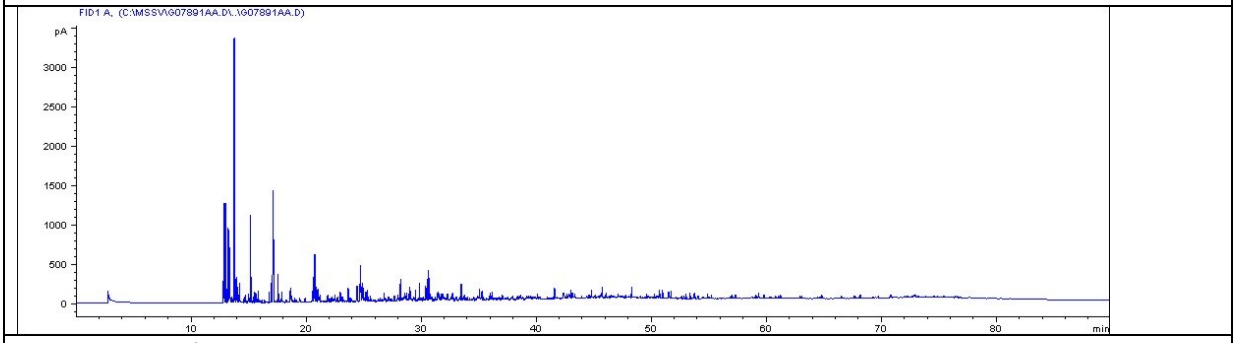

GC at 30% transformation ratio

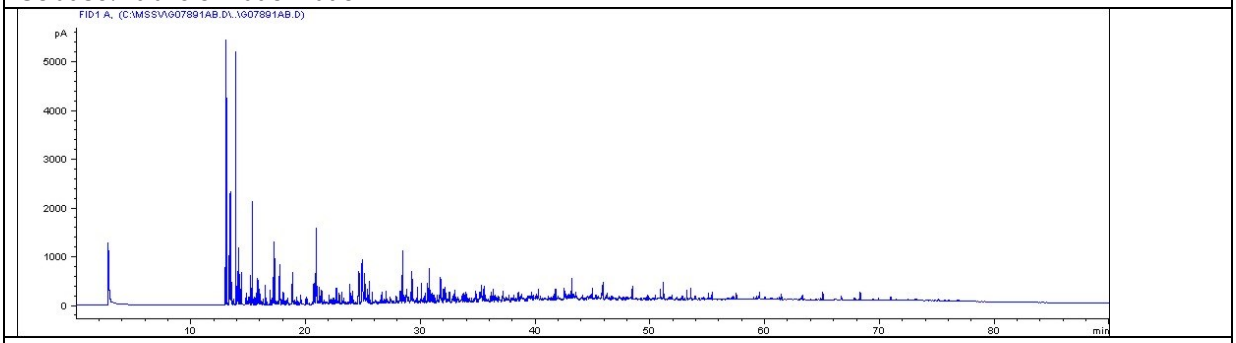

GC at 50% transformation ratio

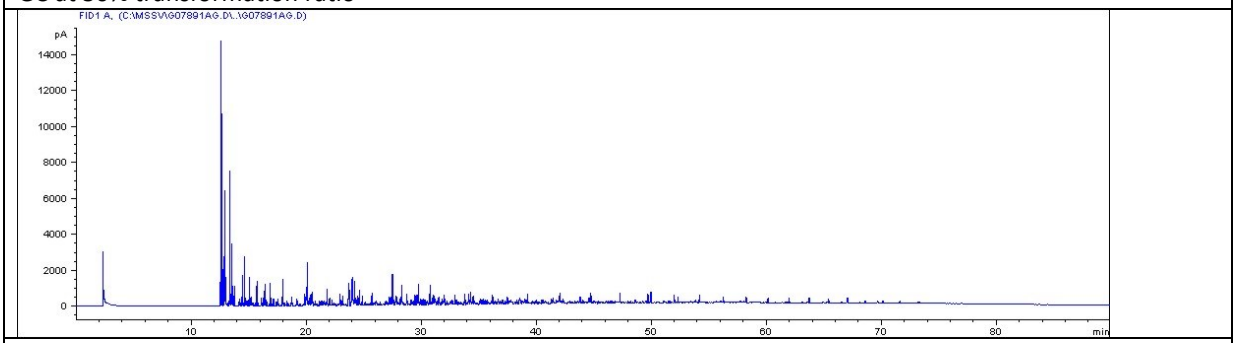

GC at 70% transformation ratio

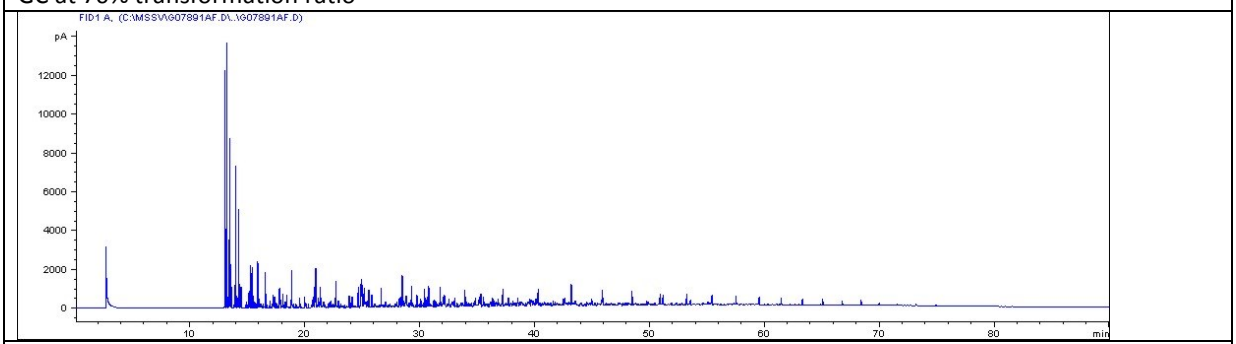

GC at 90% transformation ratio

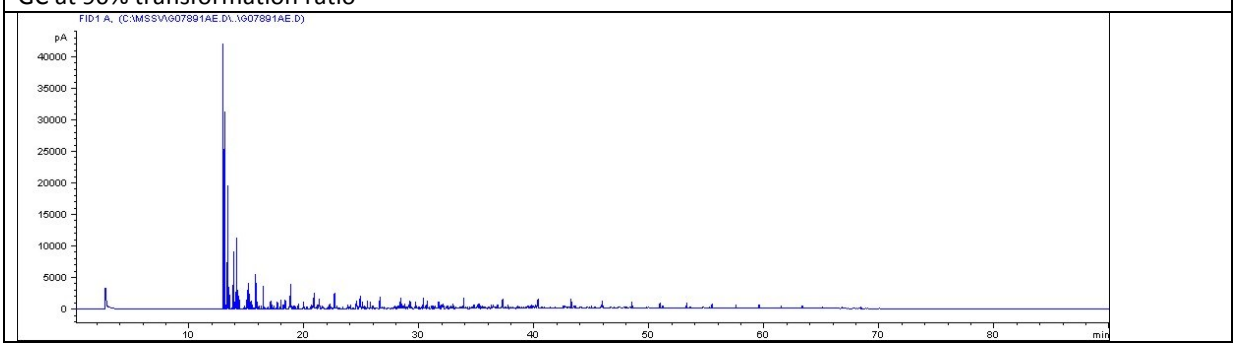

G007892	DSDP sample info and GFZ Rock-Eval data	
	Sample info	G007892
	Location	Angola Basin
	Leg	40
	Site	364
	Hole	*
	Core	24
	Section	1
	Top [cm]	52
	Bot [cm]	53
	Depth [mbsf]	673.02
	S1 (mg/g)	1.75
	S2 (mg/g)	58.36
	S3 (mg/g)	6.61
	Tmax (°C)	401
	PP (mg/g)	60.11
	PI (wt ratio)	0.03
	HI (mg HC/g TOC)	526
	OI (mg CO2/g TOC)	60
	TOC (%)*	11.1
	Chrono-stratigraphic Age	upper Albian
	Lithology (from DSDP reports)	calcareous mudstone and black sapropelic shale

Open Pyrolysis GC

Open pyrolysis GC not available.

No measurements for bulk kinetics and compositional kinetics were conducted on this sample.

*: TOC from Leco

G007893	DSDP sample info and GFZ Rock-Eval data	
	Sample info	G007893
	Location	Angola Basin
	Leg	40
	Site	364
	Hole	*
	Core	39
	Section	2
	Top [cm]	97
	Bot [cm]	98
	Depth [mbsf]	969.47
	S1 (mg/g)	0.81
	S2 (mg/g)	37.67
	S3 (mg/g)	2.93
	Tmax (°C)	407
	PP (mg/g)	38.48
	PI (wt ratio)	0.02
	HI (mg HC/g TOC)	442
	OI (mg CO2/g TOC)	34
	TOC (%)*	8.52
	Chrono-stratigraphic Age	middle Albian
	Lithology (from DSDP reports)	marly limestone and black shale, minor sapropelic

Open Pyrolysis GC

Open pyrolysis GC not available.

No measurements for compositional kinetics were conducted on this sample.

Bulk kinetics

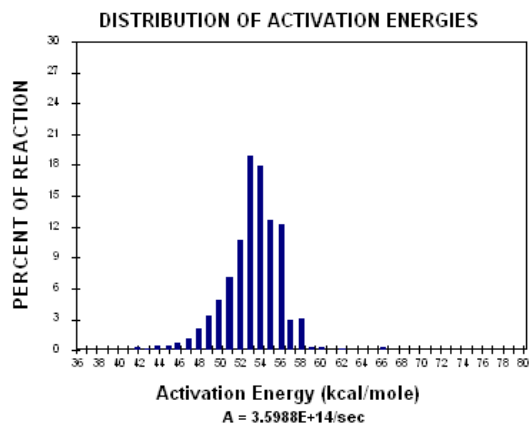

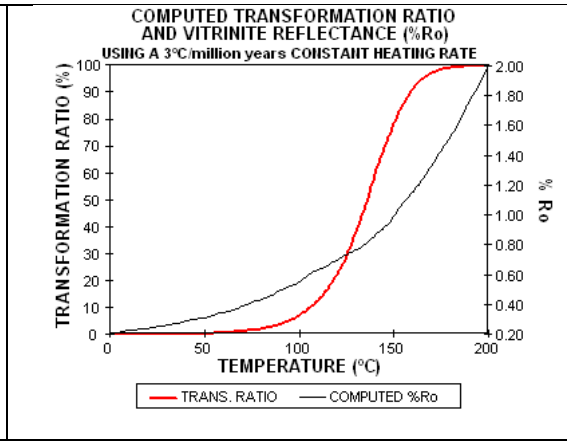

G007894	DSDP sample info and GFZ Rock-Eval data	
	Sample info	G007894
	Location	Angola Basin
	Leg	40
	Site	364
	Hole	*
	Core	42
	Section	2
	Top [cm]	11
	Bot [cm]	12
	Depth [mbsf]	1025.61
	S1 (mg/g)	3.6
	S2 (mg/g)	147.24
	S3 (mg/g)	6.88
	Tmax (°C)	415
	PP (mg/g)	150.84
	PI (wt ratio)	0.02
	HI (mg HC/g TOC)	398
	OI (mg CO2/g TOC)	19
	TOC (%)*	37
	Chrono-stratigraphic Age	lower Albian
	Lithology (from DSDP reports)	marly dolomitic limestone, alternating black shale

Open Pyrolysis GC

Open pyrolysis GC not available.

No measurements for bulk kinetics and compositional kinetics were conducted on this sample.

G007895	DSDP sample info and GFZ Rock-Eval data	
	Sample info	G007895
	Location	Angola Basin
	Leg	40
	Site	364
	Hole	*
	Core	44
	Section	2
	Top [cm]	113
	Bot [cm]	114
	Depth [mbsf]	1045.63
	S1 (mg/g)	2.13
	S2 (mg/g)	117.13
	S3 (mg/g)	3.74
	Tmax (°C)	409
	PP (mg/g)	119.26
	PI (wt ratio)	0.02
	HI (mg HC/g TOC)	377
	OI (mg CO2/g TOC)	12
	TOC (%)*	31.1
	Chrono-stratigraphic Age	Albian / Aptian
	Lithology (from DSDP reports)	dolomitic limestone, alternating black shale

Open Pyrolysis GC

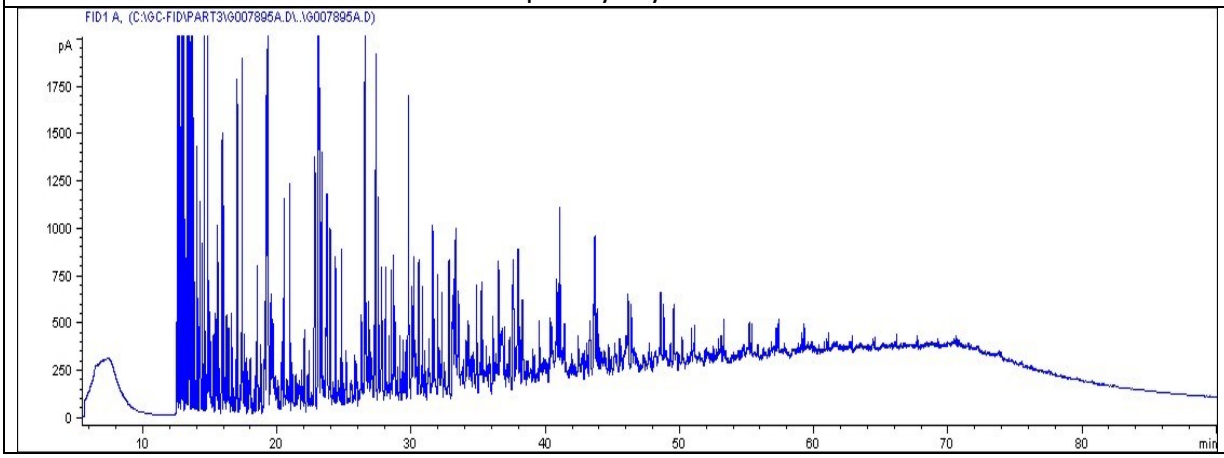

Bulk kinetics

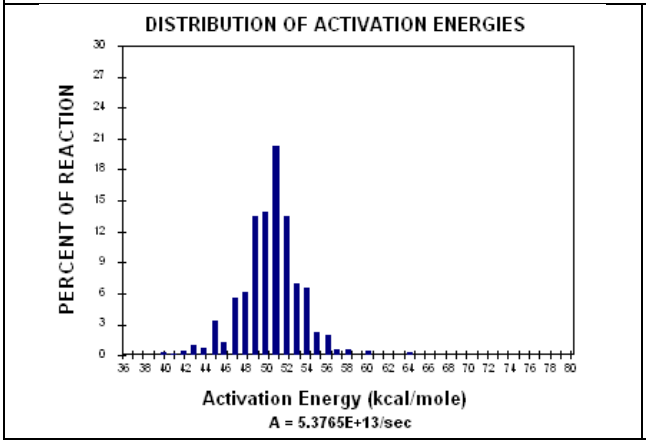

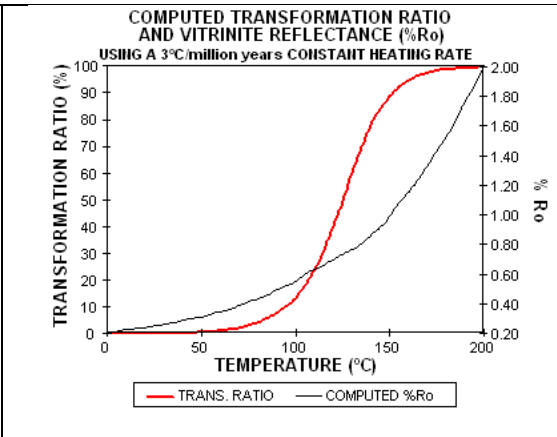

GC at 10% transformation ratio

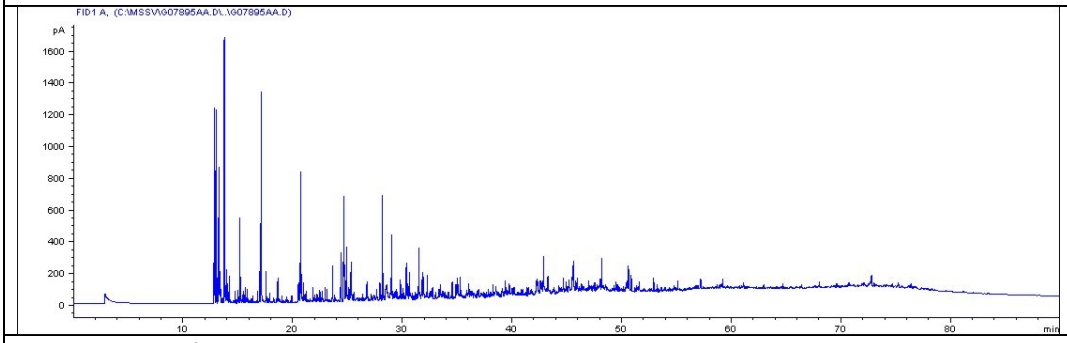

GC at 30% transformation ratio

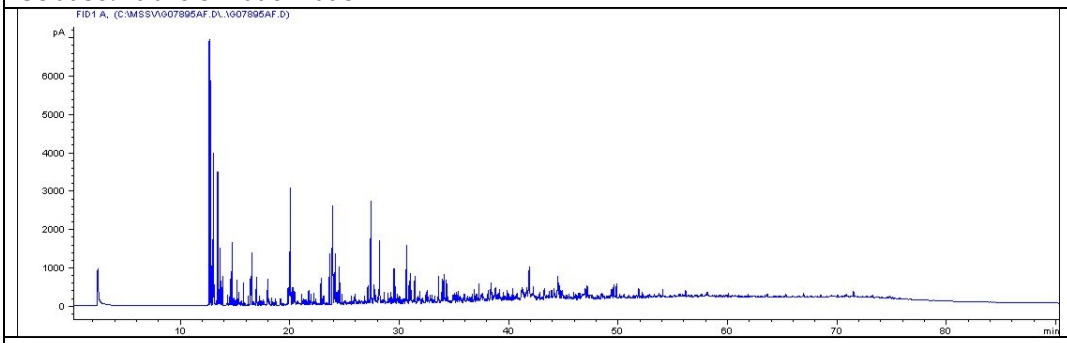

GC at 50% transformation ratio

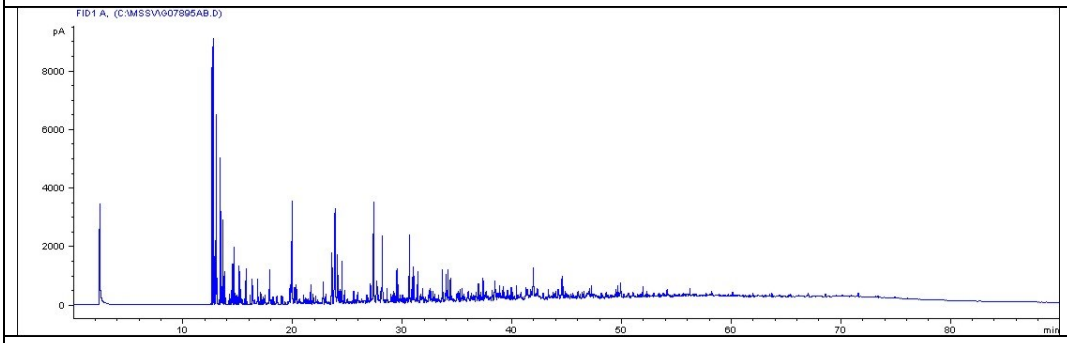

GC at 70% transformation ratio

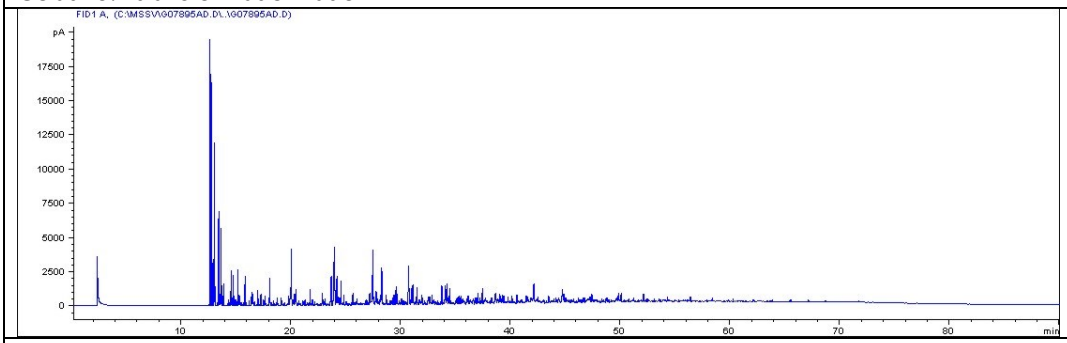

GC at 90% transformation ratio

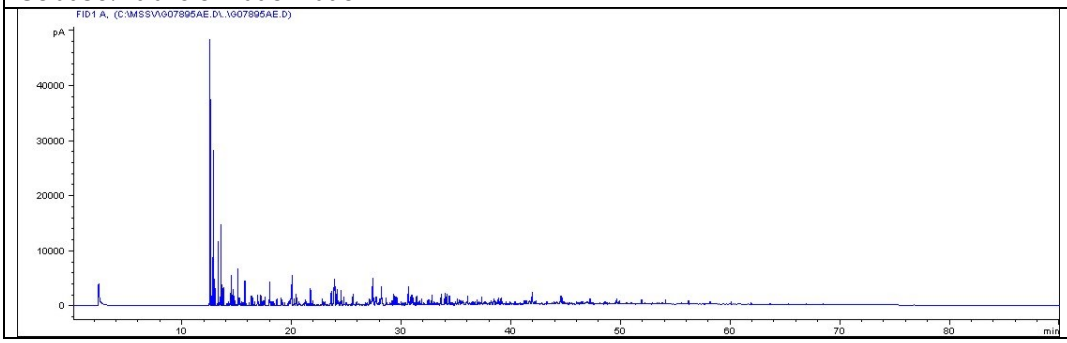

G007896	DSDP sample info and GFZ Rock-Eval data	
	Sample info	G007896
	Location	Angola Basin
	Leg	40
	Site	364
	Hole	*
	Core	44
	Section	2
	Top [cm]	142
	Bot [cm]	143
	Depth [mbsf]	1045.92
	S1 (mg/g)	1
	S2 (mg/g)	45.97
	S3 (mg/g)	2.72
	Tmax (°C)	401
	PP (mg/g)	46.97
	PI (wt ratio)	0.02
	HI (mg HC/g TOC)	476
	OI (mg CO2/g TOC)	28
	TOC (%)*	9.66
	Chrono-stratigraphic Age	Albian / Aptian
	Lithology (from DSDP reports)	dolomitic limestone, alternating black shale

Open Pyrolysis GC

Open pyrolysis GC not available.

No measurements for bulk kinetics and compositional kinetics were conducted on this sample.

G007897	DSDP sample info and GFZ Rock-Eval data	
	Sample info	G007897
	Location	Angola Basin
	Leg	40
	Site	364
	Hole	*
	Core	45
	Section	1
	Top [cm]	87
	Bot [cm]	88
	Depth [mbsf]	1062.87
	S1 (mg/g)	1.57
	S2 (mg/g)	66.99
	S3 (mg/g)	2.36
	Tmax (°C)	408
	PP (mg/g)	68.56
	PI (wt ratio)	0.02
	HI (mg HC/g TOC)	663
	OI (mg CO2/g TOC)	23
	TOC (%)*	10.1
	Chrono-stratigraphic Age	Albian / Aptian
	Lithology (from DSDP reports)	dolomitic limestone, alternating black shale

Open Pyrolysis GC

Open pyrolysis GC not available.

No measurements for bulk kinetics and compositional kinetics were conducted on this sample.

Available well data for seismic interpretation and basin model calibration

Orange Basin wells					Calibration data					Additional data
Well name	X [m] WGS84, UTM 32S	Y [m] WGS84, UTM 32S	KB [m]	TD [m]	Vitrinite refl.	Bottom hole temp.	Surface heatflow (Gouturbe et al., 2008)	Check shots for seismic depth conversion	Well tops for seismic interp.	d13C isotope & biomarker analysis
A-AA1	656252	6618059	21.50	3325.00				X	X	
A-AA2	662914	6618643	23.00	3179.40				X	X	
A-A1	682923	6544478	29.90	3805.00	X	X		X	X	
A-C1	677623	6401625	25.90	4139.00	X	X		X	X	
A-C2	671570	6421267	25.90	3613.00	X	X	X	X	X	
A-C3	668375	6397670	25.90	4150.00	X	X	X	X	X	
A-D1	678771	6641672	26.00	3722.84	X	X	X	X	X	
A-E1	624828	6692843	25.00	4475.00				X	X	
A-F1	616498	6766520	25.00	4396.00	X		X	X	X	X
A-G1	632267	6578828	25.15	4106.12	X	X		X	X	
A-H1	581132	6628753	26.00	3884.72	X		X	X	X	
A-I1	631290	6534527	25.00	4250.00	X	X	X	X	X	
A-J1	707706	6612453	25.00	3700.00	X			X	X	
A-K1	652651	6584947	25.15	3684.73	X	X		X	X	X
A-K2	654059	6583320	25.00	3780.00	X				X	
A-L1	666842	6535656	25.00	3271.00	X	X		X	X	
A-N1	667675	6377845	25.00	3750.00		X		X	X	
A-O1	613503	6797116	25.00	4605.00	X			X	X	
A-U1	642764	6497643	25.00	3427.00	X	X		X	X	
A-V1	651150	6588266	23.00	3721.31					X	
A-W1	645792	6594308	25.00	3699.00					X	
A-X1	660490	6626084	21.50	3278.00		X		X	X	X
A-X2	656270	6626423	21.50	2455.00		X			X	
A-Y1	657881	6586196	25.00	3412.00					X	X
Ba-A1	746879	6471324	25.90	1698.00		X			X	
Ba-A2	754024	6466544	29.50	2494.00		X			X	
K-A1	597161	6591237	26.00	4821.31				X	X	
K-A2	596415	6588297	25.15	5830.10			X	X	X	
K-A3	601708	6591778	26.00	4677.00			X	X	X	
K-B1	542788	6602330	26.00	4075.03	X	X		X	X	X
K-D1	626596	6488537	26.00	4699.00	X	X	X	X	X	
K-E1	541514	6611042	26.00	4132.03	X		X	X	X	X
K-F1	596082	6539477	22.00	3800.00	X	X		X	X	
K-H1	588028	6565654	25.00	4268.00	X	X		X	X	
O-A1	669942	6329326	25.90	1931.00					X	
P-A1	709286	6380912	25.00	3272.00	X	X		X	X	
P-F1	725203	6374078	26.00	1492.00	X	X	X	X	X	

Bulk kinetic parameters

Sample no.	G007868	G007869	G07871	G007873	G007878	G007879	G007883	G007885	G007887	G007891	G007893	G007895
A [1/S]	1.27 E + 14	3.26E + 14	8.46E + 13	5.38E + 13	7.41E + 13	8.08E + 13	1.83E + 14	1.34E + 14	3.04E + 16	1.23E + 15	3.60E + 14	5.38E + 13
Ea [kcal/mol]												
40	0.0		0.2	0.2	0.3	0.2						0.3
41	0.2		0.1	0.1	0.3	0.4	0.1	0.2				0.2
42	0.2	0.2	0.3	0.3	0.6	0.6	0.2	0.1			0.3	0.4
43	0.4	0.1	0.4	0.4	0.8	0.9	0.2	0.3			0.1	1.0
44	0.6	0.3	0.7	0.5	1.0	0.8	0.3	0.2			0.5	0.8
45	0.9	0.4	0.5	0.9	1.3	1.2	0.5	0.6		1.1	0.4	3.3
46	1.5	0.5	0.6	1.2	1.9	1.9	0.8	1.0		0.0	0.8	1.2
47	2.3	1.0	1.2	1.7	3.6	2.9	1.2	1.9	0.8	2.0	1.2	5.6
48	3.5	1.0	2.1	2.8	5.3	4.9	1.7	2.0	0.1	2.0	2.1	6.1
49	4.4	2.7	4.2	2.9	8.9	7.3	3.3	4.3	1.5	3.6	3.3	13.5
50	7.7	3.0	8.8	3.1	12.1	13.2	5.1	2.3	1.2	4.7	4.9	13.9
51	12.5	6.2	18.3	13.6	21.6	19.9	7.7	8.1	1.5	5.4	7.1	20.3
52	23.9	8.9	21.6	14.7	15.4	17.0	12.7	18.6	0.4	6.7	10.7	13.5
53	16.2	18.5	21.8	31.9	15.8	17.0	18.2	20.2	1.0	8.1	18.9	7.0
54	9.4	18.5	11.7	6.3	8.2	7.3	16.8	18.8	2.7	8.6	17.9	6.6
55	9.1	15.8	4.4	17.4	1.4	2.6	14.6	10.4	4.2	11.9	12.6	2.2
56	2.7	11.4	2.1	1.3	1.2	1.1	8.7	4.7	7.1	11.8	12.2	2.0
57	2.1	5.6	0.1	0.0	0.0	0.0	3.2	2.6	11.9	11.6	3.0	0.6
58	0.7	2.0	0.6	0.2	0.1	0.2	2.4	1.5	17.6	9.8	3.1	0.6
59	0.7	2.5	0.0	0.3	0.1	0.0	1.1	0.9	20.0	5.9	0.3	0.0
60	0.1	0.0	0.2	0.0	0.1	0.2	0.7	0.5	18.0	2.8	0.3	0.4
61	0.5	0.6	0.1	0.0	0.0	0.0	0.1	0.4	8.7	2.0	0.0	0.0
62	0.0	0.0	0.0	0.0	0.0	0.0	0.4	0.4	0.9	0.7	0.2	0.0
63	0.0	0.3	0.0	0.2	0.0	0.0	0.0	0.0	1.4	0.5	0.0	0.0
64	0.4	0.0	0.2		0.3	0.4	0.0	0.0	0.0	0.3	0.0	0.4
65		0.0					0.4	0.4	0.5	0.3	0.0	
66		0.3							0.0	0.0	0.2	
67									0.2	0.3		
68									0.1	0.1		
69									0.0			
70									0.0			
71									0.3			

2- and 4-Component compositional kinetic models

Sample G007868								
2-Component				4-Component				
	Gas	Oil			C1	C2-5	C6-14	C15+
40 kcal/mol	0.001	0.010		40 kcal/mol	0.000	0.001	0.003	0.006
41 kcal/mol	0.014	0.193		41 kcal/mol	0.006	0.012	0.068	0.114
42 kcal/mol	0.015	0.212		42 kcal/mol	0.006	0.013	0.075	0.125
43 kcal/mol	0.029	0.404		43 kcal/mol	0.012	0.026	0.143	0.239
44 kcal/mol	0.039	0.539		44 kcal/mol	0.016	0.034	0.191	0.319
45 kcal/mol	0.063	0.876		45 kcal/mol	0.026	0.056	0.310	0.518
46 kcal/mol	0.102	1.415		46 kcal/mol	0.043	0.090	0.501	0.837
47 kcal/mol	0.160	2.215		47 kcal/mol	0.067	0.140	0.783	1.310
48 kcal/mol	0.244	3.370		48 kcal/mol	0.102	0.214	1.192	1.993
49 kcal/mol	0.309	4.265		49 kcal/mol	0.129	0.271	1.508	2.523
50 kcal/mol	0.623	7.316		50 kcal/mol	0.288	0.569	2.550	4.313
51 kcal/mol	1.009	11.837		51 kcal/mol	0.467	0.921	4.125	6.977
52 kcal/mol	2.302	22.152		52 kcal/mol	0.963	1.818	7.866	13.263
53 kcal/mol	3.193	12.764		53 kcal/mol	0.713	1.338	4.991	9.148
54 kcal/mol	2.821	6.078		54 kcal/mol	1.419	1.316	2.774	3.881
55 kcal/mol	2.731	5.883		55 kcal/mol	1.374	1.274	2.685	3.757
56 kcal/mol	0.820	1.767		56 kcal/mol	0.413	0.383	0.806	1.128
57 kcal/mol	0.640	1.379		57 kcal/mol	0.322	0.299	0.629	0.880
58 kcal/mol	0.195	0.421		58 kcal/mol	0.098	0.091	0.192	0.269
59 kcal/mol	0.201	0.434		59 kcal/mol	0.101	0.094	0.198	0.277
60 kcal/mol	0.039	0.084		60 kcal/mol	0.020	0.018	0.038	0.054
61 kcal/mol	0.135	0.291		61 kcal/mol	0.068	0.063	0.133	0.186
62 kcal/mol	0.000	0.000		62 kcal/mol	0.000	0.000	0.000	0.000
63 kcal/mol	0.000	0.000		63 kcal/mol	0.000	0.000	0.000	0.000
64 kcal/mol	0.129	0.278		64 kcal/mol	0.065	0.060	0.127	0.178

Sample G007878								
2-Component				4-Component				
	Gas	Oil			C1	C2-5	C6-14	C15+
40 kcal/mol	0.024	0.276		40 kcal/mol	0.007	0.017	0.111	0.164
41 kcal/mol	0.026	0.294		41 kcal/mol	0.007	0.019	0.119	0.175
42 kcal/mol	0.050	0.570		42 kcal/mol	0.014	0.036	0.230	0.340
43 kcal/mol	0.062	0.708		43 kcal/mol	0.017	0.045	0.286	0.422
44 kcal/mol	0.078	0.892		44 kcal/mol	0.022	0.056	0.360	0.532
45 kcal/mol	0.104	1.186		45 kcal/mol	0.029	0.075	0.479	0.707
46 kcal/mol	0.150	1.720		46 kcal/mol	0.042	0.108	0.695	1.025
47 kcal/mol	0.290	3.320		47 kcal/mol	0.081	0.209	1.342	1.978
48 kcal/mol	0.423	4.837		48 kcal/mol	0.119	0.304	1.955	2.883
49 kcal/mol	0.739	8.151		49 kcal/mol	0.228	0.511	2.991	5.160
50 kcal/mol	1.007	11.103		50 kcal/mol	0.311	0.696	4.074	7.029
51 kcal/mol	1.872	19.758		51 kcal/mol	0.564	1.308	6.664	13.093
52 kcal/mol	1.601	13.759		52 kcal/mol	0.506	1.095	5.613	8.146
53 kcal/mol	2.628	13.132		53 kcal/mol	0.891	1.738	7.112	6.020
54 kcal/mol	1.364	6.816		54 kcal/mol	0.462	0.902	3.691	3.125
55 kcal/mol	0.230	1.150		55 kcal/mol	0.078	0.152	0.623	0.527
56 kcal/mol	0.192	0.958		56 kcal/mol	0.065	0.127	0.519	0.439
57 kcal/mol	0.000	0.000		57 kcal/mol	0.000	0.000	0.000	0.000
58 kcal/mol	0.010	0.050		58 kcal/mol	0.003	0.007	0.027	0.023
59 kcal/mol	0.022	0.108		59 kcal/mol	0.007	0.014	0.059	0.050
60 kcal/mol	0.013	0.067		60 kcal/mol	0.005	0.009	0.036	0.031
61 kcal/mol	0.000	0.000		61 kcal/mol	0.000	0.000	0.000	0.000
62 kcal/mol	0.000	0.000		62 kcal/mol	0.000	0.000	0.000	0.000
63 kcal/mol	0.000	0.000		63 kcal/mol	0.000	0.000	0.000	0.000
64 kcal/mol	0.043	0.217		64 kcal/mol	0.015	0.029	0.117	0.099

Sample G007883								
2-Component				4-Component				
	Gas	Oil			C1	C2-5	C6-14	C15+
41 kcal/mol	0.010	0.090		41 kcal/mol	0.003	0.007	0.032	0.058
42 kcal/mol	0.015	0.135		42 kcal/mol	0.005	0.010	0.048	0.088
43 kcal/mol	0.020	0.180		43 kcal/mol	0.006	0.013	0.064	0.117
44 kcal/mol	0.031	0.289		44 kcal/mol	0.010	0.021	0.102	0.187
45 kcal/mol	0.051	0.469		45 kcal/mol	0.016	0.035	0.166	0.304
46 kcal/mol	0.075	0.695		46 kcal/mol	0.024	0.051	0.245	0.450
47 kcal/mol	0.118	1.092		47 kcal/mol	0.038	0.080	0.385	0.707
48 kcal/mol	0.161	1.489		48 kcal/mol	0.051	0.110	0.526	0.963
49 kcal/mol	0.319	2.951		49 kcal/mol	0.102	0.217	1.042	1.909
50 kcal/mol	0.495	4.585		50 kcal/mol	0.158	0.338	1.618	2.966
51 kcal/mol	0.824	6.916		51 kcal/mol	0.270	0.554	2.397	4.519
52 kcal/mol	1.349	11.321		52 kcal/mol	0.443	0.907	3.923	7.397
53 kcal/mol	2.161	16.069		53 kcal/mol	0.727	1.435	5.671	10.398
54 kcal/mol	2.216	14.534		54 kcal/mol	0.769	1.447	5.137	9.396
55 kcal/mol	2.562	11.998		55 kcal/mol	0.938	1.624	5.176	6.822
56 kcal/mol	1.524	7.136		56 kcal/mol	0.558	0.966	3.079	4.058
57 kcal/mol	0.554	2.596		57 kcal/mol	0.203	0.351	1.120	1.476
58 kcal/mol	0.428	2.002		58 kcal/mol	0.157	0.271	0.864	1.139
59 kcal/mol	0.185	0.865		59 kcal/mol	0.068	0.117	0.373	0.492
60 kcal/mol	0.114	0.536		60 kcal/mol	0.042	0.072	0.231	0.305
61 kcal/mol	0.014	0.066		61 kcal/mol	0.005	0.009	0.028	0.037
62 kcal/mol	0.074	0.346		62 kcal/mol	0.027	0.047	0.149	0.197
63 kcal/mol	0.000	0.000		63 kcal/mol	0.000	0.000	0.000	0.000
64 kcal/mol	0.000	0.000		64 kcal/mol	0.000	0.000	0.000	0.000
65 kcal/mol	0.063	0.297		65 kcal/mol	0.023	0.040	0.128	0.169

Sample G007887								
2-Component				4-Component				
	Gas	Oil			C1	C2-5	C6-14	C15+
47 kcal/mol	0.091	0.749		47 kcal/mol	0.026	0.065	0.424	0.325
48 kcal/mol	0.012	0.098		48 kcal/mol	0.003	0.009	0.056	0.043
49 kcal/mol	0.163	1.337		49 kcal/mol	0.046	0.117	0.758	0.580
50 kcal/mol	0.127	1.043		50 kcal/mol	0.036	0.091	0.591	0.452
51 kcal/mol	0.159	1.311		51 kcal/mol	0.045	0.114	0.743	0.568
52 kcal/mol	0.046	0.374		52 kcal/mol	0.013	0.033	0.212	0.162
53 kcal/mol	0.113	0.927		53 kcal/mol	0.032	0.081	0.525	0.402
54 kcal/mol	0.296	2.434		54 kcal/mol	0.083	0.213	1.379	1.055
55 kcal/mol	0.456	3.754		55 kcal/mol	0.128	0.328	2.127	1.627
56 kcal/mol	0.765	6.295		56 kcal/mol	0.215	0.550	3.567	2.728
57 kcal/mol	1.284	10.566		57 kcal/mol	0.361	0.923	5.987	4.579
58 kcal/mol	2.969	14.581		58 kcal/mol	0.935	2.035	8.962	5.618
59 kcal/mol	4.833	15.117		59 kcal/mol	1.718	3.115	9.422	5.695
60 kcal/mol	5.766	12.234		60 kcal/mol	2.358	3.408	7.184	5.049
61 kcal/mol	2.777	5.893		61 kcal/mol	1.136	1.642	3.461	2.432
62 kcal/mol	0.536	0.404		62 kcal/mol	0.357	0.179	0.191	0.214
63 kcal/mol	0.787	0.593		63 kcal/mol	0.523	0.263	0.280	0.314
64 kcal/mol	0.000	0.000		64 kcal/mol	0.000	0.000	0.000	0.000
65 kcal/mol	0.262	0.198		65 kcal/mol	0.174	0.088	0.093	0.105
66 kcal/mol	0.000	0.000		66 kcal/mol	0.000	0.000	0.000	0.000
67 kcal/mol	0.108	0.082		67 kcal/mol	0.072	0.036	0.039	0.043
68 kcal/mol	0.080	0.060		68 kcal/mol	0.053	0.027	0.028	0.032
69 kcal/mol	0.000	0.000		69 kcal/mol	0.000	0.000	0.000	0.000
70 kcal/mol	0.000	0.000		70 kcal/mol	0.000	0.000	0.000	0.000
71 kcal/mol	0.182	0.138		71 kcal/mol	0.121	0.061	0.065	0.073

Sample G007891								
2-Component				4-Component				
	Gas	Oil			C1	C2-5	C6-14	C15+
45 kcal/mol	0.130	0.970		45 kcal/mol	0.036	0.094	0.417	0.553
46 kcal/mol	0.000	0.000		46 kcal/mol	0.000	0.000	0.000	0.000
47 kcal/mol	0.238	1.772		47 kcal/mol	0.066	0.172	0.762	1.010
48 kcal/mol	0.234	1.736		48 kcal/mol	0.065	0.169	0.747	0.990
49 kcal/mol	0.427	3.173		49 kcal/mol	0.118	0.309	1.365	1.808
50 kcal/mol	0.555	4.125		50 kcal/mol	0.154	0.401	1.774	2.351
51 kcal/mol	0.643	4.777		51 kcal/mol	0.178	0.465	2.055	2.722
52 kcal/mol	0.730	5.920		52 kcal/mol	0.218	0.512	2.429	3.491
53 kcal/mol	0.888	7.202		53 kcal/mol	0.265	0.622	2.955	4.247
54 kcal/mol	0.890	7.700		54 kcal/mol	0.277	0.613	2.368	5.331
55 kcal/mol	1.235	10.685		55 kcal/mol	0.385	0.851	3.286	7.398
56 kcal/mol	1.478	10.272		56 kcal/mol	0.477	1.001	3.853	6.419
57 kcal/mol	1.463	10.167		57 kcal/mol	0.473	0.991	3.813	6.354
58 kcal/mol	1.844	7.976		58 kcal/mol	0.658	1.187	3.815	4.160
59 kcal/mol	1.110	4.800		59 kcal/mol	0.396	0.714	2.296	2.504
60 kcal/mol	0.528	2.282		60 kcal/mol	0.188	0.340	1.092	1.190
61 kcal/mol	0.370	1.600		61 kcal/mol	0.132	0.238	0.765	0.835
62 kcal/mol	0.139	0.601		62 kcal/mol	0.050	0.089	0.288	0.313
63 kcal/mol	0.086	0.374		63 kcal/mol	0.031	0.056	0.179	0.195
64 kcal/mol	0.047	0.203		64 kcal/mol	0.017	0.030	0.097	0.106
65 kcal/mol	0.047	0.203		65 kcal/mol	0.017	0.030	0.097	0.106
66 kcal/mol	0.000	0.000		66 kcal/mol	0.000	0.000	0.000	0.000
67 kcal/mol	0.049	0.211		67 kcal/mol	0.017	0.031	0.101	0.110
68 kcal/mol	0.023	0.097		68 kcal/mol	0.008	0.014	0.047	0.051

Sample G007895								
2-Component				4-Component				
	Gas	Oil			C1	C2-5	C6-14	C15+
40 kcal/mol	0.021	0.249		40 kcal/mol	0.006	0.015	0.085	0.163
41 kcal/mol	0.016	0.184		41 kcal/mol	0.005	0.011	0.063	0.121
42 kcal/mol	0.030	0.350		42 kcal/mol	0.009	0.021	0.120	0.230
43 kcal/mol	0.079	0.911		43 kcal/mol	0.023	0.056	0.313	0.598
44 kcal/mol	0.063	0.727		44 kcal/mol	0.018	0.045	0.250	0.477
45 kcal/mol	0.265	3.075		45 kcal/mol	0.076	0.189	1.058	2.018
46 kcal/mol	0.098	1.142		46 kcal/mol	0.028	0.070	0.393	0.749
47 kcal/mol	0.447	5.183		47 kcal/mol	0.129	0.318	1.783	3.401
48 kcal/mol	0.485	5.635		48 kcal/mol	0.140	0.345	1.938	3.697
49 kcal/mol	0.936	12.534		49 kcal/mol	0.275	0.661	4.040	8.494
50 kcal/mol	1.032	12.868		50 kcal/mol	0.310	0.721	4.079	8.790
51 kcal/mol	1.743	18.547		51 kcal/mol	0.541	1.202	5.948	12.600
52 kcal/mol	1.691	11.849		52 kcal/mol	0.556	1.135	4.509	7.341
53 kcal/mol	0.877	6.143		53 kcal/mol	0.288	0.588	2.338	3.806
54 kcal/mol	0.827	5.793		54 kcal/mol	0.272	0.555	2.204	3.589
55 kcal/mol	0.277	1.943		55 kcal/mol	0.091	0.186	0.739	1.204
56 kcal/mol	0.245	1.715		56 kcal/mol	0.080	0.164	0.653	1.063
57 kcal/mol	0.077	0.543		57 kcal/mol	0.025	0.052	0.206	0.336
58 kcal/mol	0.075	0.525		58 kcal/mol	0.025	0.050	0.200	0.325
59 kcal/mol	0.002	0.018		59 kcal/mol	0.001	0.002	0.007	0.011
60 kcal/mol	0.054	0.376		60 kcal/mol	0.018	0.036	0.143	0.233
61 kcal/mol	0.000	0.000		61 kcal/mol	0.000	0.000	0.000	0.000
62 kcal/mol	0.000	0.000		62 kcal/mol	0.000	0.000	0.000	0.000
63 kcal/mol	0.000	0.000		63 kcal/mol	0.000	0.000	0.000	0.000
64 kcal/mol	0.044	0.306		64 kcal/mol	0.014	0.029	0.117	0.190

14-Component compositional kinetic model

Sample G007868														
Ea	n-C1	n-C2	n-C3	i-C4	n-C4	i-C5	n-C5	n-C6	C7-15	C16-25	C26-35	C36-45	C46-55	C56-80
40 kcal/mol	0.000	0.000	0.000	0.000	0.000	0.000	0.000	0.001	0.003	0.003	0.002	0.001	0.000	0.000
41 kcal/mol	0.006	0.004	0.003	0.002	0.002	0.000	0.001	0.013	0.056	0.051	0.031	0.017	0.008	0.006
42 kcal/mol	0.006	0.004	0.003	0.003	0.002	0.000	0.001	0.014	0.061	0.056	0.034	0.018	0.009	0.007
43 kcal/mol	0.012	0.008	0.006	0.005	0.004	0.001	0.001	0.026	0.117	0.107	0.065	0.035	0.018	0.014
44 kcal/mol	0.016	0.011	0.009	0.007	0.006	0.001	0.002	0.035	0.155	0.143	0.087	0.047	0.024	0.018
45 kcal/mol	0.026	0.017	0.014	0.011	0.009	0.001	0.003	0.057	0.253	0.233	0.141	0.076	0.038	0.029
46 kcal/mol	0.043	0.028	0.022	0.018	0.015	0.002	0.004	0.092	0.408	0.376	0.228	0.123	0.062	0.047
47 kcal/mol	0.067	0.044	0.035	0.028	0.023	0.004	0.007	0.144	0.639	0.589	0.357	0.193	0.097	0.074
48 kcal/mol	0.102	0.067	0.053	0.042	0.035	0.005	0.011	0.220	0.972	0.896	0.544	0.293	0.148	0.113
49 kcal/mol	0.129	0.085	0.067	0.054	0.044	0.007	0.014	0.278	1.230	1.134	0.688	0.371	0.187	0.143
50 kcal/mol	0.288	0.185	0.172	0.096	0.059	0.010	0.046	0.447	2.103	1.938	1.176	0.634	0.320	0.245
51 kcal/mol	0.467	0.299	0.279	0.156	0.096	0.016	0.075	0.723	3.402	3.136	1.903	1.026	0.517	0.396
52 kcal/mol	0.963	0.620	0.575	0.151	0.279	0.030	0.163	1.399	6.467	5.960	3.618	1.950	0.983	0.752
53 kcal/mol	0.713	0.453	0.439	0.082	0.208	0.020	0.137	0.843	4.148	3.955	2.489	1.392	0.727	0.585
54 kcal/mol	1.419	1.027	0.147	0.023	0.067	0.007	0.045	0.471	2.303	1.927	1.055	0.513	0.233	0.154
55 kcal/mol	1.374	0.995	0.142	0.022	0.065	0.007	0.044	0.456	2.229	1.865	1.021	0.496	0.225	0.149
56 kcal/mol	0.413	0.299	0.043	0.007	0.019	0.002	0.013	0.137	0.669	0.560	0.307	0.149	0.068	0.045
57 kcal/mol	0.322	0.233	0.033	0.005	0.015	0.002	0.010	0.107	0.522	0.437	0.239	0.116	0.053	0.035
58 kcal/mol	0.098	0.071	0.010	0.002	0.005	0.000	0.003	0.033	0.159	0.133	0.073	0.035	0.016	0.011
59 kcal/mol	0.101	0.073	0.010	0.002	0.005	0.000	0.003	0.034	0.164	0.137	0.075	0.037	0.017	0.011
60 kcal/mol	0.020	0.014	0.002	0.000	0.001	0.000	0.001	0.007	0.032	0.027	0.015	0.007	0.003	0.002
61 kcal/mol	0.068	0.049	0.007	0.001	0.003	0.000	0.002	0.023	0.110	0.092	0.051	0.025	0.011	0.007
62 kcal/mol	0.000	0.000	0.000	0.000	0.000	0.000	0.000	0.000	0.000	0.000	0.000	0.000	0.000	0.000
63 kcal/mol	0.000	0.000	0.000	0.000	0.000	0.000	0.000	0.000	0.000	0.000	0.000	0.000	0.000	0.000
64 kcal/mol	0.065	0.047	0.007	0.001	0.003	0.000	0.002	0.022	0.105	0.088	0.048	0.023	0.011	0.007

Sample G007878														
Ea	n-C1	n-C2	n-C3	i-C4	n-C4	i-C5	n-C5	n-C6	C7-15	C16-25	C26-35	C36-45	C46-55	C56-80
40 kcal/mol	0.007	0.003	0.004	0.001	0.002	0.007	0.001	0.019	0.092	0.079	0.045	0.022	0.011	0.007
41 kcal/mol	0.007	0.004	0.004	0.001	0.002	0.007	0.001	0.020	0.099	0.085	0.048	0.024	0.011	0.008
42 kcal/mol	0.014	0.007	0.008	0.001	0.004	0.014	0.001	0.040	0.191	0.164	0.093	0.046	0.022	0.015
43 kcal/mol	0.017	0.009	0.010	0.002	0.005	0.017	0.002	0.049	0.237	0.204	0.115	0.058	0.027	0.019
44 kcal/mol	0.022	0.011	0.013	0.002	0.007	0.022	0.002	0.062	0.299	0.257	0.145	0.072	0.034	0.023
45 kcal/mol	0.029	0.014	0.017	0.003	0.009	0.029	0.003	0.082	0.397	0.342	0.193	0.096	0.045	0.031
46 kcal/mol	0.042	0.021	0.024	0.004	0.013	0.042	0.004	0.119	0.576	0.495	0.279	0.140	0.065	0.045
47 kcal/mol	0.081	0.040	0.047	0.008	0.026	0.081	0.007	0.230	1.111	0.956	0.539	0.270	0.126	0.087
48 kcal/mol	0.119	0.059	0.068	0.011	0.037	0.119	0.010	0.335	1.619	1.393	0.785	0.393	0.184	0.127
49 kcal/mol	0.228	0.159	0.117	0.029	0.055	0.127	0.024	0.411	2.579	2.349	1.408	0.749	0.373	0.280
50 kcal/mol	0.311	0.217	0.159	0.040	0.074	0.173	0.032	0.560	3.514	3.200	1.918	1.021	0.508	0.382
51 kcal/mol	0.564	0.316	0.358	0.100	0.154	0.298	0.082	1.000	5.664	5.518	3.553	2.032	1.087	0.903
52 kcal/mol	0.506	0.287	0.337	0.071	0.123	0.197	0.081	0.847	4.766	4.016	2.215	1.085	0.497	0.333
53 kcal/mol	0.891	0.431	0.568	0.135	0.203	0.261	0.140	1.019	6.092	3.764	1.488	0.523	0.171	0.074
54 kcal/mol	0.462	0.224	0.295	0.070	0.105	0.136	0.073	0.529	3.162	1.954	0.772	0.271	0.089	0.038
55 kcal/mol	0.078	0.038	0.050	0.012	0.018	0.023	0.012	0.089	0.533	0.330	0.130	0.046	0.015	0.006
56 kcal/mol	0.065	0.031	0.041	0.010	0.015	0.019	0.010	0.074	0.445	0.275	0.109	0.038	0.012	0.005
57 kcal/mol	0.000	0.000	0.000	0.000	0.000	0.000	0.000	0.000	0.000	0.000	0.000	0.000	0.000	0.000
58 kcal/mol	0.003	0.002	0.002	0.001	0.001	0.001	0.001	0.004	0.023	0.014	0.006	0.002	0.001	0.000
59 kcal/mol	0.007	0.004	0.005	0.001	0.002	0.002	0.001	0.008	0.050	0.031	0.012	0.004	0.001	0.001
60 kcal/mol	0.005	0.002	0.003	0.001	0.001	0.001	0.001	0.005	0.031	0.019	0.008	0.003	0.001	0.000
61 kcal/mol	0.000	0.000	0.000	0.000	0.000	0.000	0.000	0.000	0.000	0.000	0.000	0.000	0.000	0.000
62 kcal/mol	0.000	0.000	0.000	0.000	0.000	0.000	0.000	0.000	0.000	0.000	0.000	0.000	0.000	0.000
63 kcal/mol	0.000	0.000	0.000	0.000	0.000	0.000	0.000	0.000	0.000	0.000	0.000	0.000	0.000	0.000
64 kcal/mol	0.015	0.007	0.009	0.002	0.003	0.004	0.002	0.017	0.101	0.062	0.025	0.009	0.003	0.001

Sample G007883														
Ea	n-C1	n-C2	n-C3	i-C4	n-C4	i-C5	n-C5	n-C6	C7-15	C16-25	C26-35	C36-45	C46-55	C56-80
41 kcal/mol	0.003	0.002	0.002	0.001	0.001	0.000	0.000	0.003	0.029	0.026	0.016	0.009	0.004	0.003
42 kcal/mol	0.005	0.003	0.003	0.002	0.002	0.001	0.001	0.005	0.043	0.040	0.024	0.013	0.006	0.005
43 kcal/mol	0.006	0.004	0.004	0.002	0.002	0.001	0.001	0.006	0.058	0.053	0.032	0.017	0.009	0.006
44 kcal/mol	0.010	0.006	0.006	0.003	0.004	0.001	0.001	0.010	0.092	0.085	0.051	0.027	0.014	0.010
45 kcal/mol	0.016	0.010	0.009	0.005	0.006	0.002	0.002	0.016	0.150	0.137	0.083	0.044	0.022	0.017
46 kcal/mol	0.024	0.014	0.014	0.008	0.009	0.003	0.003	0.023	0.222	0.203	0.123	0.066	0.033	0.025
47 kcal/mol	0.038	0.022	0.022	0.013	0.014	0.004	0.005	0.037	0.349	0.320	0.193	0.103	0.052	0.039
48 kcal/mol	0.051	0.030	0.030	0.017	0.019	0.006	0.007	0.050	0.476	0.436	0.263	0.141	0.071	0.053
49 kcal/mol	0.102	0.060	0.059	0.035	0.037	0.012	0.014	0.099	0.943	0.864	0.521	0.279	0.140	0.106
50 kcal/mol	0.158	0.093	0.092	0.054	0.058	0.019	0.022	0.154	1.464	1.342	0.809	0.433	0.217	0.165
51 kcal/mol	0.270	0.167	0.160	0.056	0.102	0.019	0.049	0.247	2.150	2.005	1.232	0.672	0.343	0.267
52 kcal/mol	0.443	0.274	0.262	0.092	0.166	0.031	0.081	0.404	3.519	3.281	2.017	1.101	0.561	0.437
53 kcal/mol	0.727	0.446	0.438	0.110	0.259	0.033	0.147	0.663	5.008	4.643	2.836	1.538	0.780	0.602
54 kcal/mol	0.769	0.480	0.454	0.075	0.257	0.026	0.155	0.612	4.525	4.195	2.562	1.390	0.705	0.543
55 kcal/mol	0.938	0.520	0.543	0.079	0.275	0.029	0.178	0.704	4.472	3.552	1.839	0.845	0.363	0.223
56 kcal/mol	0.558	0.309	0.323	0.047	0.163	0.017	0.106	0.419	2.660	2.113	1.094	0.503	0.216	0.133
57 kcal/mol	0.203	0.113	0.118	0.017	0.059	0.006	0.038	0.152	0.968	0.769	0.398	0.183	0.079	0.048
58 kcal/mol	0.157	0.087	0.091	0.013	0.046	0.005	0.030	0.117	0.746	0.593	0.307	0.141	0.061	0.037
59 kcal/mol	0.068	0.038	0.039	0.006	0.020	0.002	0.013	0.051	0.323	0.256	0.133	0.061	0.026	0.016
60 kcal/mol	0.042	0.023	0.024	0.004	0.012	0.001	0.008	0.031	0.200	0.159	0.082	0.038	0.016	0.010
61 kcal/mol	0.005	0.003	0.003	0.000	0.002	0.000	0.001	0.004	0.025	0.020	0.010	0.005	0.002	0.001
62 kcal/mol	0.027	0.015	0.016	0.002	0.008	0.001	0.005	0.020	0.129	0.102	0.053	0.024	0.010	0.006
63 kcal/mol	0.000	0.000	0.000	0.000	0.000	0.000	0.000	0.000	0.000	0.000	0.000	0.000	0.000	0.000
64 kcal/mol	0.000	0.000	0.000	0.000	0.000	0.000	0.000	0.000	0.000	0.000	0.000	0.000	0.000	0.000
65 kcal/mol	0.023	0.013	0.013	0.002	0.007	0.001	0.004	0.017	0.111	0.088	0.045	0.021	0.009	0.006

Sample G007887														
Ea	n-C1	n-C2	n-C3	i-C4	n-C4	i-C5	n-C5	n-C6	C7-15	C16-25	C26-35	C36-45	C46-55	C56-80
47 kcal/mol	0.026	0.011	0.013	0.002	0.013	0.024	0.002	0.038	0.386	0.215	0.076	0.024	0.007	0.003
48 kcal/mol	0.003	0.001	0.002	0.000	0.002	0.003	0.000	0.005	0.051	0.028	0.010	0.003	0.001	0.000
49 kcal/mol	0.046	0.019	0.023	0.004	0.024	0.043	0.004	0.068	0.689	0.384	0.136	0.043	0.013	0.005
50 kcal/mol	0.036	0.015	0.018	0.003	0.018	0.033	0.003	0.053	0.538	0.300	0.106	0.033	0.010	0.004
51 kcal/mol	0.045	0.019	0.022	0.004	0.023	0.042	0.004	0.067	0.676	0.376	0.133	0.042	0.012	0.005
52 kcal/mol	0.013	0.005	0.006	0.001	0.007	0.012	0.001	0.019	0.193	0.108	0.038	0.012	0.004	0.001
53 kcal/mol	0.032	0.013	0.016	0.003	0.016	0.030	0.003	0.047	0.478	0.266	0.094	0.030	0.009	0.003
54 kcal/mol	0.083	0.035	0.042	0.007	0.043	0.078	0.008	0.124	1.255	0.699	0.247	0.078	0.023	0.009
55 kcal/mol	0.128	0.054	0.064	0.011	0.066	0.120	0.012	0.192	1.935	1.078	0.381	0.120	0.035	0.013
56 kcal/mol	0.215	0.091	0.108	0.019	0.111	0.201	0.020	0.322	3.245	1.807	0.639	0.201	0.059	0.022
57 kcal/mol	0.361	0.152	0.181	0.032	0.186	0.338	0.034	0.540	5.446	3.034	1.073	0.337	0.099	0.037
58 kcal/mol	0.935	0.408	0.440	0.109	0.394	0.579	0.104	0.962	8.000	3.944	1.223	0.337	0.087	0.028
59 kcal/mol	1.718	0.673	0.741	0.187	0.568	0.750	0.195	1.113	8.309	4.028	1.226	0.331	0.084	0.025
60 kcal/mol	2.358	0.786	0.878	0.206	0.617	0.686	0.237	1.048	6.136	3.370	1.174	0.362	0.105	0.038
61 kcal/mol	1.136	0.378	0.423	0.099	0.297	0.330	0.114	0.505	2.956	1.623	0.565	0.174	0.051	0.019
62 kcal/mol	0.357	0.059	0.066	0.008	0.031	0.004	0.011	0.037	0.153	0.116	0.057	0.025	0.010	0.006
63 kcal/mol	0.523	0.086	0.097	0.012	0.045	0.006	0.016	0.055	0.225	0.170	0.084	0.036	0.015	0.008
64 kcal/mol	0.000	0.000	0.000	0.000	0.000	0.000	0.000	0.000	0.000	0.000	0.000	0.000	0.000	0.000
65 kcal/mol	0.174	0.029	0.032	0.004	0.015	0.002	0.005	0.018	0.075	0.057	0.028	0.012	0.005	0.003
66 kcal/mol	0.000	0.000	0.000	0.000	0.000	0.000	0.000	0.000	0.000	0.000	0.000	0.000	0.000	0.000
67 kcal/mol	0.072	0.012	0.013	0.002	0.006	0.001	0.002	0.008	0.031	0.023	0.012	0.005	0.002	0.001
68 kcal/mol	0.053	0.009	0.010	0.001	0.005	0.001	0.002	0.006	0.023	0.017	0.008	0.004	0.002	0.001
69 kcal/mol	0.000	0.000	0.000	0.000	0.000	0.000	0.000	0.000	0.000	0.000	0.000	0.000	0.000	0.000
70 kcal/mol	0.000	0.000	0.000	0.000	0.000	0.000	0.000	0.000	0.000	0.000	0.000	0.000	0.000	0.000
71 kcal/mol	0.121	0.020	0.023	0.003	0.010	0.001	0.004	0.013	0.052	0.039	0.019	0.008	0.003	0.002

Sample G007891														
Ea	n-C1	n-C2	n-C3	i-C4	n-C4	i-C5	n-C5	n-C6	C7-15	C16-25	C26-35	C36-45	C46-55	C56-80
45 kcal/mol	0.036	0.015	0.015	0.002	0.011	0.048	0.004	0.098	0.319	0.271	0.150	0.074	0.034	0.023
46 kcal/mol	0.000	0.000	0.000	0.000	0.000	0.000	0.000	0.000	0.000	0.000	0.000	0.000	0.000	0.000
47 kcal/mol	0.066	0.028	0.027	0.003	0.020	0.088	0.007	0.179	0.583	0.494	0.275	0.136	0.062	0.042
48 kcal/mol	0.065	0.027	0.026	0.003	0.019	0.086	0.007	0.176	0.571	0.485	0.269	0.133	0.061	0.042
49 kcal/mol	0.118	0.050	0.048	0.005	0.036	0.157	0.013	0.321	1.044	0.886	0.492	0.243	0.112	0.076
50 kcal/mol	0.154	0.065	0.063	0.007	0.046	0.204	0.017	0.418	1.357	1.151	0.640	0.316	0.146	0.099
51 kcal/mol	0.178	0.075	0.072	0.008	0.053	0.236	0.019	0.484	1.571	1.333	0.741	0.366	0.169	0.114
52 kcal/mol	0.218	0.118	0.113	0.023	0.054	0.171	0.032	0.358	2.071	1.733	0.949	0.461	0.209	0.139
53 kcal/mol	0.265	0.144	0.137	0.028	0.066	0.208	0.039	0.435	2.519	2.108	1.154	0.561	0.255	0.169
54 kcal/mol	0.277	0.160	0.158	0.035	0.078	0.131	0.051	0.329	2.039	2.097	1.431	0.868	0.492	0.443
55 kcal/mol	0.385	0.223	0.219	0.048	0.108	0.182	0.071	0.457	2.829	2.910	1.986	1.204	0.682	0.615
56 kcal/mol	0.477	0.262	0.284	0.060	0.146	0.149	0.099	0.519	3.333	2.981	1.752	0.914	0.446	0.326
57 kcal/mol	0.473	0.260	0.281	0.059	0.145	0.148	0.098	0.514	3.299	2.950	1.734	0.905	0.442	0.323
58 kcal/mol	0.658	0.327	0.371	0.069	0.183	0.113	0.124	0.584	3.231	2.337	1.095	0.455	0.177	0.096
59 kcal/mol	0.396	0.197	0.224	0.042	0.110	0.068	0.074	0.352	1.945	1.407	0.659	0.274	0.106	0.058
60 kcal/mol	0.188	0.094	0.106	0.020	0.052	0.032	0.035	0.167	0.925	0.669	0.313	0.130	0.051	0.027
61 kcal/mol	0.132	0.066	0.075	0.014	0.037	0.023	0.025	0.117	0.648	0.469	0.220	0.091	0.035	0.019
62 kcal/mol	0.050	0.025	0.028	0.005	0.014	0.008	0.009	0.044	0.243	0.176	0.082	0.034	0.013	0.007
63 kcal/mol	0.031	0.015	0.017	0.003	0.009	0.005	0.006	0.027	0.151	0.109	0.051	0.021	0.008	0.004
64 kcal/mol	0.017	0.008	0.009	0.002	0.005	0.003	0.003	0.015	0.082	0.060	0.028	0.012	0.005	0.002
65 kcal/mol	0.017	0.008	0.009	0.002	0.005	0.003	0.003	0.015	0.082	0.060	0.028	0.012	0.005	0.002
66 kcal/mol	0.000	0.000	0.000	0.000	0.000	0.000	0.000	0.000	0.000	0.000	0.000	0.000	0.000	0.000
67 kcal/mol	0.017	0.009	0.010	0.002	0.005	0.003	0.003	0.015	0.086	0.062	0.029	0.012	0.005	0.003
68 kcal/mol	0.008	0.004	0.005	0.001	0.002	0.001	0.002	0.007	0.039	0.029	0.013	0.006	0.002	0.001

Sample G007895														
Ea	**n-C1**	**n-C2**	**n-C3**	**i-C4**	**n-C4**	**i-C5**	**n-C5**	**n-C6**	**C7-15**	**C16-25**	**C26-35**	**C36-45**	**C46-55**	**C56-80**
40 kcal/mol	0.006	0.004	0.003	0.000	0.002	0.006	0.001	0.017	0.069	0.068	0.044	0.026	0.014	0.012
41 kcal/mol	0.005	0.003	0.002	0.000	0.002	0.004	0.000	0.012	0.051	0.050	0.033	0.019	0.010	0.009
42 kcal/mol	0.009	0.005	0.004	0.000	0.003	0.008	0.001	0.023	0.097	0.096	0.062	0.036	0.019	0.016
43 kcal/mol	0.023	0.013	0.012	0.001	0.008	0.021	0.002	0.061	0.253	0.249	0.162	0.094	0.051	0.043
44 kcal/mol	0.018	0.010	0.009	0.001	0.006	0.016	0.002	0.048	0.202	0.199	0.129	0.075	0.040	0.034
45 kcal/mol	0.076	0.044	0.039	0.004	0.026	0.069	0.007	0.205	0.853	0.840	0.547	0.316	0.171	0.144
46 kcal/mol	0.028	0.016	0.015	0.001	0.009	0.026	0.003	0.076	0.317	0.312	0.203	0.117	0.063	0.054
47 kcal/mol	0.129	0.074	0.066	0.006	0.043	0.117	0.012	0.345	1.438	1.415	0.922	0.533	0.288	0.243
48 kcal/mol	0.140	0.080	0.072	0.006	0.047	0.127	0.013	0.375	1.563	1.538	1.002	0.579	0.313	0.264
49 kcal/mol	0.275	0.167	0.157	0.025	0.100	0.168	0.044	0.449	3.591	3.535	2.302	1.331	0.720	0.607
50 kcal/mol	0.310	0.191	0.190	0.031	0.113	0.139	0.058	0.405	3.674	3.635	2.380	1.384	0.752	0.639
51 kcal/mol	0.541	0.331	0.344	0.059	0.194	0.161	0.114	0.559	5.388	5.276	3.417	1.965	1.057	0.885
52 kcal/mol	0.556	0.311	0.353	0.060	0.186	0.107	0.118	0.493	4.016	3.500	2.001	1.017	0.483	0.340
53 kcal/mol	0.288	0.161	0.183	0.031	0.096	0.055	0.061	0.256	2.082	1.815	1.038	0.527	0.250	0.176
54 kcal/mol	0.272	0.152	0.173	0.029	0.091	0.052	0.058	0.241	1.963	1.711	0.979	0.497	0.236	0.166
55 kcal/mol	0.091	0.051	0.058	0.010	0.030	0.018	0.019	0.081	0.658	0.574	0.328	0.167	0.079	0.056
56 kcal/mol	0.080	0.045	0.051	0.009	0.027	0.015	0.017	0.071	0.581	0.507	0.290	0.147	0.070	0.049
57 kcal/mol	0.025	0.014	0.016	0.003	0.009	0.005	0.005	0.023	0.184	0.160	0.092	0.047	0.022	0.016
58 kcal/mol	0.025	0.014	0.016	0.003	0.008	0.005	0.005	0.022	0.178	0.155	0.089	0.045	0.021	0.015
59 kcal/mol	0.001	0.000	0.001	0.000	0.000	0.000	0.000	0.001	0.006	0.005	0.003	0.002	0.001	0.001
60 kcal/mol	0.018	0.010	0.011	0.002	0.006	0.003	0.004	0.016	0.128	0.111	0.064	0.032	0.015	0.011